TU Delft

Delft University of Technology

MSc Thesis

Experimental Investigation of Submarine Landslide Induced Tsunami Waves

Nataliya Filipouskaya

Cover picture retrieved from: https://www.redwallpapers.com/wallpaper/photography-of-barrel-wave-free-stock-photo-image-wallpaper

Delft University of Technology, May 2019

EXPERIMENTAL INVESTIGATION OF SUBMARINE LANDSLIDE INDUCED TSUNAMI WAVES

MSC thesis

in partial fulfilment of the requirements for the degree of

Master of Science in Geo-Engineering

at Delft University of Technology

by Nataliya Filipouskaya

Student number: 4743601

Supervisor: Dr. Amin Askarinejad

Thesis committee: Prof. Dr. Michael Hicks, TU Delft

Dr. ir. Robert Lanzafame, TU Delft

Arash Maghsoudloo MSc., TU Delft

to be defended publicly on May 24th, 2019

Delft, 2019

TU Delft Delft University of Technology

Contents

1. Motivation 1

2. Introduction 3

3. Research objectives 4

4. Literature review 6

5. Experimental set-up in the Liquefaction Tank 10

5.1 Introduction 10

5.2 Instrumentation 10

5.3 Summary of experiments 15

5.1 Synchronisation of data 21

5.2 Wavelet analysis 22

6. Analysis of experiments results 28

6.1 Test 1 28

6.1.1 Slope failure image analysis 28

6.1.2 Wave localisation 29

6.1.3 Extracted wave 30

6.1.4 Pressure measurements 33

6.1.5 Soil mass acceleration 34

6.2 Test 2 & 3 38

6.2.1 Slope failure image analysis 38

6.2.2 Wave localisation 39

6.2.3 Extracted wave 41

6.2.4 Pressure measurements 43

6.2.5 Soil mass acceleration 46

6.3 Test 4 49

6.3.1 Slope failure image analysis 49

6.3.2 Wave localisation 51
6.3.3 Extracted wave 54
6.3.4 Pressure measurements 61
6.3.5 Soil mass acceleration 66
7. Evaluation of the experiments outcome and discussion 70
7.1 Summary wave characteristics vs. slope failure parameters 70
7.2 Validation of predictive formulae 75
7.3 Recommendations and remarks on experimental set-up 78
7.4 Wave reflection 80
8. Summary and Conclusions 82
8.1 Recommendation for future research 85
Appendix A – Experiments in a wave flume, wave absorber design 87
Appendix B – Measurements Tests 1 – 4 101
Appendix C – Validation of predictive formulae, calculation sheets 119
Appendix D – MatLab code for sensitivity study of predictive formulae 124
Appendix E – Schedule 129
Bibliography 130

1. Motivation

This MSc thesis was initiated as part of an interdisciplinary project researching post-disaster coastal reconstruction in the Tohoku region of Japan. On March 11, 2011, a highly destructive earthquake induced tsunami hit the north-eastern part of Honshu island, causing enormous damage to numerous small towns along the coast. Since 2011 various studies have been completed to better understand this historical event and explain the nature of tsunamis. However, some researchers have noted the inability of tsunami models, using only an earthquake as a source, to reproduce the timing, frequency and wave heights recorded along the Tohoku coast in March 2011. The differences are especially striking for the Sanriku coast – a relatively small area north of Sendai plain characterised by a ria-type coastline. D. R. Tappin et al. (2014) suggested that a secondary source is required to explain the deviating model results and locally higher tsunami waves, such as a submarine landslide.

Several other historical tsunami events have been caused by a submarine mass failure (SMF). The tsunami in Papua New Guinea in 1998 was caused by a submarine slump (D. R. Tappin, Watts, P., McMurtry, G. M., 1998) as well as the tsunami in Skagway, Alaska in 1994 that was induced by the sliding of loose alluvial sediments down the fjord (Watts et al., 2005). The recent tsunami in Sulawesi, Indonesia on September 28, 2018, was unexpected, as strike-slip faults typically do not create vertical seabed displacement and therefore are considered unlikely to cause a large tsunami. However, the Sulawesi earthquake was followed by a series of destructive tsunamis causing over 2000 casualties. To explain this event, field investigations were performed which found sufficient evidence of landslides and liquefaction flow in coastal areas of Palu bay, which could possibly induce tsunami waves (Sassa & Takagawa, 2018).

In low-lying coastal areas, tsunamis are an unavoidable hazard to human lives. A common way of addressing natural disasters of this scale is with timely warning and evacuation, which in turn requires appropriate techniques for prediction of an upcoming disaster. While earthquake induced tsunamis provide a sort of a warning signal, tsunamis generated by a submarine landslide can be much more difficult to predict. Landslide tsunamis are usually concentrated in local areas and do not propagate far, as they are more dispersive than earthquake tsunamis. However, the source of landslide tsunamis is often located on a continental slope near the coastal line. As a result, waves reach the shore in a very short period of time and run-up heights can reach extremely high levels (Harbitz et al., 2006). Thus, landslide generated tsunamis pose a serious hazard to densely populated coastal areas.

Within the scope of this thesis, a number of experimental simulations on submarine slope failures were conducted in a so-called static liquefaction tank – a unique testing facility for large scale experiments at the Geo-Engineering Laboratory of TU Delft. To improve the understanding of tsunami generation, this study focuses on the moment of onset of a submarine slope failure and

wave generation, linking the processes within failing soil mass to initial characteristics of waves. This study illustrates the connection between these two processes that are usually only considered individually from either a geotechnical or hydraulic perspective.

This study is unique due to its multidisciplinary approach, as the landslide and the process of wave generation are observed from geotechnical and hydraulic engineering points of view, in order to join both disciplines to better understand the complex nature of tsunami generation. The focus is primarily on physical modelling, development of an experimental set-up for wave generation by submarine slope failure, laboratory experiments and analysis of obtained data. This study aims to provide foundational knowledge for future research on the generation of tsunami to allow better prediction of possible future disasters.

2. Introduction

The objective of this study is to investigate the relationship between submarine mass failure (SMF) characteristics and induced waves by means of physical modelling. Using facilities of the Geo-Engineering laboratory of TU Delft, we conduct a number of experiments on wave generation by a submarine landslide. Experimental data is used to investigate the geotechnical processes within the failing slope body and the induced wave formation as well as the interaction between both.

Based on available scientific literature, the state-of-the-art formulae for prediction of wave amplitude and wave length are determined. These equations mostly result from numerous analytical and numerical models, such as presented in Pelinovsky and Poplavsky (1996), Watts and Grilli (2005), Mohammed and Fritz (2012), McFall and Fritz (2016). Moreover, multiple case studies and some experimental work have been done to validate and prove these models.

Due to the problem complexity and large number of influence parameters, all of the models adopt a number of simplifications. For instance, idealised geometry and motion trajectory of the SMF, or a simplified description of soil behaviour using a single value of friction angle. The experimental work, that validates these models, often contains certain limiting assumptions and does not cover all the possible scenarios of SMF. For the sake of simplicity, submarine landslides are often simulated with rigid Gaussian shaped bodies, e.g. made of metal. This simplification disregards the ability of a landslide to change its shape and volume during failure. The retrogressive behaviour of failures also cannot be seen from such models as well as interaction between water in soil pores and water column above the soil surface.

Furthermore, idealised mass motion along a pre-defined sliding plane can be hardly compared to deep-seated rotational SMF (the so called submarine slump) or more complex flow-type of failures. Earlier experiments on submarine landslide induced waves, presented by Wiegel (1955), P. L. F. Liu et al. (2005), Grilli and Watts (2005), Enet and Grilli (2007), applied a solid body moving on a pre-defined sliding plane in order to simulate the slide. In contrast, the experiments described in this thesis use a different approach: an underwater sand slope is triggered to failure, where the type of failure and slide motion is not pre-defined. This results in complex landslide morphology, similar to the real landslides occurring in nature, such as liquefaction flow or deep-seated slumps.

In this study, close attention is paid amongst others to design of a triggering mechanism for controlled slope failure, creation of a suitable wave environment and minimising wave reflection by means of wave absorbers, signal processing and enabling proper interpretation of data.

3. Research objectives

Main research objectives

The main research objectives for the current study can be summarised as follows:

1. Using the static liquefaction tank, develop an experimental set-up, suitable for triggering of a submarine landslide, while enabling measurements of generated waves;
2. Using the test results, investigate the link between geotechnical parameters (density of material, type of failure, excess pore water pressure, acceleration of failing soil mass) and hydrodynamic parameters of induced waves (wave amplitude, length, period and frequency) at the source of wave generation.
3. Validate the available formulae for prediction of initial wave characteristics.

Sub-tasks

Physical modelling of a large scale can be extremely time and material consuming. This creates a range of sub-tasks and questions related to technical performance of laboratory experiments to be addressed prior to tests, for example:

1. Triggering mechanism for controlled slope failure
2. Wave absorber to reduce reflection from the tank walls
3. Wave measuring equipment
4. Data acquisition and synchronisation

Design of wave absorbing elements is separately discussed in Appendix A, which includes a separate experimental investigation, based on tests in a wave flume.

Signal processing poses a challenge for any kind of experimental work analysis. Obtained at a high frequency, test data often can't be analysed directly and require first a significant level of pre-processing e.g. to remove noise and unwanted trends. Measurements performed in a very sensitive wave field are usually strongly affected by surface waves and perturbations. A powerful tool to denoise, detrend and decompose obtained data into a time-frequency spectrum is the wavelet analysis, which is discussed in detail in this study.

At the time point of tsunami wave generation by a SMF, the decisive wave characteristics are the initial wave amplitude and wave length. For these characteristic values there are several predictive equations suggested in the literature (see the literature review). The equations for a deep-seated type of SMF and the liquefaction flow type are lacking sufficient validation e.g. by physical modelling. Based on results of our physical experiments, we want to validate and possibly improve the available formulae for wave amplitude and wave length prediction at the moment of initiation of the wave. Here, special attention will be paid to mass acceleration at the moment of failure, as this parameter has not been yet included into the predictive formulae.

In summary, the sub-tasks can be categorised and included to the main research objectives as follows:

1. *Using the static liquefaction tank, develop an experimental set-up, suitable for triggering of a submarine landslide, while enabling measurements of generated waves:*
    a. Triggering mechanism for controlled slope failure
    b. Wave absorber design based on experiments in a wave flume
    c. Wave measuring equipment and synchronisation of data
    d. Evaluation of measuring equipment limitations
    e. Recommendations for laboratory set-up for future research
2. *Using the test results, investigate the link between geotechnical parameters (density of material, type of failure, excess pore water pressure, acceleration of failing soil mass) and hydrodynamic parameters of induced waves (wave amplitude, length, period and frequency) at the source of wave generation.*
    a. Data acquisition and pre-processing
    b. Decomposition of wave data and extraction of relevant waves
3. *Validation of the available formulae for prediction of initial wave characteristics.*
    a. Comparison of predicted and measured parameters
    b. Sensitivity analysis of predictive wave models

4. Literature review

In general tsunami waves originate from vertical displacement of seabed. This displacement can be caused by certain types of earthquakes, volcanic activity or underwater landslides. While seismic activity account for the major part of great tsunami events, roughly 10% of tsunamis observed in the oceans are triggered by submarine mass failures (SMF) (Mohammed & Fritz, 2012). Whereas both submarine slide (translational type of mass failure) and slumps (rotational type of mass failure) are equally common.

Submarine slides or slumps can be seen as comparably small source of initial displacement of water column, taking into account its typical spatial extension (10^2 – 10^3 m) in comparison to dimensions of a seismic source (10^4 – 10^5 m) (Levin & Nosov, 2005). As a result, SMF can be considered as a point source, generating waves that are usually shorter and more dispersive than co-seismic waves. However, tsunamis generated by SMF often have high initial wave amplitudes and due to their nearshore location, can locally produce very large run-up heights, resulting in a disastrous impact to highly populated coastal areas. In addition, failures of submarine slopes are often triggered by earthquakes, so that the generated wave can overlap with the coseismic wave creating a local increase of wave impact.

A term 'submarine landslide' used in this thesis describes a general definition for submarine high density flows, i.e. slides, slumps, debris flow, mud or granular flow (Harbitz et al., 2006). Submarine landslides have been extensively studied by i.a. Wiegel (1955), Jiang and Leblond (1992, 1994), Pelinovsky and Poplavsky (1996), Watts (1997). Physical modelling that underlies these studies considered in most cases a 2D condition with a solid body (a block or a body of Gaussian shape in later studies) sliding on a pre-defined inclined surface. Further development went towards three-dimensional landslides and wave propagation as well as modelling of a deformable slide body with granular material instead of rigid block. 3D landslides were studied by i.a. Grilli and Watts (2005), Enet and Grilli (2007). Physical modelling using granular material was conducted for a planar slope by Mohammed and Fritz (2012) and for a conical island by McFall and Fritz (2016). Using granular material includes an important feature of deformation of the slide during its motion. Slide deformation has been observed having an increasing effect on the wave length and reducing wave's dispersive behaviour (Harbitz et al., 2006). As a result, models with granular landslides describe generation of a tsunami wave more accurately.

In the meantime a number of numerical models were developed to simulate tsunami waves generated by SMF. These models are mainly focused on reproducing of well-known historical tsunami events, for which the wave heights were recorded and the geometry of SMF could be estimated based on field data. Grilli and Watts (2005) conducted numerical modelling of tsunami generation by SMF with 2D fully nonlinear potential flow (FNPF) model. Modelling results for translational slides were validated by laboratory experiments, performed with a 2D rigid body

frictionless sliding on an aluminium sloping surface. Using this validated numerical model, Watts et al. (2005) performed a number of simulations for different geometries of SMF, taking into account and pointing out the distinction between translational and rotational types of SMF. Based on the simulations results, predictive equations for initial wave amplitude and wave length were empirically developed. The equations are given for submarine slides and slumps, along with restrictions and recommendations for their appropriate use. The equations are explicitly developed for the time period of wave initiation and therefore valid only for the wave characteristics near the tsunami source.

Predictive equations for wave characteristic parameters

In this study we focus on rotational 2D submarine mass failures, as this model represents the most probable experimental conditions. Thereby the initial wave amplitude η_{init} can be calculated with the following predictive formula suggested by Watts et al. (2005):

$$\eta_{init} = S_0 \left(\frac{0.131}{\sin\theta}\right)\left(\frac{T}{L}\right)\left(\frac{b\sin\theta}{d}\right)\left(\frac{L}{R}\right)^{0.63}(\Delta\Phi)^{0.39}(1.47 - 0.35(\gamma - 1))(\gamma - 1) \qquad (1)$$

Where S_0 is SMF motion defined by Eq. (2), θ – slope angle, T – slump thickness, L – slump length, R – radius of the rotation, ΔΦ – angular displacement d – initial submergence of the mass centre, γ – density of the soil.

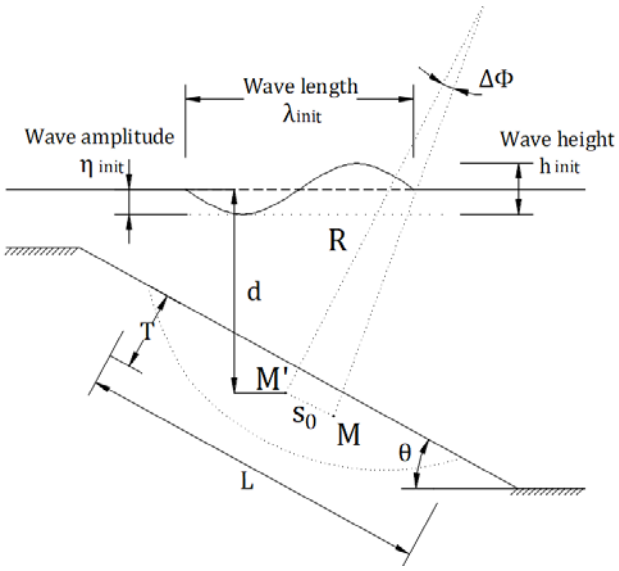

Figure 1: Sketch of SMF generating tsunami wave, geometry and main parameters

The motion of the soil mass is defined as linear displacement of the mass centre of the slump. This displacement can be determined as follows:

$$S_0 = \frac{R\Delta\Phi}{2} = R\,C_n\cos\theta \qquad (2)$$

where C_n is a basal Coulomb friction coefficient. In case of slumps it represents a shear term, based on the assumption of constant shear stress S_u during the motion (Watts et al., 2005). For normally consolidated marine deposits, by averaging along the failure plane assuming ratio of thickness to length of the slump being small (T/b << 1), shear stress can be found as:

$$S_u \cong 0.19\,(\rho_l - \rho_w) g\, T \tag{3}$$

For typical slumps C_n can be then determined according to Grilli and Watts (2005) as:

$$C_n = S_u \frac{4}{\pi(\rho_l - \rho_w) g\, T \cos\theta} \cong 0.76 \frac{1}{\pi \cos\theta} \tag{4}$$

The angular displacement ΔΦ can be then calculated from Eq. (2). However, Watts et al. (2005) is mentioning that the assumption made with Eq. (3) can be argued. The equation is not uniformly valid as in some cases the shear stress and therefore the angular displacement can be expected being less, while taking into account e.g. remoulding effects at the failure plane, a higher value can result. So, the actual angular displacement, if measured, can be a starting point to back figure the actual shear stress along the failure surface. As well as the mass motion may be determined by observation.

The importance of the initial acceleration of the slide is often mentioned in the literature. The initial acceleration determines the velocity of the slump motion and therefore its Froude number. As the Froude number influences the character of wave generating process, it basically controls what type of wave is generated. In other words the wave length is highly dependent on Froude number, also the wave amplitude but to a lesser extent.

Grilli and Watts (2005) suggest the following way to determine initial acceleration of a submarine slump:

$$a_0 = \frac{S_0}{t_0^2} \tag{5}$$

$$\text{with} \quad S_0 = \frac{R\Delta\Phi}{2} \quad \text{and} \quad t_0 = \sqrt{\frac{R}{g}}\sqrt{\frac{\gamma + C_m}{\gamma - 1}} \tag{6}$$

$$a_0 = \frac{\Delta\Phi}{2} \frac{g(\gamma - 1)}{\gamma + C_m} \tag{7}$$

Whereas C_m is a hydrodynamic mass coefficient, which is in general a function of SMF shape and a weak function of submergence depth d (Grilli & Watts, 2005). An appropriate value of mass

coefficient C_m = 1 is suggested, based on experimental work by Watts (1997), Grilli and Watts (2005), Enet and Grilli (2007).

Finally, the initial wave length of generated tsunami wave can be expressed as:

$$\lambda_{init} = t_0\sqrt{g\ d} \tag{8}$$

Whereas t_0 is a characteristic motion time of the SMF and can be determined with Eq. (6). The characteristic motion time represents also the duration of slope failure process that contributes to the most of the wave generation. Simplified this period of time can be assumed as the one representing the initial state of a wave at its source.

It is highly important to take into account the limitation of the applicability of the formulae mentioned by authors. The predictive equations of wave characteristics are developed for a 2D condition and apply only to the wave near the source. No wave propagation was taken into account. For 3D SMF there are correction factors available. Moreover, due to interpolation implied by curve fitting, certain ratios of geometric parameters introduce inaccuracies and should be avoided. So, most precise results follow with low ratio of T/b and low values of slope inclination. Large d/b ratio result in more accurate output and its lower bound at d/b > 0.06 is required to prevent nonlinear breaking wave generation.

The equations (1) – (8) are considered in this work as the state-of-the-art for predictive tsunami formulae. While performing the physical modelling, the major attention will be paid to the parameters mentioned in these formulae, such as initial acceleration a_0, mass motion S_0 and angular displacement $\Delta\Phi$. The limitations applicable to the predictive equations will be taken into account when preparing the model. Finally, we aim to measure the main wave characteristics such as wave amplitude and length just at the onset of slope failure.

5. Experimental set-up in the Liquefaction Tank

5.1 Introduction

An experimental set-up is developed at the Geo-Engineering Laboratory of Delft University of Technology for laboratory simulations of submarine slope failures while measuring elevation of the water surface. These experiments focus on investigation of tsunami generation by submarine landslides. Using a unique testing facility – the liquefaction tank – an underwater slope is constructed from uniform fine sand and then triggered to failure. In order to record water waves, a set of two wave gauges is installed above the slope as well as an electromagnetic liquid velocity meter (EMS) to measure horizontal water velocity. The waves are studied at the moment of initiation of landslides, excluding the period of wave propagation. Due to relatively short length of the tank, propagating waves reach the walls of the tank within a short period of time. To minimise wave reflection from the walls two wave absorbing elements are designed and installed at both ends of the tank.

In total 4 large-scale experiments are performed. Results from each experiment are used to improve subsequent tests.

5.2 Instrumentation

Liquefaction tank

The liquefaction tank was originally designed for large-scale experiments on static liquefaction and flow slides. For these experiments it has been proven to be able to provide consistent and reproducible testing conditions and outcome data (De Jager et al., 2017). The tank with dimensions of 5 x 2 x 2 m (length x width x height) is mounted on a base frame which allows the tank to be tilted. The walls made of glass provide a view inside the tank, which is filled with fine sand and water. The tank can be tilted with a controlled tilting rate up to max. 10°.

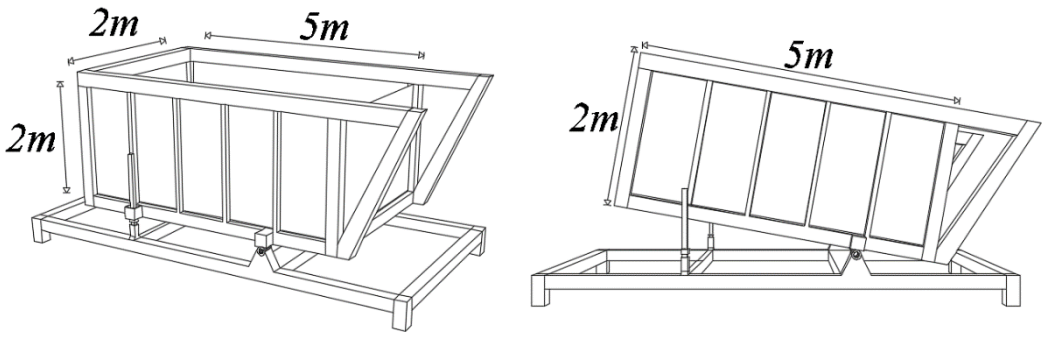

Figure 2: Schematic view of the structure of the liquefaction tank (Maghsoudloo et al., 2018)

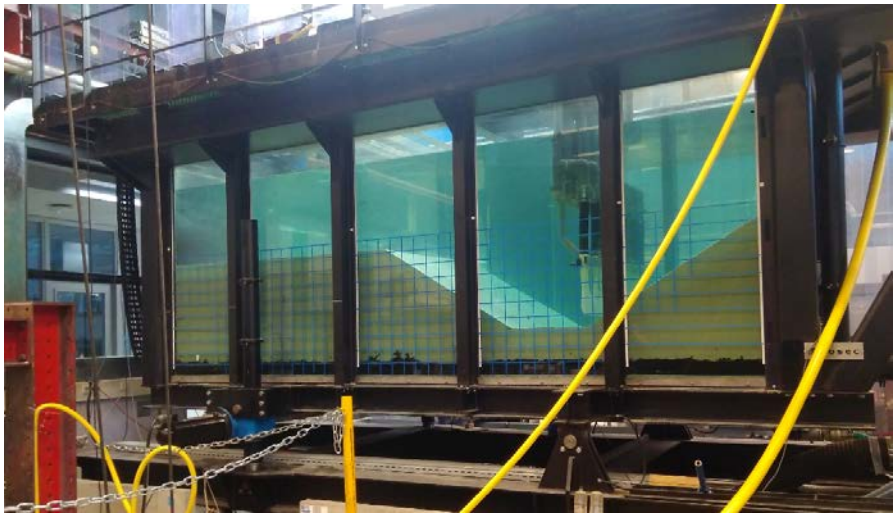

Figure 3: Liquefaction tank with a prepared slope model

For soil preparation the liquefaction tank is equipped with a fluidisation system at its base, which contains ten perforated tubes covered by several layers of filter. The soil sample can be fluidised by pumping water into the system with a controlled flow rate. The fluidised sand is then allowed to settle in order to create a uniformly packed loose sand bed.

The liquefaction tank also includes a suction dredger mounted to a steel rack, which is placed on top of the tank. The dredging rack can be moved horizontally and vertically as well as rotated anticlockwise from a fully vertical (90°) to approx. 20° position.

The liquefaction tank is instrumented with a number of built-in pressure sensors at the base and inside the walls of the tank. Furthermore, there are accelerometers, temperature sensor, flow meter and a fluid pressure sensor in the fluidisation system, amongst other instrumentation. The liquefaction tank including its structure and instrumentation is described more detailed by De Jager et al. (2017) and Maghsoudloo et al. (2018).

Soil properties

Inside the liquefaction tank, the slope is composed of a granular material: very fine uniform silica sand, the so-called Geba sand. The characteristic of Geba sand were determined by means of conventional soil mechanics laboratory experiments, as shown in Table 1. Figure 4 presents curves for particle size distribution of Geba sand samples as well as a picture of representative grain shapes.

Geba sand predominantly contains sand particles with only an 8% fraction of silt. During the sample preparation, the silt particles are partially washed away and its fraction is reduced even further to ca. 4%, as can be seen in Figure 4 (Maghsoudloo et al., 2018).

Table 1: Material properties of Geba sand (Maghsoudloo et al., 2018)

Soil parameter	Value
Permeability (at void ration e = 0.94)	4.2e-5 (m/s)
Cohesion	0 (kPa)
Residual friction angle (at e = 0.94 and mean effective stress > 20 kPa)	36 (°)
Min/ max void ratio acc. to Japanese standard	0.64 / 1.07
Particle shape	Sub-rounded
Median grain size diameter (D_{50})	0.11 (mm)
Fines content (silt fraction)	4 (%)

Preparation of the sample includes adjusting of relative density of the sand to the level required for the test. The achievable values of relative densities range between 30 and 60%. In order to be able to dredge a slope the relative density during experiments was chosen at about 45 – 47%. An estimation of relative densities is performed with the measurement tapes at each window of the tank. Assuming that the sand bed is homogeneous, relative density is estimated as an average for the entire volume of the tank. The precision of such density calculation is proven by De Jager et al. (2017) to be acceptable.

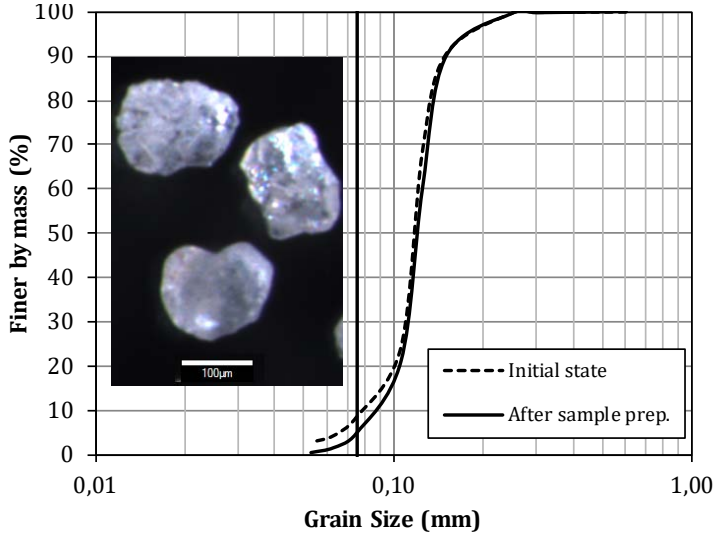

Figure 4: Particle size distribution curves of Geba sand before and after sample preparation; representative particle shapes (Maghsoudloo et al., 2018)

Triggering mechanism

Design of an appropriate triggering mechanism for a slope failure is of a particular importance for this study. As one of the major challenges of experimental work on submarine landslides, triggering mechanism should enable to fail the slope in a controlled manner providing consistent and repeatable response. Furthermore, the triggering mechanism should not pose a disturbance for sample preparation and measuring equipment.

Several designs were carefully selected and tested: (1) water injection by means of a grid of perforated tubes installed within the slope body; (2) fluidisation of the slope toe by injecting water through a perforated pipe buried underneath the slope toe; (3) excess pressure applied to the base of the sand bed; (4) tilting of the tank. Triggering mechanisms (1) and (2) did not satisfy the requirements and showed to be less effective. The current work focuses mainly on the experiments whereas triggering mechanisms (3) and (4) initiated a slope failure.

The pressure application at the base can be conducted in two ways. The fluidisation system of the liquefaction tank, once it's turned off and valves are closed, often still contains some pressure trapped within the system. By opening the valve, which connects fluidisation system to the base filter layer of the liquefaction tank, the trapped pressure can be released into the tank. The filter contains coarse granular material reinforced with a layer of geotextile with a steel grid on top, so that the pressure wave almost instantaneously propagates within the filter layer, reaching approx. 3 kPa (Figure 5). As pressurised water propagates through the sand bed, the excess pore water pressure increases reducing the effective stresses within the soil skeleton. This in turn results in a reduction of shear strength of sand and finally slope instability.

This triggering mechanism was successfully applied in the first experiment of the series. However, this method is not always reliable, as the magnitude and even the presence of a trapped in the system pressure is mostly unknown. In order to control the triggering process, the source of pressure for the triggering mechanism was modified. In later experiments pressure application was conducted by means of a pressurised chamber filled with water, with a pressure in the chamber of about 3 bar. The chamber is connected to the valve in the tank, which in turn leads to the filter layer at the base of the tank. During experiments slope failure is triggered by opening the valve for about 20 s. The applied pressure, redistributed evenly over the tank base via the filter layer, yields approx. 1.5 kPa (Figure 5).

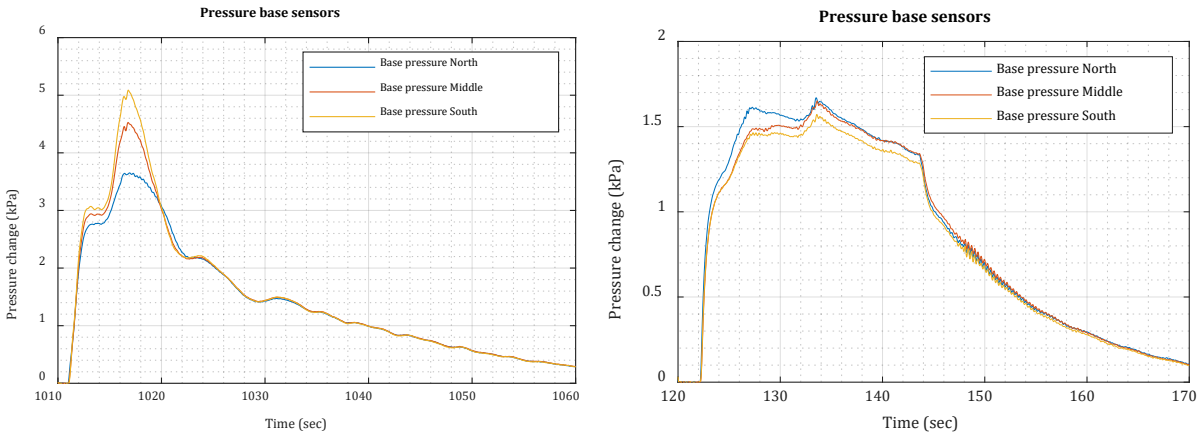

Figure 5: Pressure increase in the filter layer due to application of triggering mechanism, by trapped in the system pressure release (left), by controlled pressure application with a chamber (right)

Application of a triggering mechanism, which suddenly increases water pressure within the base filter layer, including both methods described above, includes adding of some amount of water to the closed system within the tank. The amount of water, however, is negligibly small. During release of a trapped in the fluidisation system pressure wave the water level in the tank increases by about 1.5 mm, whereas the pressure application with a chamber results in approx. 2 mm water level rise. In both cases this negligibly small water level rise occurs gradually over a period time of more than 50 s, as can be seen from the duration of pressure dissipation for both methods, shown in Figure 5.

Wave absorber

For the set of experiments on waves generated by submarine landslides the liquefaction tank was equipped with wave absorbing elements at both ends of the tank. These wave absorbers consist of several layers of fibrous PPC filter material, so-called Japanese filter mats. The layers are combined in two 30 cm thick wave absorbing elements which are then mounted inside the liquefaction tank. Design of these elements was based on experimental work in a wave flume for a similar type of fibrous material, which is described in detail in Appendix A of this thesis. Table 2 summarises the material properties and dimensions of the wave absorbing elements.

Table 2: Wave absorbers: material properties and geometrical parameters

Material type	Fibre diameter [mm]	Free volume/ porosity [%]	Thickness per layer [cm]	Total number of layers	Total thickness [cm]
Japanese filter mat	0.25 ± 0.1	97.5	5	6	30

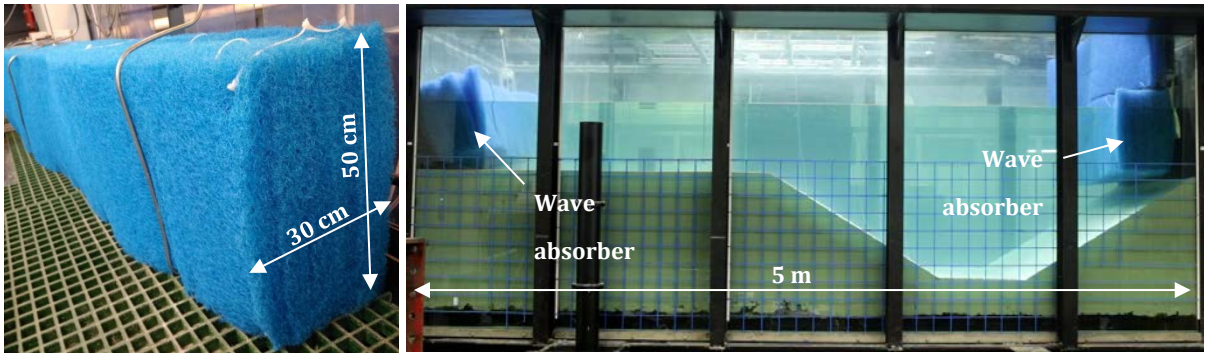

Figure 6: Wave absorbers for the liquefaction tank

It is important to mention, that design of the wave absorbing elements was based on wave period < 1.50 s. Waves with larger wave period can lead to reduced wave energy absorbing and higher chance of wave reflection to influence the measurements.

Dredging

Slopes inside the tank are created with a suction dredger. By sucking and removing the sand-water mixture, a V-shaped trench is created with approx. 30° slopes on both sides The trench can be later extended horizontally to construct a wider toe for the slope.

Dredging process is highly prone to slope failures, as it results in a sudden unloading of the sandy slope while advancing downwards. Despite the fact that dredging was done extremely slowly in very small steps, slope failures during dredging were often the reason for experiments delay, as the whole sample preparation procedure had to be restarted.

Wave measuring equipment

In order to measure water surface elevations above the slope during the landslide, a set of two wave gauges and an electromagnetic liquid velocity meter (EMS, type E30) was installed in the liquefaction tank. The gauges were arranged along the centre line parallel to the longitudinal axis of the tank. Gauge 1 was located above the sloping sand bed, while gauge 2 was placed above the slope crest. The distance between two gauges was about 65-70 cm during the experiments. EMS gauge is installed above the slope crest with its probe located approx. 5 cm above the sand surface. It insures that horizontal velocity measurements is barely influenced by short surface waves but can indicate propagation of a long wave.

5.3 Summary of experiments

The current thesis presents results of in total 4 large-scale physical modelling experiments conducted in the liquefaction tank. As mentioned earlier, during these tests slope failures were triggered by pressurising water at the base of the tank, with an exception of the test 1, which also included several trials of another triggering mechanism: fluidisation of the toe by means of a perforated pipe. Figure 7 shows schematically the slope model during the experiments, whereas h, w, L and α are geometrical parameters of the slope (height, width, length and slope angle, respectively), w_{toe} is the toe width, WL – water level above the slope crest. Soil mechanical properties of the sand bed are described with RD – relative density, e – void ratio and γ_{sat} – saturated density of sand.

Measurements of accelerations and pore water pressure within the slope are obtained by means of 10 mobile sensors during tests 1, 2 and 4; for the third test 9 MS's were used. Position of sensors, wave gauges and EMS will be further discussed in details. Table 3 summarises the geometrical features of the slope and soil characteristics during tests 1 - 4.

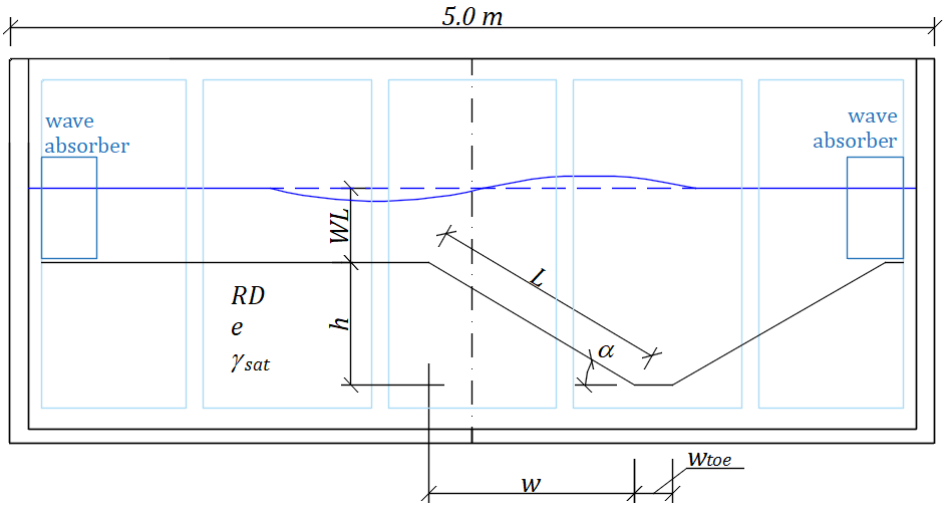

Figure 7: Scheme of a slope model

Table 3: Geometry of the slope and soil properties during experiments 1 - 4

Test	h [m]	w [m]	L [m]	α [°]	WL [cm]	w_{toe} [cm]	RD [%]	e [-]	γ_{sat} [kN/m^3]
T 1	0.67	1.09	1.30	31	40	20	48.6	0.860	18.97
T 2	0.64	1.05	1.23	31	40	130	46.4	0.869	18.93
T 3	0.67	1.10	1.29	31	28	90	47.1	0.866	18.94
T4	0.63	0.99	1.17	32	40	52	57.9	0.820	19.17

Slightly changing geometry of the slope is mainly due to unpredictability of the dredging process; however, the overall slope geometry is kept nearly the same for all test sequences. The area of the slope toe is widened in tests 2 - 4 to prevent supporting of the failing slope mass by the slope on the right-hand side of the tank. With a lower water table in test 3 we expected to increase the height of generated waves. Higher density of material in test 4 allows faster dredging of the slope as well as enables to model different soil behaviour during failure, while the water table is increased to 40 cm level because the tank tilting is applied.

Each test run provided lessons to learn and ideas for improvement of the set-up, which were then applied in subsequent experiments. Various failure triggering methods, slight changes in slope geometry as well as adapted set-up equipment resulted in some significant differences between each test run. Table 4 presents an overview of specific characteristics for each of the tests.

Table 4: Overview of major characteristics and remarks to tests 1 - 4

Test	Triggering mechanism	Sensors arrangement	Remarks
T 1	Trapped pressure release by a quick opening of the valve of fluidisation system	Mostly around sloping part of sand bed, 2 – 3 sensors in out of plane direction. 10 MS's (MS 3 defect).	Toe loosened by preceding attempts to trigger a failure
T 2	Controlled pressure application with a pressurised chamber	Inline along the centre of the slope, wider redistribution of sensors. 10 MS's (MS 2 defect).	-
T 3	Controlled pressure application with a pressurised chamber	Inline along the centre of the slope, 9 MS's (no MS 4 installed).	Toe reinforcement with gravel bags
T4	(4.1) Tilting of the tank to up to 8°; (4.2) Controlled pressure application with a chamber; (4.3) Trapped pressure release by an opening of the fluidisation system valve	Inline along the centre of the slope, additional sensor at the slope crest. 9 MS's (MS 7 broke at a later stage of failure).	Changing slope angle and width due to tilting preceding failures. Accumulation of loose soil at the slope toe

Test 1 – 21/12/2018

The first test of the series of experiments on wave generation by submarine landslides was conducted on a slope of a length of 1.30 m with an inclination of 31°, which was dredged closely to the centre of the tank. The toe of the slope was widened to 20 cm. The total height and width of the slope reached 66 cm and 1.10 m, respectively. The relative density of the sand bed was estimated as 48.6%. Water depth above the slope crest was set at 40 cm.

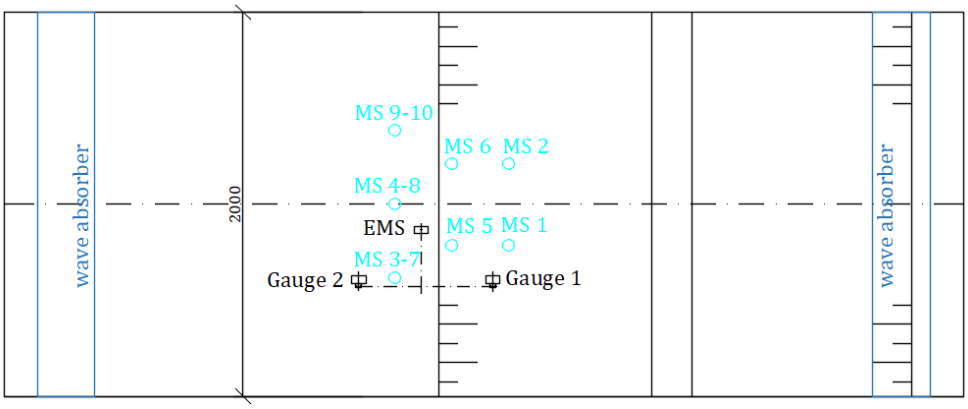

Figure 8: Top view of the experimental set-up during test 1

To record accelerations and pore water pressure within the slope, 10 mobile sensors (MS) were installed. The initial location of the MS's, wave gauges, EMS device and wave absorbers as well as the slope geometry are shown in Figure 9.

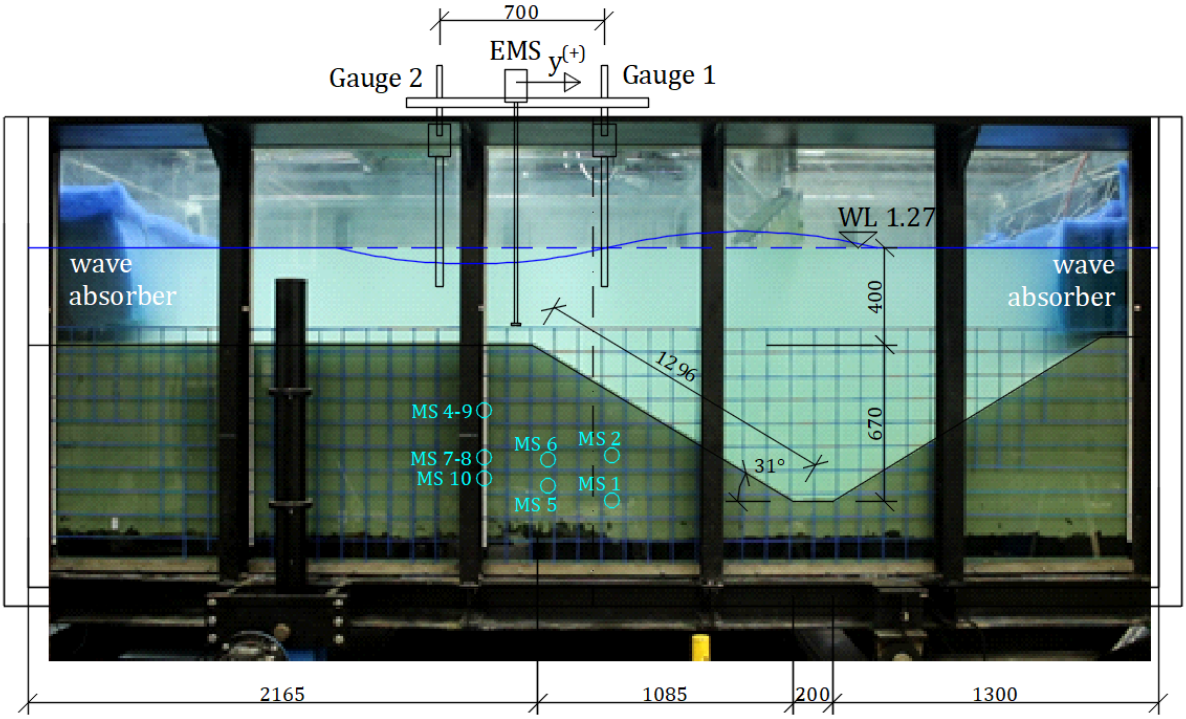

Figure 9: Side view the experimental set-up during test 1 and initial MS's location

During test 1 the slope was first aimed to be failed using fluidisation of the slope toe by means of water injection through a perforated buried pipe. However, application of this triggering mechanism did not result in a slope failure, but only loosened partially the toe. As the slope remained stable, a trapped pressure wave was released by opening the base valve connected to fluidisation system. This resulted in an increased pressure within the filter layer at the base of the tank, which finally triggered the slope instability. Before the final failure the slope geometry was slightly changed by previous trials, as it is shown in Figure 10.

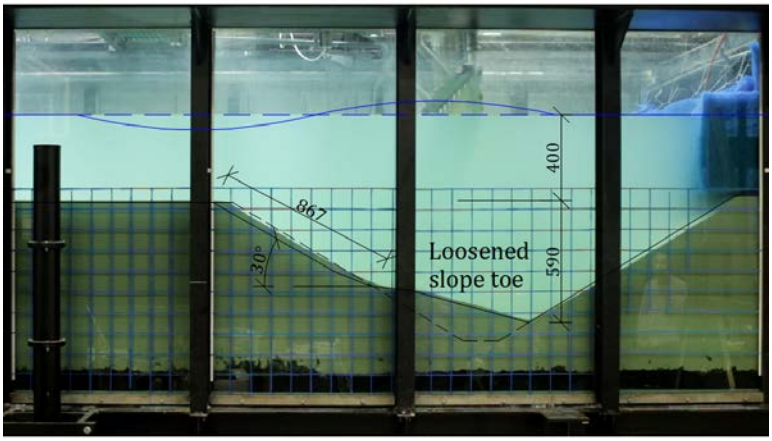

Figure 10: Slope geometry before final failure, test 1

Test 2 – 18/01/2019

The second test of the series was conducted in January 2019 and included a 1.20 long slope with an inclination of 31°. The relative density of sand was estimated as 46.4%. Wave gauges and EMS were arranged in the same way as during test 1.

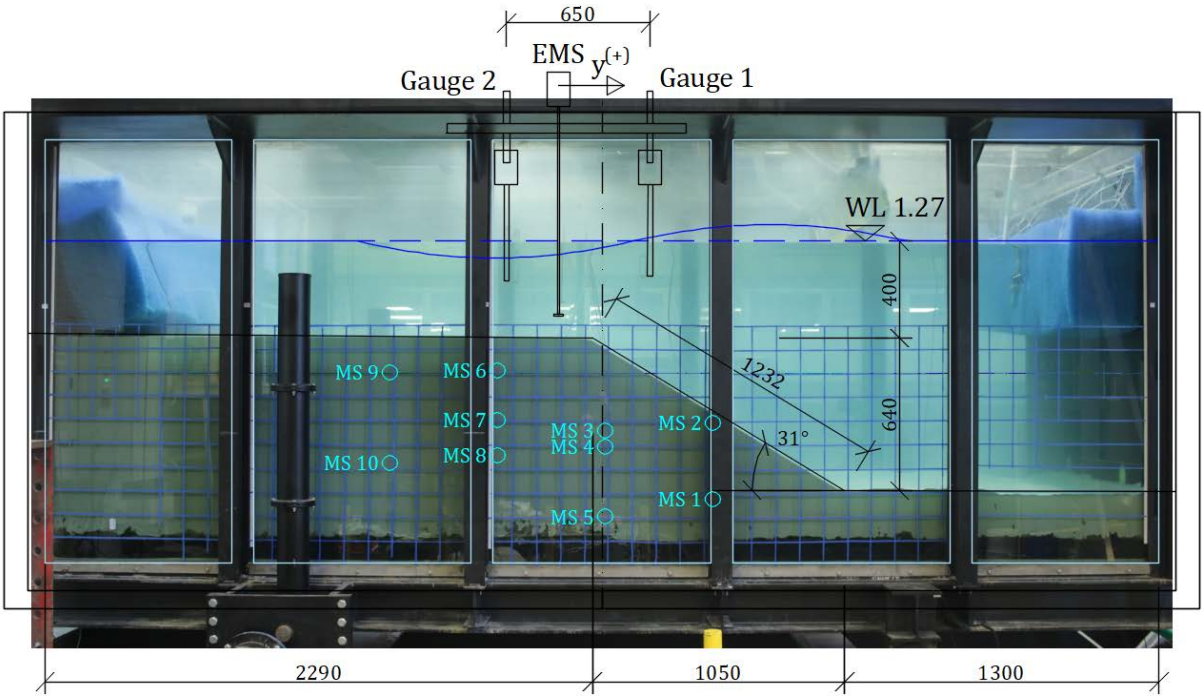

Figure 11: Side view the experimental set-up during test 2 and initial MS's location

It was decided to install MS's in one row along the centre line of the tank to minimise the influence of boundaries on the measurements and to cover a larger area of the slope cross section with sensors. Figure 11 shows the set-up and slope geometry as well as the approximate initial location of MS's and arrangement of wave gauges. The toe of the slope was widened to 1.30 m to prevent stabilizing effect of the slope on the opposite side. As a result the sand bed on the right side of the tank was lower than in the previous test and the wave absorber did not cover the entire water column. In such conditions the effectiveness of the wave absorber could be significantly reduced.

For triggering of a slope failure, a pressure chamber was connected to the base filter layer, which allowed increasing water pressure within the filter layer by approx. 1.5 kPa for 20 s.

Test 3 – 20/02/2019

The test number 3 was conducted in a similar manner as test 2, including nearly identical slope geometry and material density (Figure 12). In order to increase the expected amplitude of the wave, the water table was lowered to 28 cm above the crest of the slope. Furthermore, the same triggering mechanism and gauges arrangement were chosen as in test 2. However, the experiment was performed on a slope with a toe protection layer. This toe reinforcement consisted of gravel

bags that uniformly applied a load of 0.6 kPa on the toe and approx. a third of the slope. The toe reinforcement was installed for the sake of another experimental study, investigating liquefaction flow induced slope erosion. However, for the current study it provided an opportunity to observe a different kind of failure, varying from the previous tests in its scale and dynamic features.

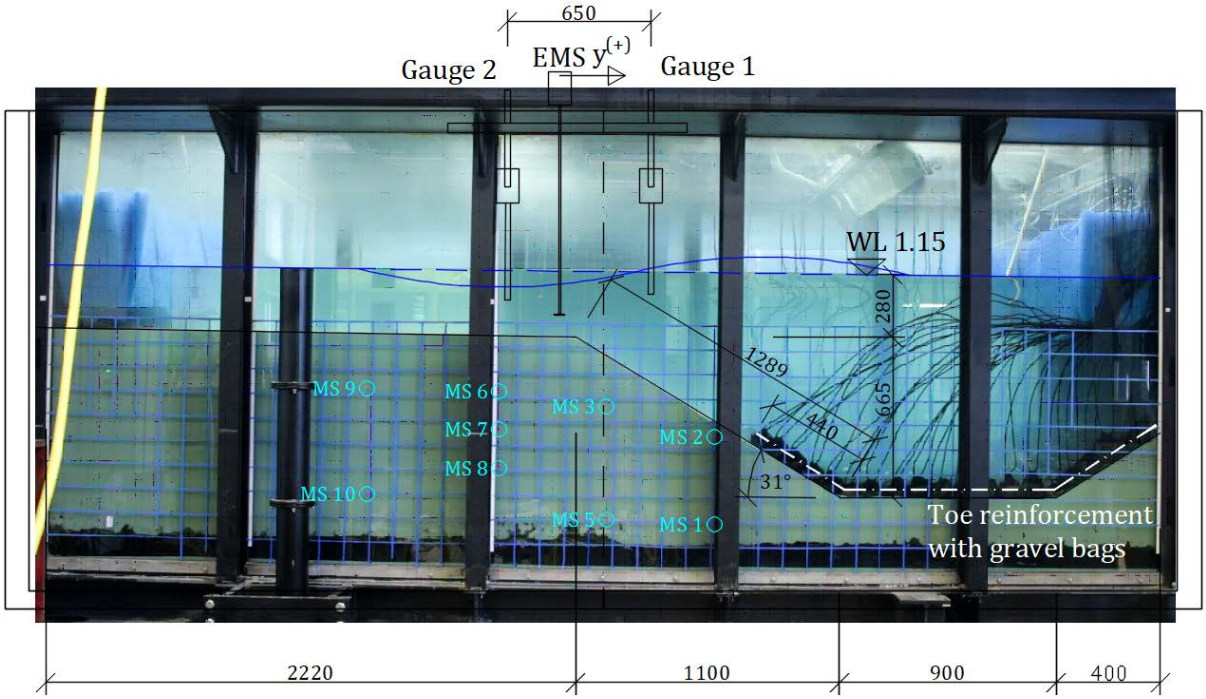

Figure 12: Side view the experimental set-up during test 3 and initial MS's location

Test 4 – 09/03/2019

During test 4 it was decided to construct the slope from a denser soil material, hence, the relative density of the sand was increased to 57.9%. As a result the slope remained more stable during dredging, however, the triggering of a slope failure for such a dense material posed an additional challenge. Therefore, during this experiment the tank was tilted stepwise to 8°.

Overall, during the test 4 we were able to successfully trigger 3 failures, whereas the first one occurred during tilting at the angle of 3.7°. The first failure was localised around the edge of the crest and impacted only a small part of the slope. After the tank was tilted to its final position, the second failure was triggered with a controlled pressure application by means of a chamber. As this failure did not result in a full collapse of the soil structure, but formed a gentler slope, the third landslide was triggered with a release of a trapped pressure wave by opening the base valve. The initial geometry of the slope and location of MS's as well as the chosen arrangement of wave gauges and EMS during test 4 is shown in Figure 13.

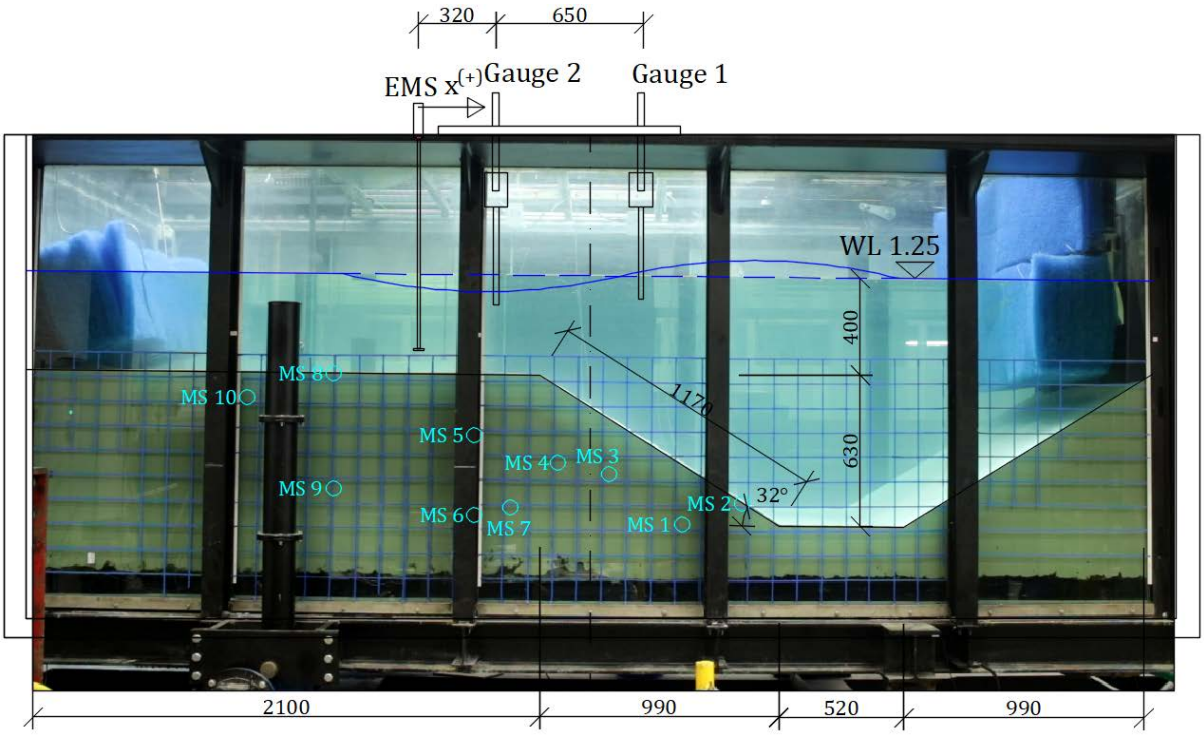

Figure 13: Side view the experimental set-up and slope geometry before test 4 with an initial MS's location

5.1 Synchronisation of data

Data was collected with two separate data acquisition systems. Measurements from the liquefaction tank instruments including MS's were logged separately from the wave gauges and EMS and as a result the data had to be synchronised.

During the first experiment we started the data logging and then increased the water table by pumping water into the tank with a constant rate. The water table increase was supposed to be detected by MS's as well as the wave gauges, which was meant to give two time points for synchronisation: time point of the start of pumping and when the pump was switched off. This method, however, did not provide sufficiently precise results, as synchronisation could only be done approximately with a deviation of ± 1.5 s.

To avoid future issues with data synchronisation, during all following tests we used a different method. Two accelerometers, each one connected to one of data acquisition systems, were fixed on a rigid steel beam. After starting data logging before the main test procedure, two hammer hits were applied to the steel beam, producing two distinct spikes in recordings of both accelerometers (Figure 14), which were then used for synchronisation. Using this method, we were able to achieve a very high precision of synchronisation with possible deviation of less than 0.1 s.

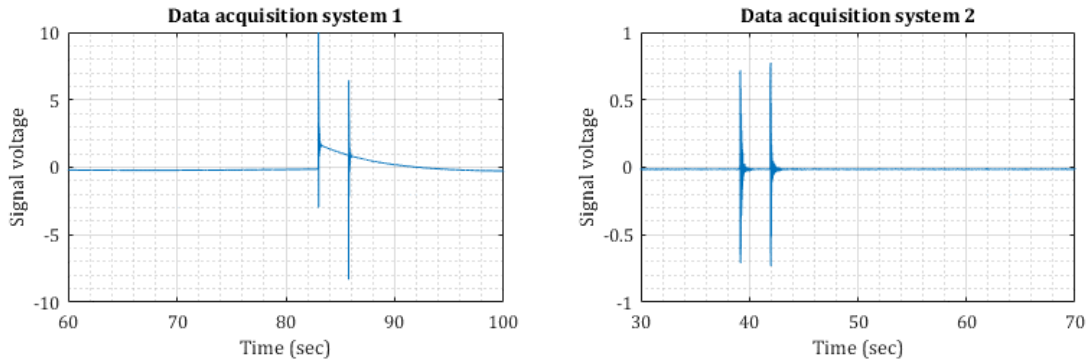

Figure 14: Data for synchronisation: two hammer hits recorded by two accelerometers connected to different data acquisition systems, example from test 2.

5.2 Wavelet analysis

Wavelet transform is a powerful mathematical tool for data analysis, which is relatively new to the field of civil engineering. In recent years it found its application in a number of studies in ocean engineering, as it was recognised that in addition to the typical features of wavelet transform, such as data filtering, smoothing and compression, it offers a great analysis tool for studies of water waves (Smolentsev, 2014). A brief introduction to the theory of the wavelet transform is given here to provide a sufficient understanding of the following data analysis.

In comparison to the well-known Fourier transform, which represents input signal as a sum of never-ending sine waves without its localisation in time, wavelet transform can capture the abrupt changes in data as well as signal components, localised only at a discrete period of time. These features of wavelet transform is based on definition of wavelets as rapidly decaying wave-like oscillation with zero-mean, existing only for a finite duration (Devleker, 2016).

So, the wavelet transform decomposes a time series into time-frequency space. In principle, it can be also described as a band-pass filter with a specified response function defined by a wavelet function (Torrence & Compo, 1998).

Continuous wavelet transform (CWT)

The continuous wavelet transform is mathematically formulated by equations (1)-(2) (P. C. Liu, 1998), (Smolentsev, 2014).

$$\widetilde{X}(a,b) = \int_{-\infty}^{\infty} X(t)\ \underbrace{|a|^{-\frac{1}{2}}\ \overline{\psi\left(\frac{t-b}{a}\right)}}\, dt \qquad (1)$$

$$\text{with a family of functions: } \psi_{ab}(t) = |a|^{-\frac{1}{2}}\ \psi\left(\frac{t-b}{a}\right) \qquad (2)$$

where $X(t)$ is the original data in time domain, $\widetilde{X}(a,b)$ – transformed data outcome, ψ is a fixed basic wavelet function, so called mother wavelet, which is scaled and shifted by means of factors $a\ (a>0)$ and $b\ (-\infty<b<\infty)$, respectively. $\bar{\psi}$ represents a complex conjugate of ψ.

As a and b act as two additional independent variables, in practice, the dilation and translation factors are set as $a=2^s$ and $b=\tau\times 2^s$, which modifies (2) as follows:

$$\psi_{s\tau}(t)=2^{-s/2}\ \psi(2^{-s}t-\tau) \tag{3}$$

Where s and τ are the scale and time representing factors. Wavelet transform formulation changes then respectively to:

$$\widetilde{X}(s,\tau)=\frac{1}{2^{s/2}}\int_{-\infty}^{\infty}X(t)\ \overline{\psi(2^{-s}t-\tau)}dt \tag{4}$$

Scaling factor, or scale, s is inverse proportional to the frequency of wavelet. As each type of wavelet has a specified centre frequency C_f, the corresponding equivalent signal frequency F_{sig} can be then calculated as:

$$F_{sig}=\frac{C_f}{\delta t}\times\frac{1}{s} \tag{5}$$

Where δt is the sampling rate.

In order for the function to be reconstructed from the wavelet transform coefficients, a mother wavelet has to provide certain features:

$$\int_{-\infty}^{\infty}|\psi(x)|^2dx<1 \tag{6}$$

$$C_\psi=\int_{-\infty}^{\infty}\frac{\left|\hat{\psi}(\omega)\right|}{|\omega|}d\omega<\infty \tag{7}$$

Where $\hat{\psi}(\omega)$ is the mother wavelet function in Fourier frequency space and ω is a frequency. From (7) also follows:

$$\int_{-\infty}^{\infty}\psi(x)dx=0 \tag{8}$$

Discrete wavelet transform (DWT)

The data processing with DWT results in a decomposition of a signal into levels with different frequency ranges. Conceptually, DWT applies stepwise a high- and a low-pass filter, dividing the original signal into so called detail coefficients (output of high-pass filter) and approximation coefficients (result of low-pass filter). While detail coefficients are stored, approximation coefficients are passed to the next decomposition level, whereas the signal is again split into two frequency components.

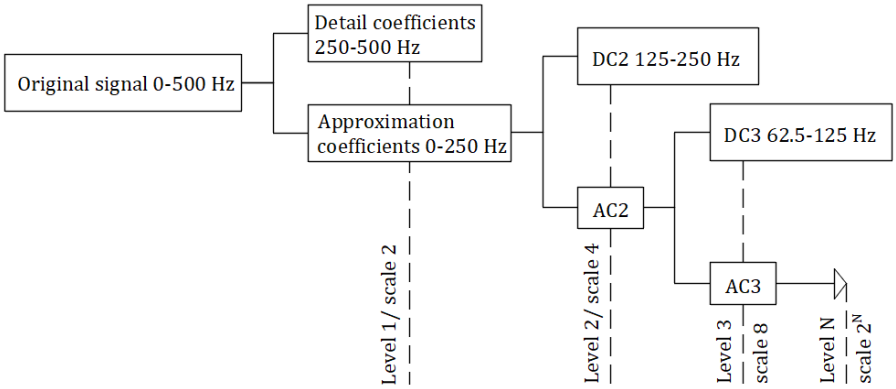

Figure 15: Schematic representation of DWT signal decomposition

Each DWT decomposition level reduces the span of signal frequencies by a half. As the original sampling rate of the signal during experiments is 1000 samples per second, it corresponds to frequency band of ± 500 Hz at the start of the analysis. First level of detail coefficients contains signal component with a frequency range of 250-500 Hz, second level 125-250 Hz etc. (Table 5). At the final level of decomposition the approximation coefficients represent the remaining signal after removal of all higher frequency detail components. For example, the approximation coefficients of level 12 represent signal frequencies of 0 – 0.122 Hz.

Table 5: Signal frequency represented by detail coefficients of DWT signal decomposition to level 12

Level	Frequency	Level	Frequency	Level	Frequency
Level 1	250-500 Hz	Level 5	15.625-31.25 Hz	Level 9	0.977-1.95 Hz
Level 2	125-250 Hz	Level 6	7.81-15.625 Hz	Level 10	0.488-0.977 Hz
Level 3	62.5-125 Hz	Level 7	3.91-7.81 Hz	Level 11	0.244-0.488 Hz
Level 4	31.25-62.5 Hz	Level 8	1.95-3.91 Hz	Level 12	0.122-0.244 Hz

Type of wavelets

In general cases wavelets are described by two functions: a mother wavelet function ψ and a scaling function φ, whereas scaling function for some wavelets is left out. Amongst hundreds of developed wavelet functions combined into different wavelet families, the most commonly used families are pictured in Figure 16. These are also examples of wavelets supported by the MATLAB wavelet toolbox.

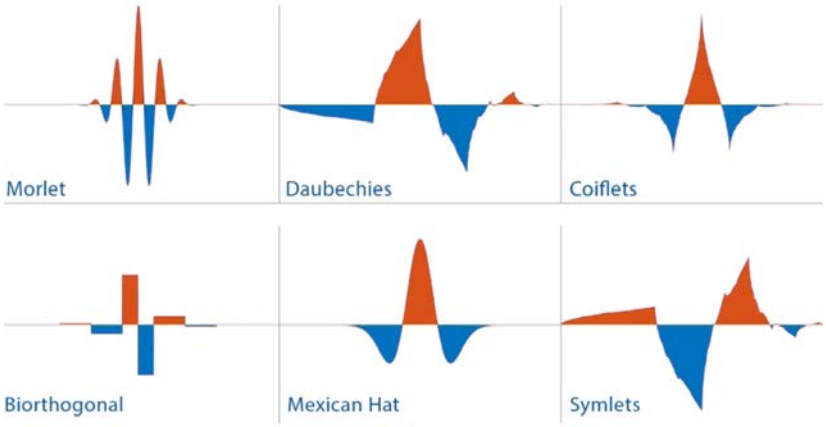

Figure 16: Examples of commonly used wavelet families, adopted from (Devleker, 2016)

While choosing a wavelet function, one should make a decision based on following considerations (Torrence & Compo, 1998):

1. Orthogonal or non-orthogonal. Orthogonal wavelets produce a most compact signal representation, but can result in differing spectrums if shift is aperiodic. Non-orthogonal wavelets can be redundant at large scales, but in general should be preferred for time series analyses with continuous and smooth changes in wavelet amplitudes.
2. Complex or real. As a real wavelet can output only one component, it will return only the amplitude, while complex wavelets return amplitude and phase values. Thus, the complex wavelets are generally better suitable to process the oscillating signals.
3. Width. While wavelet functions can range from narrow and wide in time, their resolution in time and frequency varies respectively. Time-narrow functions are resolved better in time, but poor in frequency; wide wavelets provide only a poor time resolution but are resolved good in frequency domain.
4. Shape. Finally the shape of a wavelet function is supposed to be in good agreement with the shape of time series curves, taking into account if any sharp and abrupt changes in signal are present, or the data is rather of a smoothly oscillating type.

However, if wavelet transform is used to obtain qualitative information about localisation of signal frequencies or solely wavelet power spectra, the choice of function for the wavelet transform reduces to fulfilling of the requirements of techniques used, such as e.g. a discrete

wavelet transform which requires an orthogonal wavelet. For such applications different wavelet functions produce in general qualitatively equal results.

In this study we applied discrete and continuous wavelet transforms to decompose and analyse the data obtained during the experiments on wave generation by submarine landslides. Discrete wavelet transform was employed to decompose the signal into several levels based on the signal frequency and then remove the high frequency noise and detrend the data (e.g. Figure 27 shows decomposition of pressure data by means of DWT). The continuous wavelet transform in turn was applied to identify presence of the long waves and localise them in the time-frequency space (e.g. Figure 21 presents results of CWT for gauge data).

For discrete wavelet transform an orthogonal asymmetric Daubechies 12 (db12) wavelet function was chosen (Figure 17). The wavelet functions family is defined by a scaling function $\varphi(x)$ and a mother wavelet $\psi(x)$. The functions are obtained by spectral factorisation and provide no closed-form formulae for $\varphi(x)$ and $\psi(x)$. The functions are constructed based on different choices of coefficients for scaling and wavelet functions, which is in detail described by Daubechies (1992).

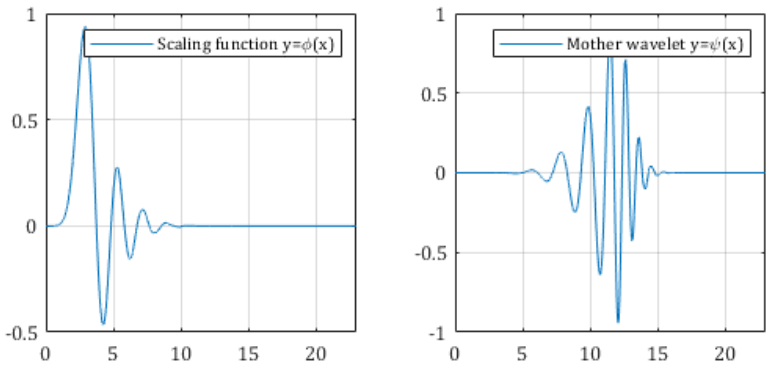

Figure 17: Orthogonal Daubechies 12 (db12) wavelet: scaling function(left) and mother wavelet function(right)

For continuous wavelet analysis the analytic Morlet or Gabor wavelet was applied, which scaled version is pictured in Figure 18. The analytic Morlet wavelet is an example of a non-orthogonal wavelet, which is defined by a complex mother wavelet function ψ, which can be formulated in Fourier domain as:

$$\hat{\psi}_{s\omega}(\omega) = \pi^{-\frac{1}{4}} e^{-\frac{1}{2}(s\omega-\omega_0)^2} U(s\omega) \tag{9}$$

Where $U(s\omega)$ is the Heaviside step function:

$$U(s\omega) = \begin{cases} 0, & s\omega < 0 \\ 1, & s\omega \geq 0 \end{cases} \tag{10}$$

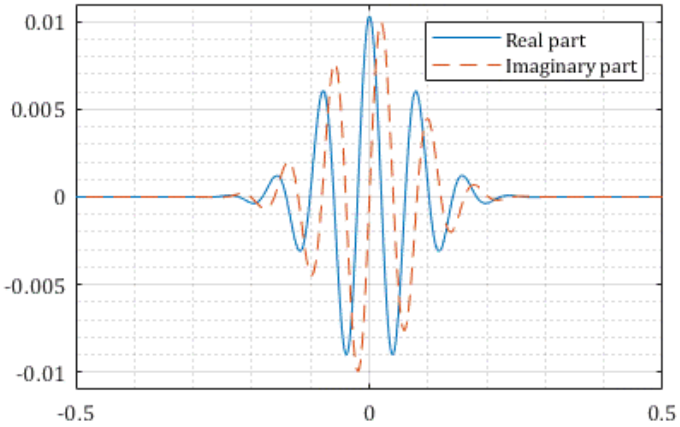

Figure 18: Non-orthogonal Morlet (Gabor) wavelet function, real and imaginary parts

6. Analysis of experiments results

6.1 Test 1

6.1.1 Slope failure image analysis

During the test 1 slope failure occurs approx. 1200 s after the start of data logging. The observed mass movement can be divided into two stages. The first stage is associated with predominantly horizontal movement, while the crest of the slope slightly moves downwards. Deformation of the slope as well as estimated location of MS's is shown in Figure 19.

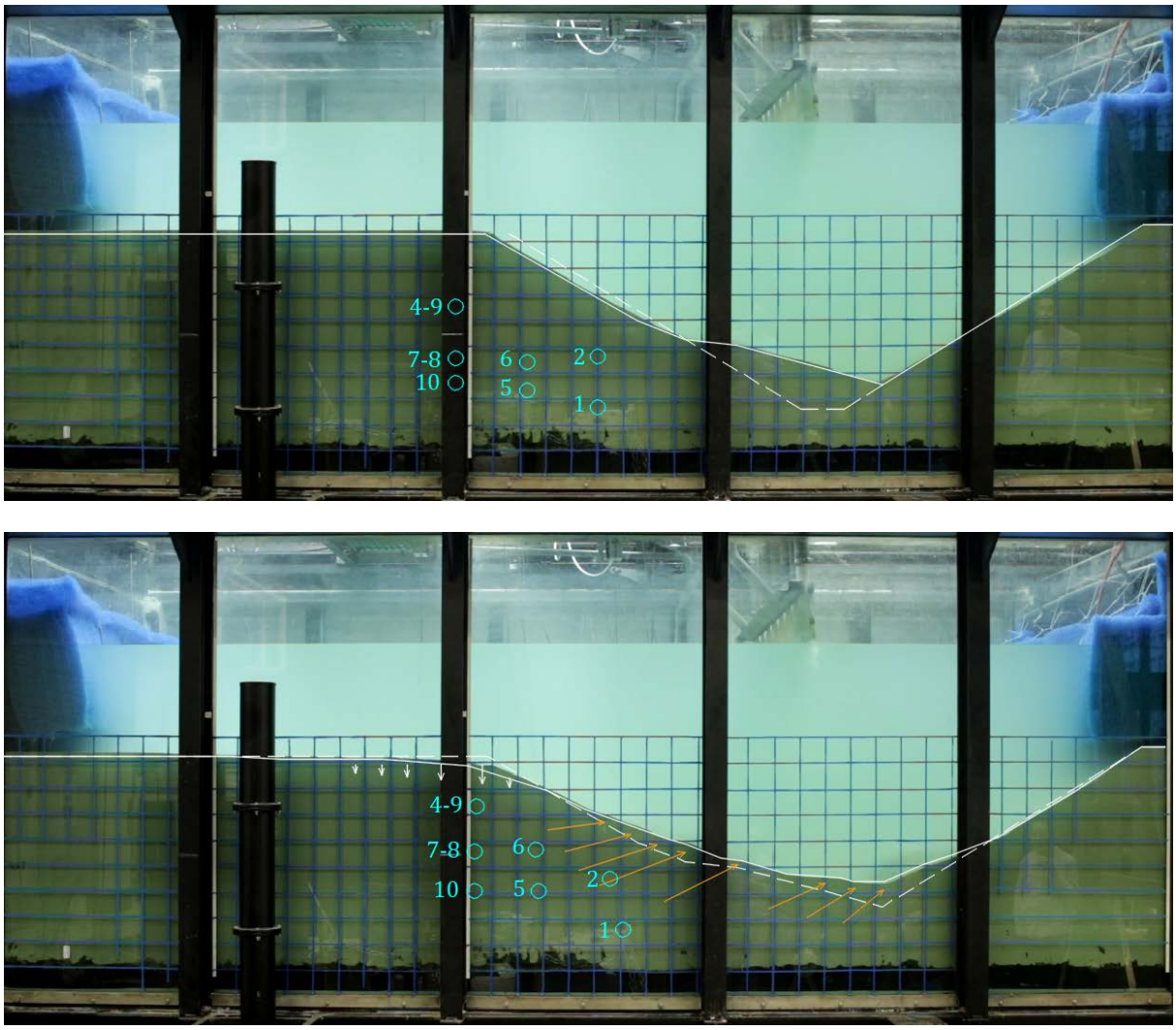

Figure 19: Sequences of slope failure during experiment 1 before failure (top), after first stage of failure (bottom). Location of mobile sensors (MS) is estimated approximately.

Second stage of failure develops approx. 6.5 s after the onset of failure. A sudden downward movement of the crest of the slope indicates a deep seated failure, while at the toe of the slope sand liquefaction can be observed. Figure 20 shows deformation of the slope at the moment of

onset of the failure stage two. The MS's are indicated at their estimated location. During further slope deformation it is rather problematic to track MS's location precisely.

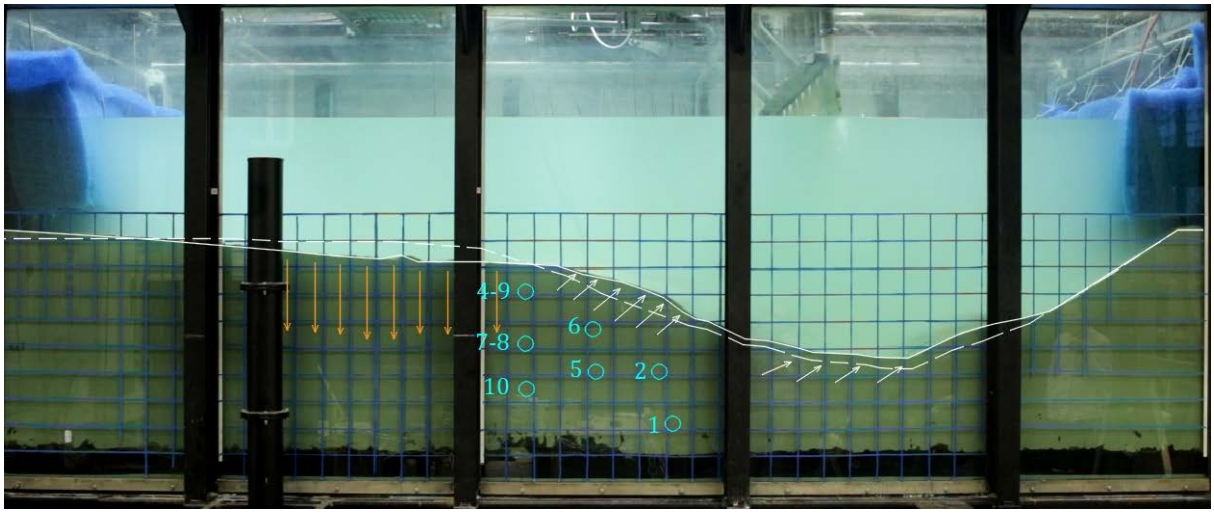

Figure 20: Slope deformation during second stage of failure with an estimated location of mobile sensors

6.1.2 Wave localisation

Continuous wavelet transform (CWT) is used to indicate occurrence of long waves with low frequencies generated by slope failure. Original wave gauge data are presented in Appendix B. The signals from two wave gauges are analysed separately. Both signals show presence of waves with frequencies ranging from 0.35 Hz to 0.8 Hz, generated during landslide, as can be seen in Figure 21 by a well localised yellow area in the magnitude scalogram.

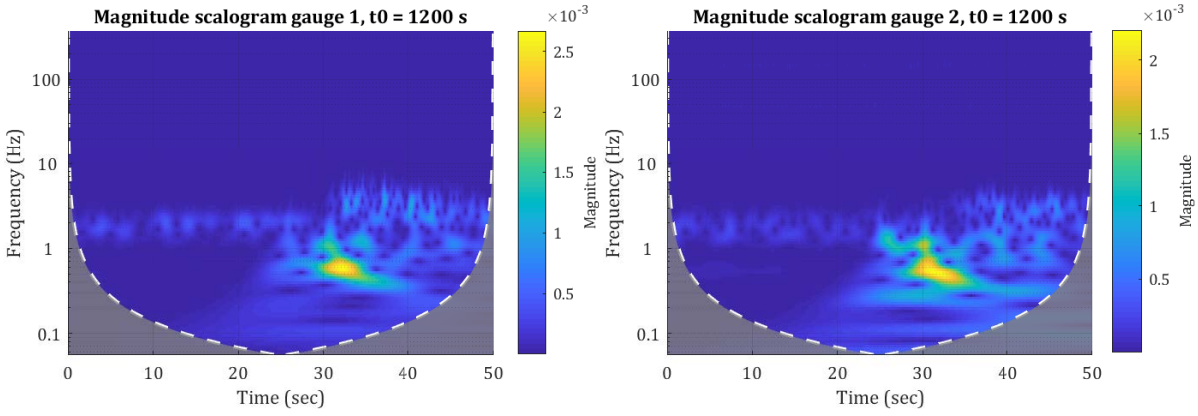

Figure 21: Test 1, results of continuous wavelet transform: signal from gauge 1 and 2 in time-frequency space

For a better readability, Figure 22 presents a contour diagram of CWT for gauge 2 data with data tips, indicating the range of frequencies for the following wave extraction.

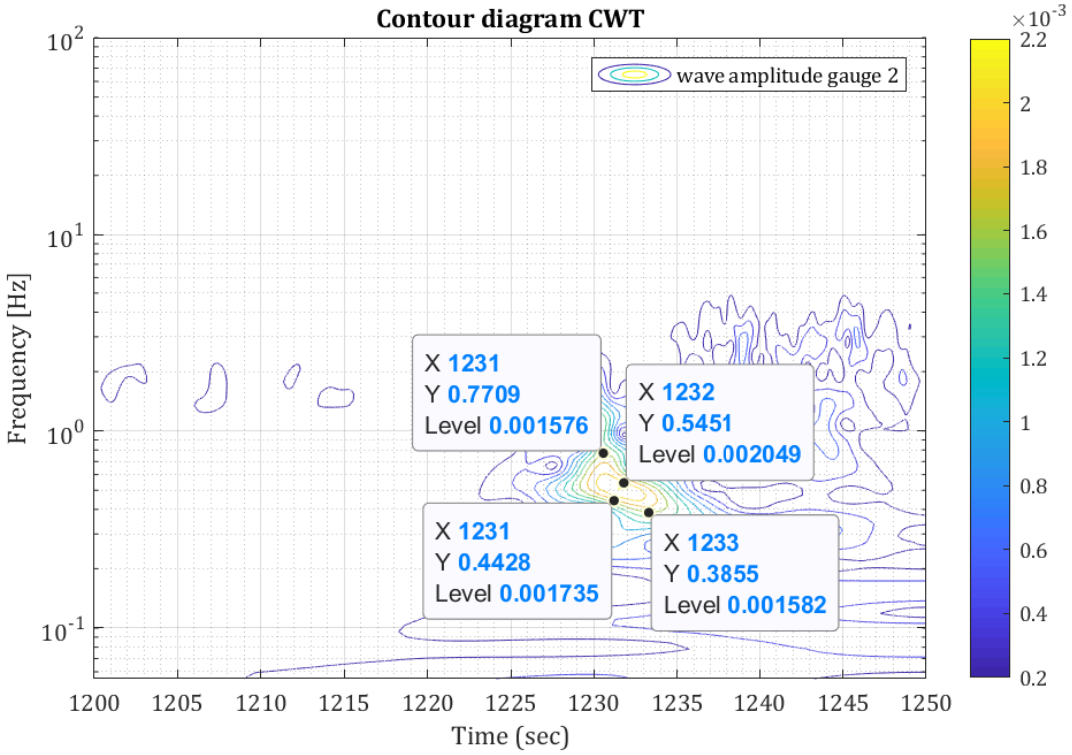

Figure 22: Test 1, contour diagram of CWT with data tips indicating location of generated waves in time-frequency space; X – time, Y – frequency, Level – magnitude of CWT coefficients

6.1.3 Extracted wave

Based on CWT we localised the generated waves within the time-frequency domain. By applying inverse CWT function, the waves with the frequency range 0.35 - 0.8 Hz can be extracted from the signal. The extracted data represents superposition of the wave trains that were generated during submarine slope failure and represent a long tsunami wave (Figure 23).

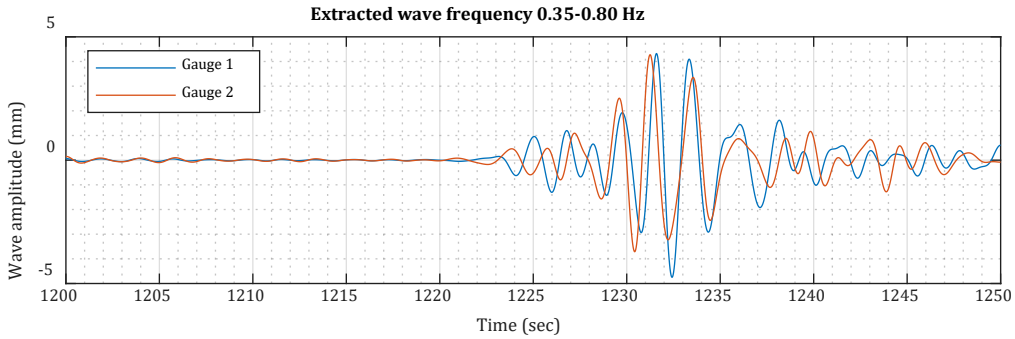

Figure 23: Test 1, wave extracted from the data of wave gauges 1 and 2, frequency range 0.35 – 0.80 Hz

The generated wave can be decomposed into several wave trains with amplitude ranging from 1 to 2 mm (Figure 24). The superposed wave envelop exhibits maximum wave amplitude of ca. ± 5 mm.

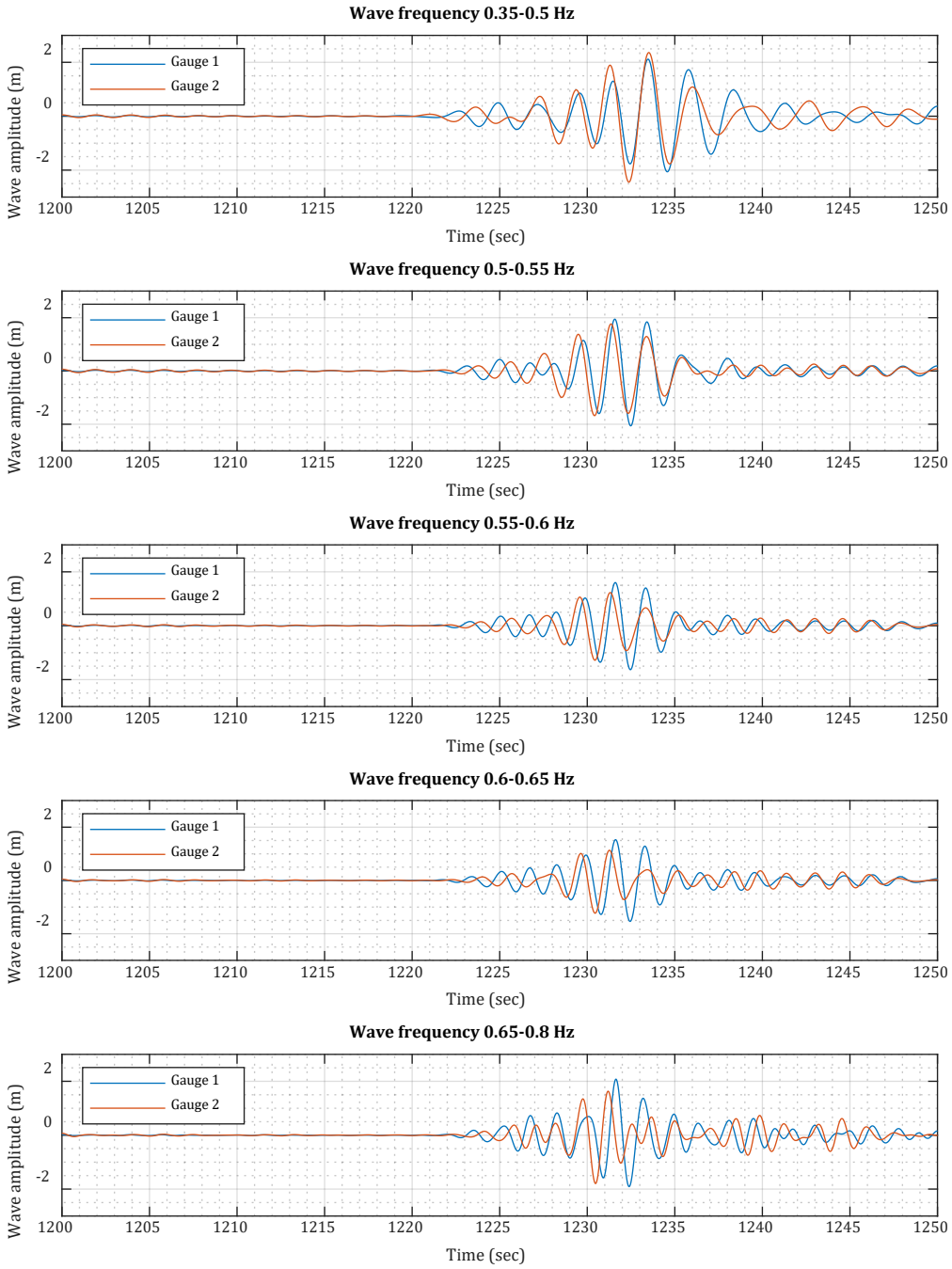

Figure 24: Test 1, wave decomposition

The method of discrete wavelet transform (DWT) is applied to filter the data obtained from EMS. Figure 25 presents generated wave data in comparison to results of DWT (decomposition to level 8 and level 12) for horizontal water velocity measured by EMS.

The measurements of EMS show good agreement with the data extracted by means of CWT. As water velocity is measured at the bottom of water column just above the slope crest, it remains close to zero during the time period before the failure. Shorter surface waves that were present in the system, did not influence the measurements of EMS, because water particles at a depth are barely displaced by short waves (equivalent to deep-water waves, Figure 26). As velocity data

shows a sudden increase, it indicates the slope failure and propagation of long waves. This abrupt velocity increase agrees well with increase in wave amplitude, while the velocity peak corresponds to the onset of the second stage of failure. Predominantly positive direction of horizontal water velocity corresponds to a water flow towards upper side of slope crest, or in other words towards the shore, which is opposite to the direction of soil mass movement. Furthermore, the EMS measurements reveal no visible influence of wave reflection from the tank walls. DWT decomposition to level 12 removes further higher frequency of the signal, which reveals oscillations in water velocity corresponding to particle movements on an elliptical trajectory as it is typical for the shallow-water or transitional-water waves (Figure 26). The velocity oscillations can thus indicate the time period of long wave passages.

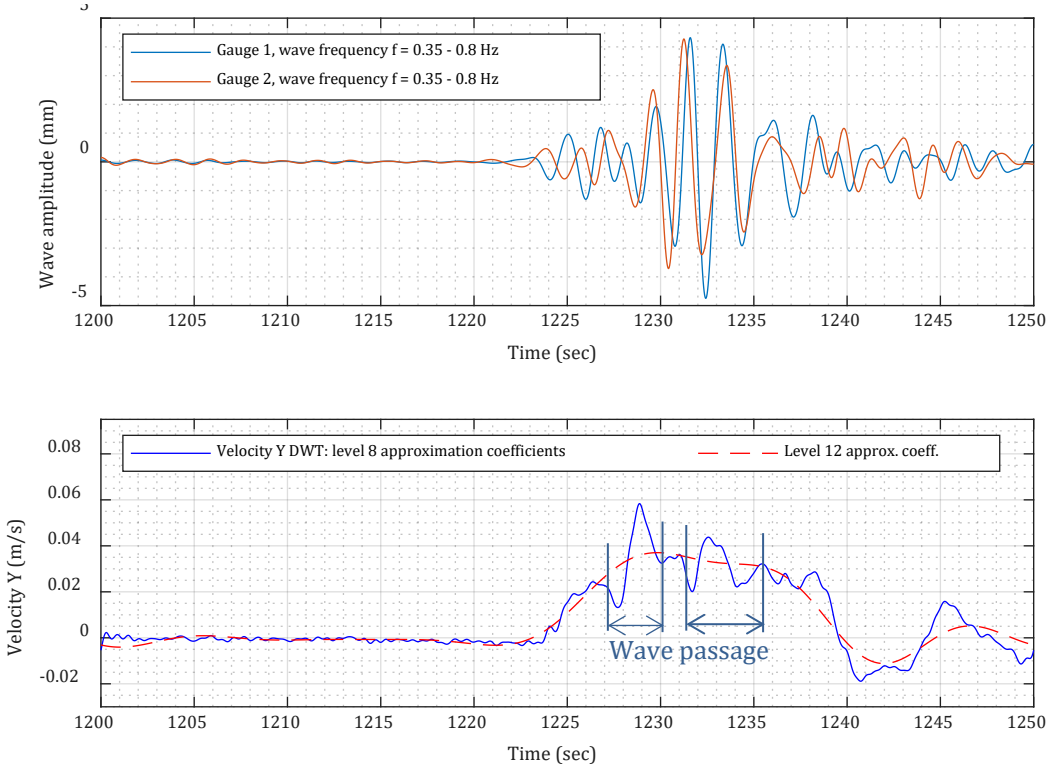

Figure 25: Test 1, extracted wave data (top) vs. EMS horizontal velocity DWT decomposed signal (bottom).

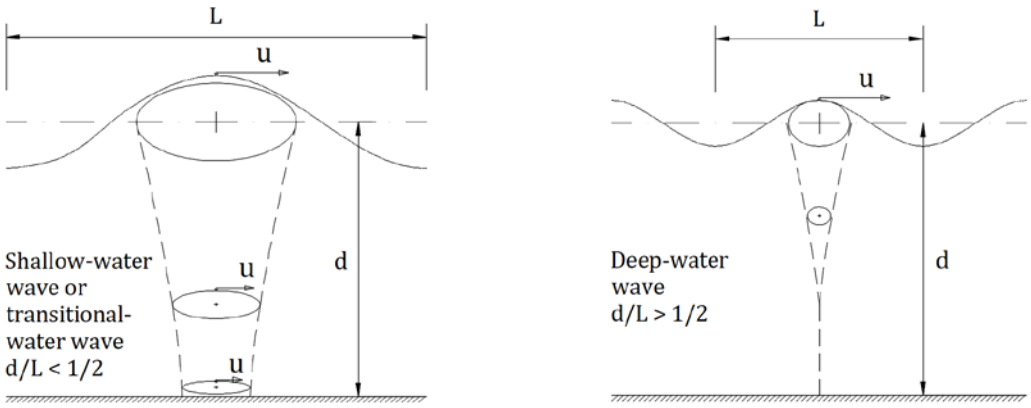

Figure 26: Water displacement for shallow-, transitional- and deep-water waves acc. to linear wave theory

6.1.4 Pressure measurements

During the failure of the slope the changes in water pressure is measured by mobile sensors installed within the soil body. As the sensors move, the measured changes in pressure are partially caused by changing position of a sensor in a water column. Thus, this pressure change corresponds to change in hydrostatic pressure. Further pressure increments result from a grain-water-interaction on microscale, such as excess pore water pressure generated due to collapsing soil skeleton. The excess pore pressure decreases effective stresses of soil body causing loss of bearing capacity which leads to instability of the slope.

Because the sandy soil material, which was used to construct the slope, exhibits relatively high permeability, pore water is able to drain rapidly. Therefore, the excess pore water pressure can dissipate relatively quickly. In contrast, the vertical movement of the sensors and, thus, the change in measured hydrostatic water pressure occurs more gradually, producing low frequency pressure data. As a result, pressure measurements can be decomposed by signal frequency to separate pressure increments due to sensor movements from the local changes in water pressure resulting from processes on micro scale.

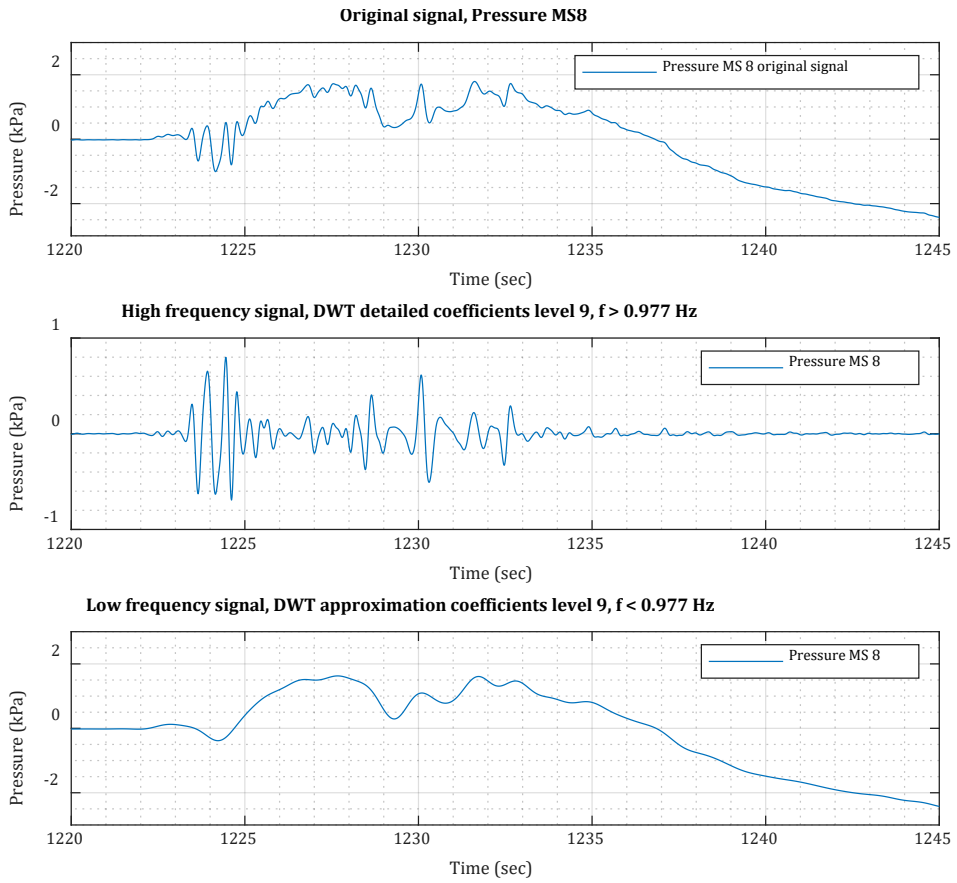

Figure 27: Test 1, pressure measured by MS 8, whereas the initial hydrostatic pressure is subtracted; signal decomposition with DWT level 9: original pressure data (top), high frequency component with f > 0.977 Hz (top), low frequency component with f < 0.977 Hz (bottom)

Figure 27 shows an example of data decomposition for the pressure measured by MS 8. Application of the DWT technique allows splitting pressure data measured by MS 8 into two components: low and high frequency components, which are likely to represent the global vertical movement of a sensor and locally measured pore water pressure, respectively. As the high frequency component contains abrupt changes and oscillations of the pressure data, it can capture rapid accumulation of excess pore water pressure and its dissipation, which can be of particular interest for studies of slope stability and liquefaction. Low frequency component is in turn useful for tracking and describing mobile sensors vertical movement during a slope failure.

Pressure measurements of wall sensors are presented in Appendix B. No pressure oscillations after the slope failure can be found in these measurements, as all waves are successfully absorbed by wave absorbers.

6.1.5 Soil mass acceleration

As described earlier, two stages of slope failure could be distinguished. First stage shows predominantly horizontal movement, while second stage is characterised by a rapid downwards displacement of the slope crest. Both stages of failure are followed by low frequency waves being generated, whereas the second stage adds the most to the wave amplitude.

To assess stresses and accelerations within the slope body, 10 mobile sensors (MS's) are installed in the sand. The MS's measure pore water pressure as well as accelerations in X-, Y- and Z-direction. Within reach of the connecting wires, mobile sensors can freely move with the moving soil mass, so that recorded accelerations can be associated with the acceleration of the failing mass movement. Due to rotation of the sensors, however, it is not possible to determine global directions of measured X, Y and Z accelerations. Thus, for the data assessment a resultant total acceleration is calculated, which is oscillating around gravitational acceleration *g*.

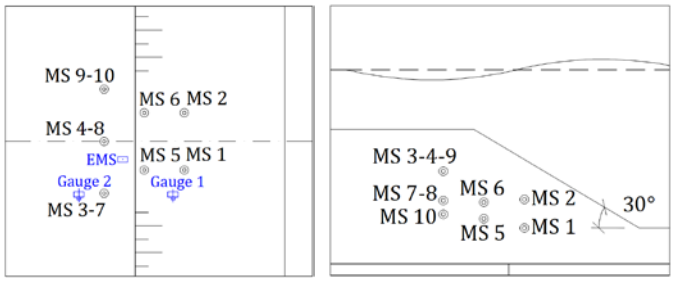

Figure 28: Mobile sensors initial location during test 1: top view (left), side view (right)

Before the slope failure occurred, MS 4 was located at a horizontal distance of only ca. 10 cm from the velocity measuring EMS, so that the horizontal water velocity was measured in only a short distance away from sensors location. As Figure 29 shows, onset of a gradual change of horizontal water velocity measured by EMS corresponds well to the first large acceleration peak measured by MS 4. Further acceleration peaks are associated with wave trains generation and while the mean velocity does not increase anymore, long wave passages bring water particle into

circulating movement creating oscillations in velocity data, as mentioned earlier. However, it is important to notice that while the horizontal movement of the failing soil mass is mainly directed towards the slope toe, the positive increment of mean velocity indicates a major water flow in opposite direction towards the shore side.

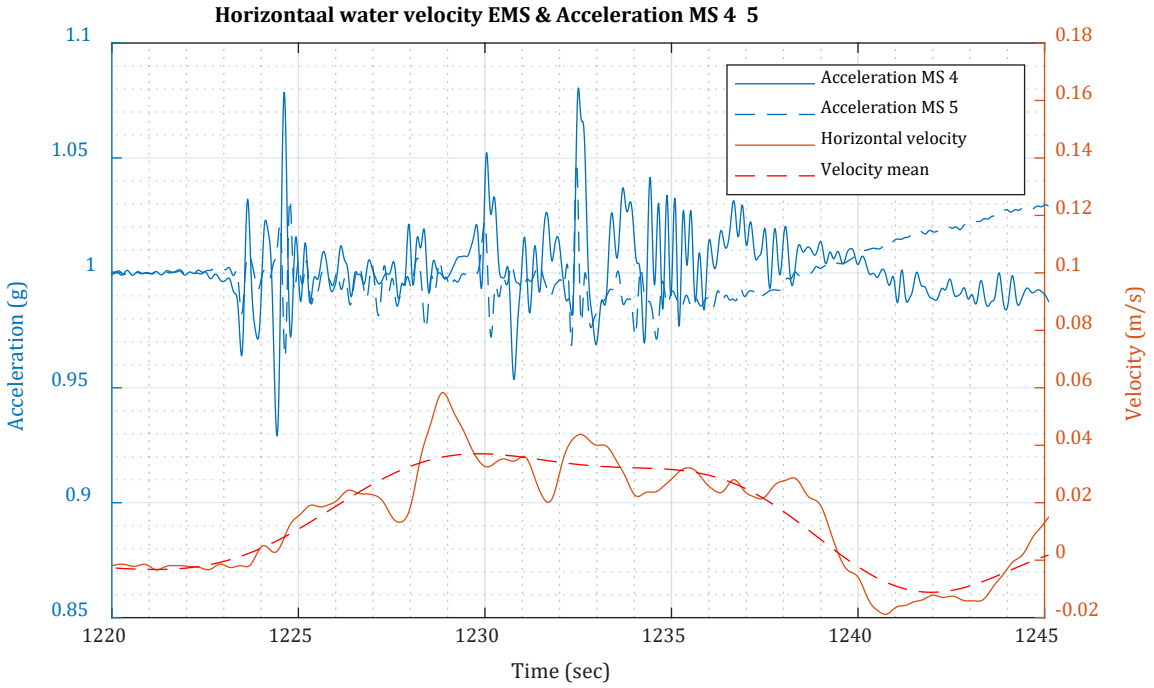

Figure 29: Test 1, time-series of acceleration MS 4 & 6 and horizontal water velocity measured by EMS

Two stages of slope failure can be clearly distinguished from acceleration measurements of MS's. Figure 30 (a - c) shows an example of accelerations measured by MS's 4 – 8 in comparison to the amplitude development of induced water waves.

In general the acceleration peaks can be associated with increase in wave amplitude, as can be seen from the time-series of acceleration measured by MS 4, pictured in Figure 30-a. However, one can notice that the wave amplitude is not directly proportional to the value of acceleration, as the peak acceleration during the failure stage 1 reaches values as high as or even higher than the peak acceleration during the stage 2, while the maximum amplitude of generated waves is less than a half of the maximum amplitude in stage 2. This is mainly caused by the fact, that due to unknown sensor rotation the resultant total accelerations do not provide any information about direction of the soil mass movements and can be directed vertically as well as horizontally. Horizontal component of the soil mass displacement, which appears to be predominant during failure stage 1, does not contribute to wave generation, which further provides the reason, why a relatively high peak acceleration detected by MS 6 (Figure 30-b) during the failure stage 1 is not followed by change in wave amplitude.

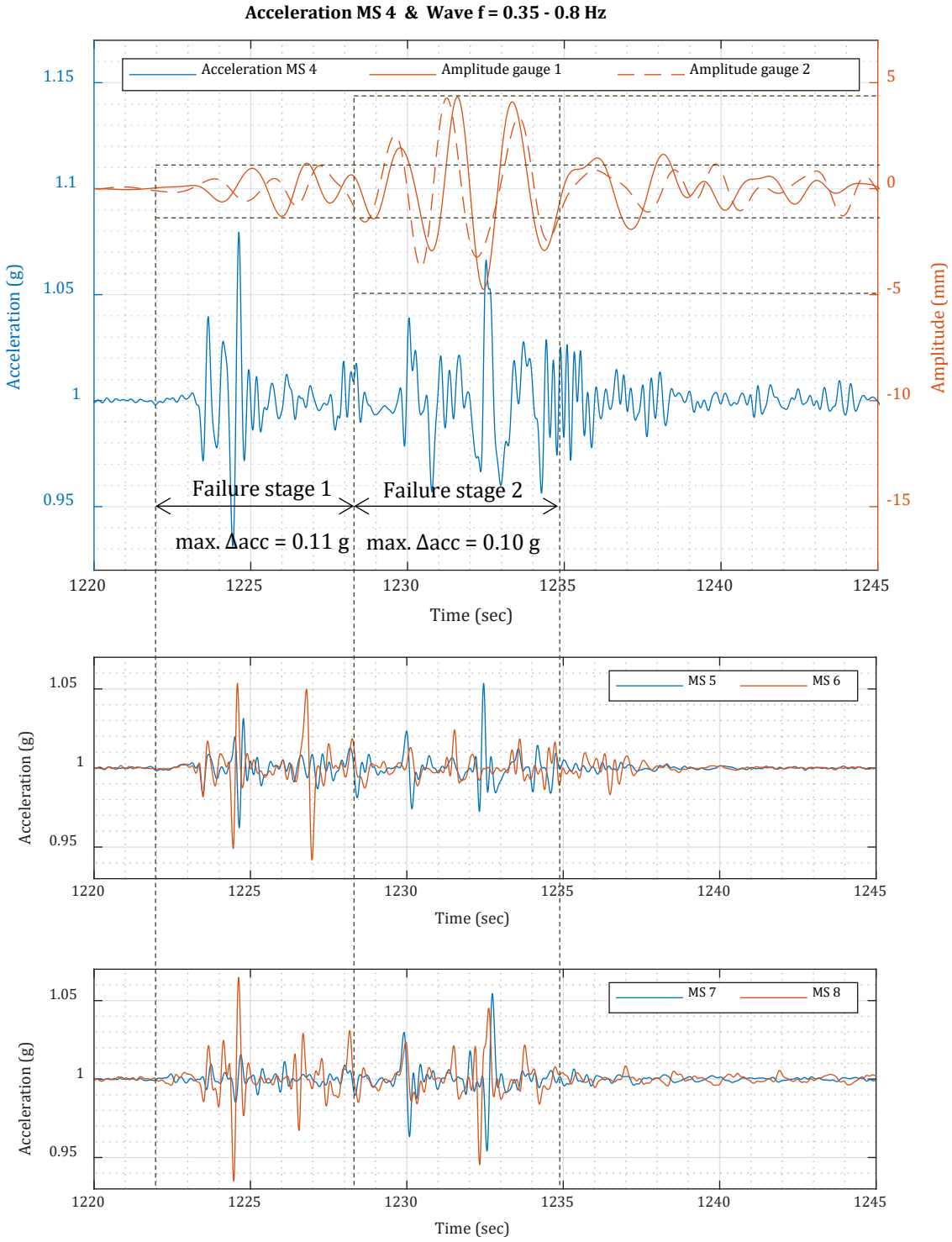

Figure 30: Test 1, time-series of a) generated wave and acceleration of MS 4, b) acceleration of MS 5 & 6, c) acceleration of MS 7 & 8. For other acceleration data see Appendix B.

The second failure stage can be recognised by a series of peaks in acceleration measured by all mobile sensors. Based on image analyses shown earlier, one can only roughly estimate the predominant direction of movement of MS's. The data from MS's 4, 7, 8 show several abrupt changes in acceleration, indicating rapid movement of the soil mass, however, a correct separation of horizontal and vertical components is hardly possible with unknown sensor

rotation. Nevertheless, the clearly visible downward crest displacement has significantly contributed to the wave amplitude, resulting in a maximum superposed wave height of nearly ±5 mm.

To appropriately evaluate the relationship between wave generation and mass acceleration, it is crucial to identify the sensors measurements representing vertically directed movement. As discussed earlier, pore water pressure data, collected by the MS's and decomposed by means of DWT, can provide an estimate of vertical movement of a sensor. An abrupt positive pressure increment, remaining after a longer period of time of ca. 15 - 20 s, gives an indication of sensors displacement directed downwards. The pressure data of all sensors is thus analysed again with the aim to find the sensors, which moved vertically during the sudden crest drop indicating failure stage 2.

As Figure 31 shows, the low frequency component of pressure measured by MS 10 exhibits an increase of pressure by approx. 3 kPa in two steps within a short time period of 2.5 s, which corresponds to 30 cm of relative vertical displacement of the sensor. Vertical acceleration, required for this displacement, can be estimated as $\frac{0.25\ m}{2.5\ s} / \frac{1}{(2.5\ s) \div 2} = 0.096\ m/s^2 \ \widehat{=}\ 0.01\ g$.

Although it is somewhat problematic to estimate a correlation between this sensor displacement and the real value of downward movement of soil mass, timewise the pressure increment is in good agreement with the wave data. Furthermore, embedded approx. 50 cm deep within the slope body, MS 10 shows the deep-seated nature of failure that occurred during stage 2.

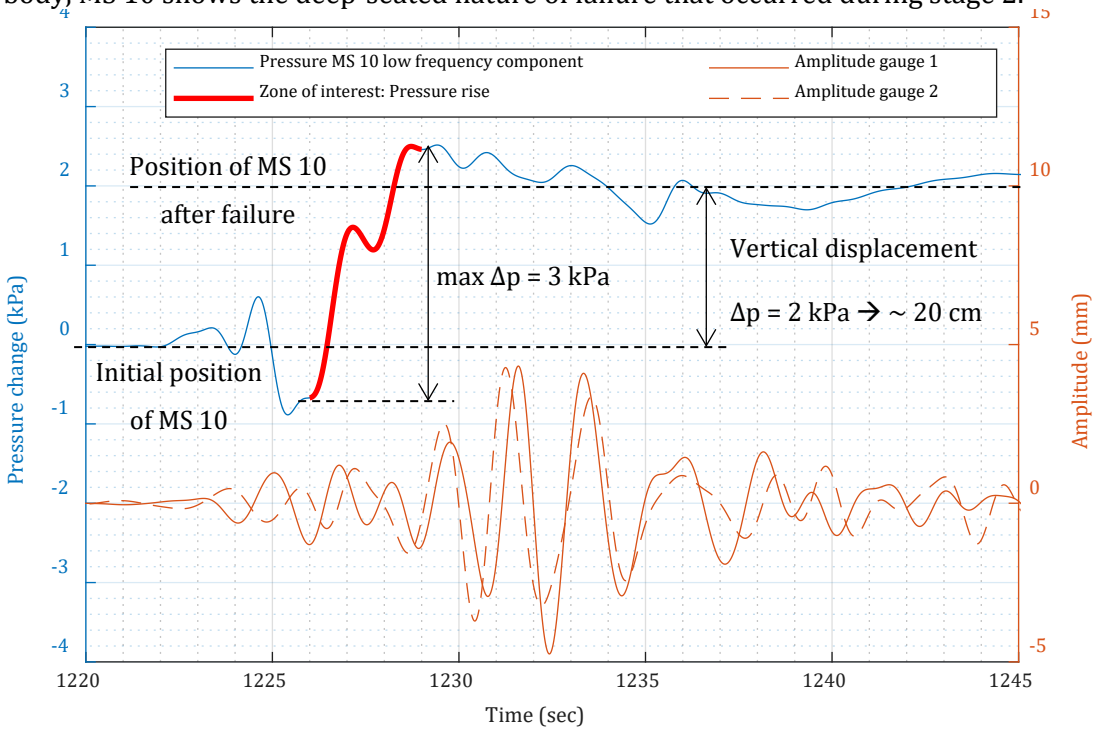

Figure 31: Test 1, pressure measured by MS 10 (frequency component < 0.977 Hz) and generated wave, indicating failure stage 1 and 2 as well as downward movement of the mobile sensor (zone of interest in red)

However, none of the sensors located closer to the crest of the slope measured similar rapid and large pressure increment, indicating vertical downward displacement. There are several factors that could have led to such an outcome. First of all, the mobile sensors during the test were installed predominantly under the sloping part and just behind the edge of the crest. This arrangement was unfavourable in this case since the crest drop down occurred further away from the edge of the slope, where no sensors were placed. Furthermore, during the failure stage 1 horizontal movement of the soil most likely shifted the sensors even further away from the part of the crest that later moved downwards. Finally, another limitation can be caused by wires attached to mobile sensors, which can restrict vertical movement of the sensor if it exceeds the wires length.

Sensors arrangement in addition to a synchronisation technique for signals from two separate acquisition systems as well as modifications of triggering mechanism sum up into the lessons learnt from the first experiment of the series. During the following landslide experiments 2,3 and 4, these features were improved to achieve a better test performance and produce more explicit results.

6.2 Test 2 & 3

During experiments 2 and 3 on wave generation by submarine landslides, the triggered landslides followed essentially the same failure pattern. The data gathered from these tests followed similar soil behaviour, geometry and motion characteristics of slope failure with correspondingly similar generated wave fields. Therefore, the evaluation of data from tests 2 and 3 is combined and presented in the following chapter.

6.2.1 Slope failure image analysis

During test 2 a failure was successfully triggered approx. 120 s after begin of data logging. For test 3 the time point of failure onset was approx. 180 s. Despite essentially the same geometry and only a slight difference in the density of the slope material, the type of failure during tests 2 and 3 significantly differs from the failure during test 1.

As Figure 32 shows, the slope failure during test 2 concentrated in the middle of the slope, creating an arching failure pattern. The progressive failure occurred relatively slow and showed mainly horizontal expansion around the centre of the sloping part. The crest of the slope displaced gradually without sudden changes in its height. Due to formation of an arch in the landslides top view, sides of the slope near glass walls of the tank, supported by the hard boundaries, have been densified and mostly remained stable during the failure.

The slope failure during test 3 followed nearly identical pattern with slightly less volume of failing mass and even slower failure progression due to stabilising effect of toe reinforcement (Figure 33).

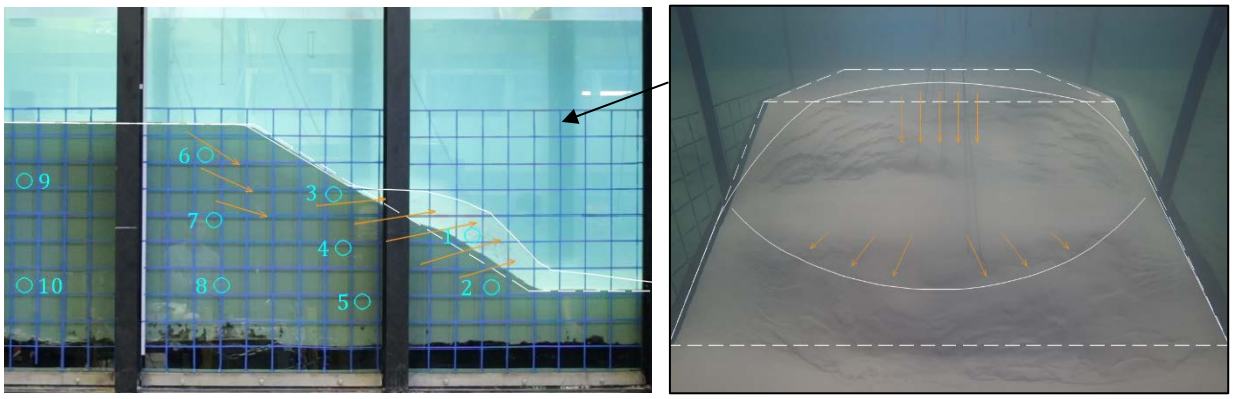

Figure 32: Slope failure during experiment 2; side view (left), front view on the slope from an under-water GoPro camera (right). Location of mobile sensors (MS) is estimated approximately.

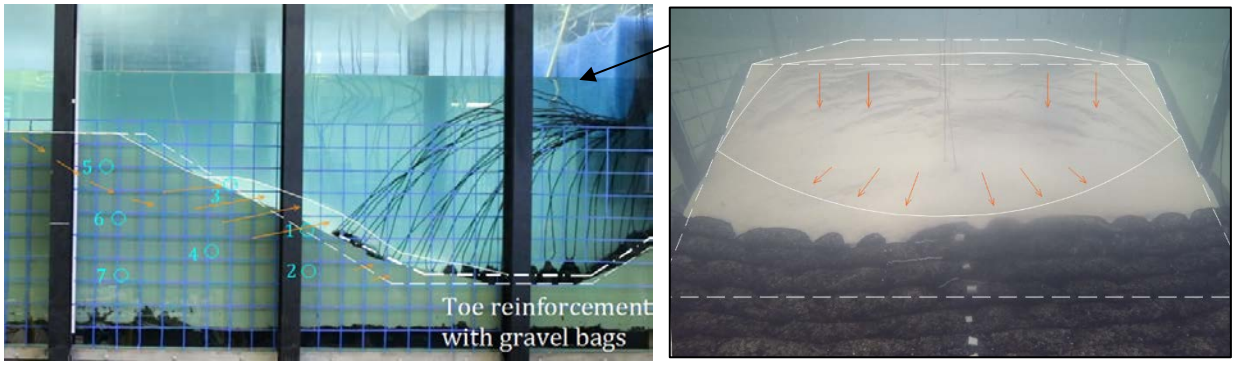

Figure 33: Slope failure during experiment 3, side view (left), front view on the slope from an under-water GoPro camera (right). Location of mobile sensors 1-7 (MS) is depicted approximately. MS's 8 and 9 are located outside of the figures boundary

Due to the fact that the slope deformation during the failure was relatively slow, gradually propagating and causing predominantly horizontal displacement, the conditions for wave generation during tests 2 and 3 were rather unfavourable. In fact, one can barely distinguish the waves from the image analysis, as they are not well defined with shorter wave length and minimal wave amplitude. The signal processing, however, provides a better picture of the water surface measurements and enables to extract and study the waves.

6.2.2 Wave localisation

Similar procedure of data analysis as in test 1 is applied to identify occurrence of long waves with low frequencies generated by slope failures during tests 2 and 3. We apply CWT to process the wave measurements, while DWT is applied to decompose signals by frequencies.

CWT performed for the data from test 2 shows an apparent presence of waves, whereas their frequencies range from 0.38 Hz to 0.58 Hz (Figure 34 - Figure 36). Directly noticeable is the extension of yellow high magnitude areas on the CWT scalograms, which demonstrates the presence of waves for a longer period of time than in test 1. However, the maximum magnitude

of CWT coefficients on the scalograms barely reaches a quarter the magnitudes in test 1, indicating the proportionally smaller wave amplitudes.

Test 3 data show even less evidence of wave generation as the maximum magnitude of CDW coefficients on the scalograms drops even more and no clearly visible zone of high coefficients is present in measurements of both gauges (Figure 35). Whereas gauge 2 signal contains a somewhat defined component around the frequency of 1 Hz, this wave appears to be a local low-energy wave, as it disperses quickly and does not reach gauge 1.

The original unprocessed wave gauge data of tests 2 and 3 are presented in Appendix B.

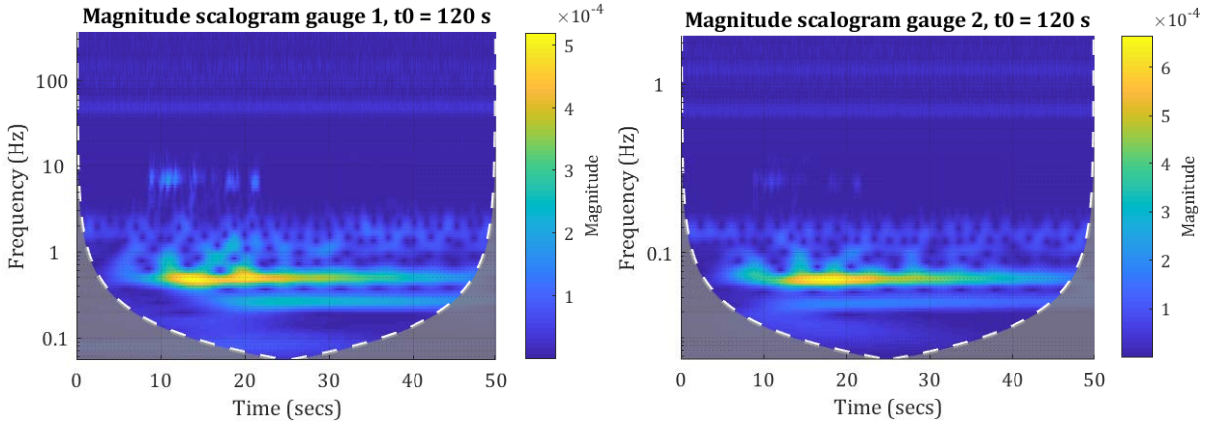

Figure 34: Test 2, results of continuous wavelet transform test 2: signal from gauge 1 and 2 in time-frequency space

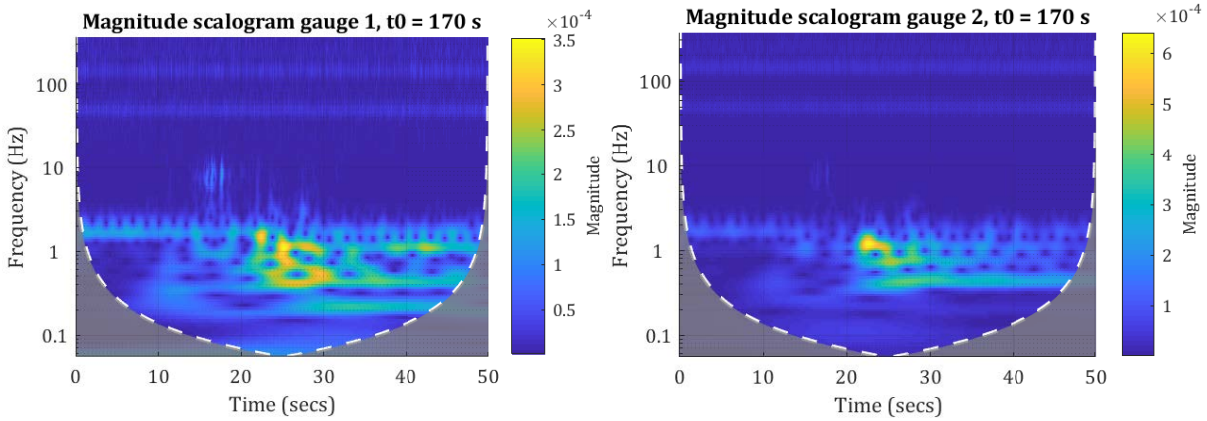

Figure 35: Test 3, results of continuous wavelet transform test 2: signal from gauge 1 and 2 in time-frequency space

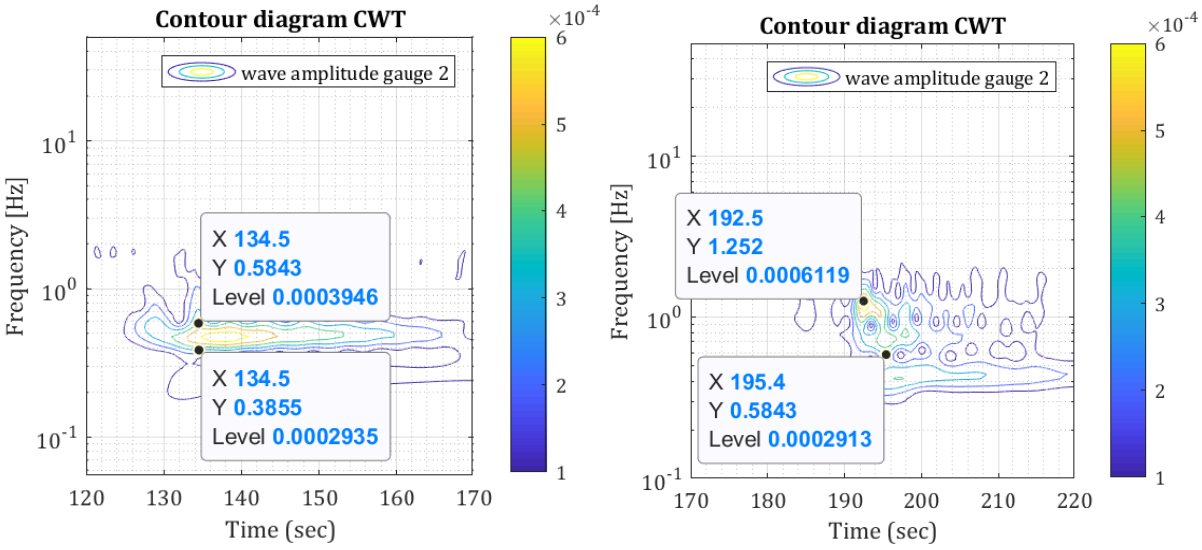

Figure 36: Contour diagrams of CWT for test 2 (left) and 3 (right), including data tips indicating location of generated waves in time-frequency space; X – time, Y – frequency, Level – magnitude of CWT coefficients

6.2.3 Extracted wave

After we localised the generated waves within the time-frequency domain, the waves can be extracted from the signal. For the data of test 2 and 3 we use a frequency band-pass of 0.38 - 0.58 Hz and 0.95 – 1.45 Hz, respectively.

As expected, the wave envelops in tests 2 and 3 differ significantly from test 1, which is clearly visible in Figure 37 - Figure 38. The maximum amplitude of a superposed wave in test 2 reaches only ±0.9 mm, while the wave does not dissipate and keeps on oscillating for over 40 s. The period of the wave reaches more than 2 s, which might result in high percentage of the wave reflection, as the wave absorber design was conducted with smaller values of wave period.

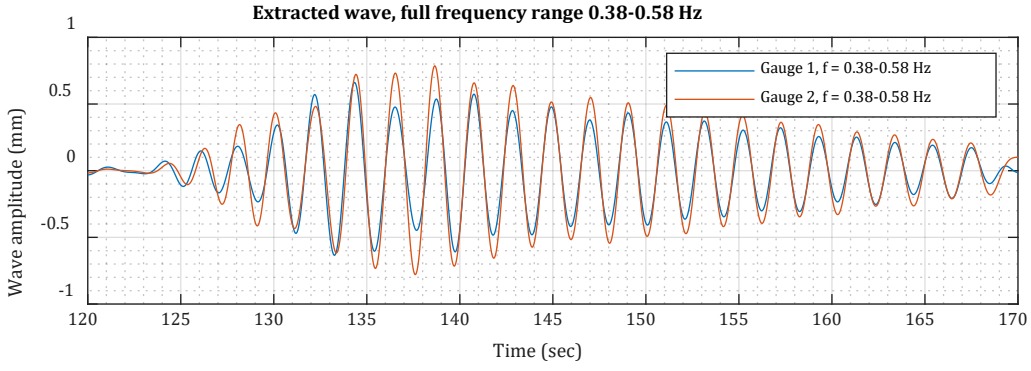

Figure 37: Test 2, wave extracted from the data of wave gauges 1 and 2, frequency range 0.38 – 0.58 Hz

The wave field in test 3 is highly dispersed. Visible solely in measurement of gauge 2, the waves reach their maximum amplitude of less than 1 mm with a delay of about 15 s after the onset of failure at the 180 second mark. These small dispersed waves are nearly negligible and will not be

further investigated in detail during this study, as they clearly do not represent a long tsunami-type of wave. Instead, we can conclude that during test 3 only negligibly small amplitude long waves were generated by a submarine landslide.

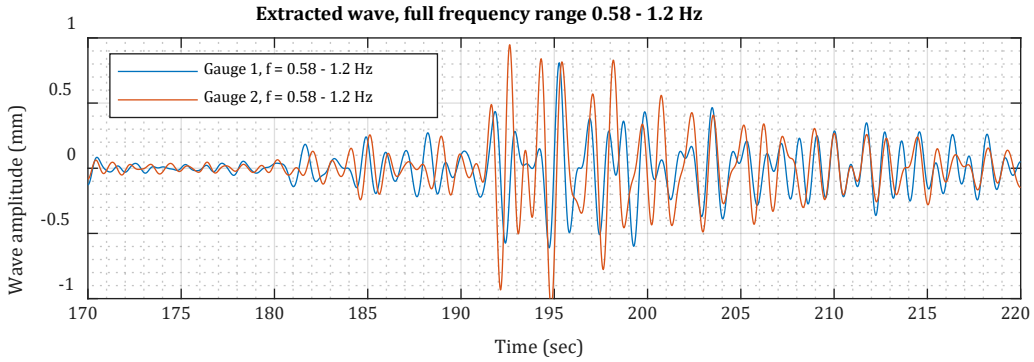

Figure 38: Test 3, wave extracted from the data of wave gauges 1 and 2, frequency range 0.95 – 1.45 Hz

One can question whether the waves in test 2 should be further considered. The nature of the waves generated during tests 2 remarkably differs from the wave in test 1. Besides their small amplitudes, the pattern of wave development shows some significant differences. In test 2, the wave amplitude increases gradually with no sudden increments during a time span of nearly 15 s. Possibly, gradually progressing slope failure induced this wave, while its slow rate of mass motion resulted in such small wave amplitudes. Furthermore, we cannot exclude the possibility that these wave trains partially occurred due to short water injection at the base of the tank, which is used as triggering mechanism for a slope failure. However, despite the fact that exactly the same triggering mechanism was applied during tests 2 and 3, the measured wave formation does not show a slight resemblance.

As Figure 39 shows, the pressure increase at the base due to application of the triggering mechanism is abrupt with a maximum increment at the start of triggering. The wave amplitude, however, increases gradually reaching its maximum at the moment when base pressure is nearly constant. Furthermore, Figure 40 shows that in test 3 the same triggering mechanism did not even slightly contribute to wave generation and peak amplitudes occur with a delay of 13 s.

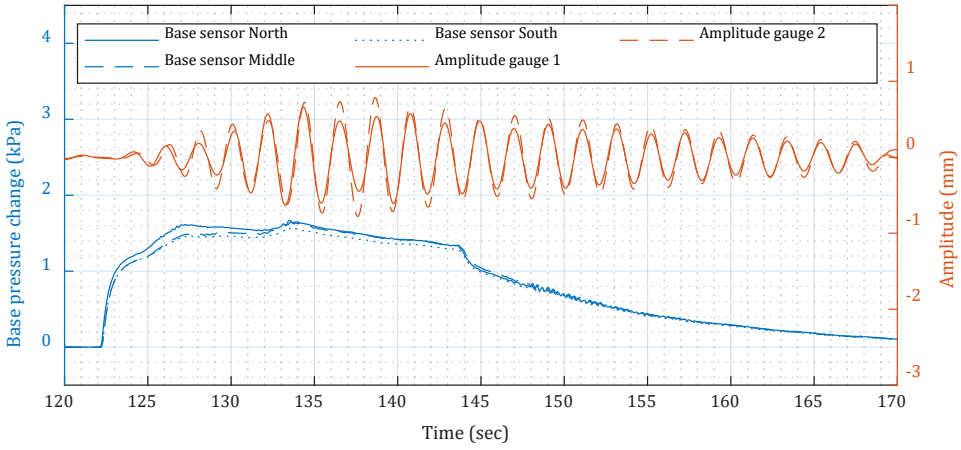

Figure 39: Test 2, base pressure increment during failure triggering in comparison to the wave amplitude

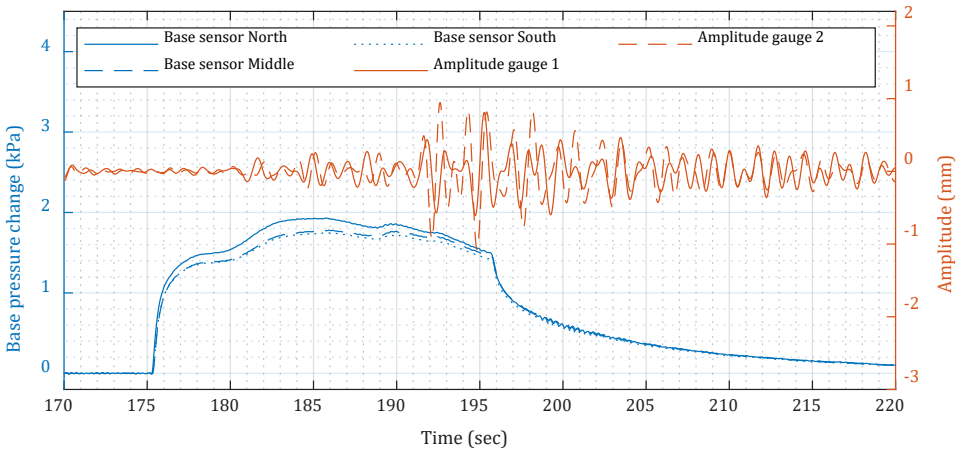

Figure 40: Test 3, base pressure increment during failure triggering in comparison to the wave formation

Measurements of horizontal water velocity by EMS show only negligibly small oscillation, while its mean remains almost at zero throughout the entire failure duration. As mentioned earlier, shorter surface waves do not influence the measurements of EMS as the ratio water depth to wave length d/L > ½ represents deep-water condition. Since during test 2 the measured horizontal water velocity remained at zero, one can conclude that the generated wave field corresponds to a deep-water condition, so that the wave length L must be less than twice the water depth d.

Reflection of waves in test 2 is another factor that can influence the measurements. By widening the toe and removing the right-hand side slope completely, an unfavourable condition for wave absorbers was created, as due to increased water depth the elements length was not enough to cover the entire water column. However, considering only a small amplitude of the measured waves, the discussion on wave reflection is not continued for results of test 2.

6.2.4 Pressure measurements

One of the major concerns of the current study is the influence of the applied triggering mechanism on the measurements performed during the tests. We have seen that the triggering mechanism is unlikely to contribute significantly to the process of wave generation. However, the pressure measurements of mobile sensors are also affected by propagation of the pressure wave from the base of the tank upwards.

Water pressure measured by base sensors generated during failure triggering is presented in combination with measurements of MS's 3, 5, 6 and 8 in Figure 41. The pressure increment due to triggering mechanism corresponds to the initial pressure increment in all mobile sensors at begin of failure. As could be expected, the MS's 5 and 8 which are located closer to the base filter layer measure a higher increment than the MS's 3 and 6, which are located higher within the slope (Figure 41). However, all sensors measure the pressure increment almost instantaneously which shows the high velocity of pressure wave propagation. After approx. 2 s, the base pressure is

nearly constant or increases only slightly, while the MS's do not show any dependence on the base pressure development anymore. One can conclude, that any relative pressure changes measured by MS's at the later stages of failure are solely due to two processes: vertical sensors displacement and micro-scale grain-water-interaction, such as excess pore water pressure. As suggested earlier, these two components can be separated by means of DWT frequency based signal decomposition.

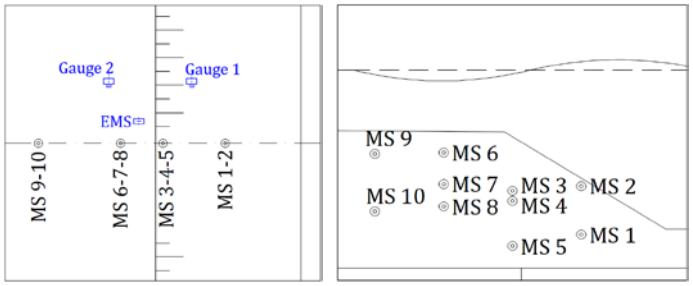

Figure 41: Mobile sensors initial location during test 2: top view (left), side view (right)

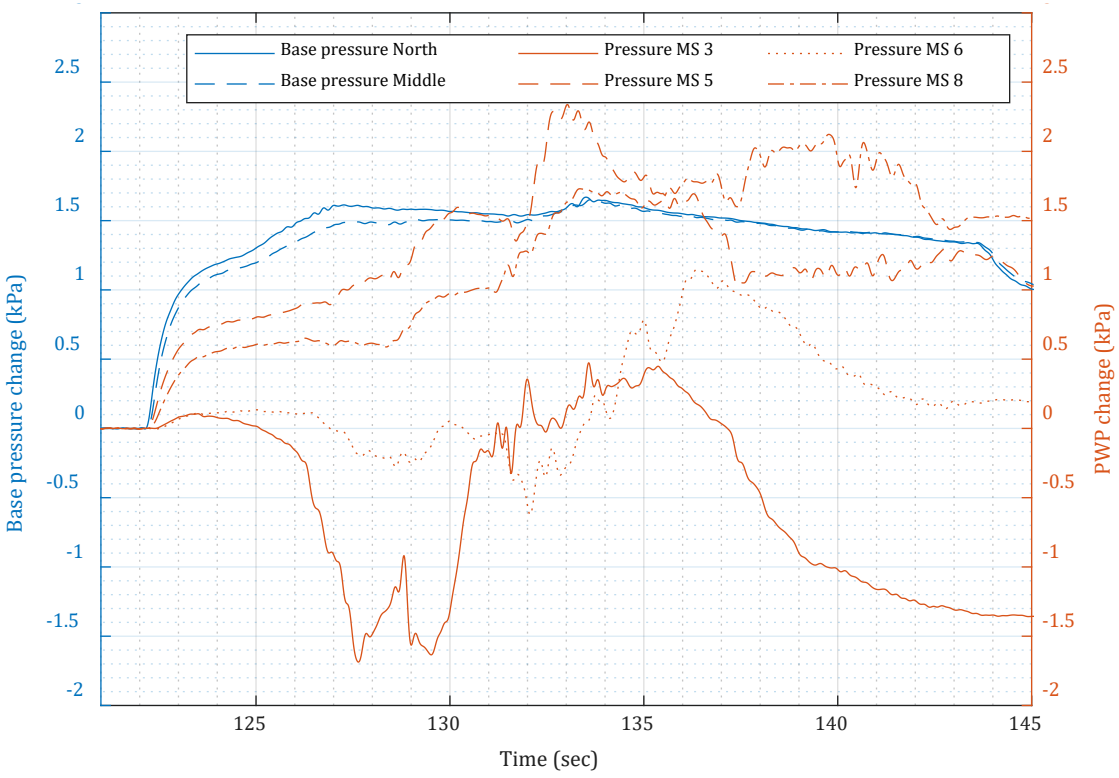

Figure 42: Test 2, pressure measured by MS's 3, 5, 6 and 8 in comparison to the measurements of base pressure sensors; the initial hydrostatic pressure is subtracted

After DWT decomposition, the pressure increment caused by application of triggering mechanism is contained within the low frequency component (Figure 43). Thus, to measure an absolute value of vertical displacement relating to the sensors initial position before the failure, one should subtract the amount of pressure increase caused by failure triggering from the total pressure

increment. However, for identification of discrete movements of MS's the pressure increment caused by triggering mechanism is not decisive.

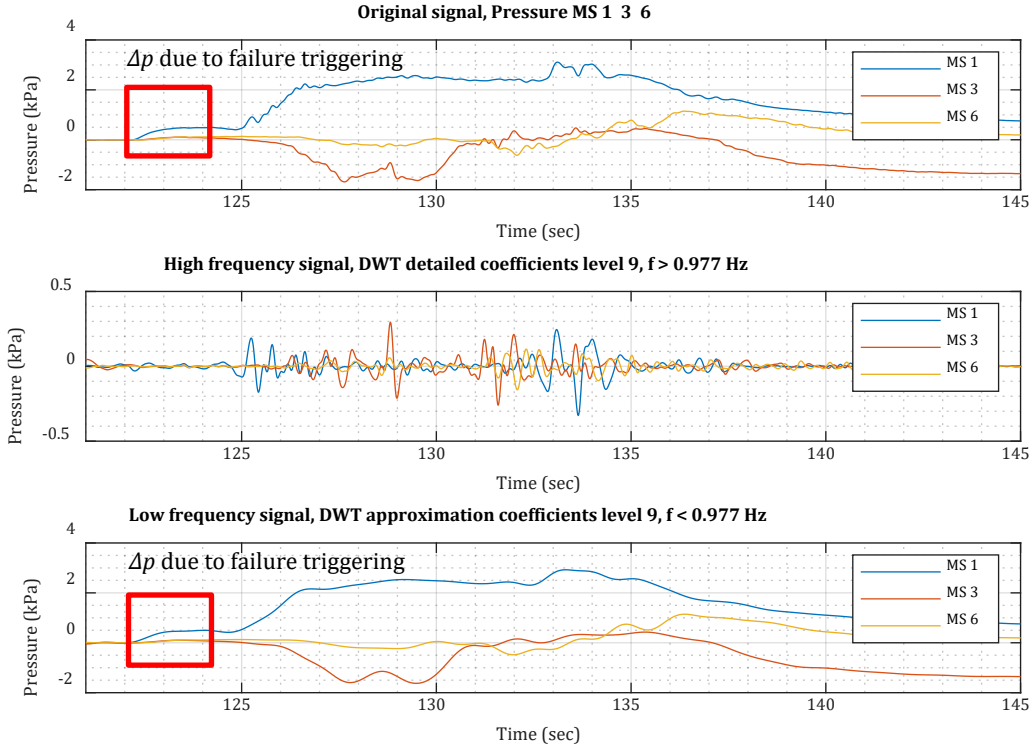

Figure 43: Test 2, MS's 1, 3, 6 pressure signal decomposition with DWT: original signal (top), high frequency component with f > 0.977 Hz (middle), low frequency component with f < 0.977 Hz (bottom); the initial hydrostatic pressure is subtracted

Using Figure 44, the mass motion during the failure in test 2 can be characterised. It is clearly visible that only sensors located close to the slope toe (MS's 1 and 3) experienced significant vertical displacement at the onset of failure. Following the progressive failure, MS's 5, 6 and 8 become active and show a vertical displacement with a delay of about 12 s. MS's 9 and 10 remain nearly motionless, at least with respect to vertical movement.

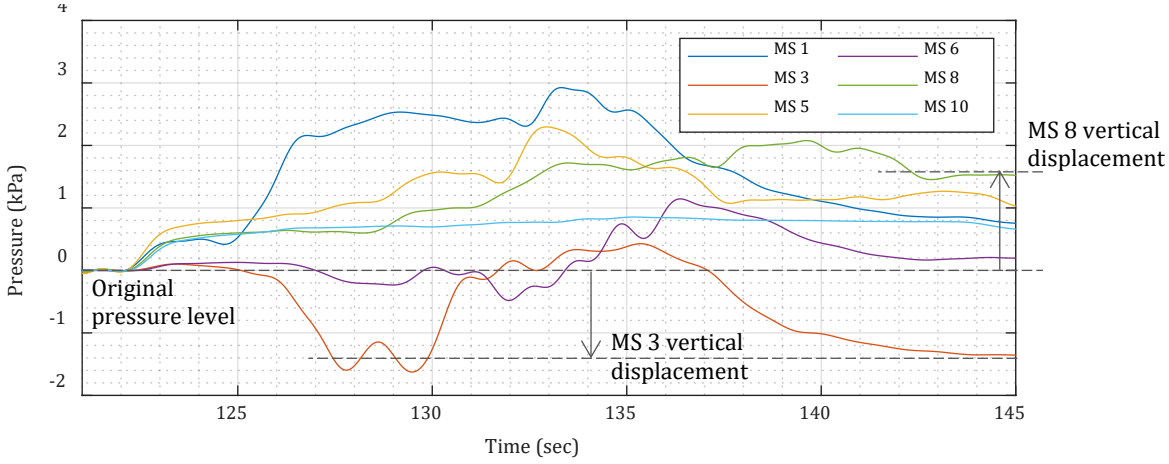

Figure 44: Test 2, MS's 1, 3, 5, 6, 8, 10 pressure signal, low frequency component f < 0.977 Hz

During test 3, the type of slope failure was analogue to the failure in test 2. Figures below show the pressure development measured by MS's during test 3, where the arrangement of sensors differs only slightly from the one in test 2 (Figure 45). While the failure duration in test 2 can be estimated at about 20 s, the failure during test 3 is even more gradual, extending to approx. 25 s. Furthermore, despite a somewhat higher triggering pressure during test 3, which reflects in a larger initial pressure increment, the later pressure development remains overall slightly lower than in test 2, supporting the visual observation of a smaller scale landslide. Water pressure, measured by MS's, returns to its original value after the slope failure (Figure 46), which suggests that MS's did not move significantly during the failure, with an exception of MS 3.

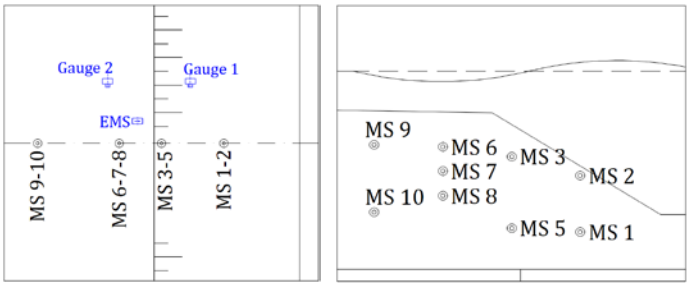

Figure 45: Mobile sensors initial location during test 3: top view (left), side view (right)

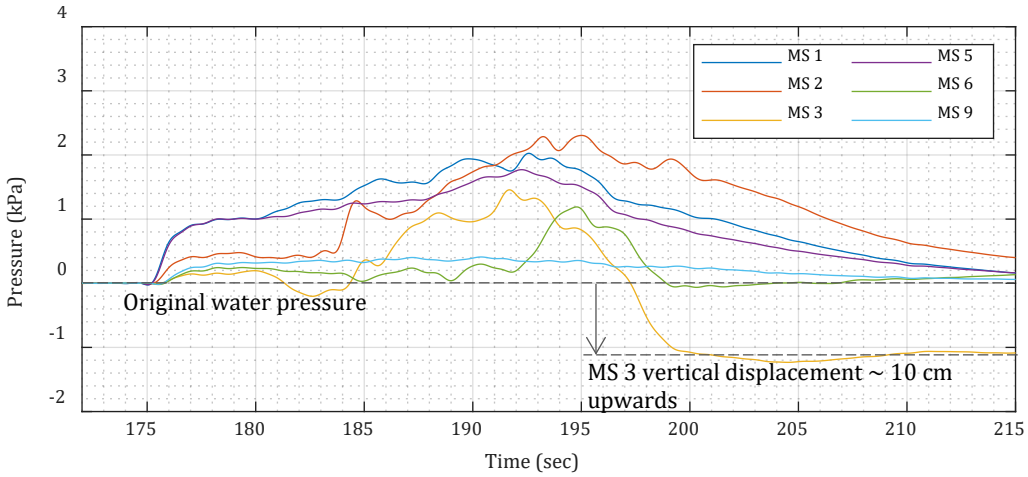

Figure 46: Test 3, MS's 1, 2, 3, 5, 6, 9 pressure signal, low frequency component f < 0.977 Hz

Pressure measurements of wall sensors can be found in Appendix B. These measurements show only negligibly small amplitude of pressure oscillation in test 2, which agrees well with the wave amplitude measured by wave gauges. In test 3 no pressure oscillations can be distinguished.

6.2.5 Soil mass acceleration

For a nearly the same initial slope conditions, wave generation was only slightly present during test 2 (small amplitudes) and completely absent during test 3 (small amplitudes and highly dispersed). Soil mass accelerations during these tests should yield the threshold of acceleration, below which a wave generation can be considered unlikely to occur.

In test 2, acceleration change measured by MS's 5, 7, 8, 9 and 10 remains nearly equal to zero throughout the entire failure duration (Appendix B), which corresponds well to the observations of low frequency component of pressure measurements. In turn, recordings of accelerometers of MS's 1, 3, 4, 5 and 6 indicate sensors motion during failure.

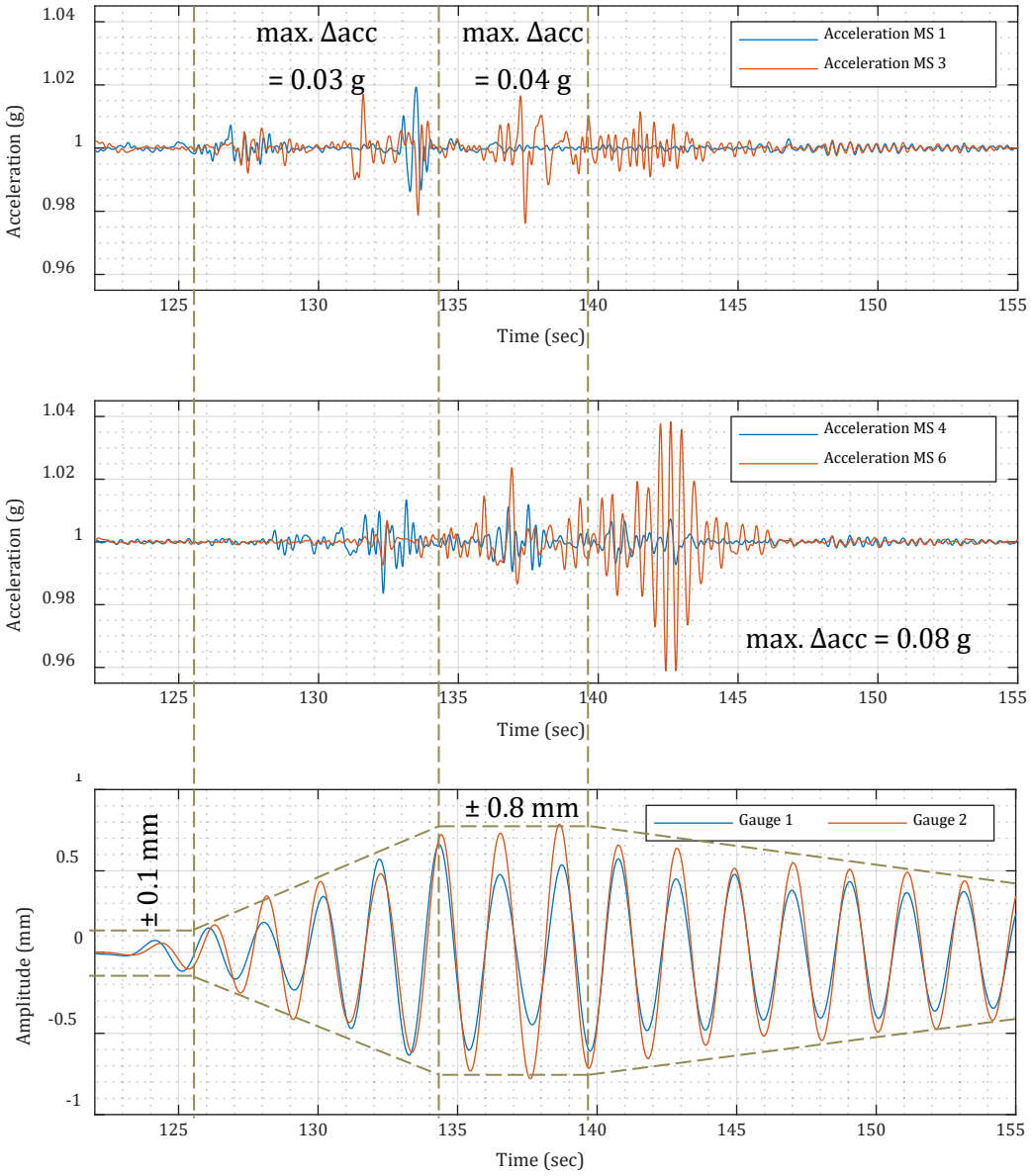

Figure 47: Test 2, time-series of acceleration measured by MS's 1, 3, 4 and 6 (top-middle), generated wave (bottom). For other acceleration data see Appendix B.

As Figure 47 shows, accelerometers get activated by a progressing failure one by one, creating delays in response. MS 6 exhibits the most delayed reaction, showing high amplitude signal oscillation more than 15 s after the failure onset, while other sensors are nearly at rest. By comparing these acceleration measurements to the waves generated during the failure, it becomes visible that before any sensor detected a movement of soil mass, a small portion of wave amplitude was already added. This can be a result of a more superficial soil displacement, that

wasn't deep enough to activate a sensor movement. However, there is also a possibility that this wave amplitude was added by triggering mechanism. If this is the case, we can quantify the impact of triggering mechanism and conclude that it is negligibly small.

Similar to conclusions from test 1, one can see in Figure 47 that peaks in acceleration do not directly correspond to an increase in wave amplitude, as the measured accelerations are of unknown orientation and can be predominantly horizontal, impacting the waves much less. Especially, this is visible from a delayed response of MS 6 acceleration, which is despite its high value does not receive a corresponding change in wave amplitude. In fact, going back to Figure 44, it becomes clear that the MS 6 barely experienced any vertical displacement at later stages of the failure, explaining absence of a wave formation.

During test 3 accelerometers of MS's 1, 2, 5, 7, 9, 10 show no acceleration increments (Appendix B), remaining at 1g value throughout the failure duration. Again, that shows how limited the displacements within the slope body remained during test 3. Only the measured by MS's 3 and 6 accelerations indicate a rather superficial mass flow, concentrated around top part of the slope and edge of the crest. Finally, Figure 48 shows that the created dispersed wave filed timely agrees well with acceleration measurements. One can conclude that such a superficial mass flow during the failure does not result in long well-defined wave formation and rather produces small dispersed waves.

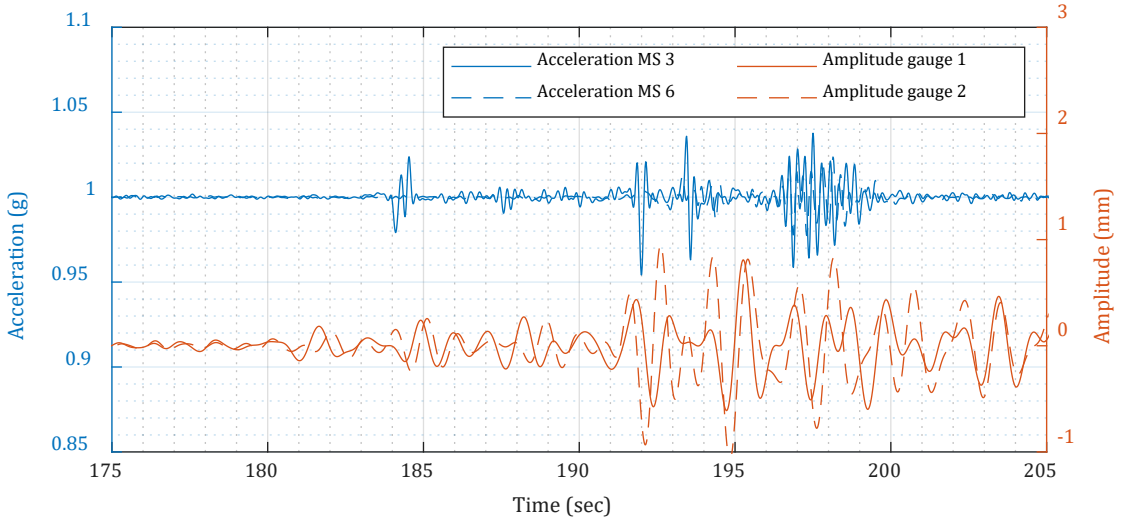

Figure 48: Test 3, time-series of acceleration measured by MS's 3 & 6 in comparison to the dispersed wave field

Since hardly any waves were generated by the landslides in tests 2 and 3, measurements during these tests provide important information about landslide conditions that are rather unfavourable for wave formation. We have seen that steady progressive slope failures increase the duration of wave oscillation, forming new wave trains throughout the time period when failure is progressing. However, in such conditions wave amplitudes remain relatively small. As expected, reduction of the landslide volume and progression rate leads to even further limitation

of wave formation, resulting in dispersive poorly defined wave field. Wave reflection possibly was present during test 2, as conditions for the wave absorbing elements were rather unfavourable because of full removal of the right-hand side slope and therefore increase in water depth on the North-side of the tank. To avoid such conditions, during subsequent experiments, toe width is reduced again to keep the right-hand side slope in place.

6.3 Test 4

The fourth experiment is the final experiment of the series analysed in the current work. Its major difference from the previous experiments 1-3 is the tilting of the tank up to 8°, which was performed during test 4 in order to insure a slope failure, even though the slope material was dense. Furthermore, during test 4 we were able to successfully trigger 3 landslides, whereas each of them was initiated by a different triggering mechanism: tilting, controlled application of base pressure with a chamber and finally, a release of a trapped in the system pressure wave.

6.3.1 Slope failure image analysis

During tilting of the tank a rather small, localised around edge of the crest, slope failure occurred at a tilting angle of 3.66°. The failure developed about 210 s after begin of data logging. Approximately 1/5 of the slope width showed rapid vertical displacement as well as the top part of the sloping sand bed has slightly expanded horizontally. Figure 49 shows an approximate outline of the failure geometry.

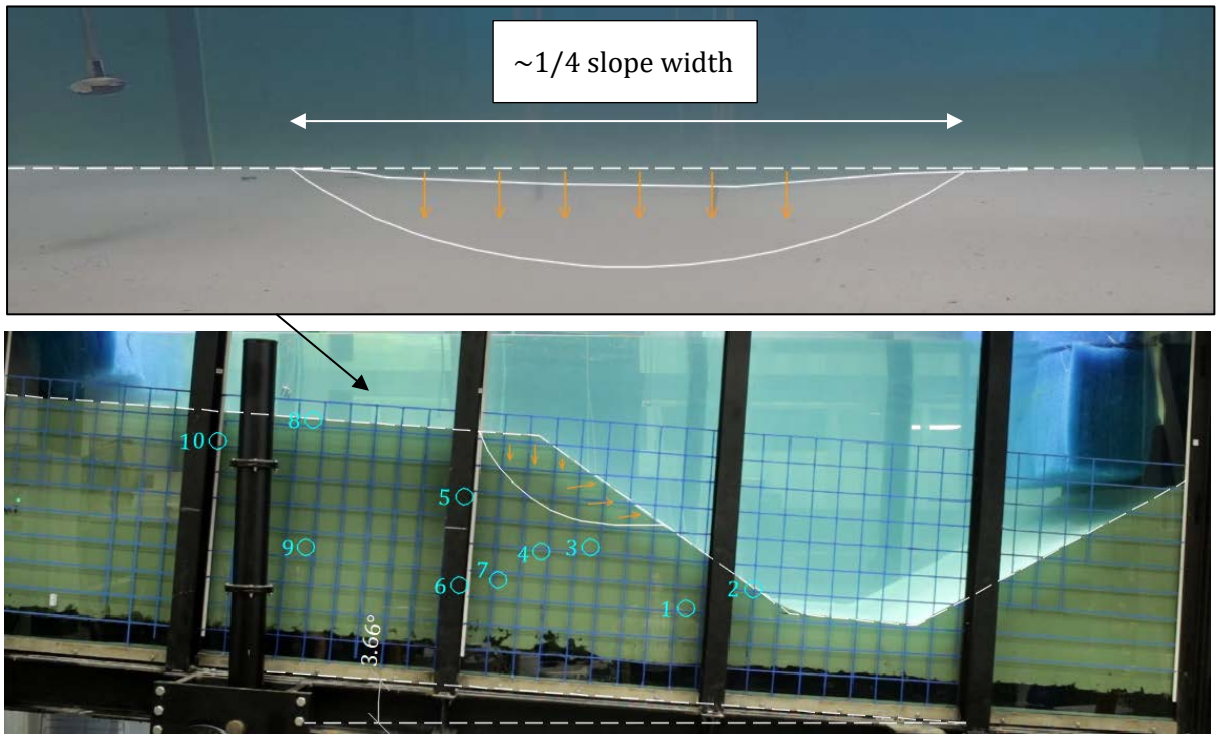

Figure 49: Test 4, failure 1; slope failure localised around centre of the crest edge, top view from an under-water camera (top), side view (bottom). Location of mobile sensors (MS 1-10) is estimated approximately.

This failure resulted in only limited wave formation due to its relatively small volume. However, it is included into the analysis, since tilting, used as slope failure triggering mechanism, has not been analysed before, but in fact offers more favourable conditions for a wave study, as it does not add water into the system, creating less disturbance of water surface.

After the tank was tilted to its final angle of 8°, the second failure was triggered by means of the pressurised chamber. A pressure of about 1.5 kPa was applied and was followed by an onset of slope failure approx. 7.5 s later. In global time scale, this failure occurred 750 s seconds after the start of data logging. The type of failure significantly differed from the failures that we have observed before. The crest of the slope experienced a very quick drop down, forming an arch at the centre of the slope top view. Some material was pushed forwards creating an expansion at the top of the slope, as can be seen in Figure 50. Rapid soil displacement was not progressive and after the major displacement occurred in less than a couple of seconds, further mass movement was only due to slow downwards flow of the pushed out material down the slope.

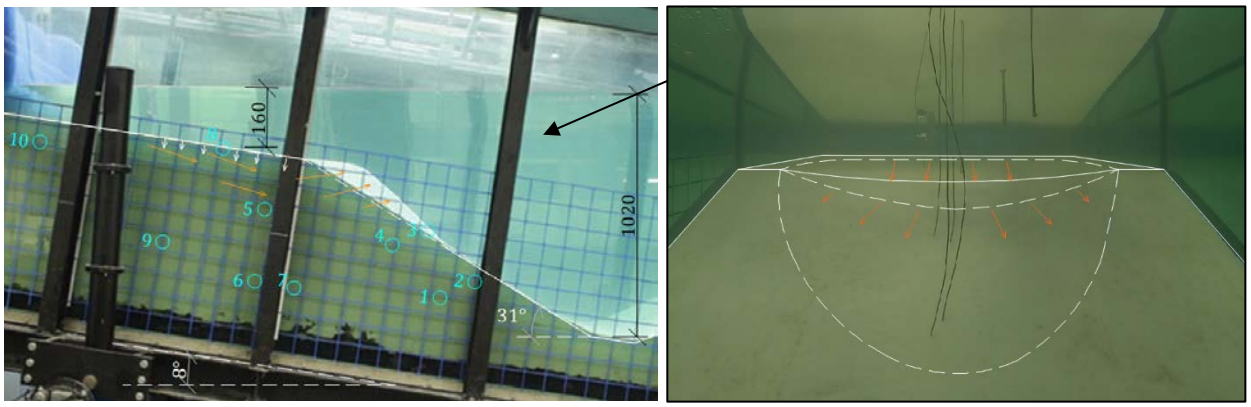

Figure 50: Test 4, failure 2; slope failure occurred around centre of the slope, side view (left), front view on the slope from an under-water GoPro camera (right). Location of mobile sensors (MS) is estimated approximately.

Finally, the third failure was triggered after the measured pressures and accelerations within the slope body stabilised. Due to tilting and mass flow resulted from the previous two failures, the slope was reshaped: the slope angle changed to about 27° and the slope length increase to approx. 1.4 m. The expanded toe area was filled with rather loose sand.

Approx. 1020 s after start of data logging, Failure 3 was triggered by means of a trapped pressure release. As described earlier, the pressure wave, which gets trapped within the fluidisation system of the tank, can be released into the base filter layer of the tank. This triggering mechanism resulted in an abrupt pressure increase of about 3 kPa, measured by the base sensors. In general, failure 3 resulted in a larger soil mass movement than the previous failure. The onset of failure was clearly noticeable by a sudden push forward of the slope area near location of sensors 3 and 4. Later the slope failure propagated inwards and resulted in large displacements and partial liquefaction of the slope.

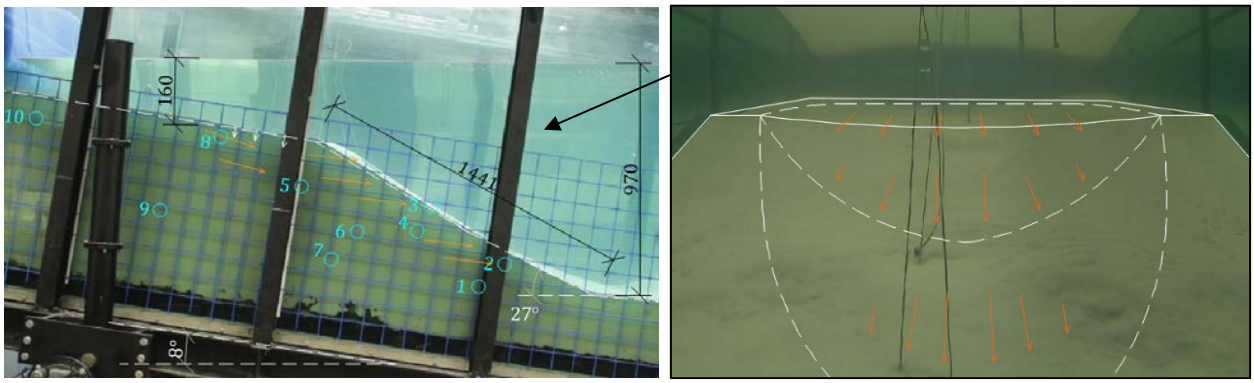

Figure 51: Test 4, failure 3; slope failure with a predominant mass flow down the slope, side view (left), front view on the slope from an under-water GoPro camera (right). Location of mobile sensors (MS) is estimated approximately.

Wave formation could be visibly recognised during failures 2 and 3, so one can expect larger wave amplitudes for these two failures. We expect, however, also a higher scattering of the wave gauge measurements, as a result of the tank tilting. Especially during the second and third failures, whereas the tank was tilted to 8°, water depth difference between the locations of gauge 1 and 2 increased enormously. Gauge 1, located above the sloping part of the sand bed, measured surface elevation at a depth of approx. 80 cm, while at the location of gauge 2 the water depth was less than a half of it, reaching approx. 38 cm. The effects of shoaling and reverse shoaling, due to propagation of waves from a deep- to shallow-water or other way around, is likely to be a significant factor for the measurements evaluation of failure 2 and 3.

6.3.2 Wave localisation

Similar to the previous tests, a CWT is applied to localise waves, if generated, within the time-frequency space. During the first slope failure, triggered by tilting of the tank, a well-defined wave can be seen at the magnitude scalogram of gauge 2 (Figure 52). However, the data of gauge 1 does not show the same wave pattern, as the magnitudes of the CWT coefficients are less than a half the magnitude of coefficients for the gauge 2 data. Proportionally, the water surface elevations measured by gauge 1 are much lower than the elevations measured by gauge 2.

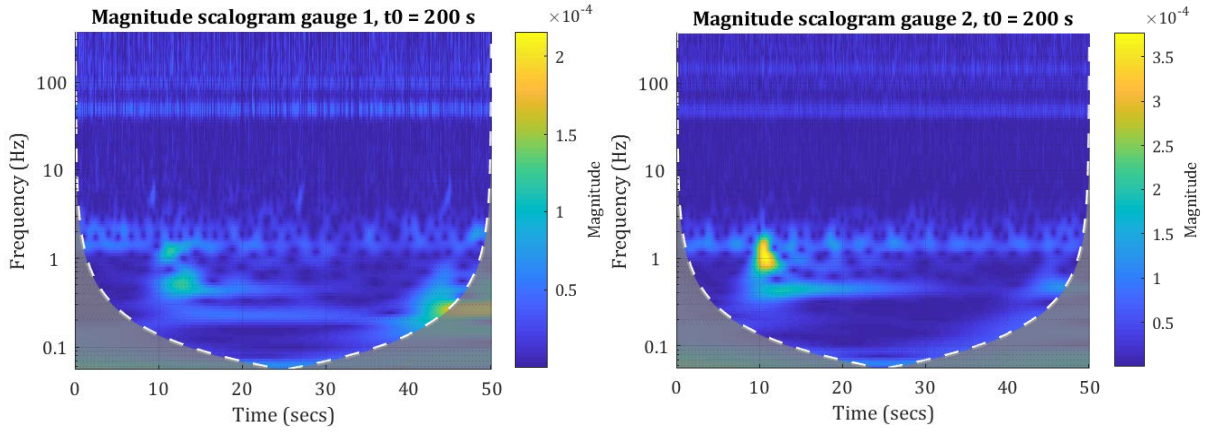

Figure 52: Test 4, failure 1, results of CWT: signal from gauge 1 and 2 in time-frequency space

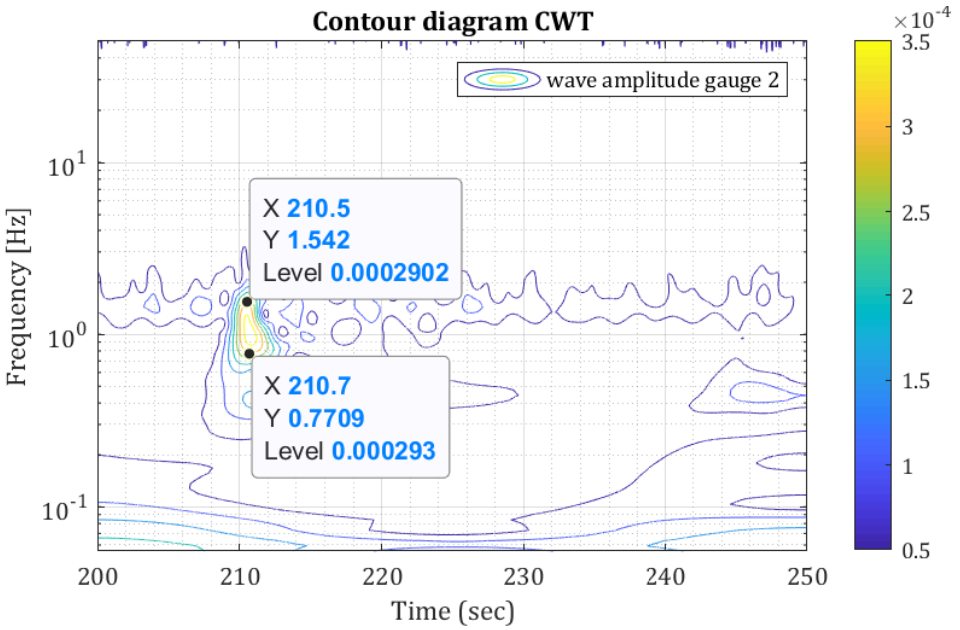

Figure 53: Test 4, failure 1, contour diagram of CWT with data tips indicating location of a generated wave in the time-frequency space

During the second slope failure, we again notice a different pattern of CWT coefficients for the measurements of gauges 1 and 2. The CWT of the surface elevation measured by gauge 1 shows a presence of two clearly defined waves, generated during a slope failure (Figure 54). Furthermore, the wave with a lower frequency range (f = 0.18-0.25) exhibits a significantly longer duration of oscillation, by being visible on the scalogram for over 20 s. The other wave, which corresponds to a higher frequency range (f = 0.5-0.7), dissipates rapidly within about 5 s.

Results of CWT for the data of gauge 2 present a visibly different wave formation. With a somewhat spread frequency range between 0.38 and 0.95, the superposed wave dissipates for the most part within 10 s (Figure 54). The lower frequency wave, in turn, is not distinguishable from the CWT data at all.

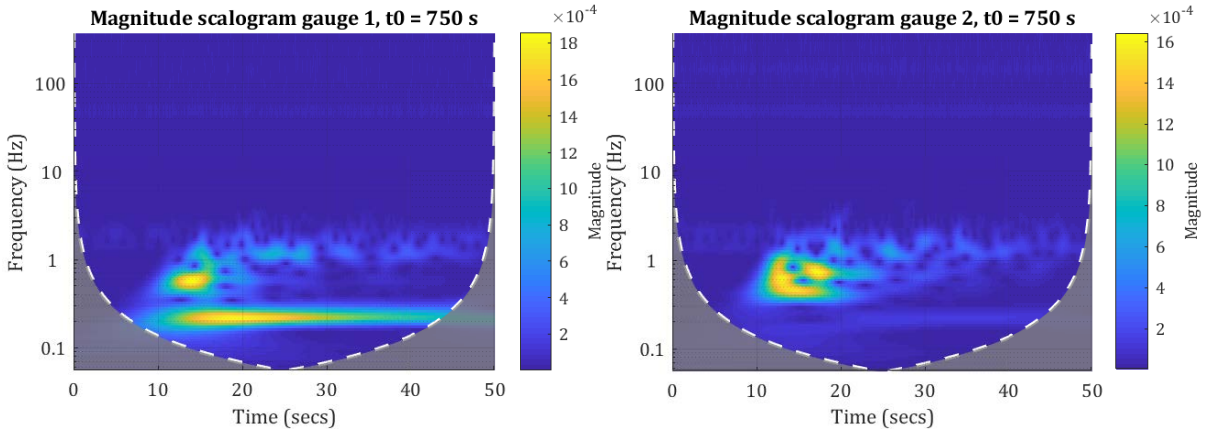

Figure 54: Test 4, failure 2, results of CWT: signal from gauge 1 and 2 in time-frequency space

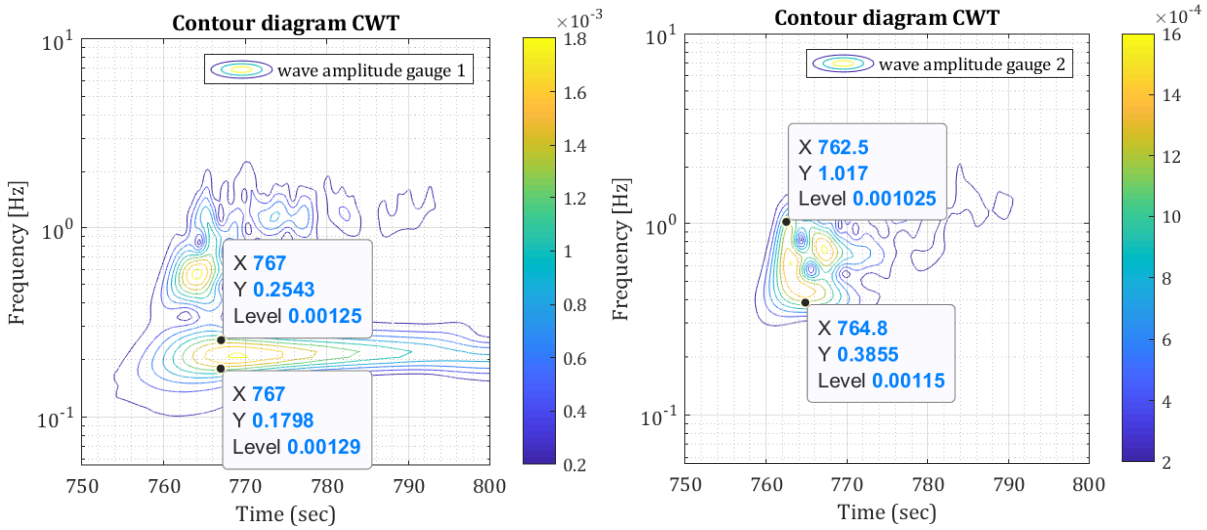

Figure 55: Test 4, failure 2, contour diagram of CWT with data tips indicating location of generated waves in the time-frequency space: lower frequency wave gauge 1 (left), higher frequency wave gauge 2 (right)

A similar wave formation pattern can be observed from the results of CWT during failure 3 (Figure 56). The two wave gauges seem to have measured a completely different wave fields, whereas the signal of gauge 1 shows evidence of two waves being generated: the first wave with a lower frequency (f = 0.20-0.25), oscillating for over 15 s, and the second wave with a higher frequency (f = 0.50-0.70) and more rapid dissipation. CWT of the data from gauge 2 in turn presents a more dispersed wave field, with a rather delaying occurrence of maximum amplitude. The localisation within a frequency domain also shows some scattering, with lower frequencies (f = 0.38 – 0.58 Hz) as well as higher frequencies (f = 0.77 – 1.10 Hz) waves. However, the overall magnitudes of CWT coefficients are lower for gauge 2, indicating lower maximum wave amplitudes measured by this gauge.

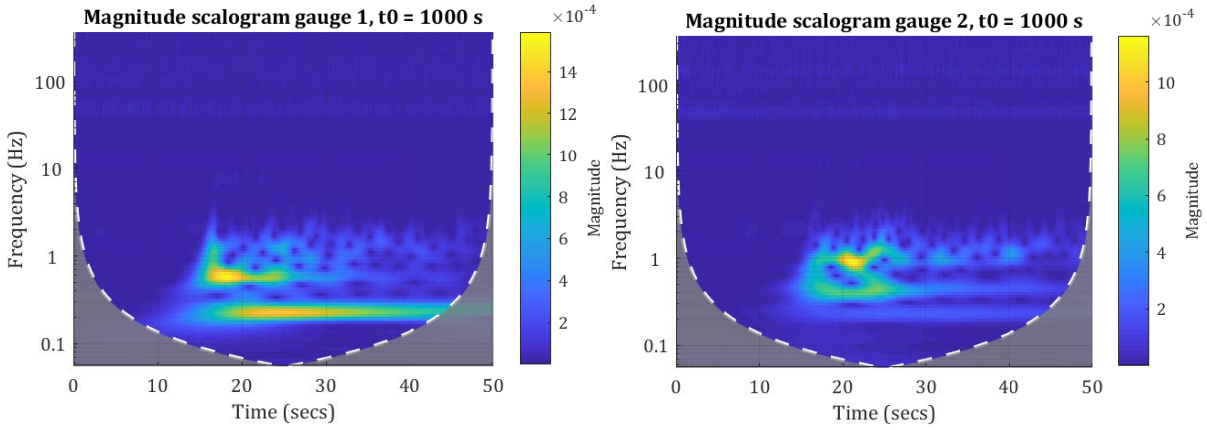

Figure 56: Test 4, failure 3, results of CWT: signal from gauge 1 and 2 in time-frequency space

Such a scattering of measurements is most probably a result of large water depth differences between locations of gauge 1 and 2. A wave, propagation throughout rapidly changing in height water column, can be significantly affected by shoaling (wave propagating from deep- to shallow water) or reverse shoaling (wave propagating from shallow- to deep-water). Shoaling causes an

increase in wave amplitude, reduction in wave length and wave propagation speed, while reverse shoaling reduces amplitude of a wave, dispersing and dissipating wave energy. Due to mentioned processes, it is potentially possible, that a generated wave train, detected by a gauge in more shallow water, e.g., reduces in its amplitude due to propagation towards deep-water and is not that clearly visible anymore from the measurements of the second wave gauge, installed in a deeper water conditions. However, the wave period or frequency remains typically unaffected by shoaling, so that the data of both gauges should contain same frequency components with possibly different amplitudes. The original unprocessed data of wave gauges can be found in Appendix B.

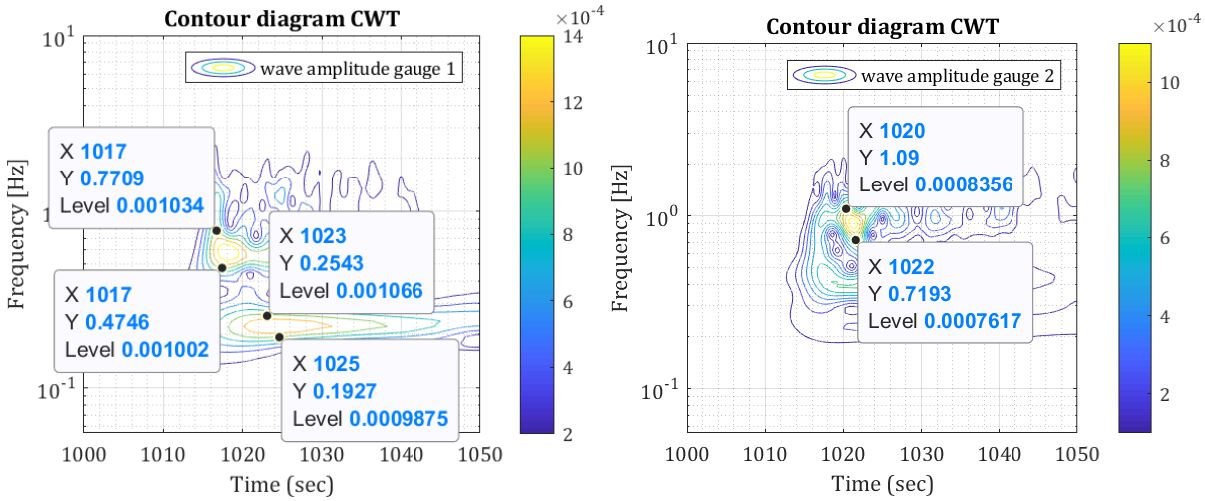

Figure 57: Test 4, failure 3, contour diagram of CWT with data tips indicating location of generated waves in the time-frequency space: lower frequency wave gauge 1 (left), higher frequency wave gauge 2 (right)

6.3.3 Extracted wave

To be able to follow wave formation and its further development, wave components are extracted for narrow ranges of frequencies for each of failures during test 4. The comparison of surface elevations measured by gauge 1 and 2 can provide an indication of how different water depth influences wave characteristics during its propagation. As mentioned earlier, wave frequency should not be impacted by direct or reverse shoaling, but the wave amplitude can be significantly changed. Furthermore, special attention is paid to identification of wave reflection, as some of the generated waves exhibit a wave period larger than the wave period that was taken into account during the wave absorber design. As a result, one can expect that the measurements of these wave components are highly impacted by their reflection. Presence of standing waves would provide an indication for such cases.

A standing wave, in contrast to a commonly known progressive wave, occurs when two waves with equal wave period and amplitude, but propagating in opposite directions superpose and either add up or cancel each other out. The total wave profile oscillates in time but the maximum amplitude of oscillation is different for different location. The peak amplitudes of a standing wave

do not travel in space, creating a vision of a stationary wave profile. Standing wave in our case can occur due to strong wave reflection and a superposition of an incident and reflected waves.

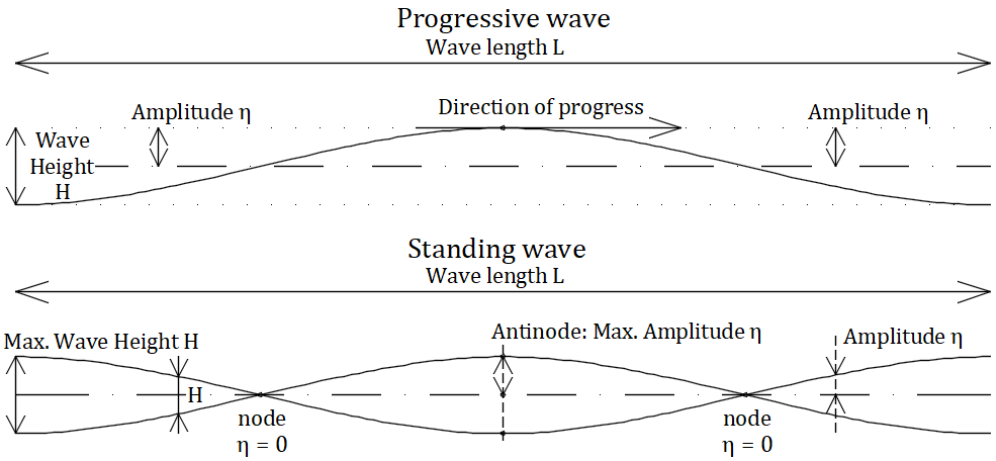

Figure 58: Schematic picture of progressive and standing waves

As Figure 59 shows, during the first failure of test 4 the maximum wave amplitude generated by the small sized landslide reaches ±0.8 mm, measured solely by gauge 2. The wave dissipates rapidly within 3 oscillations, as the wave frequencies are high enough for the wave absorber to effectively prevent wave reflection. However, gauge 1 measures only a quarter of the wave amplitude measured by gauge 2, which clearly indicates a decay of wave amplitude due to wave propagation towards deeper water, or so called reverse shoaling.

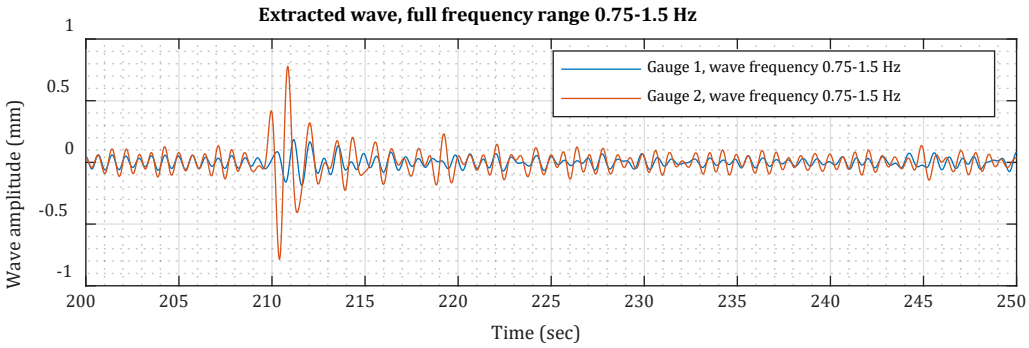

Figure 59: Test 4, failure 1, wave extracted from the data of wave gauges 1 and 2, frequency range 0.75-1.5 Hz

During failure 2, several wave trains were generated with a wider range of frequencies. We use a frequency band-pass of 0.15 - 0.35 Hz to extract the long wave, clearly visible from CWT of gauge 1 data, and further a frequency band-pass of 0.35-0.95 Hz to extract the remaining wave component, which was predominantly visible in the data of gauge 2.

As Figure 60 presents, the wave with a low frequency range oscillates for a period of time longer than 40 s. Gauge 1 measures maximum wave amplitude of ca. ± 3 mm, while measurements of gauge 2 remain near zero amplitude. Furthermore, the oscillations with the same frequency are also present in the measurements of water velocity, proving the assumption, that a standing wave

was formed during failure 2. In fact, the wave period reaches more than 5 s, which is far beyond the design period for the wave absorbing elements. The clear presence of wave reflection explains differences in measured wave amplitudes, as for a standing wave measured amplitudes depend on the position of wave gauge in a wave field. Moreover, it is somewhat problematic to give an estimate of the real amplitude of a generated wave, as reflection can double the amplitude or reduce it to zero, as it is the case for gauge 2, e.g. In the conditions of a changing water depth as well as closely located reflecting boundaries, a standing wave can hardly be analytically resolved into incident and reflected waves without knowing the wave characteristics of generated waves.

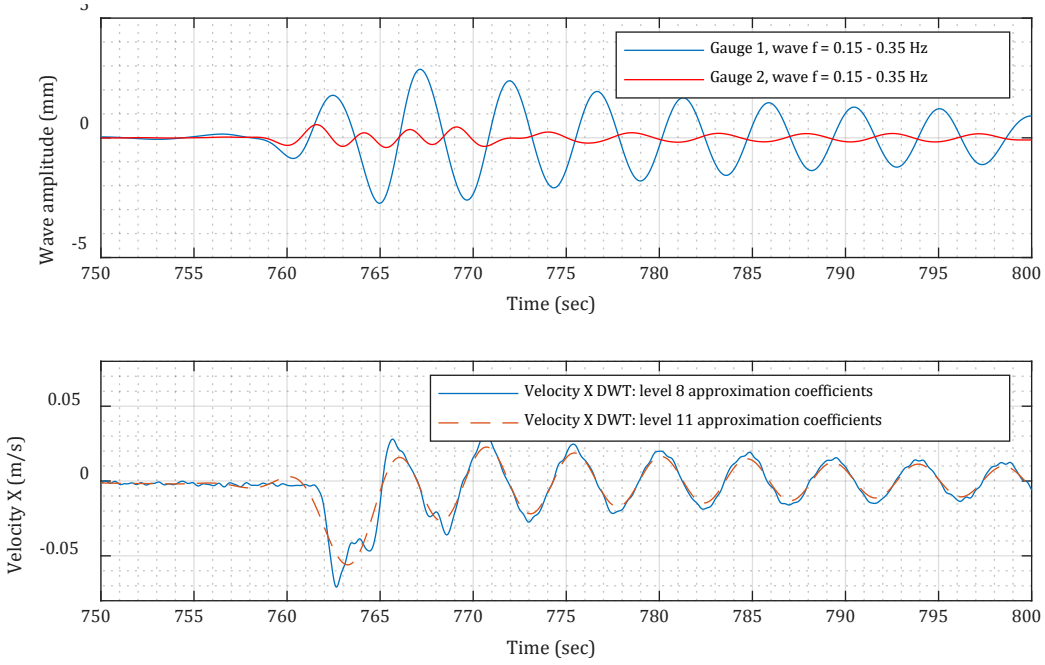

Figure 60: Test 4, failure 2, wave extracted from the data of wave gauges 1 and 2 with f = 0.15-0.35 Hz (top), in comparison to horizontal water velocity measured by EMS (bottom)

At reflecting boundaries the wave amplitude should reach nearly the double of its real wave amplitude, assuming that the reflection of the wave with a wave period larger than 5 s is nearly 100%, so that incident and reflected waves have an equal wave amplitude. Based on the measurements of pressure sensors, installed inside the liquefaction tank walls, we can determine the maximum wave amplitude at the hard boundary by applying CWT and extracting the data with a frequency range of 0.15 – 0.35 Hz.

Figure 61 shows results of CWT for the pressure measurement of wall sensors, whereas the waves at the water surface result in pressure oscillations measured by wall sensors. As the sensors are located below the sand bed, within first 18 s after the failure triggering the measured pressure is influenced by a pressure build-up due to triggering mechanism and excess pore pressure within the sand body at failure. After 18 seconds, the pressure begins to dissipate and then the oscillations due to surface waves become visible. The maximum pressure increase measured by walls sensors reaches 0.04-0.05 kPa, which by neglecting effects of the tank tilt, results in

maximum wave amplitude at the boundary of 4-5 mm. Based on assumption that the wave height of a standing wave at the boundary is a double the incident wave height, we can estimate the maximum wave amplitude for the low frequency waves generated during failure 2 reaching ± 2-2.5 mm.

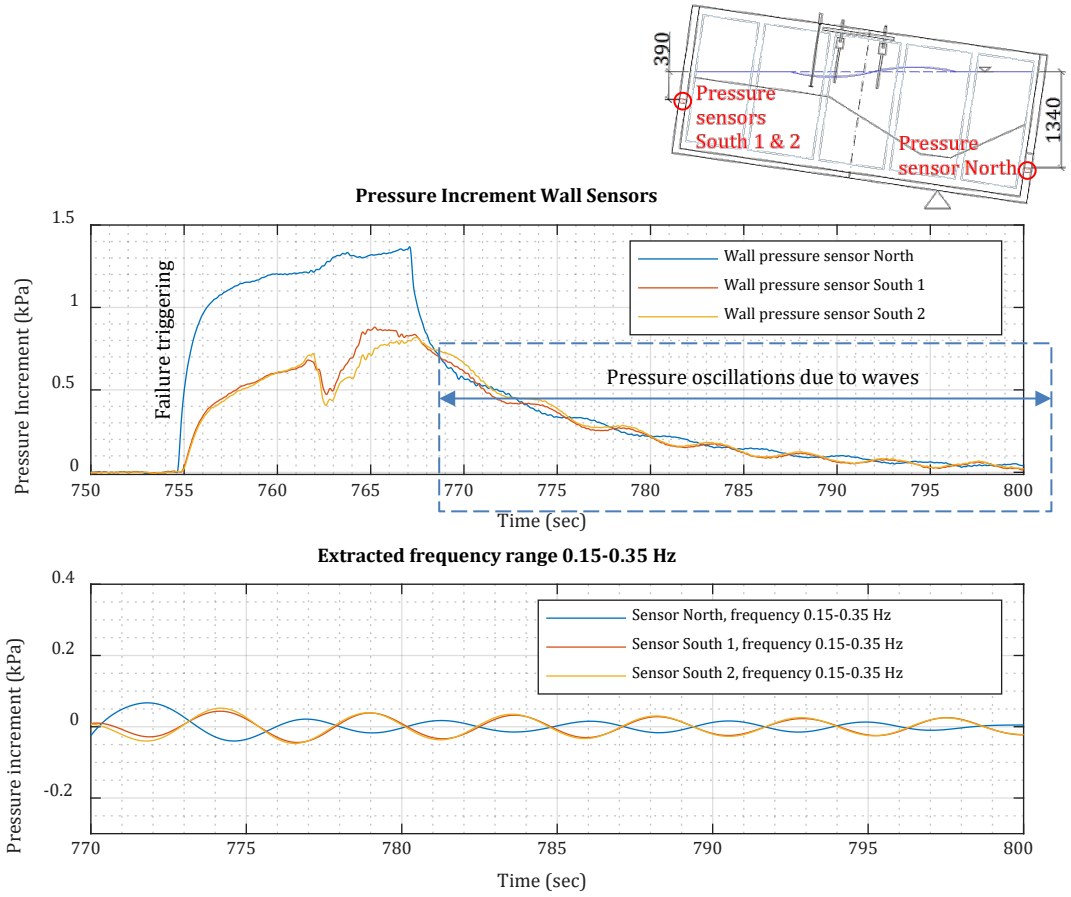

Figure 61: Test 4, failure 2, Pressure increment measurements of wall sensors (top), extracted data with a pressure oscillations due to wave action (bottom)

For the waves with a higher frequency range f = 0.35 – 0.95 Hz, wave amplitudes dissipate for the most part within the 10 s after the onset of failure. Maximum amplitude of a superposed wave reaches nearly ±4 mm, as shown in Figure 62.

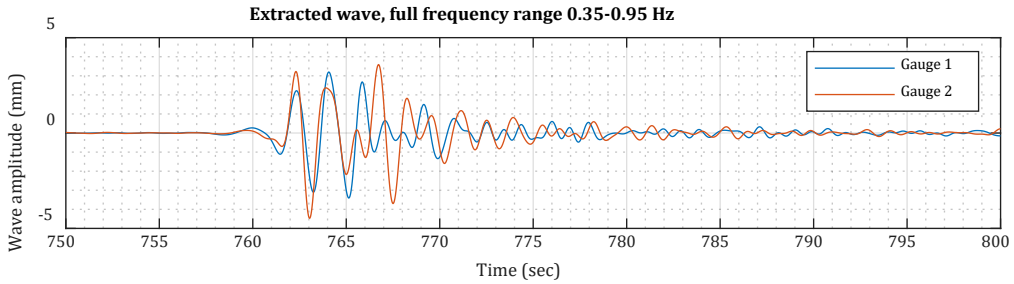

Figure 62: Test 4, failure 2, wave extracted for wave gauges 1 and 2, frequency range 0.35 – 0.95 Hz

By decomposing the signal in more narrow frequency ranges, one can distinguish separate wave trains with amplitudes reaching up to 2 mm (Figure 63). For the frequencies between 0.35 and

0.60 Hz, the timing of the wave generation corresponds well to the onset of slope failure. As the maximum wave amplitude is reached shortly after the initial displacement and the waves start dissipating within the first 5 s, the initial abrupt displacement at the onset of failure can be considered as the main source of the waves with f = 0.35 – 0.60 Hz, while any further soil mass motion did not contribute to their amplitude. Furthermore, an important conclusion can be made regarding the wave reflection: the waves with f > 0.35 Hz (wave period T < 2.8 s) seem to be effectively absorbed by the wave absorbing elements, as wave amplitudes dissipate quite rapidly and no standing wave occurrence is detected.

For the frequency components larger than 0.65 Hz, one can distinguish an additional amplitude increase at later stages of failure. The maximum amplitude is reached again approx. 7 s after the failure onset, which requires a second wave generating impact, given by soil displacement. These waves can possibly be influenced by a downward flow of the soil mass, which was pushed forwards during the first impact of failure. As this motion was slower and more gradual in comparison with the initial displacement at the onset of failure, the wave amplitudes remain quite small, reaching maximum ± 1.2 mm. These waves are similar to the waves generated during test 2, whereas a gradual progressive slope failure resulted in max. wave amplitudes of ± 0.8 mm.

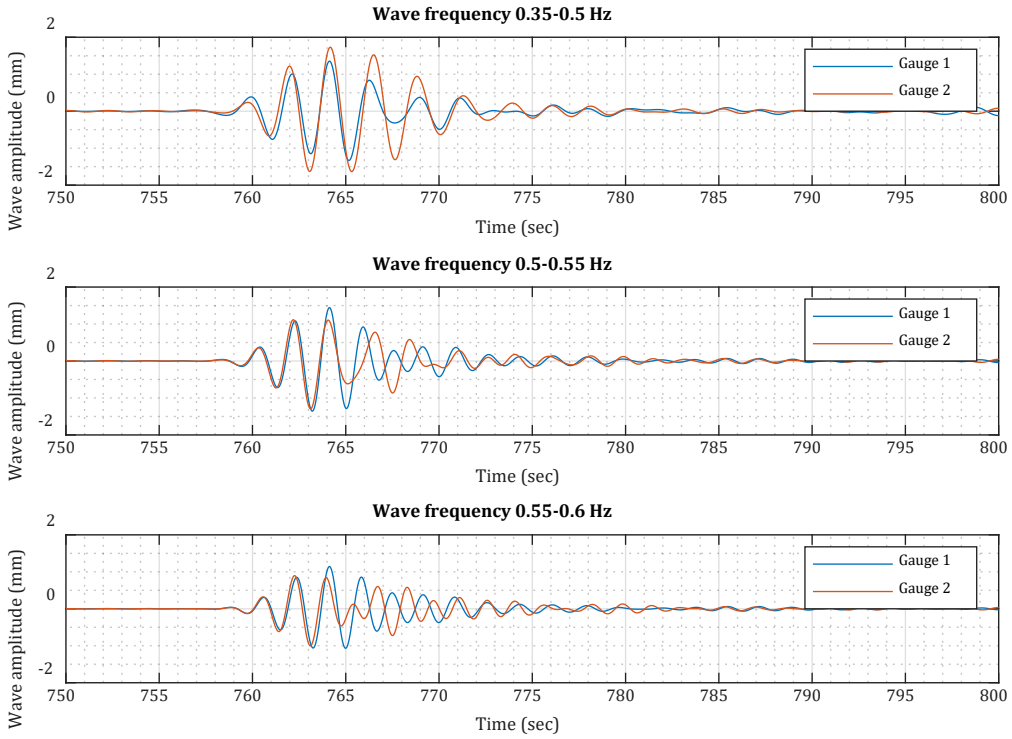

Figure 63: Test 4, failure 2, wave decomposition by frequency, f = 0.35 - 0.6 Hz

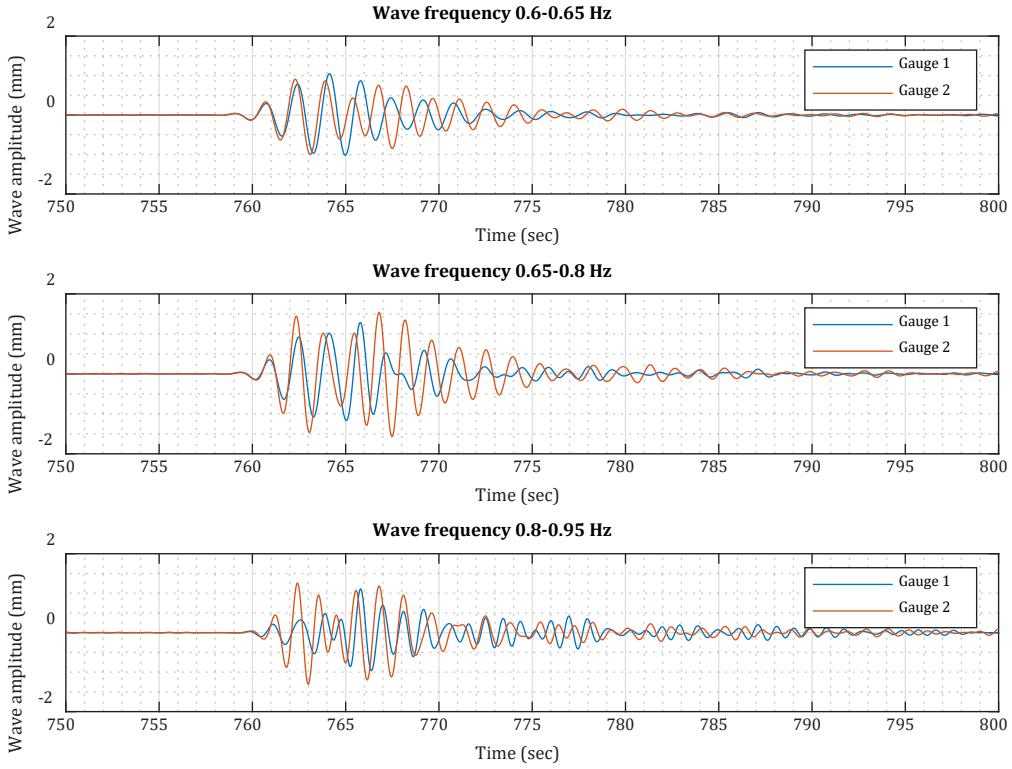

Figure 64: Test 4, failure 2, wave decomposition by frequency, f = 0.6 – 0.95 Hz

An indication of waves passing above the location of the EMS can be found in the horizontal velocity measurements, as shown in Figure 65. Gauge 2 and EMS were installed at a distance of about 32 cm during test 4, so based on the time difference between the wave peak and the peak in measured velocity an average of traveling speed of a wave above the slope can be calculated. For the first wave train the propagation speed results in approx. 1.06 m/s and slows down to approx. 0.40 m/s for the later wave trains. For the range of frequencies f = 0.35-0.95 Hz, the wave length $L = \vartheta \times T = \frac{\vartheta}{f}$ then would range between 1.11 and 3 m.

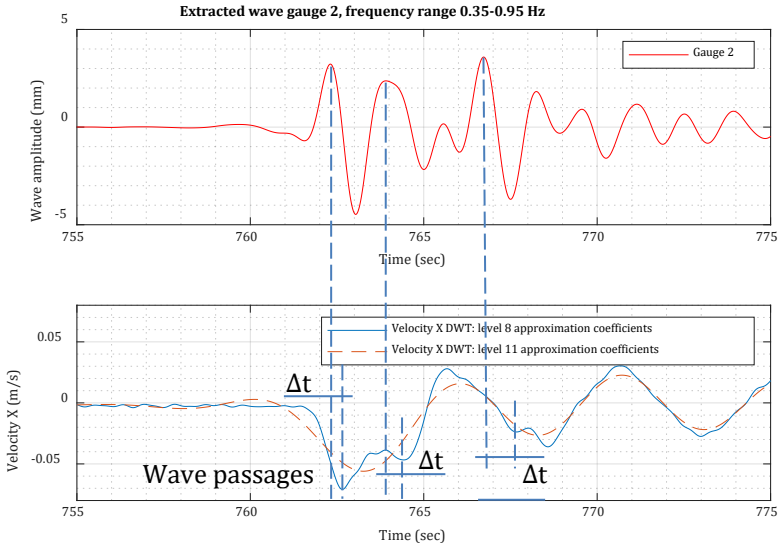

Figure 65: Test 4, failure 2, wave measured gauge 2(top) in comparison to the horizontal velocity measured by EMS (bottom); indication of waves passing the EMS

In a similar way, we determine the approximate wave length for the waves with the range of frequencies between 0.15 and 0.35 Hz. With a propagation speed of about 0.92 m/s, the wave length results in approx. 2.6 – 6.1 m

During failure 3 an identical type of wave formation has taken place, with a slight difference in duration of failure, resulting in overall longer wave generation period. As this final slope failure was a progressive mass flow, the failing mass motion was rather slow in comparison to the previous failures. As a result, the amplitudes of the generated waves remain somewhat lower, despite an overall much larger extend of slope deformation.

Similarly to the failure 2, two types of waves can be distinguished: a low frequency wave with f = 0.15 – 0.35 Hz (or wave period T = 2.8 – 6.5 m), which forms a standing wave due to strongly present wave reflection; the second group of waves ranges over a higher frequency range f = 0.45 – 1.1 Hz (T = 0.9 – 2.2 s) and shows a more rapid decrease in wave amplitudes. Unlike the previous failures, the amplitudes recorded by gauge 1 are higher than measured by gauge 2. This difference, however, can be simply explained by changes in the slope geometry. As the slope was widened by the previous landslides, position of gauge 1 was shifted further away relatively to the slope toe. Also, a sudden soil displacement indicating the onset of failure 3 occurred around the location of sensors 3 and 4, whereas gauge 1 was positioned exactly above. Such a direct proximity to the source explains the higher amplitudes measured by gauge 1.

Wave data analysis for the third failure follows the same procedure as for the failure 2 and is therefore not discussed in detail again. The figures shown below present the most important wave formation features, followed by a brief summary of estimated wave characteristics. A complete collection of data, obtained from failure 3 measurements by data processing, can be found in Appendix B of the current thesis.

The standing wave, formed due to strong wave reflection, reached during failure 3 the maximum measured amplitude of ±2 mm from the data of gauge 1. From the pressure measurements of the wall sensors, the maximum wave amplitude of the generated low frequency waves is estimated to be slightly over ±2.5 mm.

Waves with a higher range of frequencies, in turn, exhibit a maximum amplitude of the superposed wave of nearly ±3 mm, whereas the decomposed by frequency wave trains show oscillation of 1 to 1.5 mm amplitude. For all wave trains the amplitudes remain nearly constant for about 8-9 s, while especially the highest frequency waves (f > 0.75 Hz) show slight dissipation, but later a further increase in wave amplitude due to progression of failure, resulting in a slow gradual mass movement.

Furthermore, we can estimate a range of possible wave celerities during failure 3, based on horizontal velocity measurements and wave amplitudes measured by gauge 2. For the waves with a frequency f = 0.45 – 1.1 Hz, the estimated wave celerity ranges from 0.64 to 1.10 m/s. An

approximate wave length results then in 0.6 – 2.5 m. For the longer waves with a frequency f = 0.15 – 0.30 Hz, the wave celerity results in 0.68 – 1.41 m/s. An approximate wave length results then in 2.27 – 9.4 m.

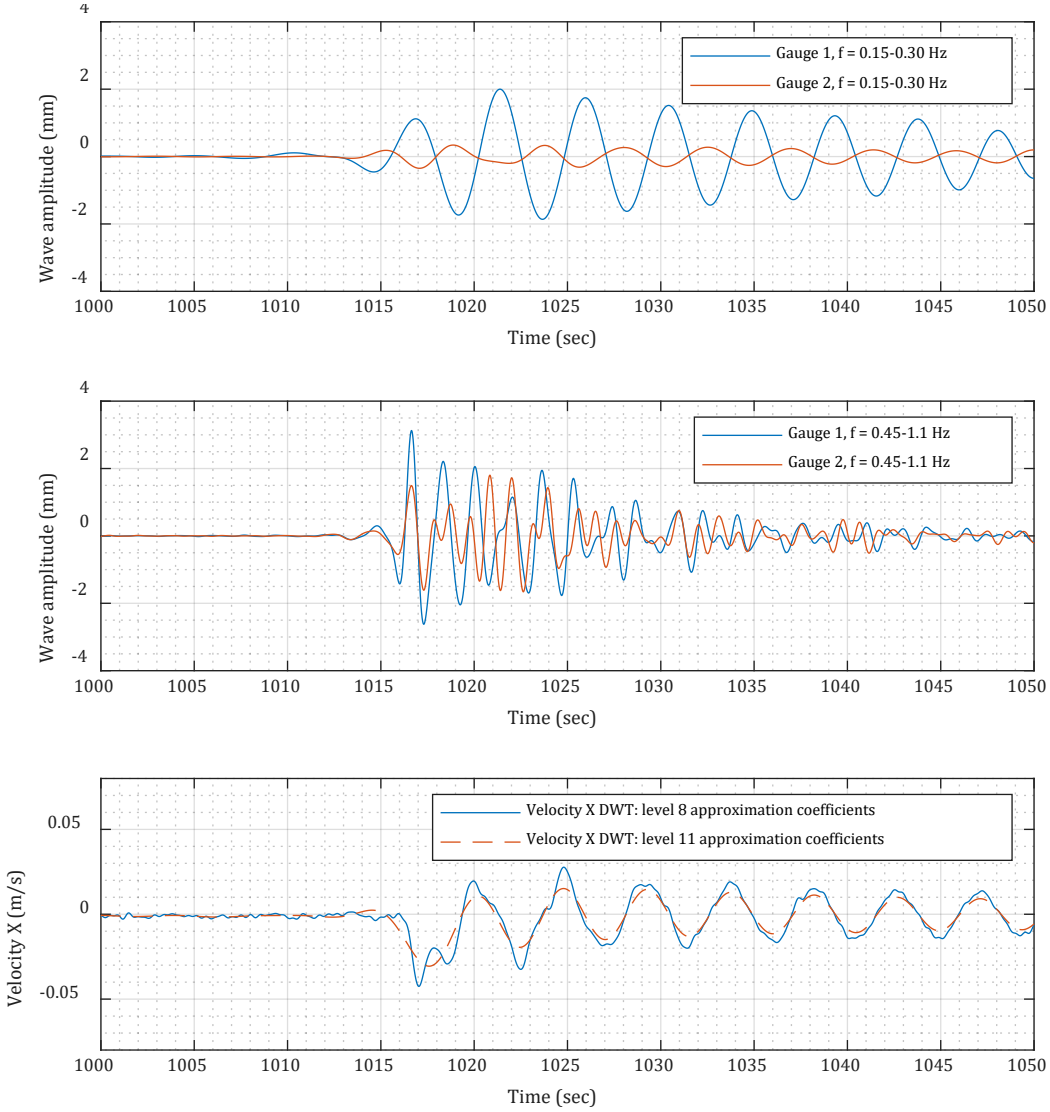

Figure 66: Test 4, failure 3, wave extracted from the measurements of gauges 1 & 2: low frequency standing wave f = 0.15-0.35 Hz (top), superposed wave of higher frequencies f = 0.45-1.1 Hz (middle) in comparison to horizontal water velocity measured by EMS (bottom)

6.3.4 Pressure measurements

An important feature of the pressure measurements during the first failure of test 4 is that the measurements are barely affected by the triggering mechanism. Because the displacements during failure 1 occurred rapidly, followed by a pressure dissipation within just couple of seconds, tilting of the tank with a slow tilting rate (= 0.033°/s) results solely in a negligibly small changes in water level at the sensors locations.

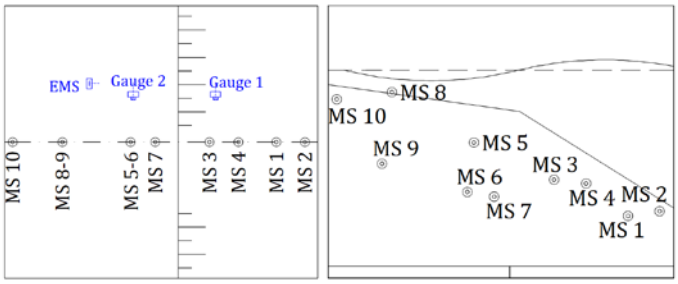

Figure 67: Mobile sensors initial location during test 4: top view (left), side view (right)

Pressure measurements during failure 1, shown in Figure 68, are decomposed into a low and a high frequency components by means of DWT, as it was done before for the previous test data. For mobile sensor 4, the high frequency component show a pressure increment during failure of 0.3 kPa, while the pressure change due to sensor displacement reaches nearly 0.5 kPa, which is visible in the low frequency component. MS's 1, 2, 4 and 5, presented in Figure 68, measured the highest values of pressure increment during failure 1. However, the values are about 10 times smaller than the measured pressure increment during other experiments, indicating the limited motion of soil mass due to only a small slope failure.

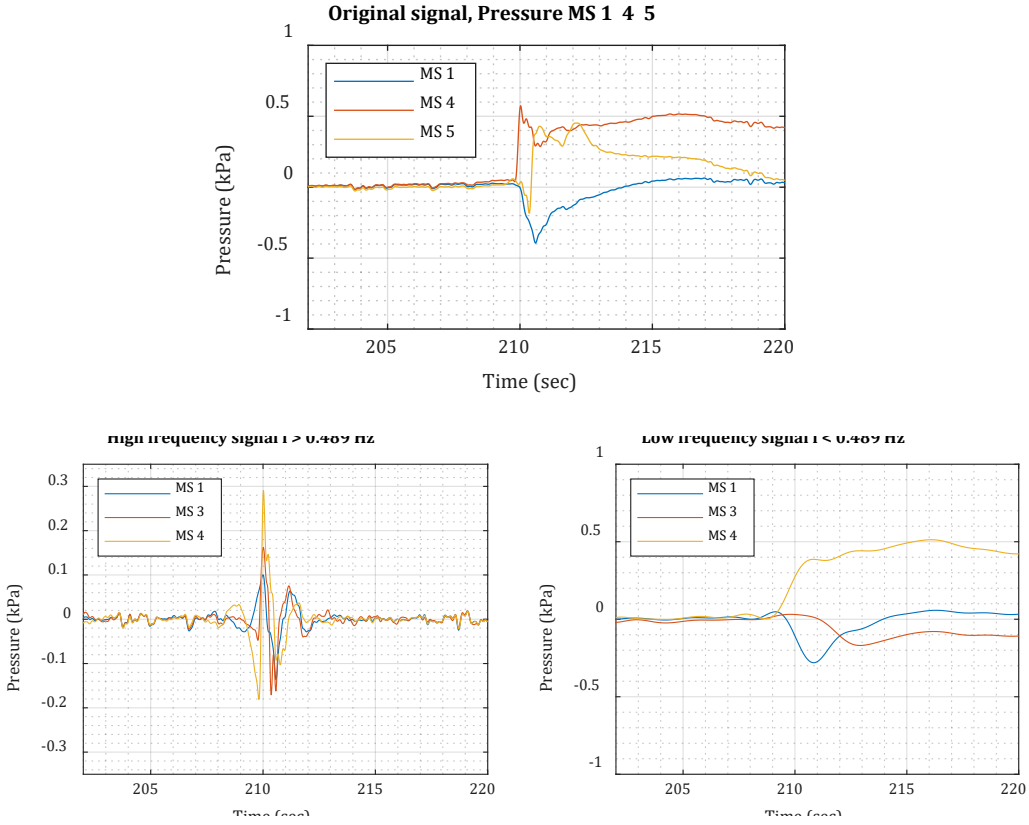

Figure 68: Test 4, failure 1, pressure increment measurements of MS's 1, 4 and 5: original signal (top), high and low frequency components (bottom); the initial hydrostatic pressure is subtracted

Using pressure application by means of a pressurised chamber as a triggering mechanism, second slope failure results in a pressure increase by approx. 1.5 kPa measured by the base sensors. As Figure 69 presents, the onset of slope failure occurs nearly 7 s after the time point of application

of the triggering pressure. The MS's 5, 6 and 9 experience then an abrupt pressure increase, highest for the deeper imbedded sensors 6 and 9. Arguably, this pressure increment can be the propagated pressure wave from the base. On one hand, this assumption can be supported by the fact, that the relative pressure increment of MS's 6 and 9 exhibits nearly the same value as the applied base pressure, namely 1.7 and 1.4 kPa, respectively. However, the delay of 7 s seems rather unlikely to be the duration of pressure wave propagation, as it is usually significantly faster or almost instantaneous in media like water. Also, we see a totally different pressure change pattern in measurements of MS's 1, 3 and 4, rather showing a negative pressure increment. Especially the long durations of pressure changes, ranging between 5 and 10 s, prove that it is unlikely to be an excess pore water pressure or suction due to dilation, but rather the hydrostatic pressure changes due to sensor displacements. This assumption also agrees well with the image analysis results, as the sudden downward displacements were clearly visible at the slope crest (near location of MS's 5, 6, 8, 9) time corresponding to the soil mass push forward around the slope toe (MS's 1, 3, 4).

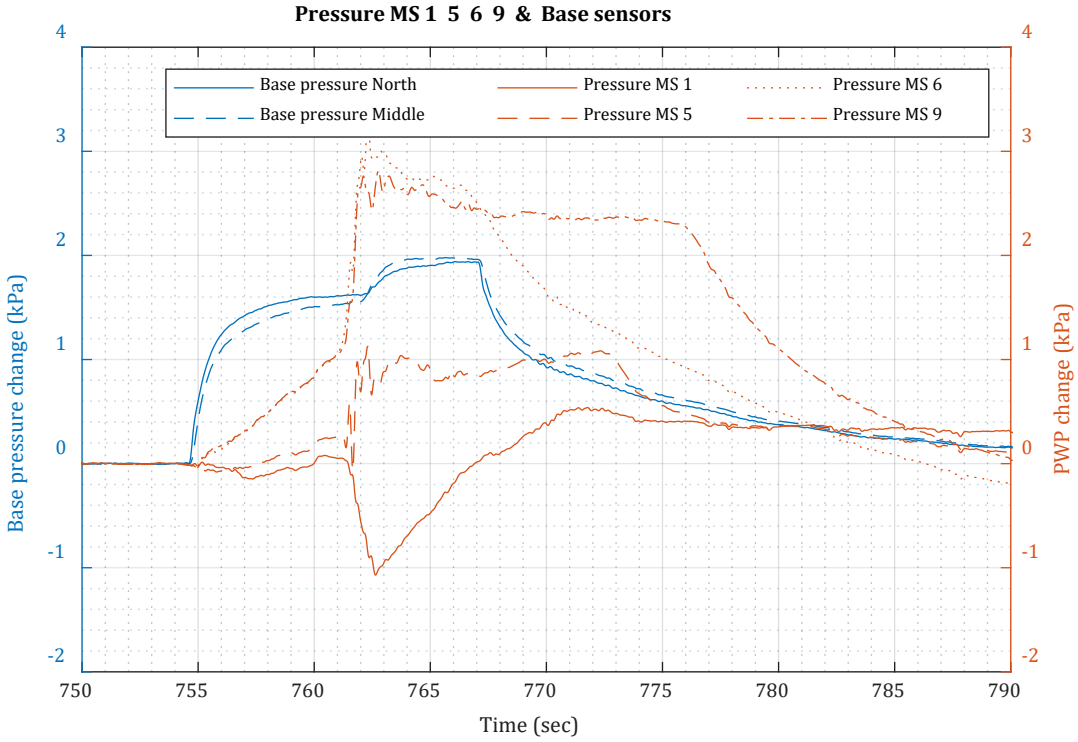

Figure 69: Test 4, failure 2, pressure measurements by MS's 1, 5, 6 and 9 and base sensors North and Middle

So, we can distinguish two groups of sensors, showing a similar trend of pressure increment within a group during failure 2. MS's 1, 2, 3 and 4, that show a negative pressure increment, while MS's 5, 6, 8, 9 exhibit an abrupt positive increment (Figure 70). Combined the image analysis with the pressure data, we can estimate more detailed, how the MS's moved during the failure. Assumed that the sensors followed the same path as the soil during the slope failure, the mass motion during failure 2 s is shown in Figure 71.

Overall, the landslide during the second failure can be subdivided in two zones, which are characterised by a different type of soil behaviour. Formed by predominantly loose sand and exhibiting low effective stress level, the top layer of sand bed with a thickness of about 30 cm experienced liquefaction, resulting in positive pressure increment measured by MS's 5, 6, 8 and 9. As the slope crest showed an abrupt downward displacement, the sensors located within this zone possibly moved downwards relative to its previous location, which would additionally contribute to the positive pressure increment measured by these sensors.

The bottom sand bed layer, composed by more dense material with a higher pre-loading pressure, possibly formed a shear band stretching from the location of MS's 3 and 4 to the location of MS 1. These sensors measure a large negative increment, resulting from a dilative behaviour of dense sand along a shear band. Also, an additional negative pressure increment results from the movement of sensors during the failure, which is for this zone predominantly horizontal with a vertical component directed upwards. Especially, it is the case for MS 3, as the sensor by the end of the mass movement due to the failure reaches the surface of the slope.

Finally, one can recognise the positive pressures measured by MS 2, which would indicate compressive soil behaviour. In fact, the toe of the slope is filled with loose sand, resulted from the previous slope failure and superficial mass flow during tank tilting.

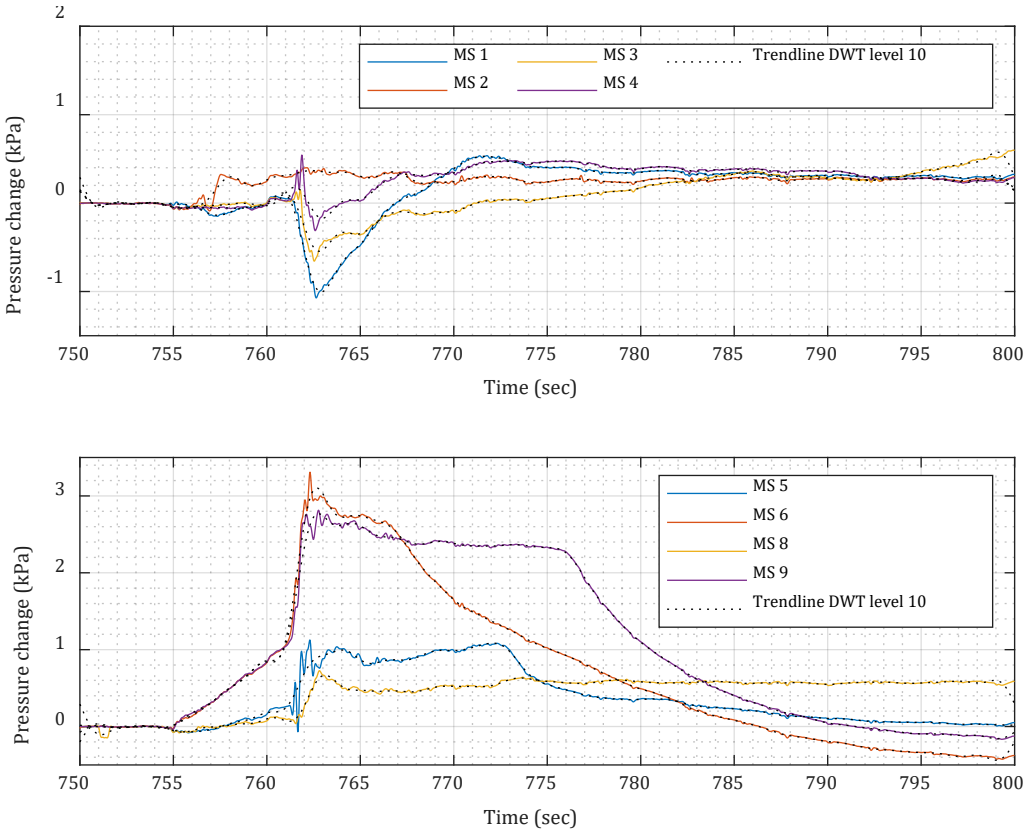

Figure 70: Test 4, failure 2, pressure increment during slope failure measured by groups of sensors: MS's 1, 2, 3 & 4 (top), MS's 5, 6, 8 & 9 (bottom)

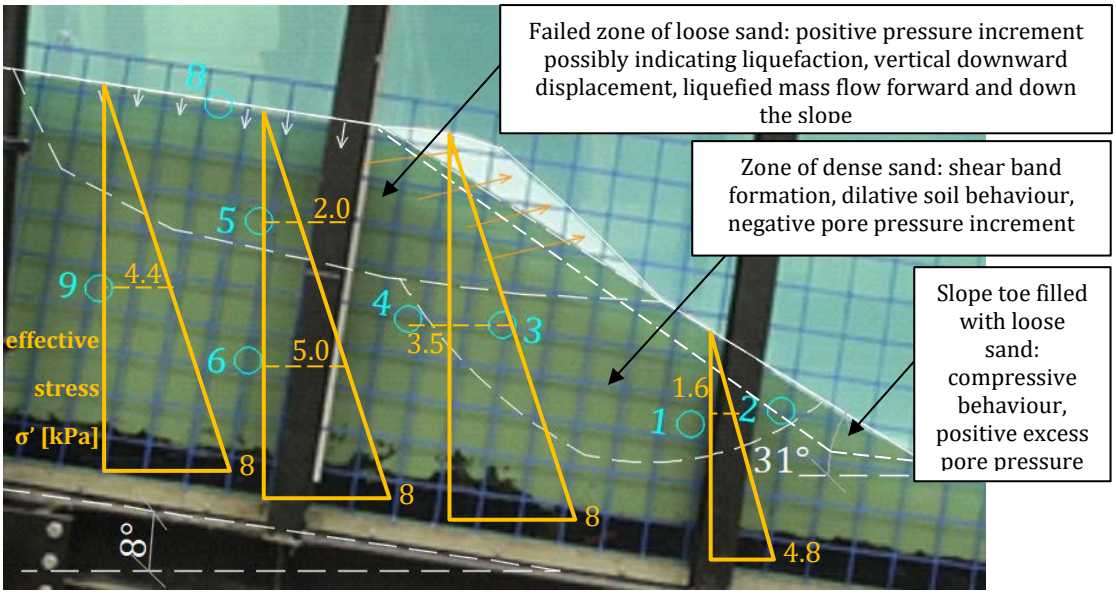

Figure 71: Test 4, failure 2, mass motion during the slope failure, with an approximate location of the MS's after the failure and rough estimation of effective stresses at the location of MS's. Effective stresses (in yellow) are estimated with buoyant sand density γ´ = 8 kN/m³ (top layers) and γ´ = 9 kN/m³ (bottom layers).

During failure 3, the MS's located near the slope crest measure only a very low pressure increment, while the largest pressure change is detected by MS's 6 and 9, embedded deep inside the slope body. Predominantly positive pressure increments, measured by all MS's, indicates rather compressive behaviour of sand and liquefaction type of slope failure. Overall pressure measurements remain lower than during failure 2, despite a higher applied pressure resulted from triggering mechanism and visibly larger soil mass displacement.

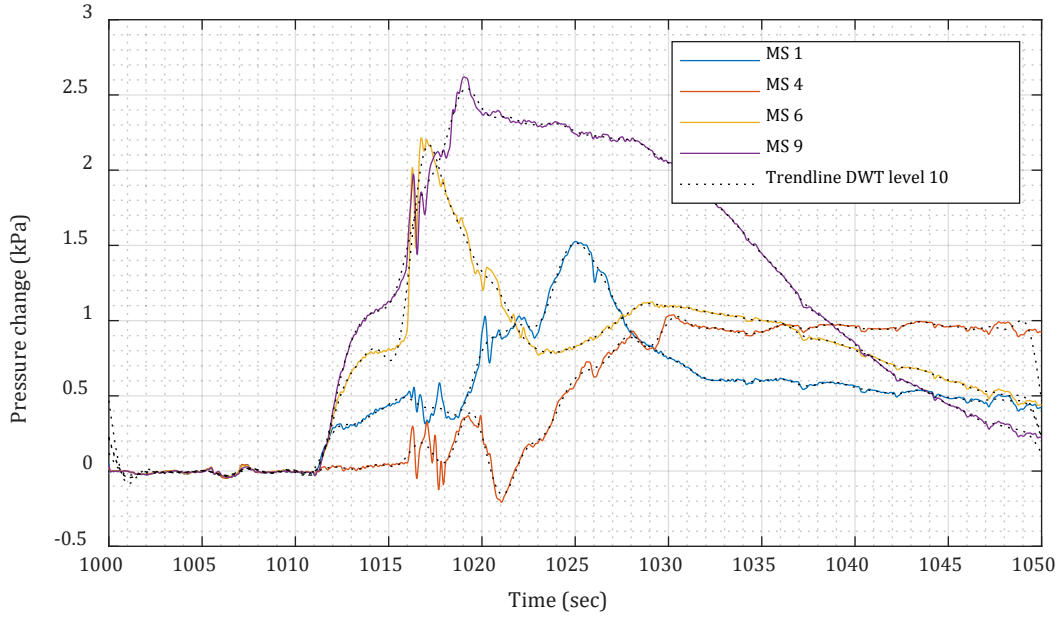

Figure 72: Test 4, failure 3, pressure measurements by MS's 1, 4, 6 and 9

Pressure level measured by MS's 4, 6 and 9 approaches the effective stress level at the location of sensors and can indicate liquefaction occurrence at the intermediate soil layer (Figure 73). In turn

MS 5 measures rather negative pore pressure increment (Appendix B), indicating a different zone within the slope body.

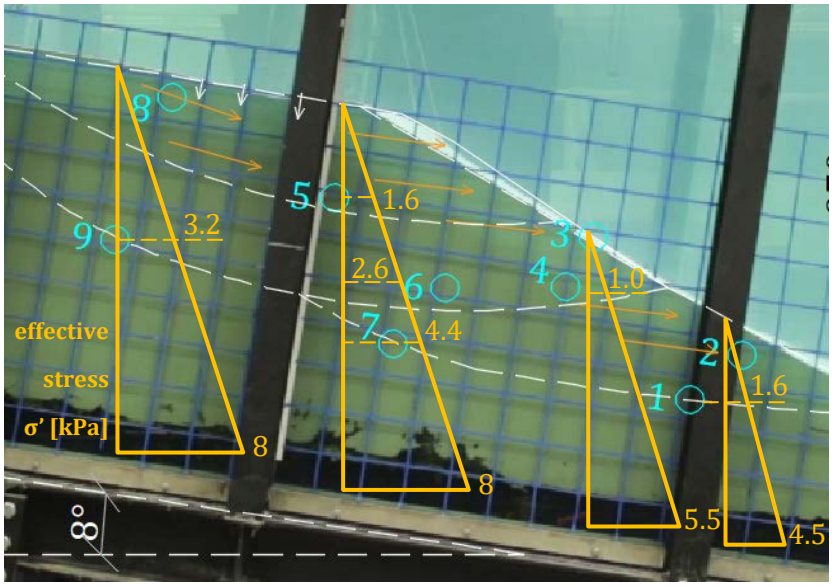

Figure 73: Test 4, failure 3, mass motion during the slope failure, with an approximate location of the MS's after the failure and rough estimation of effective stresses at the location of MS's. Effective stresses (in yellow) are estimated with buoyant sand density γ´ = 8 kN/m³ (top layers) and γ´ = 9 kN/m³ (bottom layers).

6.3.5 Soil mass acceleration

During the first failure of test 4, solely the MS 4 and 5 measured a changed in acceleration (Figure 74), for accelerations measured by other MS's see Appendix B. From the pressure analysis, we concluded that MS 4 was displaced vertically by about 4-5 cm. The acceleration measurements also show that displacement occurred; however, as mentioned earlier, this acceleration also includes its horizontal components. Finally, the measured accelerations remain relatively small, reaching barely a fifth the acceleration measured during previous tests.

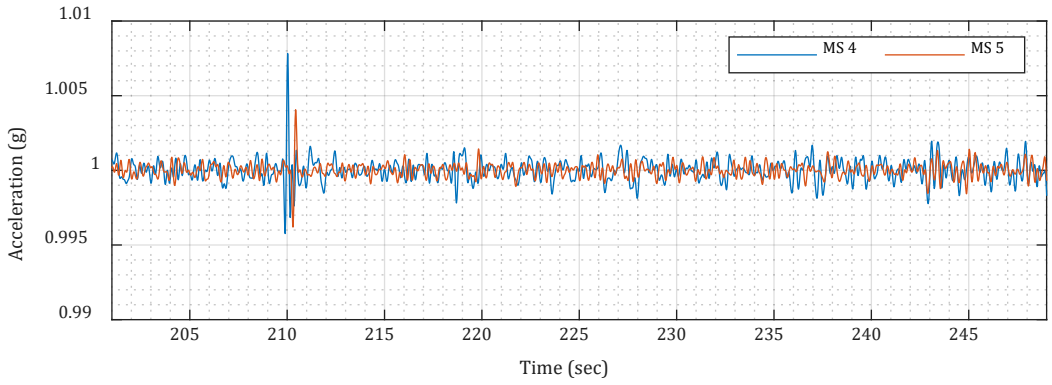

Figure 74: Test 4, failure 1, accelerations measured by MS's 4 and 5 during the landslide. For other acceleration data see Appendix B.

The second failure overall caused much larger soil displacements, especially concentrated around the top part of the slope, where an abrupt downward movement of the slope surface was observed

during the failure. Largest accelerations are shown by MS's 5, 6 and 8, as presented in Figure 75, which agrees well with the largest pressure increments measured by the same sensors. As these sensors are mostly located in a liquefied zone, the measured accelerations also indicate the amount of liquefied soil mass displacements and where the displacements reached their maximum. MS 8, located at the surface of the slope crest, shows the highest measured acceleration, which represents the accelerations of slope crest during failure. The predominant direction of this movement is vertical and one can clearly see the timely match between the first acceleration peak and the wave generation (Figure 76).

Acceleration measurements clearly show only abrupt displacements. After reaching the 763 second mark, most of acceleration measurements reduce to nearly zero, while the soil mass motion is still present. The gradual soil flow along the slope, thus, is barely visible from accelerations recorded by MS's. Even for MS 3, which by the end of the gradual mass flow is pushed to the slope surface and overall has experienced a large displacement relative to its initial location, the accelerations do not provide an indication for any displacement.

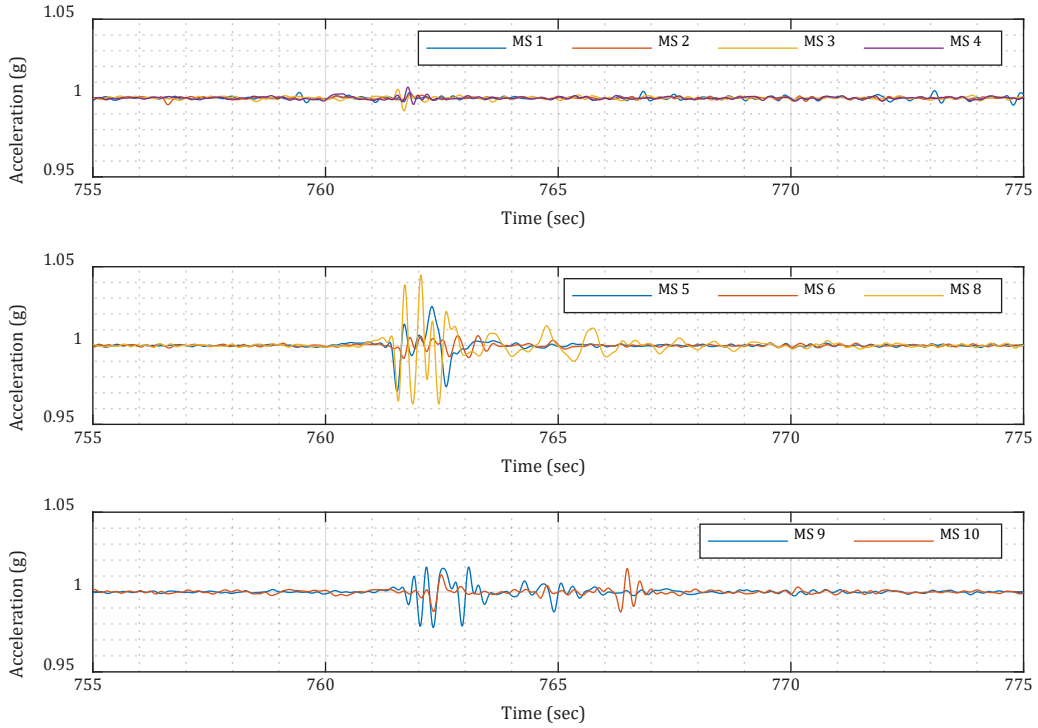

Figure 75: Test 4, failure 2, accelerations measured during the landslide by MS's 1 – 4 (top), MS's 5, 6, 8 (top), Ms's 9 & 10 (bottom). For other acceleration data see Appendix B.

Whereas during failure 2 an abrupt initial displacement is followed by a gradual mass flow, the two generated wave types correspond timely to these two different failure types. The high frequency waves are clearly generated during the sudden crest settlement at the onset of failure, while the waves with a low frequency ($f < 0.35$ Hz) show a delayed response, building up in amplitude only after the 763 second mark (Figure 76).

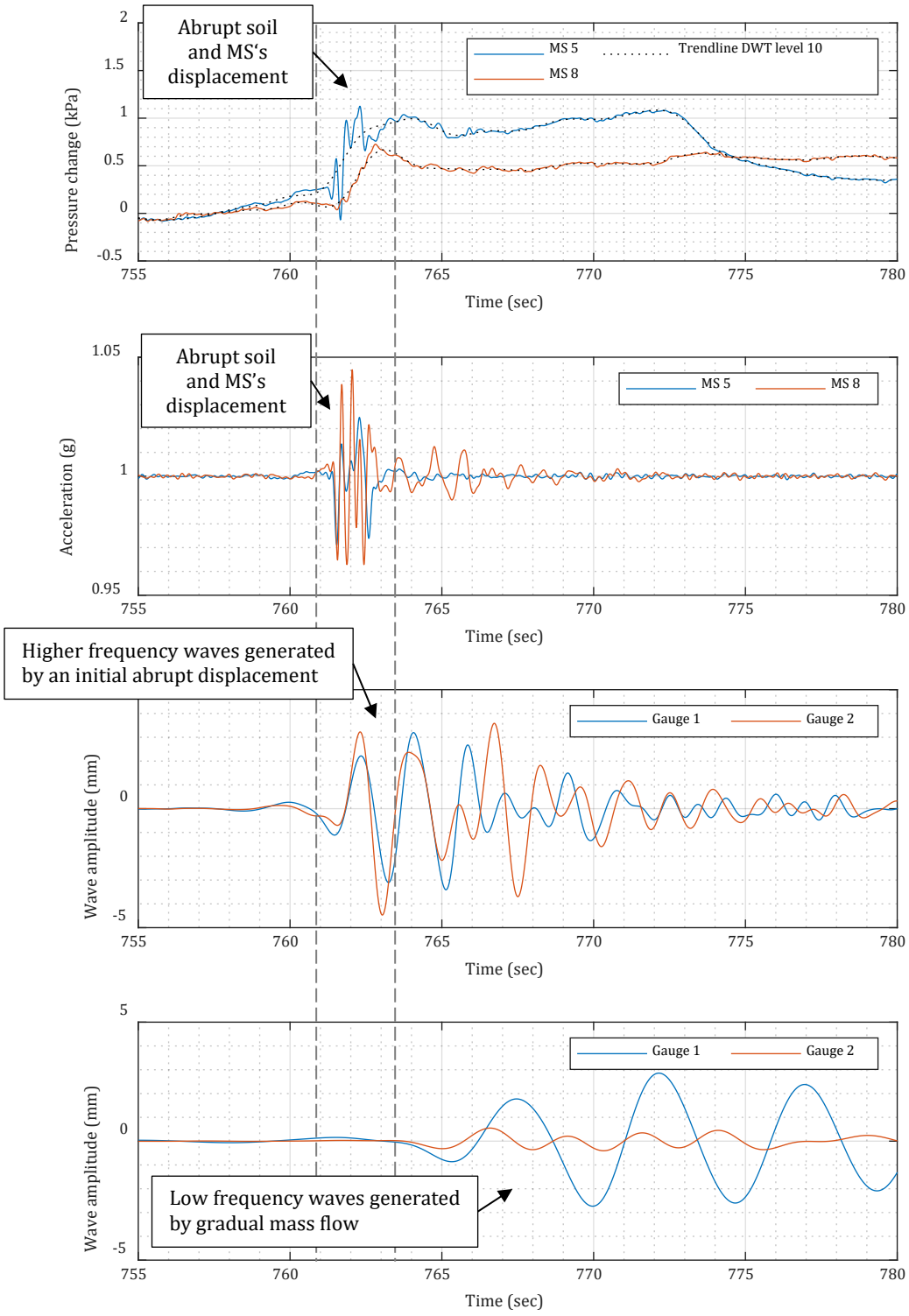

Figure 76: Test 4, failure 2, accelerations of MS's 5 & 8 (top) in comparison to two wave types generated: higher frequency wave f = 0.35-0.95 Hz (middle), low frequency wave f = 0.15 – 0.35 Hz (bottom)

This observation agrees well with modes of failure and corresponding wave formation during the previous experiments. The onset of failure, characterised by a large abrupt slope deformation and a vertical crest displacement, exhibits strong similarities in wave formation with the first test of the series of experiments. The waves, induced by such a highly dynamic slope failure, exhibit larger amplitudes and higher wave frequency ranging from approx. 0.40 to 1.0 Hz. The later

occurring gradual mass flow shows similar dynamic features as the landslide in test 2 and results in a similar long wave formation. These waves exhibit smaller wave amplitudes, but much larger wave lengths, shown by extremely large values of wave period. During the experiments in the liquefaction tank, such waves, due to strong wave reflection, cause standing waves.

Failure 3 shows a similar pattern but rather slower kinematics of a slope failure, with a sudden initial soil displacement concentrated around the top part of the slope followed by a gradual mass flow. Despite the fact that the overall displacements during failure 3 are larger than during failure 2, generated wave field exhibit smaller wave amplitudes. In fact, the major displacement of sensors occurred during the second stage of failure due to mass flow, while the onset of failure resulted in less mass being displaced. As a result the higher frequency waves reach smaller amplitudes in comparison with waves during failure 2. However, the low frequency waves possibly reach slightly higher wave heights, which are somewhat problematic to quantify precisely, as standing wave resolution in both cases is based on several assumptions and the real amplitudes can differ slightly from the estimated number.

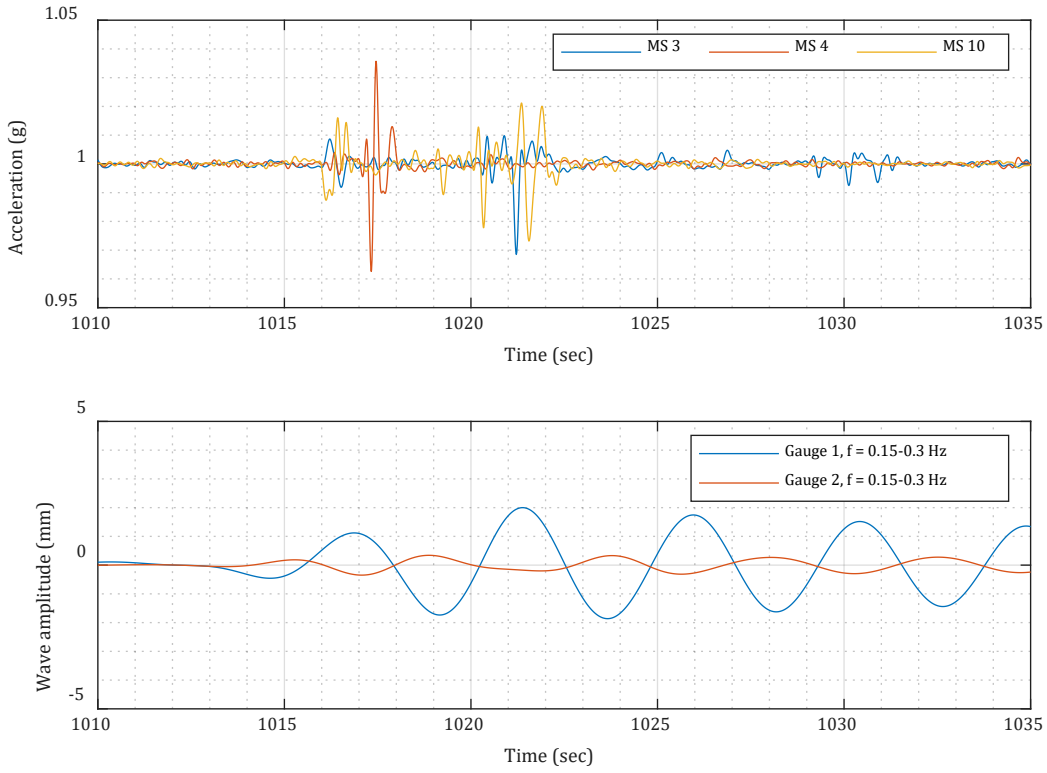

Figure 77: Test 4, failure 3, accelerations of MS's 3, 4 & 10 (top) in comparison to the generated low frequency wave (bottom). For other acceleration data see Appendix B.

Generation of low frequency waves in failure 3 occurs even before the first acceleration peak, which proves that a steady soil mass flow cannot be detected by accelerometers measurements, and only abrupt displacements are visible in acceleration data. Thus, only the pressure change measured by MS's can be used to characterise or recognise a slow soil mass failure, as the one during the third failure of test 4, and give an indication of low frequency wave generation.

7. Evaluation of the experiments outcome and discussion

7.1 Summary wave characteristics vs. slope failure parameters

After a detailed description of each test in chapter 5, the test results are now summarised to have a better overview of similarities and differences of slope failures. The characteristics of waves generated during these tests as well as the measured kinematics of slope failure are presented in Table 7.

Accelerations are measured by MS's with respect to g (gravitational acceleration) and result from two components: horizontal and vertical accelerations. As shown earlier, acceleration measurements oscillate around 1g value. In Table 7, 1g-acceleration is subtracted from the measured values. As a result, the negative accelerations represent sensor movement directed toward the centre of the Earth, while a positive value of acceleration indicates opposite direction of movement or deceleration of MS's. Furthermore, maximum vertical displacements of MS's, presented in Table 7, are roughly estimated from recorded pressure changes and its low frequency components. Only pressure changes that remain for longer than 20 s are assumed to indicate sensors displacements.

Table 6: Overview of the results of tests 1 – 4: wave characteristics vs. slope kinematics

	Wave characteristics			Slope kinematics	
	Frequency range [Hz]	Wave period [s]	Max. amplitude [mm]	Min/Max acceleration MS's [g]	Max. vertical displacement MS's [cm]
T1	0.35 – 0.80	1.25 – 2.85	± 5	-0.08 / 0.08	20 - 25
T2	0.38 – 0.58	1.72 – 2.63	± 0.8	-0.02 / 0.02	11
T3	0.95 – 1.45	0.69 – 1.05	± 0.8	-0.05 / 0.03	10
T4.1	0.75 – 1.50	0.67 – 1.33	± 0.8	-0.004 / 0.008	3.5
T4.2	0.15 - 0.35 0.35 – 0.95	2.85 – 6.7 1.05 – 2.85	± 2 ± 4	-0.04 / 0.045	8-13
T4.3	0.15 - 0.30 0.45 – 1.10	3.33 – 6.7 0.91 – 2.22	± 2.5 ± 3	-0.04 / 0.035	10

Due to limitation of measuring equipment, measurements of MS's do not directly represent soil movement during failure, but they provide an overall indication of kinematics of slope failure. In other words, whether the slope failure exhibited rapid mass displacements or had a steady progressive failure. Combining maximum vertical MS's displacements and recorded accelerations, measured data show good agreement with measured wave formation (Table 6). For

instance, the slope failures in tests 1 and 4 (failure 2 and 3) exhibit the highest kinematics of failure, shown by largest values of acceleration of soil mass and large vertical displacements, result also in highest wave amplitudes. As mentioned, however, the acceleration measurements rather provide an indication of abrupt slope deformations, with no information about global direction of displacements. The values of acceleration measured by MS's cannot be directly linked to the wave generation process. As could be seen from the test data, not each peak in acceleration is followed by an increase in wave amplitude. This inconsistency is due to the fact that horizontal component of soil mass displacement does not induce water waves, whereas the measured accelerations combine both vertical and horizontal movements.

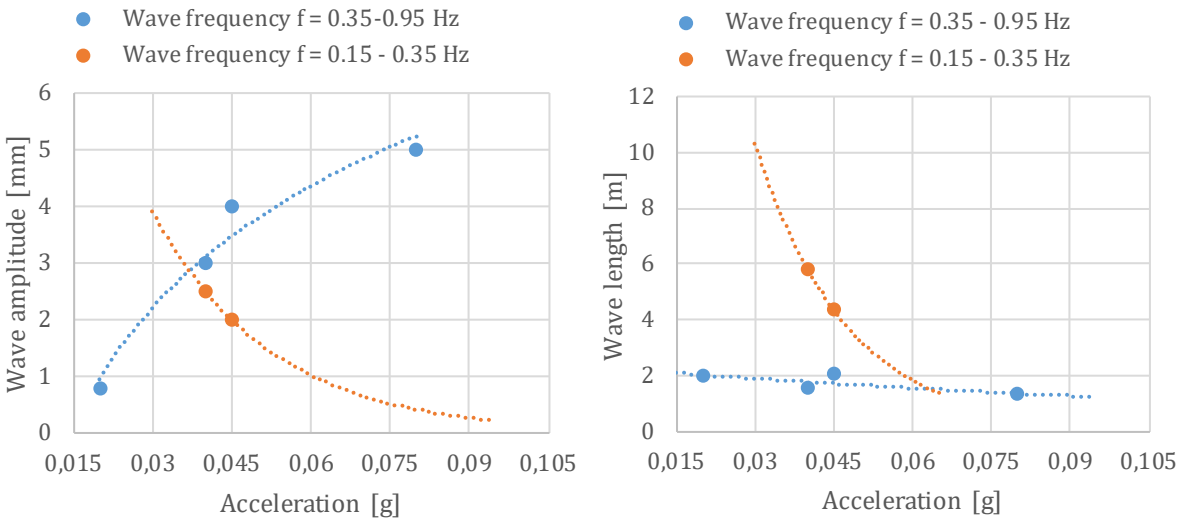

Figure 78: Acceleration vs. generated wave amplitude (left) and wave length (right) for two wave type with wave frequency f = 0.15 – 0.35 Hz and f = 0.35 – 0.95 Hz. Curves are constructed based on limited test data and serve only a rough qualitative estimation of correlation between landslide acceleration and characteristics of generated waves.

Large vertical displacement, which is determined based on pressure change measured by MS's, in combination with high values of acceleration indicate the most favourable conditions for wave with frequency range between 0.35 – 0.95 Hz. Furthermore, wave amplitude and wave length are proportional and inverse proportional to slope acceleration, respectively (Figure 78).

Steady progressive slope failures in turn do not induce waves with large wave amplitude. However, the waves, generated during a slow propagating mass motion, are usually very long and exhibit a very large wave period. It is somewhat problematic to define a favourable condition for these waves to be generated, as accelerations during a slow slope failure remain very low and barely visible from measurements of MS's. The volume of failed mass possibly defines the amplitude of generated waves, while duration of progressive failure influences the wave length of the waves.

During experiments different complex types of slope failure have occurred. In most cases slope failures could not be classified as a single ideal failure mode common for a certain soil condition, but showed development of zones within a failing slope body, with corresponding diverse failure

patterns and soil behaviour for each of zones. So, e.g. a toe of the slope exhibits usually a higher density of soil as well as higher pre-loading and confined stresses, typically resulting in dilative behaviour and development of negative pore pressure increments. The crest of a slope in turn can be covered by a layer of very loose material, prone to liquefaction and typically experiencing a positive increase in pore pressure. Other various types of zoning can occur due to model preparation or failure triggering method. However, formation of different zones within a slope model does not necessarily a disadvantage for experiments. In fact, it somewhat represents the heterogeneity of natural slopes, which usually show layering and formation of pockets of material with different properties and compaction.

Based on measured data (pressure and accelerations) as well as on analysis of images and video recordings from the experiments, slope failure type and motion pattern are estimated for the landslides triggered during tests 1 – 4 (Figure 79 - Figure 84).

T1: Two stages of failure: steady horizontal mass movement around top part of the slope and edge of the crest followed by a deep-seated failure with an abrupt downward displacement of the crest and a progressive horizontal expansion around the slope toe. Excess pore pressure build up indicates liquefaction of sand in the deeper layers near location of MS's 1, 2, 5, 10 (Figure 79).

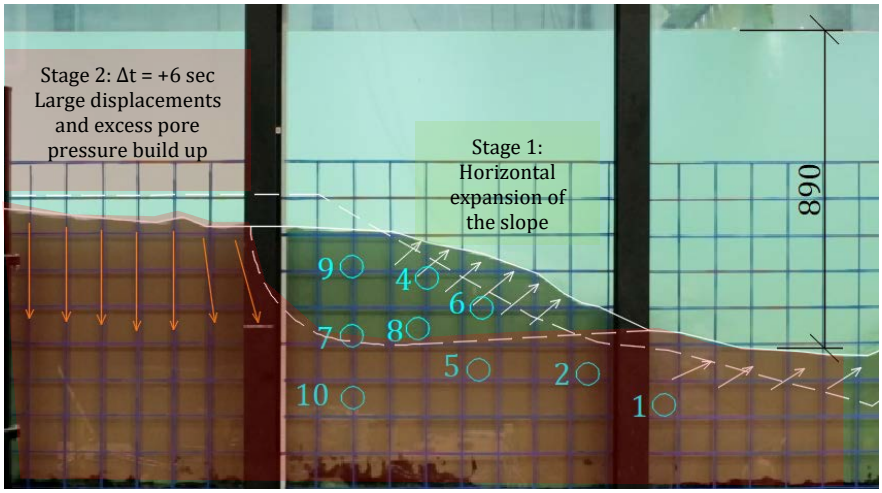

Figure 79: Estimation of slope deformation during the slope failure in test 1, side view

Waves generated during the landslide: frequency 0.35 – 0.80 Hz, max. amplitude ±5 mm. Generation of the maximum wave height timely corresponds to the abrupt crest settlement occurred during the second stage of failure.

T2: Steady progressive failure concentrated around the slope centre. Initial larger soil displacement, followed by rather smaller mass motion during failure progression inwards (Figure 80).

Waves generated: frequency 0.38 – 0.58 Hz, max. amplitude ± 0.8 mm. Possible impact of wave reflection is neglected here due to a very small wave amplitude.

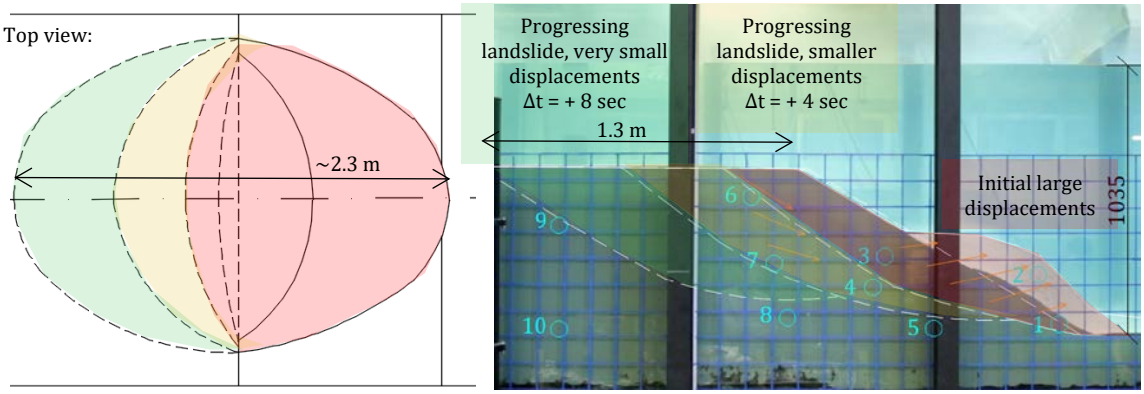

Figure 80: Estimation of slope deformation during the slope failure in test 2, top view (left), side view (right)

T3: Similar to the failure during test 2: slow progressive failure localised around top centre of the slope above the toe protection layer. Only limited extend of landslide progression due to stabilising effect of toe reinforcement results in a smaller volume of failed slope and even slower mass motion (Figure 81).

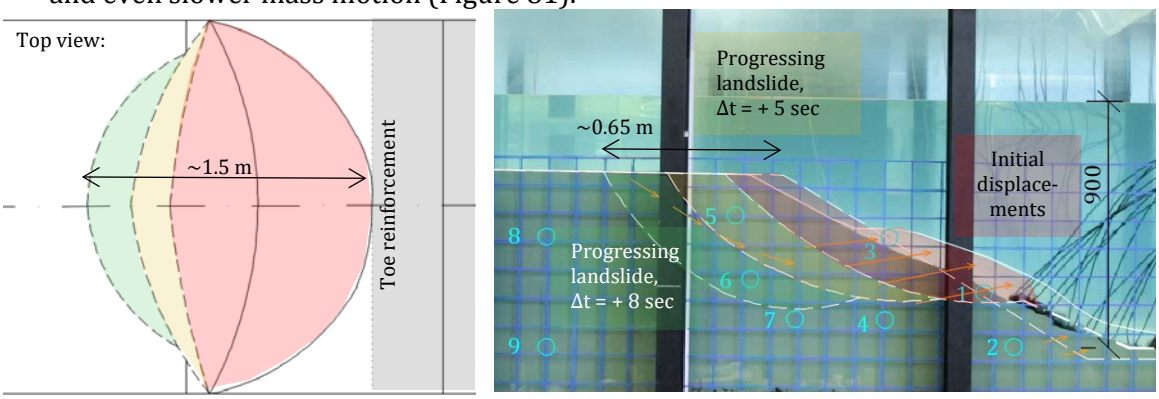

Figure 81: Estimation of slope deformation during the slope failure in test 3, top view (left), side view (right)

Only a minor wave generation: frequency 0.95 – 1.45 Hz, max. amplitude ± 0.8 mm.

T4.1 Small local failure affecting about ¼ of the slope width: top loose sand layer liquefies and abruptly drops down, deeper located MS's 1&3 measure negative pore pressure increments indicating dilative soil behaviour and a possible formation of a shear band (Figure 82).

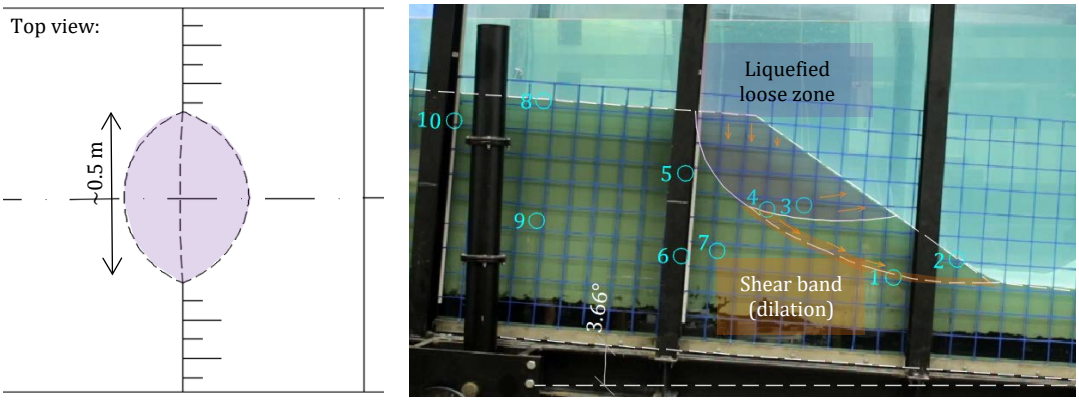

Figure 82: Estimation of slope deformation during slope failure 1 in test 4, top view (left), side view (right)

Only a minor wave generation: frequency 0.75 – 1.5 Hz, max. amplitude ± 0.8 mm.

T4.2 Similar to suggested failure pattern for the failure 4.1, two zones development can be indicated: liquefied loose sand layer within the top 30-35 cm of the slope crest. Pressure sensors indicate positive pore water pressure increment and compressive soil behaviour. Near location of MS's 1, 2 and 4 a shear band is possibly formed. Sensors measure negative pore pressure increment indicating a dilative soil behaviour in deeper layers. Liquefaction of the loose zone resulted in a rapid crest settlement. At later stages of failure loosened pushed forward soil mass flows slowly down the slope.

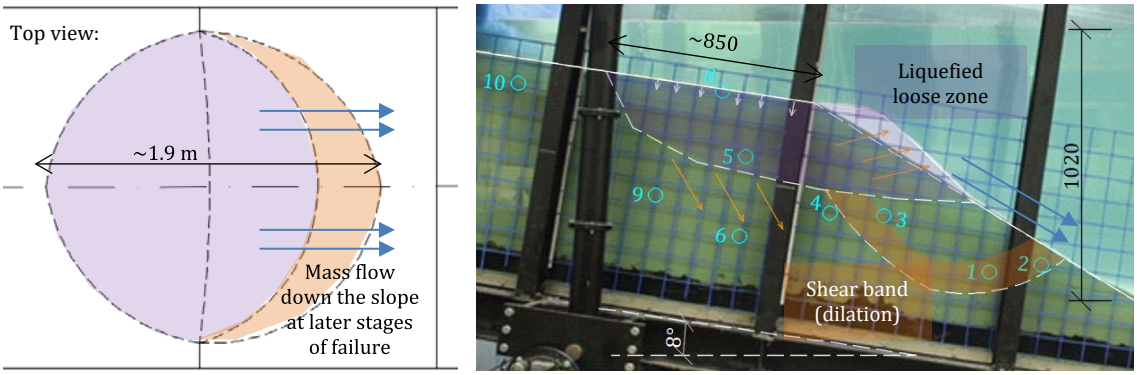

Figure 83: Estimation of slope deformation during the second slope failure in test 4, top view (left), side view (right)

Two wave types generated: waves with frequency of 0.35 – 0.95 Hz and max. amplitude of ±4 mm induced by the first stage of failure with rapid slope deformation; waves with frequency of 0.15-0.35 Hz and max. amplitude of ±2 mm induced by slow mass flow at the later stage of failure.

T4.3 Initiation of failure is indicated by a sudden push forward of soil mass near location of MS's 3 and 4, whereas pressure measurements show a rapid positive pressure increment indicating liquefaction of a soil layer stretching from MS's 3 and 4 to MS's 6 and 9. Progression of failure initiates a steady flow of top soil layers and later on the area of slope toe. Progressive failure is characterised by compressive soil behaviour.

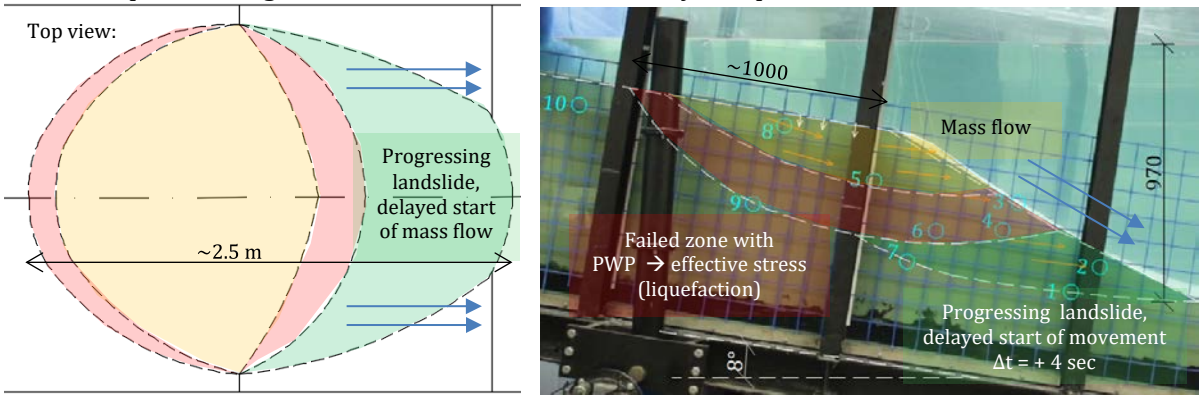

Figure 84: Estimation of slope deformation during the first slope failure in test 4, top view (left), side view (right)

Two types of wave frequencies are generated: waves with frequency of 0.45 – 1.10 Hz and max. amplitude of ±3 mm, resulting from dynamic failure components and liquefaction, as well as waves with frequency of 0.15-0.3 Hz and max. amplitude of ±2.5 mm, likely to be induced by steady mass flow and failure progression.

7.2 Validation of predictive formulae

Using the measurements and geometrical parameters from the slope failures in tests 1, 4.2 and 4.3, we apply the formulae, available for prediction of wave amplitude and wave length based on landslide geometry, described in detail in chapter 4 formulae (1) – (8). The formulae, developed for a slump type of SMF, are possibly the closest to represent the slope failure types, triggered during the tests.

The formulae only take into account the geometry of the slope and some basic soil parameters, while dynamic features of a landslide are calculated based on the soil weight and gravity as a driving force. Full calculations of expected wave height and length using the predictive formulae are presented in Appendix C. Table 7 summarises the results of calculations as well as presents the wave parameters measured during the tests.

Table 7: Measured wave characteristics vs. the results of predictive calculations (Appendix C)

	Frequency range [Hz]	Estimate of wave length [m]	Max. wave amplitude [mm]	Predicted wave amplitude [mm]	Predicted wave length [m]
T1	0.35 – 0.80	1.33	± 5	± 6	1.04
T4.2	0.35 – 0.95	1.11 – 3.0	± 4	± 5.5	1.18
	0.15 - 0.35	2.6 – 6.1	± 2	± 3.2	2.61
T4.3	0.45 – 1.10	0.6 – 2.5	± 3	± 4.1	0.556
	0.15 - 0.30	2.27 – 9.4	± 2.5	± 3.9	1.979

As Table 7 shows, the predictive formulae provide a good estimate of wave characteristics based on geometry of the slope failure. Similar to the wave trains measured during failures 2 and 3 in test 4, two separate sets of characteristic wave parameter were determined, based on proposed stages of failures that induced each of the types of wave trains. The calculations for the first wave (higher frequency waves) are based on an initial, mostly abrupt slope displacement and its geometry, while the second group of waves (low frequency waves) are compared with calculations based on subsequent soil mass flow during failure progression. In such a way calculated values agree with the measured wave parameters fairly well.

The heights of the waves, determined with formulae (1) – (8), are slightly overestimated, while the calculated wave length is rather lower than the wave length estimated based on measurements. Both, the overestimation of wave heights and the underestimation of wave lengths, are likely to be a result of a very short period of time for wave generation included into calculations. As the analytical landslide model accounts for a rapid, nearly instantaneous soil mass displacement, the characteristic time of wave generation, included in the formulae, reaches barely a second, while the granular landslides during the experiments activated their mass motion and,

hence, the wave generation over a much longer period of time, for some failures reaching up to 5 seconds. So, as the wave propagation starts immediately, wave amplitudes remain lower, while continuous impact of a moving landslide results in larger values of wave length.

Taking into account that the wave prediction method is developed for a simplified geometry of a rotational slope failure, the results of the predictive formulae (1) – (8) provide an excellent fit to the measured data. However, the outcome of calculations is highly sensitive to the geometrical input parameters, such as e.g. thickness of the landslide and the initial submergence of the landslide mass centre. These parameters are somewhat difficult to measure exactly and even more difficult to estimate before the failure has occurred.

To show the effect of variation of geometrical input parameters on predicted wave amplitude, a sensitivity study is performed for test 4, failure 2, by varying two input parameters at a time and comparing resulting wave characteristics. The calculations are performed with a MatLab code, presented in Appendix D. First sensitivity calculation is performed with varying landslide length and thickness by a constant value of initial submergence. Second includes variations of landslide thickness and submergence with a constant landslide length. Figure 85 shows lower and upper bounds for landslide geometry input as well as the values, resulting in the best fit to the measured data. Interdependency of input parameters is neglected; however, the range of values is chosen based on potentially possible landslide geometry during the experiment.

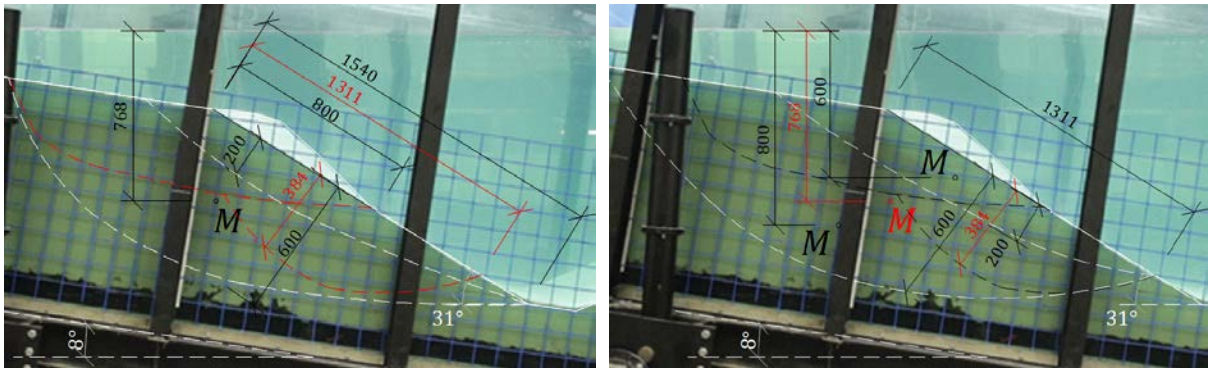

Figure 85: Test 4 failure 2: variation of input parameters landslide length and thickness (left), variation of landslide thickness and initial submergence of landslide (right). Values in red represent the best fit to the data measured during test 4.

Sensitivity study shows for the second slope failure in test 4, that based on differently assumed landslide geometry the predictions of wave amplitude can vary roughly by a factor of 4 (Figure 86, Figure 87). Variation of each input parameter can result in 2 – 3 times smaller or larger wave amplitudes, showing extreme sensitivity of predictive equations to all three varied geometrical parameters. Thickness of landslide shows the lowest influence on calculation outcome, while the highest influence is shown by initial submergence of landslide. Definition of initial submergence, however, requires an estimation of location of the landslide mass centre and therefore can be hardly determined precisely. Finally, a major part of predicted values for wave amplitude is higher

than the measured value. Therefore, one can conclude that equations provide rather a conservative prediction for wave amplitudes.

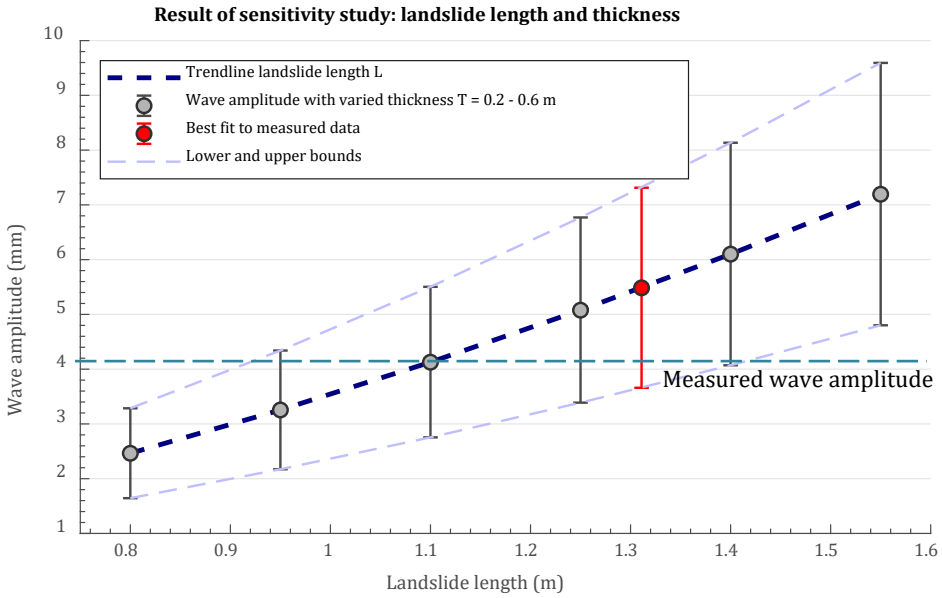

Figure 86: Wave amplitudes resulting from sensitivity study of predictive equations (1) – (8) with variation of geometrical input parameters: landslide length L varying from 0.8 to 1.54 m; landslide thickness T ranging from 0.2 to 0.6 m. Measured during experiment wave amplitude is 4 mm.

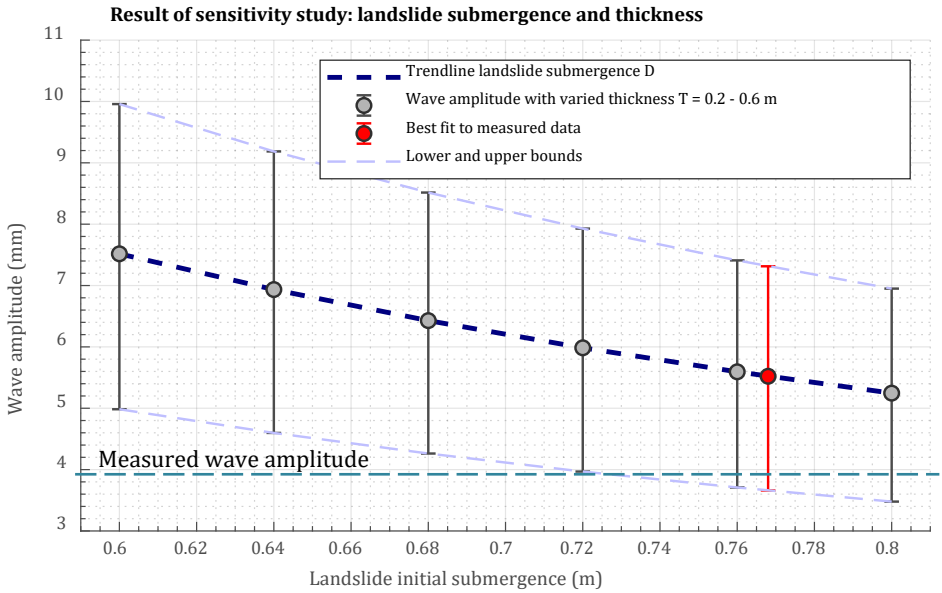

Figure 87: Wave amplitudes resulting from sensitivity study of predictive equations (1) – (8) with variation of geometrical input parameters: landslide initial submergence D varying from 0.6 to 0.8 m; landslide thickness T ranging from 0.2 to 0.6 m. Measured during experiment wave amplitude is 4 mm.

The predictive equations, however, underestimate the wave lengths. This can result in overall underestimation of a wave impact, as longer waves are less dispersive and can travel longer distances. To avoid under- or overestimations of wave characteristics, Input parameter should be determined carefully and as precise as possible. Alternatively, wave prediction can be based on probabilistic approach taking into account multiple possible slope failure patterns.

7.3 Recommendations and remarks on experimental set-up

Based on the experience from performed tests, we present a number of recommendations for design of an experimental set-up for modelling of submarine landslides and generation of tsunami waves using a liquefaction tank. In particular, the choice of slope geometry, triggering mechanism and measuring equipment is discussed. As the liquefaction tank was primarily developed for experiments and studies of soil liquefaction, it is mainly equipped and adapted to measurements within the sand bed. By performing experiments on wave formation, one of the challenges is to create inside the liquefaction tank a suitable testing environment for water waves. It requires an installation of additional measuring tools as well as removal of elements prior to a test, which could possibly disturb wave formation or reflect waves.

Favourable for wave generation test conditions include a large slope length and height with a shallow water table. Nevertheless, the water level should be kept high enough to perform measurements with the wave gauges and velocity measuring EMS device. If tank is tilted, water table should remain above the sand surface at any tilting angle. If water level is too shallow, propagating waves will break creating a turbulent flow and affecting measurements negatively. We recommend to keep the water level of at least 25 cm above the sand surface at the location of wave gauges and EMS, to ensure proper measuring performance.

Choice of the soil density influences the type of landslide and should be made based on desired type of failure. Despite the fact, that it is less complicated to trigger a failure of a loose slope, resulting type of landslide is rather slow and progressive, which usually induces only small amplitude waves. Slopes composed of a denser material, in turn, are likely to fail with in a rapid abrupt manner, increasing chance of a strong wave generation. However, a dense slope can be problematic for failure triggering.

Arguably, triggering mechanism for a controlled slope failure is the greatest challenge for the landslide induced wave modelling. The triggering methods, applied during the discussed experiments, use pressurised water to initiate slope instability. As a result, some amount of water is added to the closed system within the tank, which can possibly cause disturbance of wave measurements. Furthermore, pressurised water in the tank base can potentially follow short cuts and initiate water flow, which would significantly influence the measurements of EMS. However, during the experiments we could not notice any obvious impact of triggering mechanism on the performed wave measurements, as only a negligibly small amount of water is added.

Tilting of the tank as a triggering mechanism is rather a favourable method for landslide induced wave measurements, as no water injection is needed, so one can avoid possibility of triggering mechanism impacting wave measurements. Tilting of the tank, however, should be performed at a low rate, allowing water table to equalise and preventing waves induced by tilting. During the

experiments, a tilting rate of 0.033 °/s has been proven to be suitable, creating no waves. A major disadvantage of tank tilting with respect to wave measurements is a resulting inconstant water depth, influencing wave characteristics as it propagates from shallow to deeper regions.

Because wave propagation inside the liquefaction tank is restricted by the walls, a matter of special importance is minimising of wave reflection by installing wave absorbers on both walls of the tank. An elaborate discussion on wave reflection is presented in the chapter 7.4.

To be able to measure pore water pressure and acceleration of soil mass during a slope failure a number of mobile sensors should installed within the slope body. Most importantly, the sensors should be installed along the longitudinal axis of the tank, to avoid boundary effects, and be evenly redistributed over the zone of interest (slope and crest) to capture slope deformation entirely. The embedment of a sensor should be sufficient to prevent sensor from being washed out to the slope surface; however, too deep embedded sensors will be unable to detected superficial soil mass flow or a shallow failure. Based on performed tests, an embedment of about 15 - 20 cm can be recommended.

Despite the fact that the mobile sensors are designed to be able to follow soil movement, the connecting wires can restrict sensors movement or even completely change its pattern. As often occurs, sensors original location can differ from the initially planned position, which results in a connecting wire to be bent, applying additional drag force to the sensor and restricting the sensors movement. A possible solution for this issue can be wireless sensors or at least thinner more flexible wires. Also, to prevent wire bending during installation of sensors, the final planned location of a sensor should be ensured by checking the hydrostatic pressure measured by a sensor. Furthermore, the length of wires should be kept long enough to allow for large sensors displacements during slope failure.

The accelerations measured by mobile sensors are recorded in X-, Y- and Z-directions. However, due to sensors rotation it is hardly possible to determine the global orientation of the measured acceleration components. Since wave generation process is based on vertical component of soil mass displacements and, thus, on vertical acceleration increments, additional information about sensor rotation (e.g. with gyroscope equipped sensors) or global direction of movement is needed to enable applicability of measured accelerations for the purpose of wave generation study.

During experiments, we measured water surface elevations with a set of two wave gauges, one installed above a sloping part of sand bed, and the second one – above the slope crest. A disadvantage for such an arrangement is a various water depth at the locations of two gauges, since water depth can influence wave characteristics during its propagation. Especially, during experiments with a tilted tank, effect of reverse shoaling could be clearly distinguished in the data measured by wave gauges. To enable a better comparison of gauge data and avoid unwanted

effects of different water depth, two wave gauges should be installed above the crest of the slope. In this way, one can study the wave propagating towards the shore, while the measured by gauges waves should exhibit nearly equal wave amplitudes. If a larger number of wave gauges would be available, one could add another set of two gauges, installed above the slope toe, to enable measurement of the wave propagating in opposite direction. Installation of an EMS is not required; however, as it measures water particle velocity, it provides additional data, which can be useful for wave analysis or estimation of wave characteristics. EMS should be installed above the slope crest with its probe close to the crest surface.

7.4 Wave reflection

To be able to perform wave measurements in the liquefaction tank, it is crucial to take into account wave reflection from the tank walls. To minimise reflection we designed wave absorbing elements based on experiments in a wave flume, described in Appendix A.

Effectiveness of a wave absorbing element is highly dependent on the type of waves, defined by wave period. As the wave period increases, the absorption of wave energy reduces resulting in stronger wave reflection. The wave absorbing elements for the liquefaction tank were designed for a wave period range of T = 1.25 – 1.50 s, corresponding to a wave frequency of f = 0.6 – 0.8 Hz. Hence, wave periods larger than 1.50 s could result in these waves being reflected.

During experiments, waves induced by slope failure exhibited wave frequencies of 0.15 – 1.1 Hz, whereas waves with a frequency larger than 0.5 Hz did not show any evidence of wave reflection impacting measurements. For the lower band of frequencies, 0.15 – 0.5 Hz, wave reflection was clearly present.

Waves with low frequency showed only slow amplitude dissipation, continuing oscillating for over 40 – 50 s. From the test data, we could recognise formation of a standing wave profile, which indicates presence of wave reflection with reflection coefficient higher than ca. 60% (Goda & Suzuki, 1976).

Another parameter, impacting effectiveness of wave absorbers, is the water depth at both reflecting boundaries of the tank. The elements length was designed to fully cover tank walls above the sand, whereas on both sides sand should have reached the level mark of approx. 0.87 m. However, during test 2, the right-hand side slope was removed completely, increasing water depth at the North-wall to over a meter, while the wave absorber could cover less than a half of it. The part of the wall, uncovered by wave absorber, could significantly increase wave reflection even for higher frequency waves.

A similar problem occurred during test 4, while the tank was tilted to 8°. Due to tilting, water depth at the North-side of the tank nearly doubled, so that the wave absorbing element was

slightly too short to cover full submerged wall length. During test 4, however, wave reflection was obviously present only for long waves with wave frequency f = 0.15 – 0.35 Hz. As mentioned earlier, this frequency range is far beyond the design wave frequency, so that the very low effectiveness of the wave absorbing elements could be well expected.

Overall, the wave measurements can contain inaccuracies, as the wave absorbers were not fully suitable for all test conditions, while presence of wave reflection could significantly influence measured by gauges wave amplitudes. The wave absorbing elements can be improved by increase in size to ensure full wall coverage as well as by adding more layers to increase absorbing capacity. To ensure sufficient absorption of low frequency waves, an improved design of wave absorbers should be based on experiments in a wave flume, including a wider range of wave periods.

Finally, for the waves with a very long wave period (ca. T > 3 s) it is nearly impossible to avoid wave reflection fully. If measured wave amplitudes remain low, these waves can be neglected and removed from the signal. However, if the waves reach high amplitudes and must be considered, an estimate for wave amplitudes can be done by using the wall pressure sensors and analysing the hydrostatic pressure fluctuation at reflecting boundaries, as suggested during data analysis in test 4.

8. Summary and Conclusions

Laboratory experiments of wave generation by submarine landslides were presented in the current work. Experiments were conducted using a large scale static liquefaction tank, containing a fully submerged layer of very fine uniform silica sand with a thickness of approximately 90 cm. Inside the tank a slope was dredged with an inclination angle of 30 to 32°, after which a slope failure was induced using various triggering mechanisms, each resulting in a slightly different landslide morphology and wave formation. Modelling of a slope failure with natural granular material, sand, with no predefined or enforced failure plane, produced complex slope failures, including progressive behaviour and formation of various failure zones, which are representative of real landslides.

During each test, slope geometry and soil properties were slightly modified, as well as the initial slope submergence. At the moment of landslide initiation, water surface elevation was measured using two wave gauges and horizontal water velocity using an electromagnetic liquid velocity meter (EMS). Landslide kinematics were recorded with a number of mobile sensors, installed within the slope body and measuring accelerations in three directions. Furthermore, changes in water pressure were measured by the same mobile sensors as well as by stationary sensors at the base and inside the walls of the static liquefaction tank.

Different types of slope failure resulted in various wave amplitudes, ranging from nearly zero to maximum ±5 mm, as well as various wave frequencies, from relatively high (> 1 Hz) to very low (< 0.35 Hz). For a specified submergence the waves, recorded during tests 1, 2 and 4, could be classified as transitional water waves (Figure 26), as their approximate wave length was larger than twice the water depth, but smaller than 20 times the water depth.

Measurements of wave formation during each test significantly differed from an idealized wave generation model and results of experiments performed with a rigid landslide body sliding on a pre-defined plane, as described in the literature (e.g. Enet and Grilli (2007)). Due to deformation of the sliding mass with time and its progressive behaviour, overall kinematics of failure were rather slower than the rigid landslide models, combining abrupt rapid slope deformations with gradual mass flow. As a result, not one, but multiple wave trains were generated, with various wave frequencies and amplitudes. A superposition of these wave trains represented full wave formation induced by a landslide. In contrast to rigid body landslides, where most of the wave activity occurred for a very short time after body immersion into water column, the process of wave generation by a deformable progressive landslide continued for a significantly longer period of time, reaching the highest wave amplitudes several seconds after the onset of failure. Lower kinematics of landslides resulted in smaller wave amplitudes, while longer duration of wave generation contributed to increased wave period and wave length.

For the wave components with very low wave frequencies (f < 0.35 Hz), wave reflection caused formation of standing waves, so that one should account for some inaccuracy in measured wave amplitudes due to contamination of results by wave reflection. For shorter waves with f > 0.35 Hz, no standing waves were observed, as the installed inside the tank wave absorbers could successfully minimise wave reflection.

Based on experimental data, landslide motion was described throughout different stages of failure. Mobile sensors measuring water pressure and accelerations were compared with wave measurements for a specified wave frequency, applying wavelet transform methods to decompose the data in time-frequency space. Rapid landslide displacements, caused by partial liquefaction of a slope or development of a shear band, produced waves with a higher frequency range and reached higher wave amplitudes in most cases. Gradual progression of failure, characterised by step-wise soil mass displacement and steady mass flow, resulted in generation of very low frequency waves. These waves exhibited smaller wave amplitudes, but reached large values of wave length.

Kinematics of landslides were studied based on the acceleration, measured by mobile sensors, as well as by interpreting the water pressure, recorded by the same sensors. Due to limitations of measuring equipment, we were not able to determine the spatial components of soil mass acceleration, which contributed to wave generation. One of the reasons was unknown rotation of sensors, which made it impossible to resolve the separate directional components. Resultant accelerations contained vertical as well as horizontal components of sensors displacements, whereas only vertical components are significant for wave generation. Nevertheless, we found a direct correspondence between landslide kinematics and induced wave characteristics.

Characteristics of the landslides and waves, measured during experiments, were compared with predictive formulae from the literature. Empirical equations derived by Watts et al. (2005) were used to calculate wave height and length for a 2D rotational submarine mass failure. For specified landslide geometry, based on measurements during the tests in the liquefaction tank, predicted wave parameters agree reasonably well with the measured values. Predictive equations slightly overestimated wave amplitude, while wave length was underestimated in most cases. Both deviations can be a result of specific types of landslide during experiments in the liquefaction tank, showing rather slow failure kinematics and progressive behaviour.

The empirical equations, however, are highly sensitive to variations in geometrical input parameters. For instance, initial submergence with respect to the mass centre of a landslide and landslide thickness strongly influence the resulting calculation, while these geometrical parameters are difficult to measure precisely and can therefore exhibit large variations. Sensitivity study was conducted for the second slope failure in test 4. Varying the input parameters within a plausible range according to the test data, predictive equations resulted in a

wide range of wave amplitudes. The single values differed from each other by a factor > 2. Highest influence on outcome of calculation showed the initial submergence of the landslide as well as the landslide length.

In contrast to the models using rigid landslide body (Wiegel (1955), Jiang and Leblond (1992, 1994), Pelinovsky and Poplavsky (1996), Watts (1997), Watts et al. (2005)), waves generated by deformable landslides exhibit smaller wave amplitudes, but significantly larger wave length. These waves are less dispersive and dissipate their energy over a larger traveling distance. In comparison to the rigid slide model, run-up heights can reach higher levels despite smaller initial wave amplitudes, increasing impact of these waves on the coastal line. Thus, the models applying a rigid landslide body to simulate a slope failure can in some cases underestimate the overall wave impact.

Finally, summarising the lessons learned during the experimental work, we formulated recommendations for laboratory set-up design. With a number of modifications and additional equipment, the static liquefaction tank can be successfully used to perform experiments on landslide induced tsunami waves, as the results of the present experimental work showed. However, a number of improvements are required to create a more suitable testing environment and reduce contamination of wave data. For instance, wave absorbing elements should be modified or increased in size to ensure minimum wave reflection for a wider range of wave periods. Furthermore, modification of mobile sensors to reduce the disturbing effects of connecting wires as well as proper selection of sensors location can provide a significant improvement of obtained data.

As the present MSc thesis was initiated as a part of research on post-disaster reconstruction of the Japanese coastal line after the Great Tohoku Earthquake and Tsunami of 2011, one should question the relevance of the performed experimental investigation to actual tsunami events. The conducted experiments modelled submarine landslides with fine sand, soil material predominantly found on continental shelf and slope (Richards et al., 1975), which is often the same material in real submarine landslides. By allowing for landslide development without a predefined failure plane, we could observe complex failures including liquefaction, progressive failure, zoning and heterogeneous soil behaviour, closely representing complex material moving during real landslide events. Finally, by measuring wave formation directly above the source, different stages of slope failure could be linked to development of wave trains with various wave periods, showing that not just a single wave train is generated, but a superposition of waves induced during different stages of failure.

Development of the testing set-up would provide a suitable base for future experimental studies of landslide induced tsunami waves, allowing measurements within the soil body of a landslide as well as recording of water surface elevation, providing data for wave analysis. Combining two

disciplines, geotechnical and hydraulic engineering, landslide induced tsunami research can move a step forward in understanding of tsunami generation, increasing effectiveness of tsunami prediction techniques and minimising consequences of future disasters.

8.1 Recommendation for future research

For future experimental studies of landslide induced waves using the liquefaction tank, first of all, it is highly important to cope with wave reflection. Improvement of existing wave absorbing elements or suggestion of another design would significantly increase the quality of measured wave data. Furthermore, wave absorbing elements should be more extensively tested in a wave flume for various wave conditions, to ensure their effectiveness.

Future work should include a larger number of experiments, to be able to evaluate repeatability of experiment results. Furthermore, sensitivity of wave formation to landslide geometry, submergence depth and type of failure should be studied by repeating experiments, varying one parameter at a time.

Finally, if techniques and equipment measuring landslide kinematics were improved (mobile sensors equipped with gyroscope, with thinner connecting wires or wireless), that could significantly improve quality of obtained data. This data would enable a wide range of directions for future studies, providing required information to link kinematics of landslide motion to wave formation processes.

Appendix A – Experiments in a wave flume, wave absorber design

Introduction

Vertical wave absorbers can be a matter of special importance when wave reflection has to be minimised in spatially confined conditions, which is often the case in laboratory experiments. Investigations were conducted to assess wave absorbing properties of PPC filter mats installed on an impermeable vertical barrier and subjected to action of long waves. The absorbing material used for the investigation was the Matala® filter media, originally developed as material for the purpose of mechanical filtering for Koi ponds. This highly permeable media consists of randomly connected curly fibres and provides a large specific surface area per unit volume as well as high porosity. These properties make the media well suitable to reduce the wave energy by means of friction and turbulence.

In ocean engineering the most commonly used type of wave absorber is the sloping beach-type breakwater. However, these breakwaters occupy large space in a flume as they are typically constructed with a gentle slope of approx. 1:5 (Lim, 2014). Ippen and Goda (1963) presented one of the first studies of vertical wave absorbers, conducted on an absorber made of a number of wire mesh screens. The investigation pointed out the importance of spacing between the screens and a large number of screens to achieve required wave energy dissipation. As a rule of thumb was suggested that the length of the wave absorber should be at least the wave length L of the incident wave. Later studies could reduce the required length to 75% of the wave length L, which was still fairly large (Hughes, 1993).

Several more recent studies have proposed effective methods for wave energy reduction using vertical absorbers. Fritz (2002) and Tiedeman et al. (2012) presented wave absorbers which consisted of series of perforated steel screens with progressively reducing spacing and porosity of screens. Neelamani et al. (2017) conducted experiments on slotted vertical barriers and compared their effect to conventional sloped breakwaters. The results showed that a sufficient level of wave absorption could be achieved with vertical absorbers of relatively small thickness, which served as motivation for this investigation within the scope of the thesis project.

Material and experimental set-up

The current investigation of wave absorbing properties was carried out on a fibrous material of thermo-polypropylene compounds (TPPC) or thermo-polyethylene compounds (TPEC), which was originally designed by company Matala® as filter media for aquarium applications. The filter media is commercially available in 4 various densities, from which two (high density blue mat and extra low density black mat) were used to carry out the experiments. In Table 8 the specifications provided by manufacturer are reported. The samples were delivered in sheets with dimensions

120x100x3.8 cm and cut into 80x80 cm sheets to adjust dimensions to the cross section of the wave flume.

Table 8: Filter media specifications according to Matala® (MATALA, 2019)

Matala® Product Code	Colour	Specific surface [m^2/m^3]	Fibre diameter [mm]	Free volume/ porosity [%]
FSM190/SM190	Black	190 ± 10	1.7 ± 0.1	92
FSM365/SM365	Blue	365 ± 10	0.55 ± 0.1	94

The large free volume of the filter media provides beneficial conditions for a water flow while avoiding wave reflection from its surface. Furthermore, randomly arranged curly fibres of the filter media create turbulences on a micro scale for the water passing through, which reduces its flow velocity. High value of specific surface increases frictional resistance to the flow, while a wave travels inside the absorber. In summary, the water can easily enter the filter media, but is forced to slow down and change direction of flow on a micro scale, which in combination with frictional resistance contributes to wave energy dissipation.

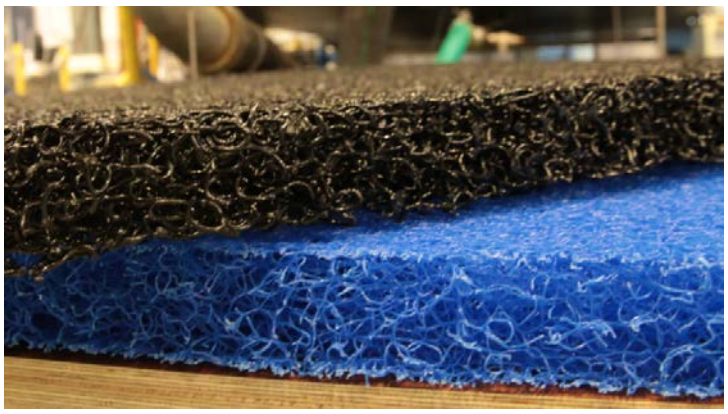

Figure 88: Matala® filter media, two density types: FSM190/SM190 black dense (top) and FSM365/SM365 blue fine media (bottom).

The experiments were conducted in a wave flume of Fluid Mechanics Laboratory of TU Delft. The flume with a length of 39 m, a width of 80 cm and a height of 130 cm is equipped with a computer controlled wave generator (Figure 89). An automated reflection compensator prevents reflection of waves from the front side of wave generator. Furthermore, the flume is also equipped with a wave absorber of sloping beach type (Haage, 2018). This wave absorber did not play a role during current experiments, as the test model was installed in front of it.

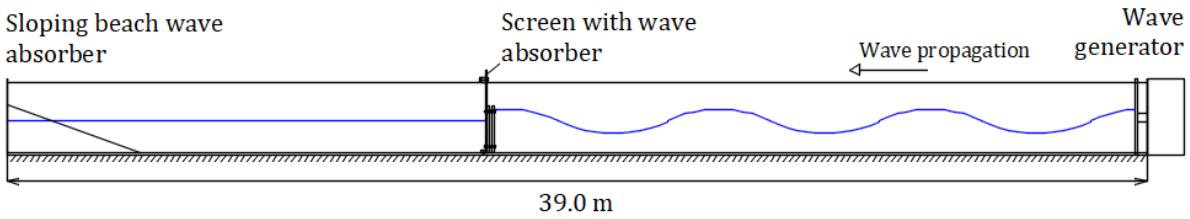

Figure 89: Wave flume, principal sketch of set-up

In order to position the wave absorber in the wave flume, sheets of filter media were mounted on a specially constructed impermeable wooden screen. The screen was designed to withstand bending due to differential hydrostatic pressure under wave action. It was bolted to the flume bottom and fastened to a wooden beam at the top. Thereby the position of the screen in the flume was stabilised and prevented from movement.

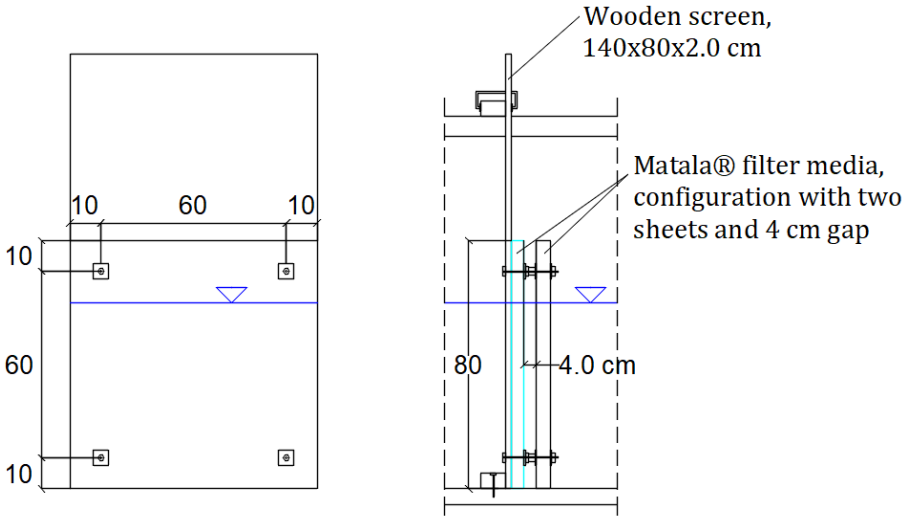

Figure 90: Experimental set-up. Filter media mounted on wooden screen

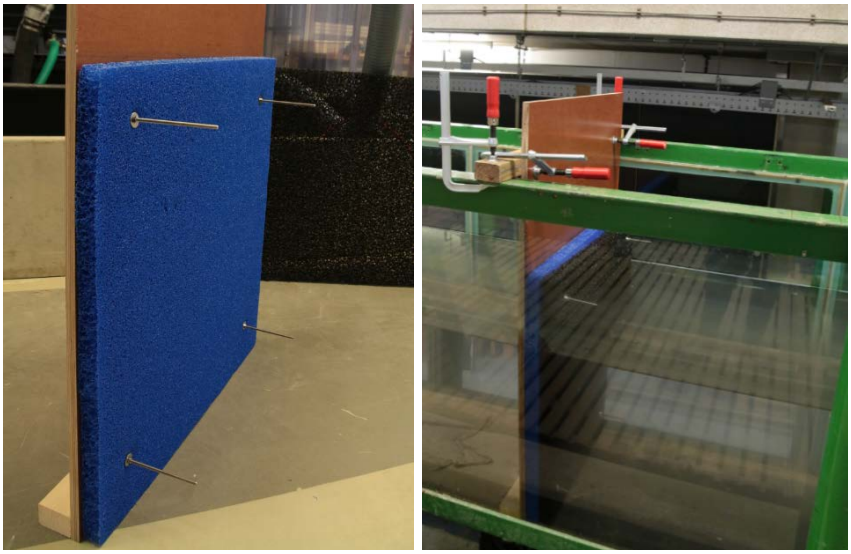

Figure 91: Wave absorber mounted on the screen, one layer configuration (left); configuration with two layers installed inside the flume (right)

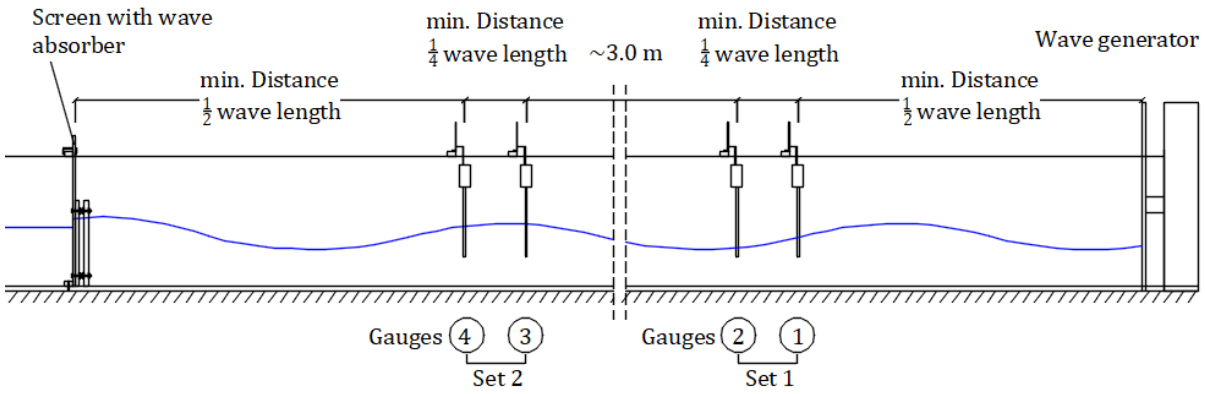

Figure 92: Scheme of the installation of gauges in the flume

During the experiments waves in the flume were measured with 4 wave gauges, which were combined in two sets of two. To resolve the incident and the reflected waves the method of Goda and Suzuki (1976) has been applied, which treats the measured composite wave field as superposition of two regular waves with constant amplitude and period.

The equations for an incident and a reflected wave with amplitudes a_i and a_r, respectively, can be formulated as follows:

$$\eta_i = a_i \cos(kx - \omega t + \varphi_i) \qquad \eta_r = a_r \cos(kx - \omega t + \varphi_r)$$

Whereas $k = {}^{2\pi}/_{L}$ is the wave number and $\omega = {}^{2\pi}/_{T}$ is the angular frequency of a wave with the length L and period T. Parameters φ_i and φ_r are phases of incident and reflected wave, respectively. The combined wave $\eta = \eta_i + \eta_r$ can be then decomposed into two harmonics as follows:

$$\eta = A \cos(\omega t) + B \cos(\omega t)$$

Knowing surface elevation at two specified points (two wave gauges) and the distance Δl between them, a composite wave can be further described as follows:

$$x_2 = x_1 + \Delta l$$

$$\eta_1 = A_1 \cos(\omega t) + B_1 \cos(\omega t)$$

$$\eta_2 = A_2 \cos(\omega t) + B_2 \cos(\omega t)$$

$$A_1 = a_i cos\Phi_i + a_r cos\Phi_r$$

$$A_2 = a_i \cos(k\Delta l + \Phi_i) + a_r \cos(k\Delta l + \Phi_r)$$

$$B_1 = a_i sin\Phi_i - a_r sin\Phi_r$$

$$B_2 = a_i sin(k\Delta l + \Phi_i) - a_r sin(k\Delta l + \Phi_r)$$

$$\Phi_i = kx_1 + \varphi_i$$

$$\Phi_r = kx_1 + \varphi_r$$

The values A_1, A_2, B_1 and B_2 are constant and can be estimated by performing a Fourier transform of a signal. The amplitudes of the incident and reflected wave can be then back figured using following estimation (Goda & Suzuki, 1976):

$$a_i = \frac{1}{2|\sin k\Delta l|}\sqrt{(A_2 - A_1 \cos k\Delta - B_1 \sin k\Delta l)^2 + (B_2 + A_1 \sin k\Delta - B_1 \cos k\Delta l)^2}$$

$$a_r = \frac{1}{2|\sin k\Delta l|}\sqrt{(A_2 - A_1 \cos k\Delta + B_1 \sin k\Delta l)^2 + (B_2 - A \sin k\Delta - B_1 \cos k\Delta l)^2}$$

The reflection coefficient in turn is defined as a ratio of the incident and reflected wave amplitudes and can be determined as $k_r = \frac{a_r}{a_i}$.

For comparison and error avoidance reflection coefficients were obtained for both sets of gauges independently. Therefore, both sets of gauges were installed according to requirements of Goda & Suzuki method: the distance between two gauges was set to one fourth the length of the wave L; the minimum required distance from the wave generator and reflecting screen of $1/5L$ was kept. The sets of gauges were located at a distance of approx. 3 m from each other to ensure that measurements of each set are not influenced by another. For calculation of reflection coefficients acc. to Goda and Suzuki method the Matlab script Refreg written by Klaasman (2005) was used.

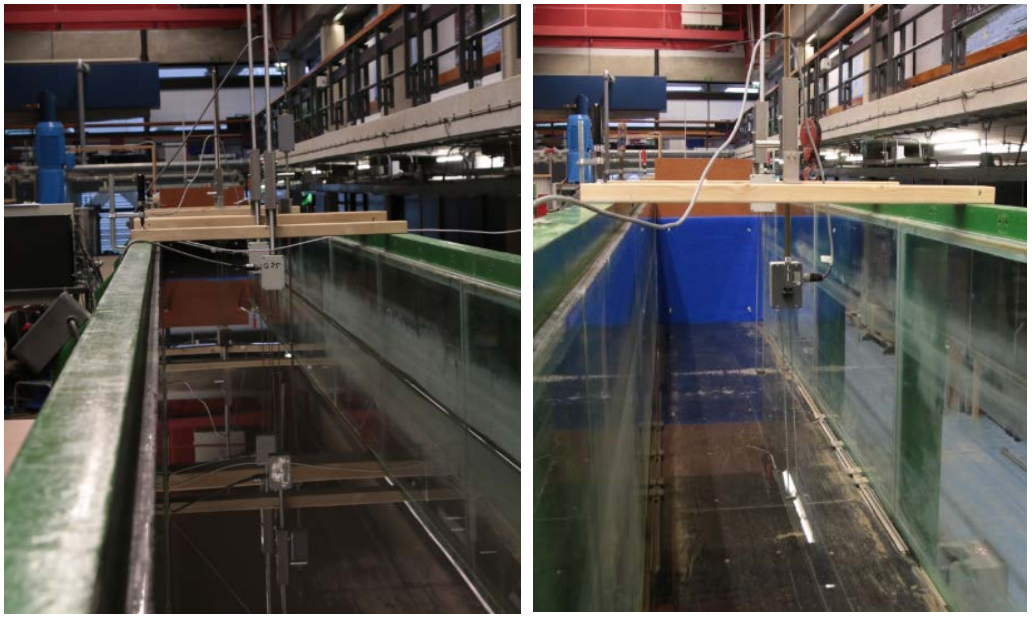

Figure 93: Gauges set-up in the flume

Table 9: Requirements to the gauges arrangement (Goda and Suzuki, 1976)

Period [s]	Wave Length [m]	Distance between gauges [m]	Min. distance from generator or screen [m]
1,25	2,270	0,568	0,454
1,50	2,990	0,748	0,598

During the sequences of the experiment water depth in the flume was kept constant at 60 cm. The wave absorber was tested in two different wave conditions: with shorter and longer waves. The first wave train was generated with a period T of 1.25 s and a wave length L of 2.27 m. For the second, longer waves were chosen with wave period T and wave length L of 1.50 s and 2.99 m, respectively.

In order to test different possible configurations of the filter media used as a wave absorber, during the experiment the filter mats were attached to the screen in various combinations. First, the fine blue filter media was fixed to the screen as a single wave absorbing layer. For the next round, coarse black mat was mounted in front of the fine blue. Further, a gap of 4 cm between two layers was added. Finally, two layers of fine blue material in combination with one layer of coarse black filter media was mounted to the screen and tested. In total the tests were carried out on 4 configurations of wave absorber.

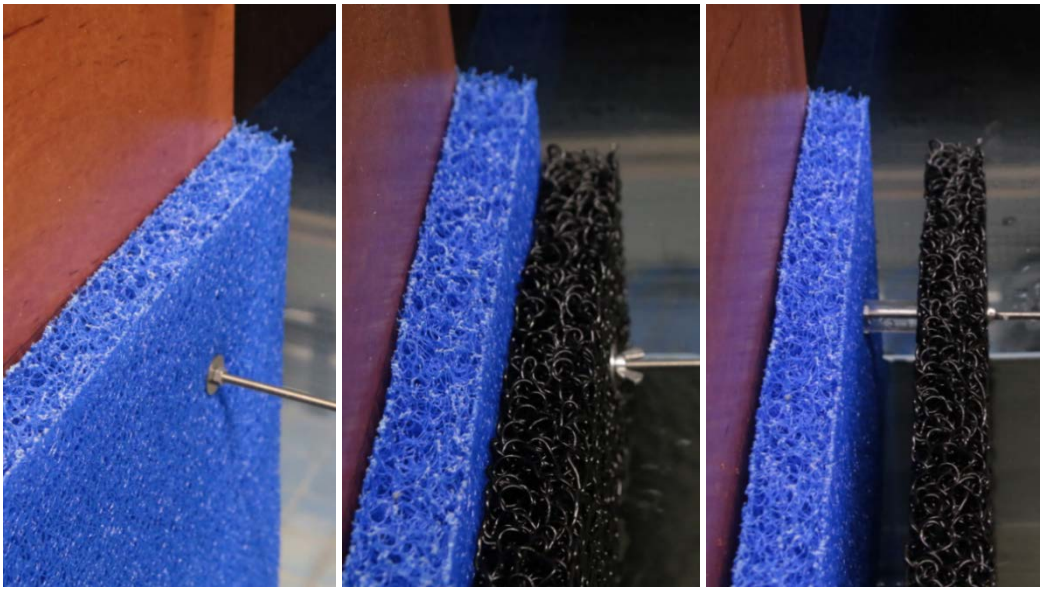

Figure 94: Various arrangements of filter media: configurations 1 (left), 2 (middle) and 3 (right).

One shall mention that during the installation of the configuration 4, the second layer of the fine blue media could not be placed over the entire submerged area of the screen. Approx. 65% of the total area was covered with the wave absorbing media. In the uncovered parts a gap between the front black media layer and the back blue media layer was left.

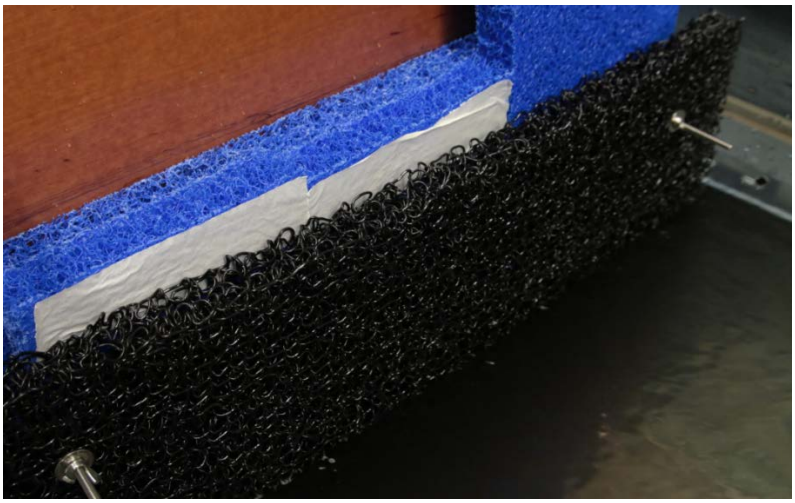

Figure 95: Arrangement of filter media in configuration 4.

For each material arrangement two values of reflection coefficient were obtained based on measurements of two sets of gauges in each of the two wave conditions. These values will be further evaluated and used to design a wave absorbing element which should yield the desired low level of a wave reflection during the landslide experiments in the static liquefaction tank. Future work will be conducted to test efficiency of the final design of wave absorber in a wave flume and determine its absorption coefficient.

Results of the experimental work

As the wave generator has been equipped with an automated reflection compensator, so any reflection from the front shield of the wave generator could be excluded, the measured wave field was composed purely of incident wave and its reflection from the wooden screen with the mounted on it wave absorber.

Figure 96 shows an example of measurements of this superposed wave field for one of the test sequences. As can be seen from the gauge measurements, during each sequence of the test it took roughly 30 seconds for the wave field to become stable. Due to the fact that the wave reflection for all material configurations was still fairly high, in all sequences of the test a formation of a standing wave system could be observed. For the wave reflection analysis a time period from second 80 to 100 was chosen with at least 16 oscillations for the waves with a period T of 1.25 s and at least 14 wave cycles for the waves with a period T of 1.50 s.

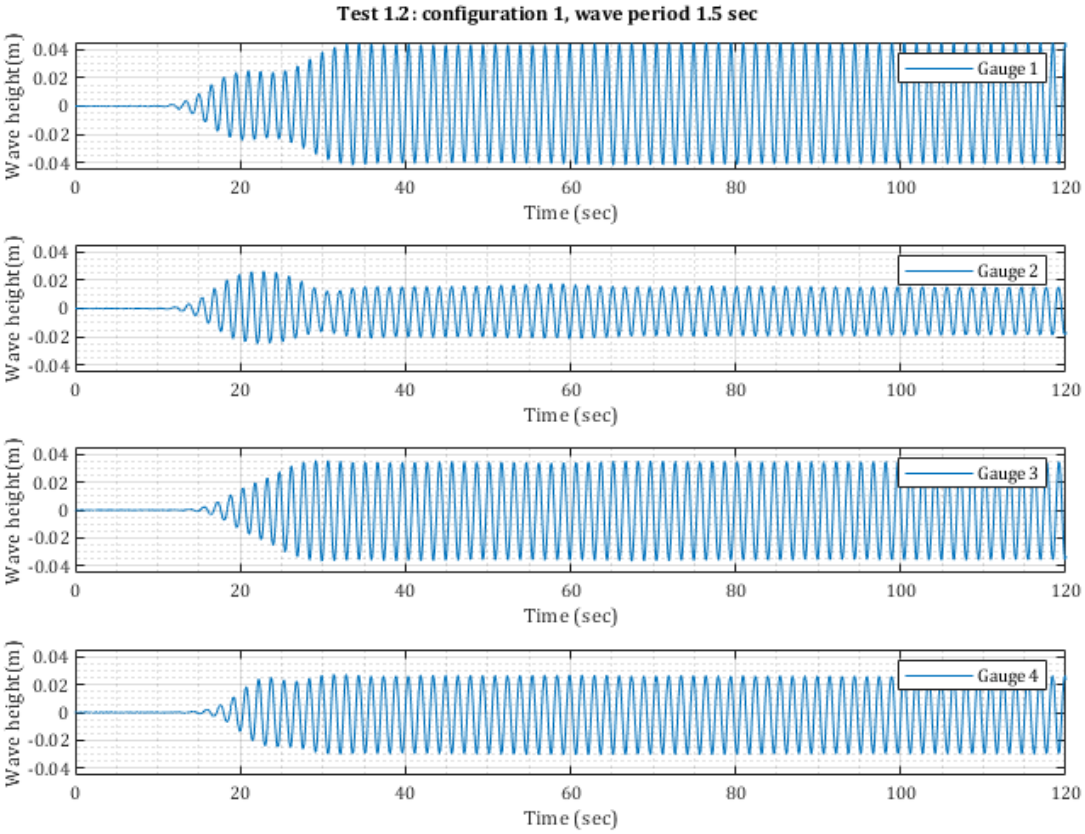

Figure 96: Time series of wave amplitude measurements during the test 1.1 by gauges 1 to 4.

In Table 10 the results of the measurement are shown for each test sequence as well as the reflection coefficients k_r and the wave absorption are calculated for each absorbing material configuration. Here the wave absorption is simply defined as $(1-k_r)$.

Table 10: Results of wave resolution for test sequences 1.1 to 4.2; black: set of gauges I (gauge 1 and 2); blue: set of gauges II (gauge 3 and 4).

*** Filter media configurations:**

1. A single layer of blue Matala®

2. One layer of blue and one layer of black Matala®.

3. One layer of blue and one layer of black Matala® with a gap of 4 cm in-between.

4. Two layers of blue and one layer of black Matala®.

Test No.	Material configu-ration*	Wave period [s] / length [m]	Incident wave height [m]	Reflected wave height [m]	Reflection coefficient [-]	Wave absorption [%]
1.1	1	1.25 / 2.27	0.0234 0.0229	0.0192 0.0187	0.820 0.818	18 18.2
1.2		1.50 / 2.99	0.0247 0.0240	0.0211 0.0209	0.853 0.870	14.7 13
2.1	2	1.25 / 2.27	0.0236 0.0230	0.0174 0.0169	0.739 0.733	26.1 26.7
2.2		1.50 / 2.99	0.0244 0.0238	0.0197 0.0195	0.808 0.819	19.2 18.1
3.1	3	1.25 / 2.27	0.0236 0.0230	0.0174 0.0169	0.739 0.736	26.1 26.4
3.2		1.50 / 2.99	0.0243 0.0235	0.0197 0.0193	0.809 0.822	19.1 17.8
4.1	4	1.25 / 2.27	0.0235 0.0230	0.0156 0.0151	0.664 0.658	33.6 34.2
4.2		1.50 / 2.99	0.0244 0.0236	0.0185 0.0181	0.758 0.765	24.2 23.5

Overall, the measurements of two sets of gauges match well and the calculated values of wave reflection differ only slightly for each test sequence. As could be expected, the performance of the wave absorber is generally better with shorter waves, while its absorbing effect decreases with an increasing wave length. The lowest value of reflection coefficient of 0.66 could be achieved with 3 layers of the absorbing media in configuration 4.

Figure 97 demonstrates the development of the wave absorption resulted with increasing number of layers of fibrous media in configurations 1 till 4 for the two tested wave periods. As the number of layers increases, the value of wave absorption increases respectively for both waves. For the shorter wave with period of 1.25 s an immediate reduction of the reflection to 82% could be achieved with only one layer of blue mat, which had a thickness of 3.8 cm. For the longer wave

with a period of 1.5 s and a wave length of 2.99 m, the same configuration of the absorbing media resulted in a wave reflection coefficient of approx. 87%.

The configuration 2 decreased the wave reflection to 74% and 82% for the shorter and longer wave, respectively. Based on these results the reflection reduction given by a black Matala® sheet with a thickness of 3.8 cm can be estimated to be approx. 8% and 5% for the waves with wave period of 1.25 and 1.50, respectively.

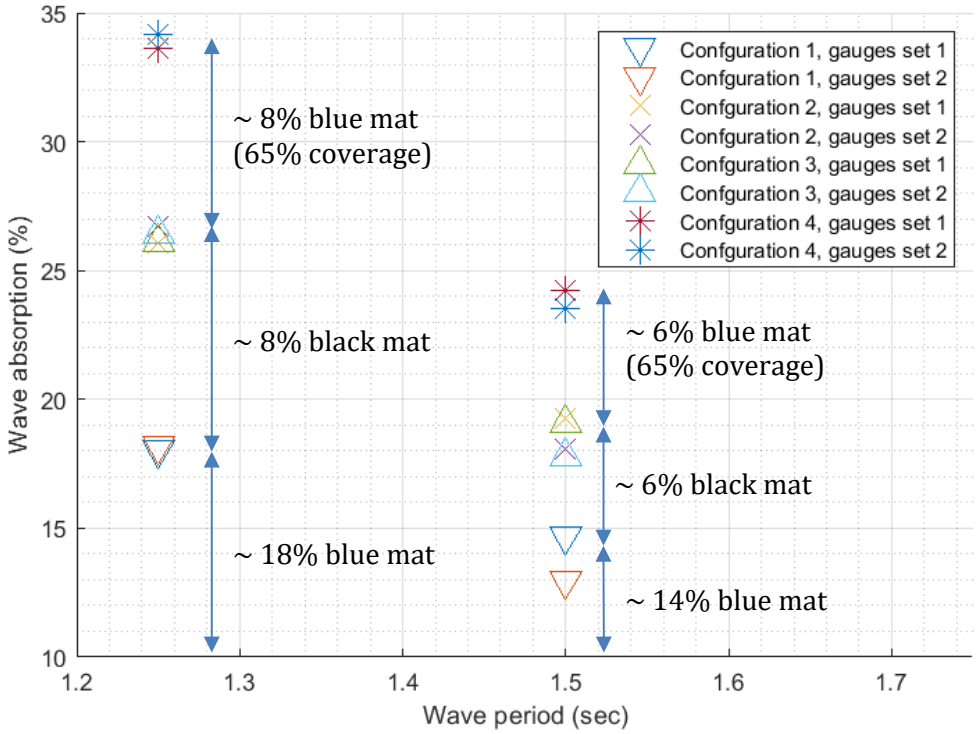

Figure 97: Plot showing the values of wave absorption achieved with different wave absorber configurations in 2 wave conditions

The results of configuration 3 showed that adding a gap of 4 cm between the sheets of the wave absorbing media had absolutely no effect on the wave reflection. This finding goes against the outcome of previous studies investigating vertical wave absorbers made of perforated steel sheets or mesh screens, where spacing between the screens contributed to wave absorbing properties significantly (Fritz, 2002; Hughes, 1993). This can be an indicator that the wave absorbing material described in this study has a different working principle as it has a value of porosity much greater than that of a perforated steel sheet, e.g. Dissipation of wave energy occurs here rather due to creation of turbulences as well as by means of friction provided by a high specific surface area per unit volume. A gap between layers of media does not contribute to any of these processes and therefore does not change the wave absorbing properties.

In the configuration 4 we added another layer of fine blue Matala®, which resulted in wave reflection dropping to 66% and 76% for the shorter and longer wave, respectively. However, as mentioned earlier the second layer of the fine blue media could only be installed partially,

covering approx. 65% of the submerged screen area. The wave absorption increased by 8% for shorter waves and by 6% for longer waves. Based on these results, a coefficient of wave absorption for a single layer of the fine blue material was increased proportionally to the partial area coverage and estimated to be 13% for the waves with a wave period of 1.25 and 10% for the waves with a wave period of 1.50, taking also into account the results for configuration 1.

For the two types of waves studied, it can be clearly seen that the blue material provides a better result in terms of wave energy absorption. Since both the blue and black Matala® mats applied during the experiment have the same thickness of 3.8 cm, higher effectiveness can be explained by higher values of porosity and thinner fibres of the media. During the experiment we were able to observe that lower bending stiffness of fibres allowed them to bend and move with the water flow, which may be linked to the higher wave energy dissipation, analogue to how sand and sea weed dissipate wave energy along a coastal line, by giving water something to play with.

Application: design of wave absorbing elements.

Based on the performed experimental work, wave absorbing elements were designed for the purpose to reduce wave reflection inside the static liquefaction tank during the experiments on wave generation by submarine landslides. During these experiments waves of small amplitude of approx. 5 to 15 mm with wave length of up to 3 m were expected. The water depth for different tests could vary between 0.4 and 1.2 m.

As earlier mentioned, the blue Matala® filter media showed a better effect of reduction of wave reflection. The results suggested that material properties such as high porosity and thin fibre thickness had a positive influence on ability of material to absorb waves. Based on this conclusion, another material was chosen for the final wave absorber design, as this material provided even better essential properties and therefore could be more suitable. Similarly to the Matala® mats, the chosen material in originally used in aquarium and aquaponic systems as a filter and is commercially available under the name Japanese filter mats.

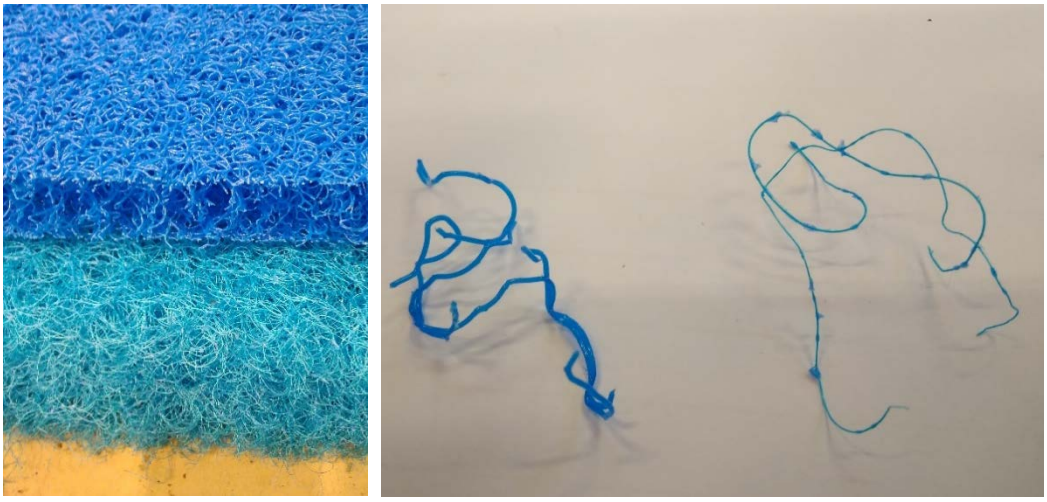

Figure 98: Blue filter media Matala® and Japanese filter mat (left); comparison of fibres: Matala® 0.55 ± 0.1 mm; Japanese filter 0.25 ± 0.1 mm (right).

Japanese filter has a fibrous texture, whereas fibres are thin and randomly connected, creating highly porous media. In comparison with the blue Matala® mat, the fibres are thinner and more flexible; within the mat the fibres are packed denser and connected less rigidly (Figure 98). Table 11 shows properties of two filter materials in comparison.

Table 11: Comparison of properties of Japanese filter mats and filter media Matala®

Material type	Fibre diameter [mm]	Free volume/ porosity [%]
Blue filter media Matala® Product code: FSM365/SM365	0.55 ± 0.1	94
Japanese filter mat	0.25 ± 0.1	97.5

With an assumption that Japanese mats perform as wave absorbers at least as good as blue Matala® mats, the wave absorbing elements were designed based on the experimental results for blue Matala® mat. Furthermore, it was assumed that the wave absorbing effect increases linearly with increasing thickness of material. The design aim is defined as reduction of wave reflection to less than 10% (wave absorption > 90%).

As one layer of blue media with the thickness of 3.8 cm provides approx. 13% of wave absorption, to reach 90% of wave absorption at least 7 layers with a total thickness of 26.6 cm were required. The wave absorbing element was then made of 6 layers of Japanese filter mats with a thickness of 5 cm each. Thus, the total thickness of the wave absorber was 30 cm.

Figure 99: Final design of a wave absorbing element: 6 layers of Japanese filter with total thickness of 30 cm.

These wave absorbing elements were applied during experiments on wave generation by submarine landslides, conducted in the Geo-Engineering Laboratory of TU Delft using the static liquefaction tank (De Jager et al. 2017). Figure 100 shows the principle how the wave absorbers were installed inside the static liquefaction tank during the experiments.

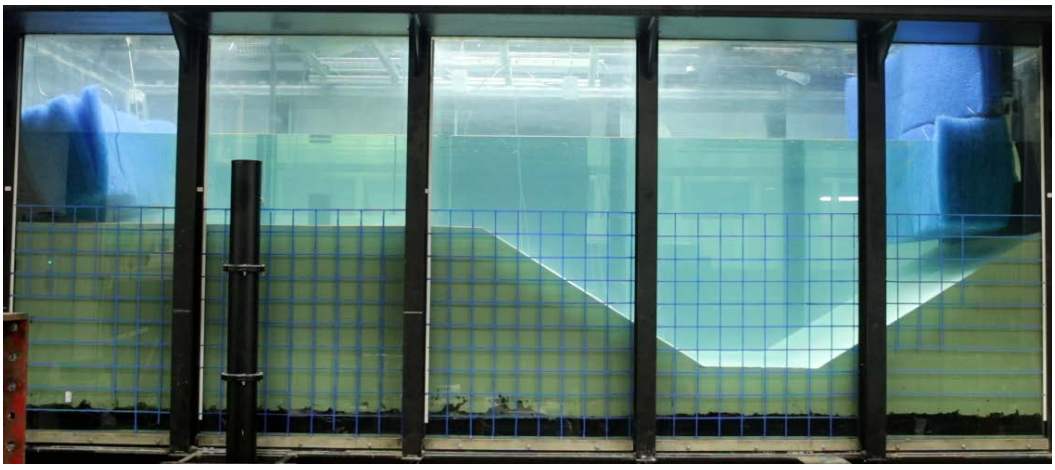

Figure 100: Wave absorber installed inside the static liquefaction tank.

Summary

The outcome of experimental investigations on vertical wave absorbers conducted in a wave flume was presented. The investigation was initiated within the scope of a study investigating wave generation by submarine landslides. Two types of fibrous PPC filter mats were suggested as absorbing material: the coarse black and fine blue filter media Matala®. The experiments were performed by installing the filter material on an impermeable vertical barrier and subjecting it to action of long waves. Two types of waves were investigated: with a period T of 1.25 s and 1.50 s. The wave length L was 2.27 m and 2.99 m, respectively. The water depth in the flume was kept constantly at 0.60 m. The wave reflection was measured with 4 wave gauges combined in two sets

of two gauges. Method proposed by Goda & Suzuki (1976) was applied to resolve incident and reflected waves and then calculate the reflection coefficient.

The experiment sequences were performed with increasing number of layers of the wave absorbing material in each sequence. The effect of an additional gap between two layers of absorbing material was tested as well. In total with 3 layers of absorbing material, two blue layers and one black with 3.8 cm thickness each, we were able to reduce wave reflection to 66% and 76% for the shorter and the longer wave, respectively. As anticipated the wave absorption of material decreases with an increasing wave period and wave length.

For the two types of waves investigated, it could be concluded that the blue material with thinner fibres and higher free volume exhibits higher absorption than that of the black one. Based on the test results, we were able to estimate wave absorbing properties of a 3.8 cm thick mat of blue Matala® to be approx. 13% and 10% for waves with period T of 1.25 s and 1.50 s, respectively. For the black Matala® these values are estimated as 8% and 6%. Furthermore, we found that there is no effect when a gap is added between two layers of wave absorber.

The results of laboratory experiments provided a starting point for a design of wave absorbing elements for the static liquefaction tank. These wave absorbers were designed and made of Japanese filter mats – a material different from the one tested but providing even more suitable geometrical properties such as fibre thickness and porosity. Observation of the behaviour of Matala® mats allowed the assumption that Japanese filter mats exhibit at least the level of wave absorption provided by the fine blue Matala®. Based on the test results, the wave absorbing elements were designed with 6 layers of Japanese filter mats with a total thickness of an absorbing element of 30 cm.

The purpose of these wave absorbers is to substantially reduce the wave reflection and to allow for a clearer wave envelop inside the static liquefaction tank during the submarine landslide experiments. The wave absorbers are considered to be sufficiently effective based on a qualitative evaluation of the wave amplitude and horizontal velocity time series obtained during the landslide experiments. This conclusion, however, cannot be extended to another wave environment or type of experiment. To provide an appropriate evidence that wave reflection is reduced by wave absorbers to less than 10%, further laboratory experiments in a wave flume are required. Furthermore, future work should include more various wave conditions to evaluate applicability of this type of wave absorbers for different wave lengths and periods. It will be also helpful to determine the dependency of the wave absorption on increasing width, increasing number of layers and variation of porosities within an absorber to be able to design a vertical wave absorbing element more precisely according to a required absorption level and a given wave condition.

Appendix B – Measurements Tests 1 – 4

Measurements wave gauges

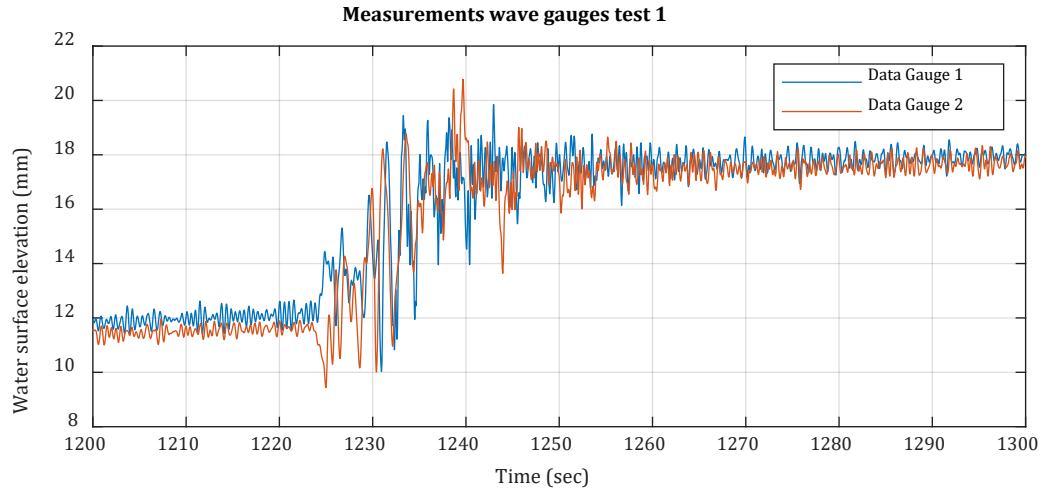

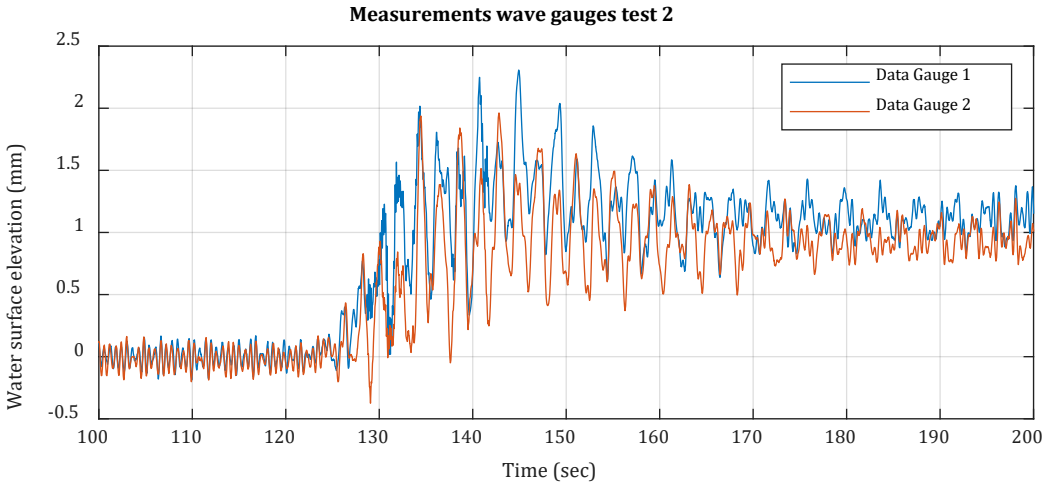

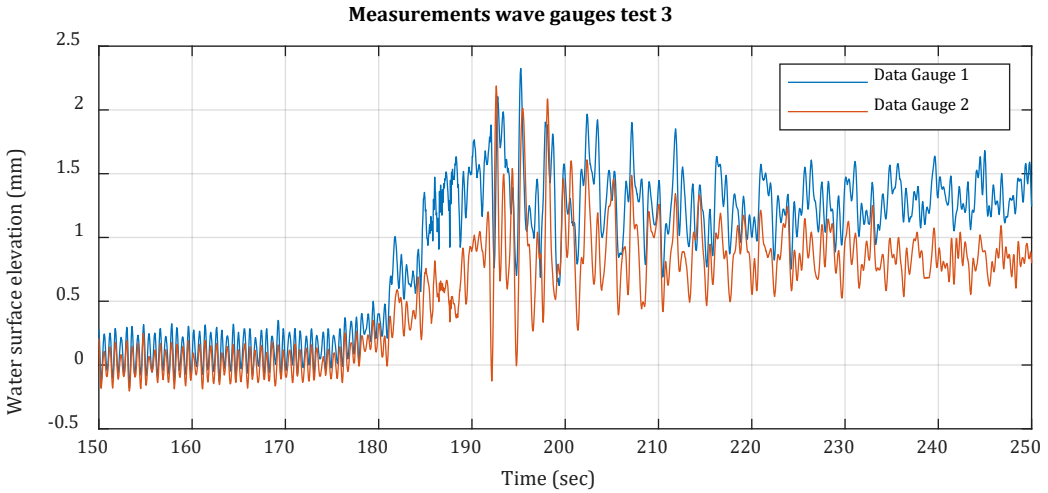

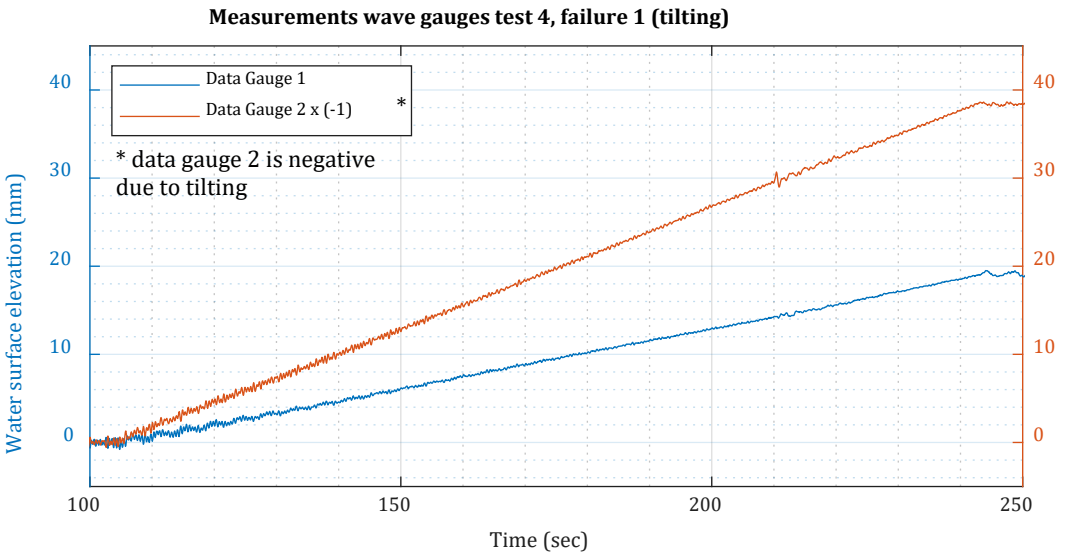
Measurements wave gauges test 4, failure 1 (tilting)
Data Gauge 1
Data Gauge 2 x (-1)
*
* data gauge 2 is negative due to tilting
Water surface elevation (mm)
Time (sec)

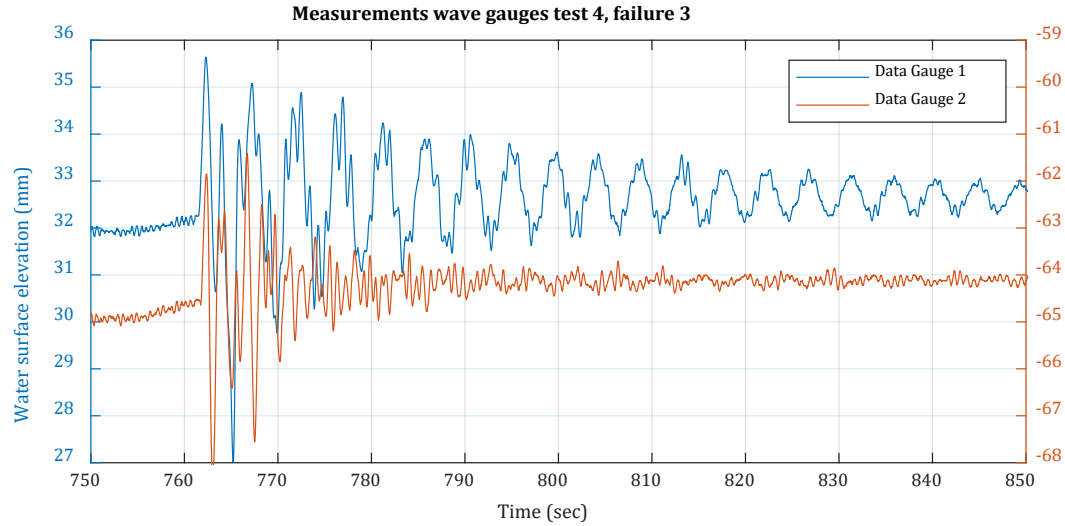
Measurements wave gauges test 4, failure 3
Data Gauge 1
Data Gauge 2
Water surface elevation (mm)
Time (sec)

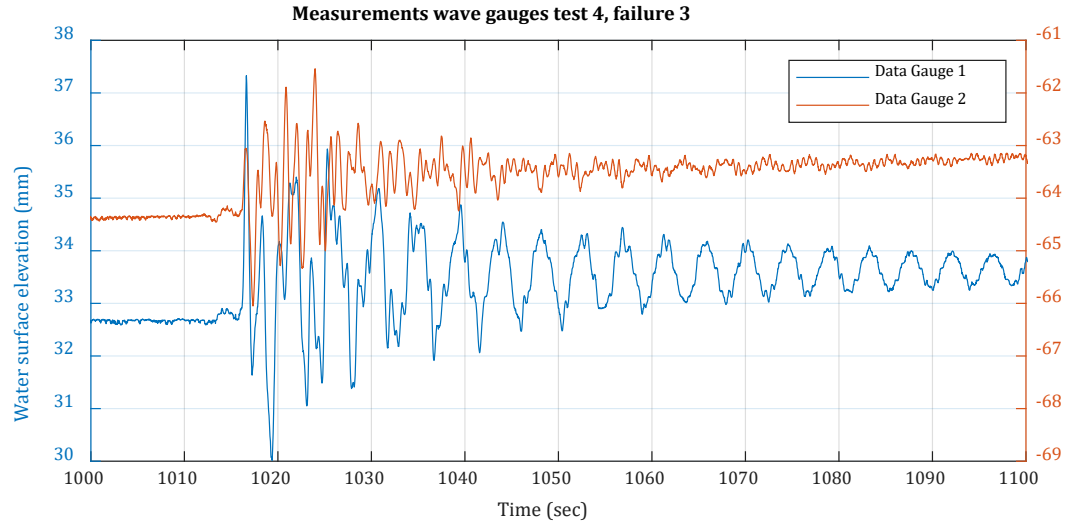
Measurements wave gauges test 4, failure 3
Data Gauge 1
Data Gauge 2
Water surface elevation (mm)
Time (sec)

EMS measured water particle velocity, horizontal along tank axis

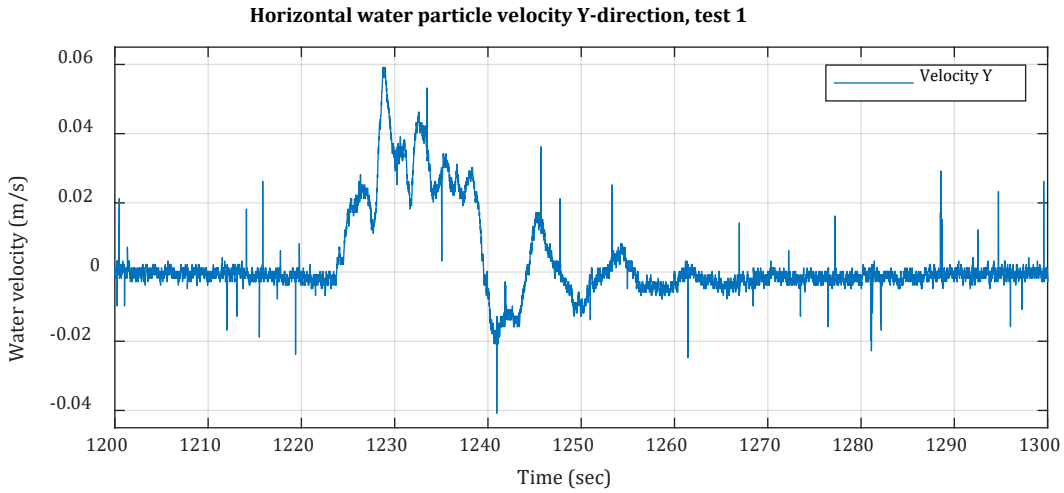

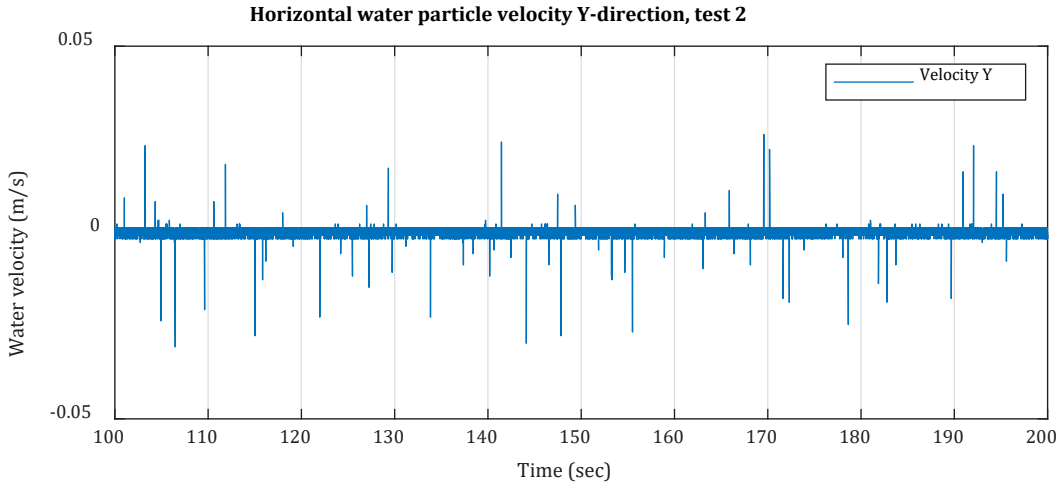

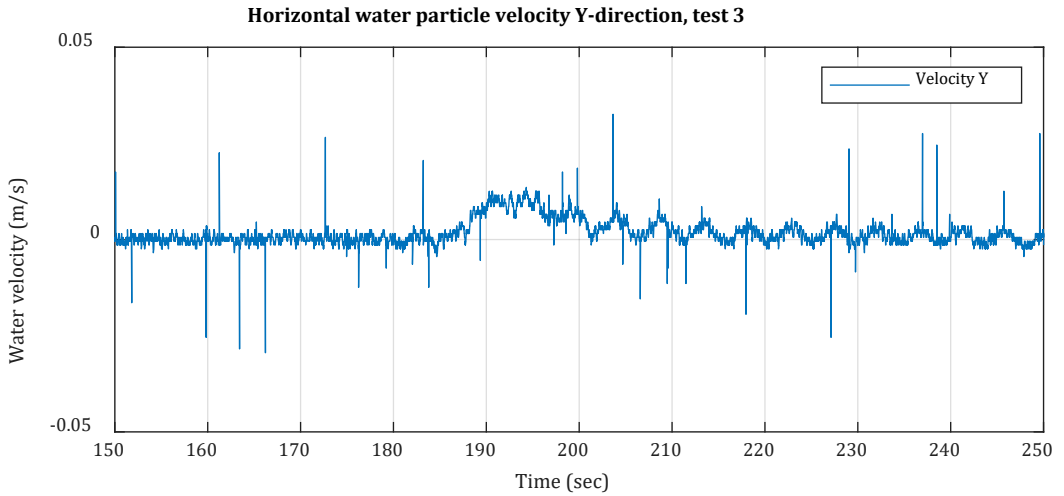

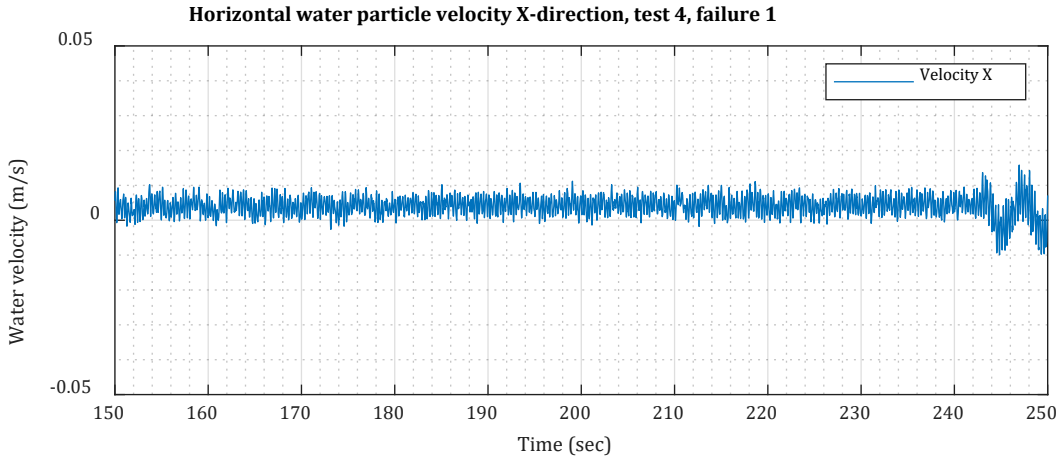
Horizontal water particle velocity X-direction, test 4, failure 1
Velocity X
Water velocity (m/s)
Time (sec)
0.05
0
-0.05
150
160
170
180
190
200
210
220
230
240
250

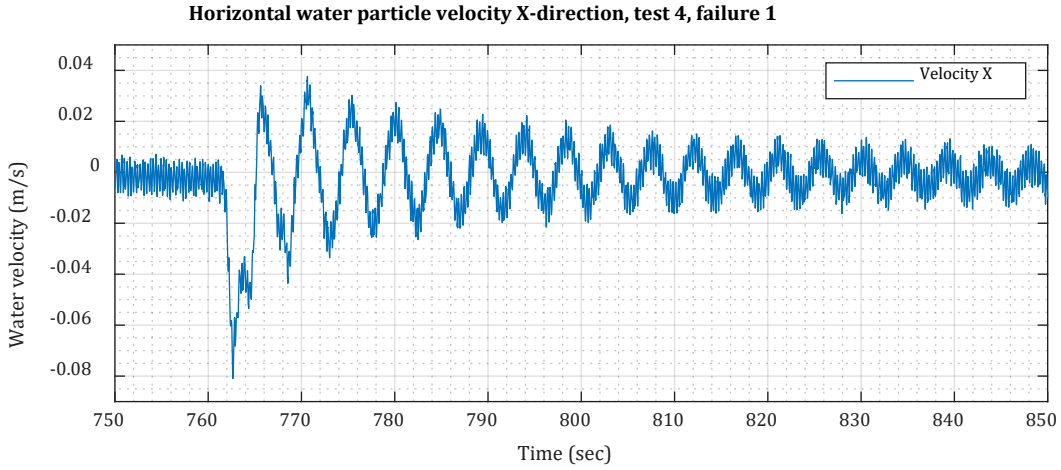
Horizontal water particle velocity X-direction, test 4, failure 1
Velocity X
Water velocity (m/s)
Time (sec)
0.04
0.02
0
-0.02
-0.04
-0.06
-0.08
750
760
770
780
790
800
810
820
830
840
850

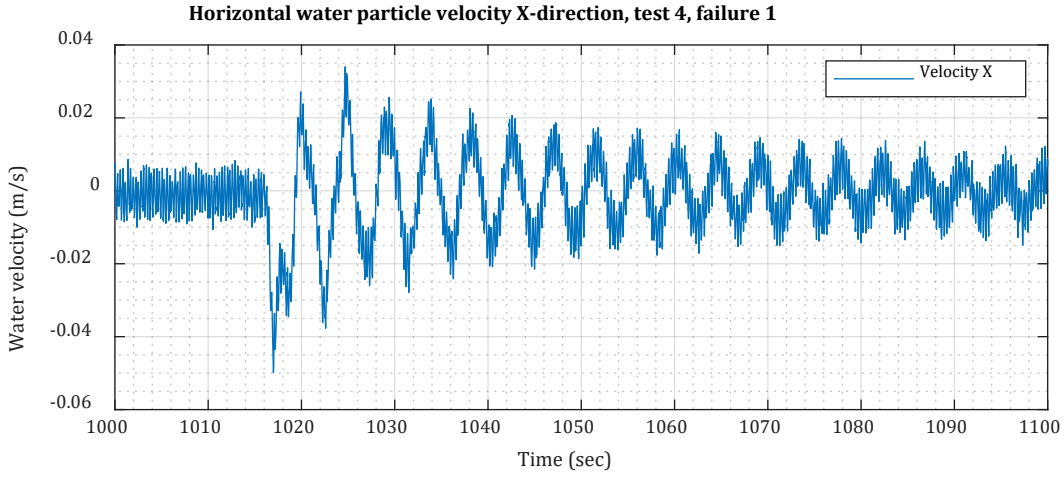
Horizontal water particle velocity X-direction, test 4, failure 1
Velocity X
Water velocity (m/s)
Time (sec)
0.04
0.02
0
-0.02
-0.04
-0.06
1000
1010
1020
1030
1040
1050
1060
1070
1080
1090
1100

Accelerations mobile sensors

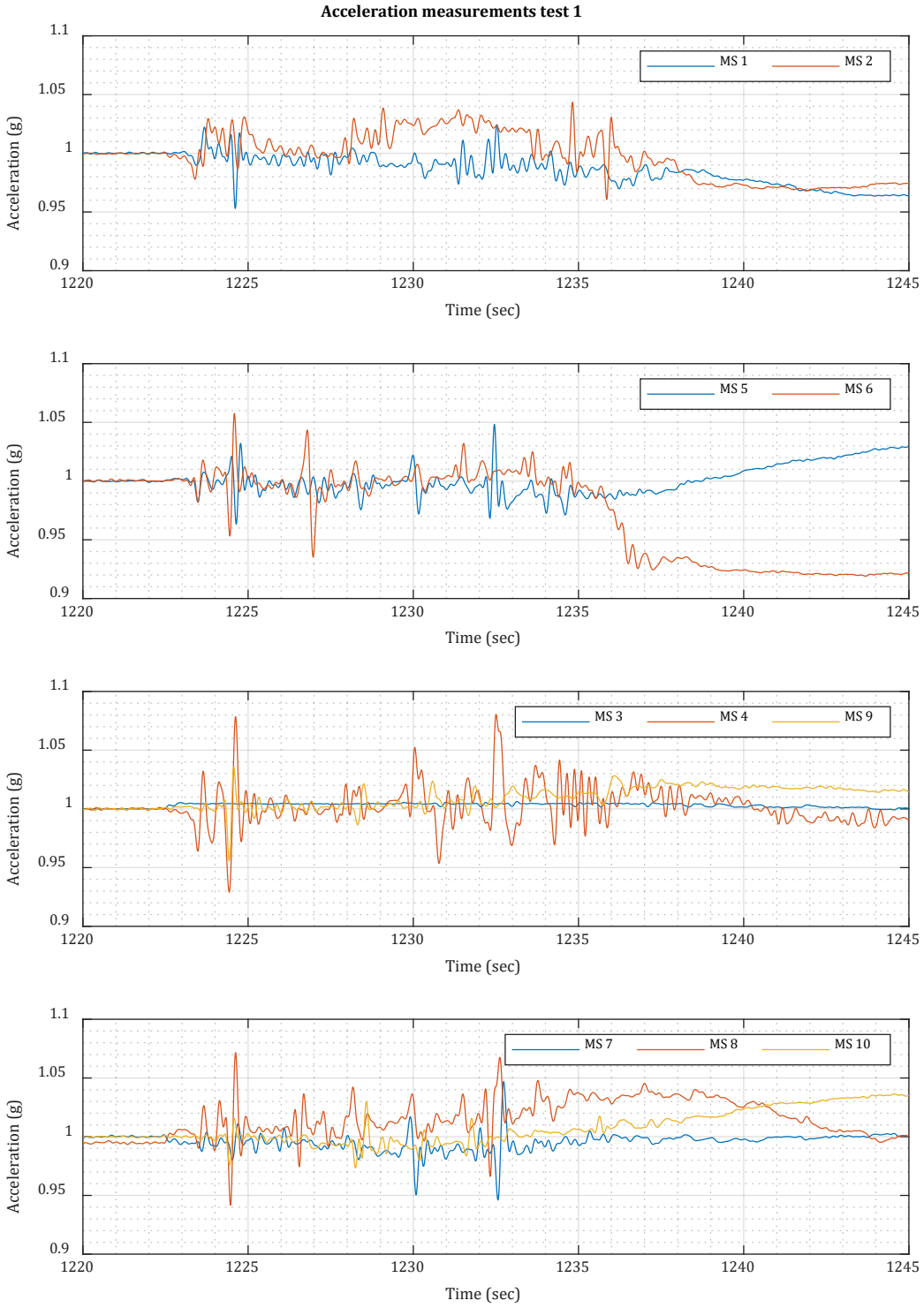

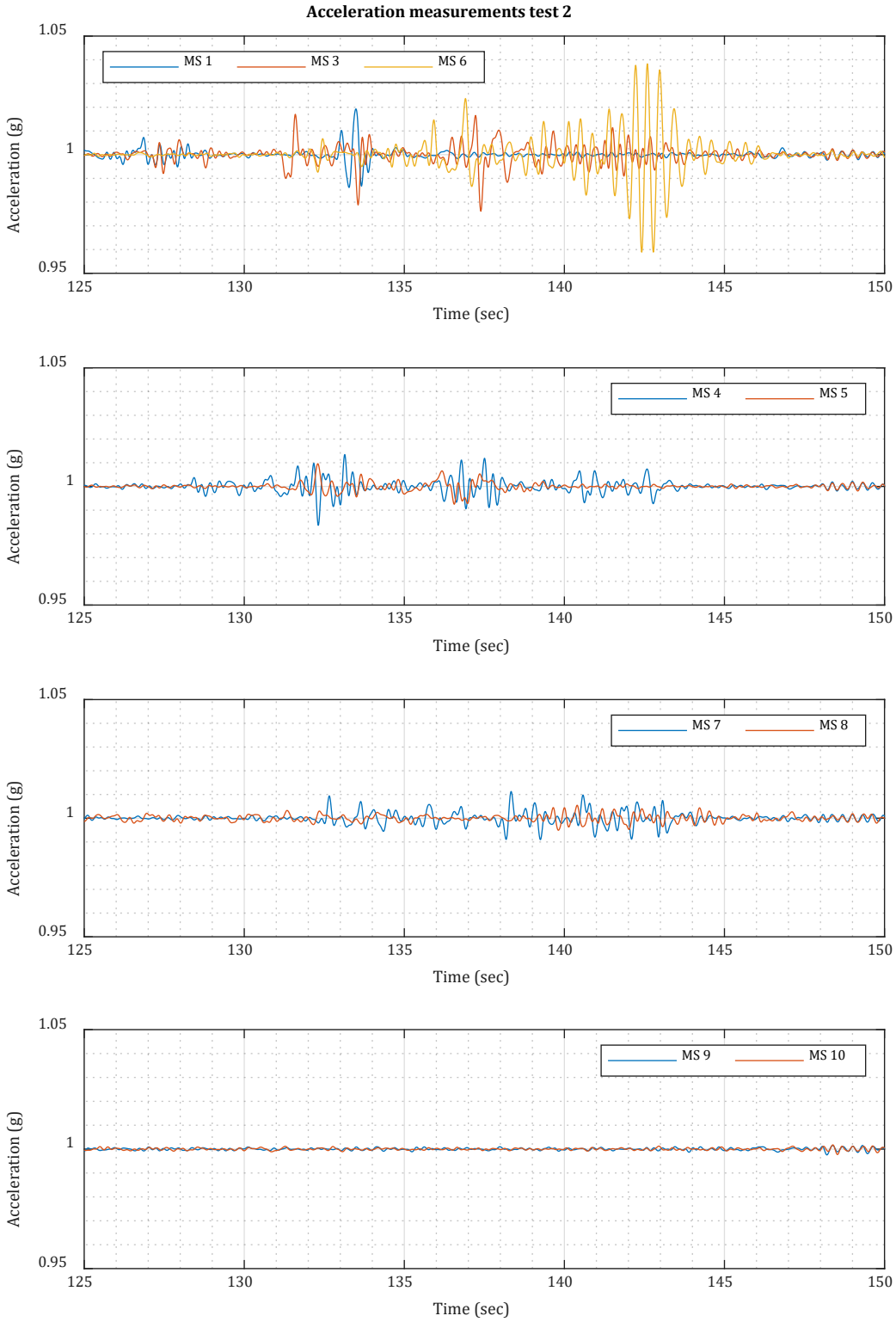
Acceleration measurements test 2
MS 1
MS 3
MS 6
MS 4
MS 5
MS 7
MS 8
MS 9
MS 10
Acceleration (g)
Time (sec)
1.05
1
0.95
125
130
135
140
145
150

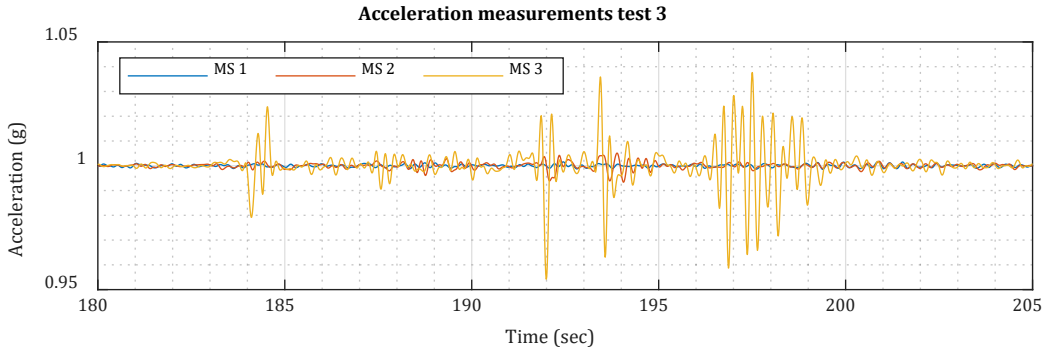
Acceleration measurements test 3
MS 1
MS 2
MS 3
Acceleration (g)
Time (sec)

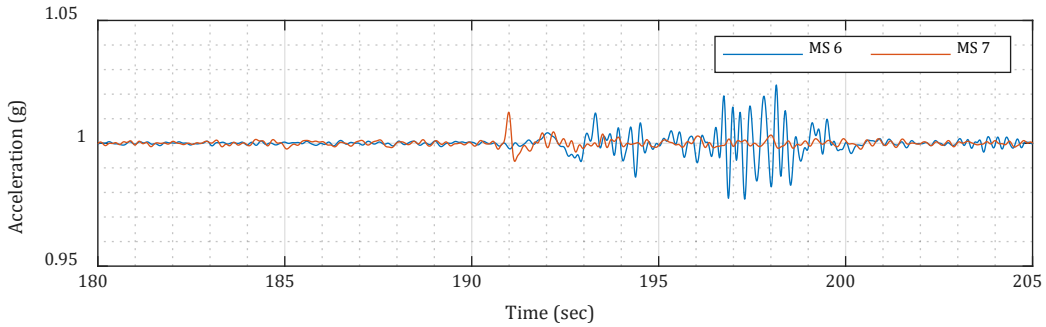
MS 6
MS 7
Acceleration (g)
Time (sec)

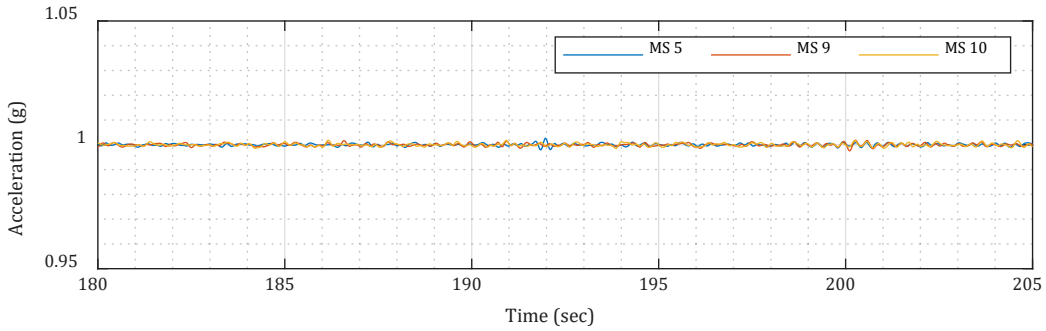
MS 5
MS 9
MS 10
Acceleration (g)
Time (sec)

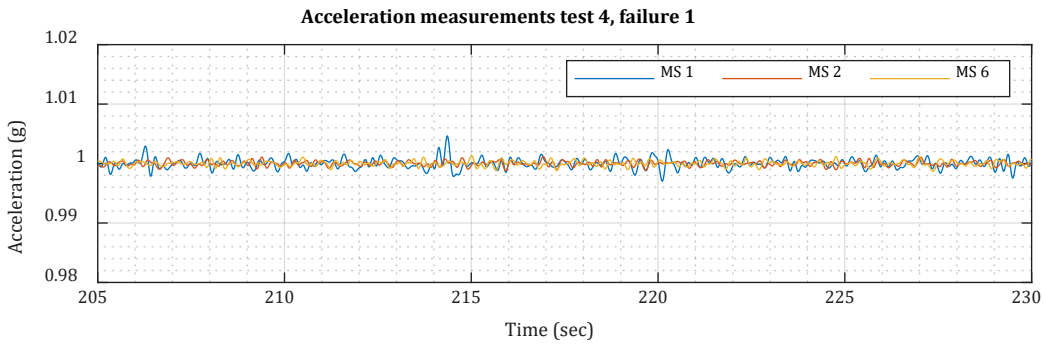
Acceleration measurements test 4, failure 1
MS 1
MS 2
MS 6
Acceleration (g)
Time (sec)

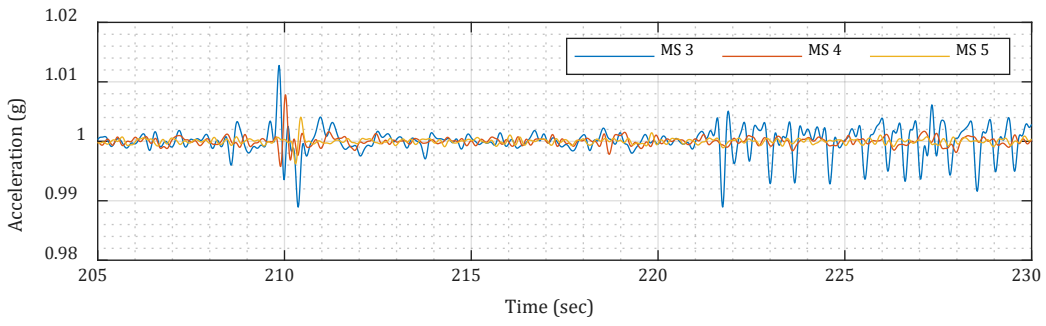
MS 3
MS 4
MS 5
Acceleration (g)
Time (sec)

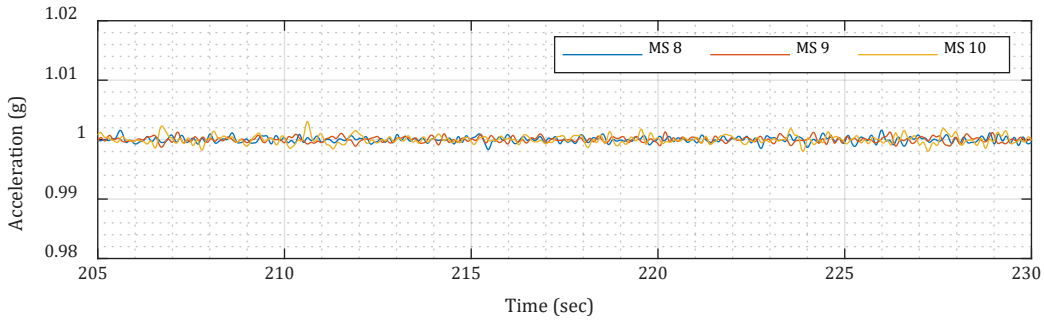
1.02
1.01
1
0.99
0.98
Acceleration (g)
205
210
215
220
225
230
Time (sec)
MS 8
MS 9
MS 10

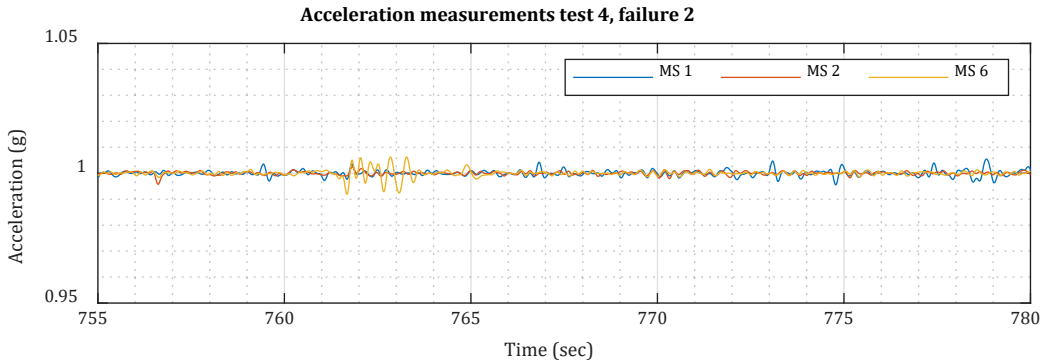
Acceleration measurements test 4, failure 2
1.05
1
0.95
Acceleration (g)
755
760
765
770
775
780
Time (sec)
MS 1
MS 2
MS 6

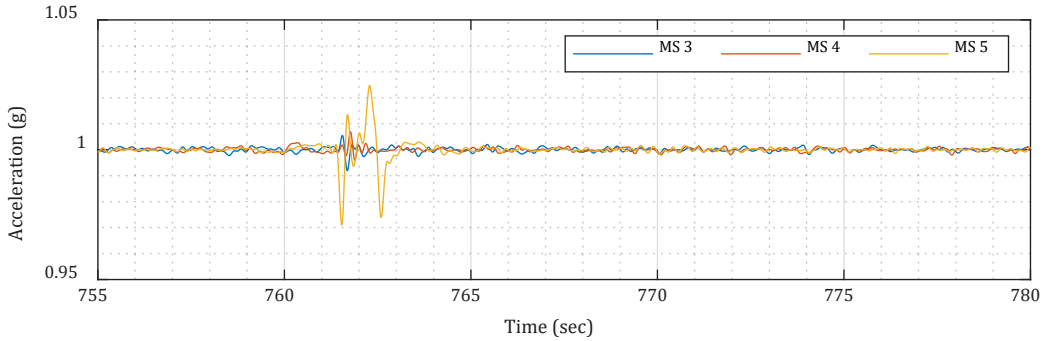
1.05
1
0.95
Acceleration (g)
755
760
765
770
775
780
Time (sec)
MS 3
MS 4
MS 5

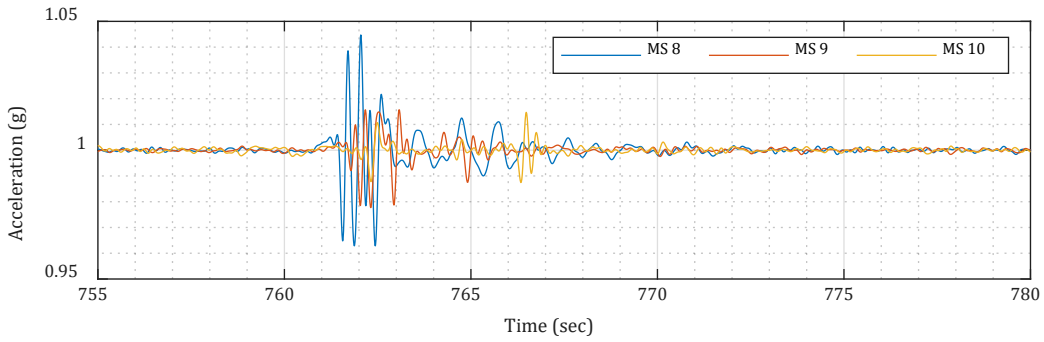
1.05
1
0.95
Acceleration (g)
755
760
765
770
775
780
Time (sec)
MS 8
MS 9
MS 10

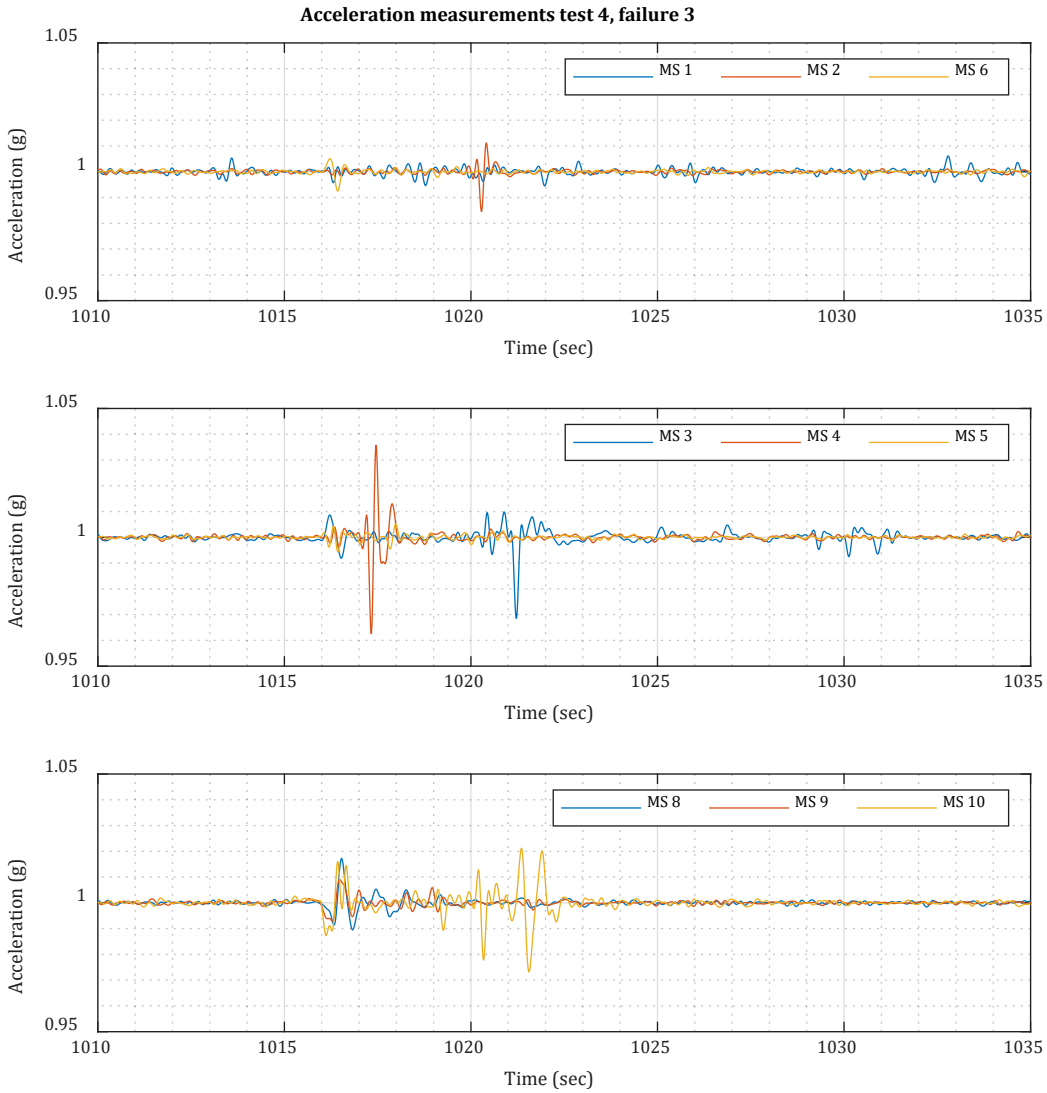
Acceleration measurements test 4, failure 3
MS 1
MS 2
MS 6
MS 3
MS 4
MS 5
MS 8
MS 9
MS 10
Acceleration (g)
Time (sec)
1.05
1
0.95
1010
1015
1020
1025
1030
1035

Pressure mobile sensors

Test 1: Pressure measurements by MSs 1-5

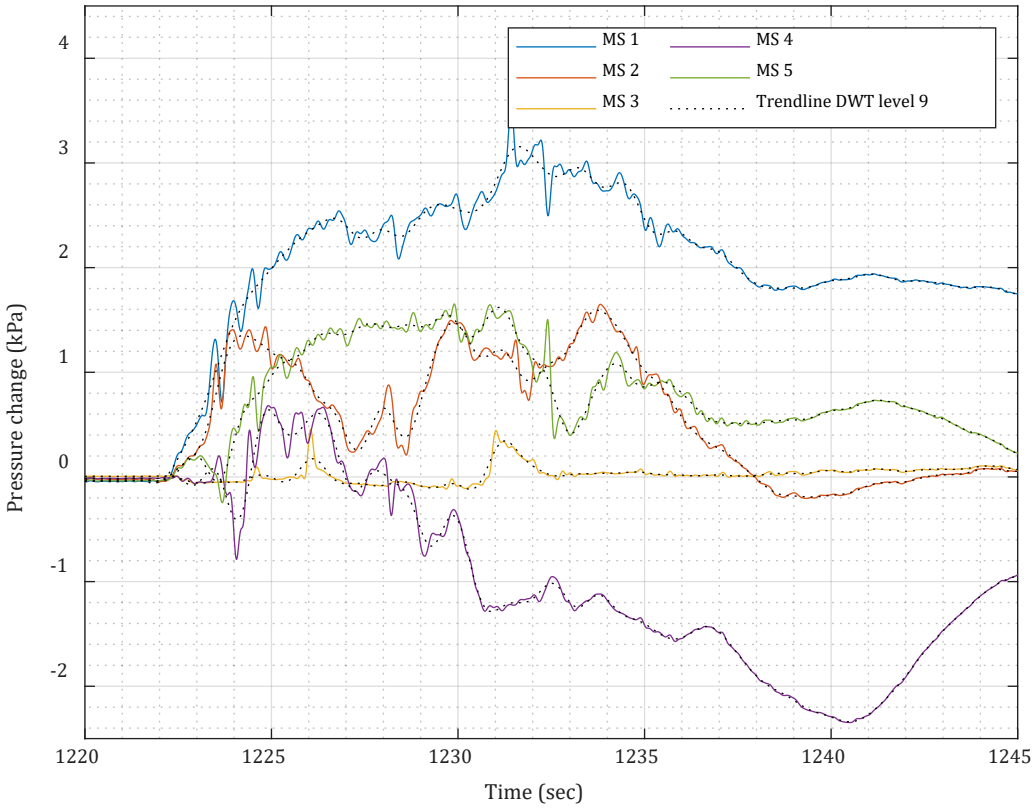

Test 1: Pressure measurements by MSs 6-10

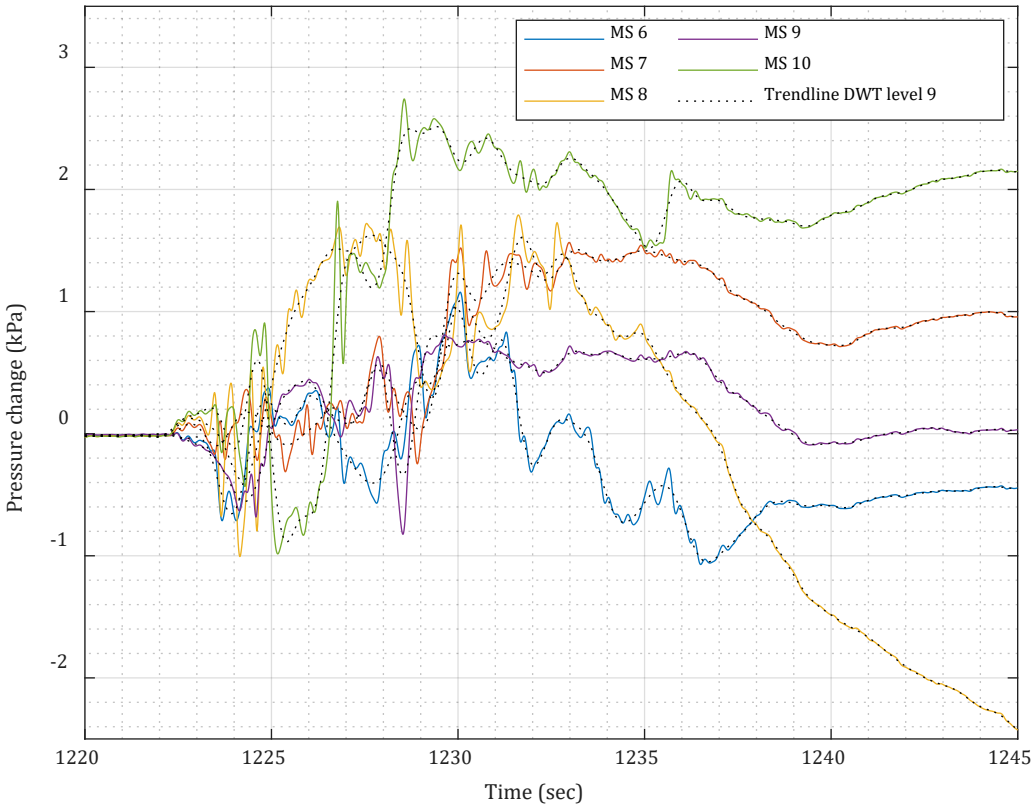

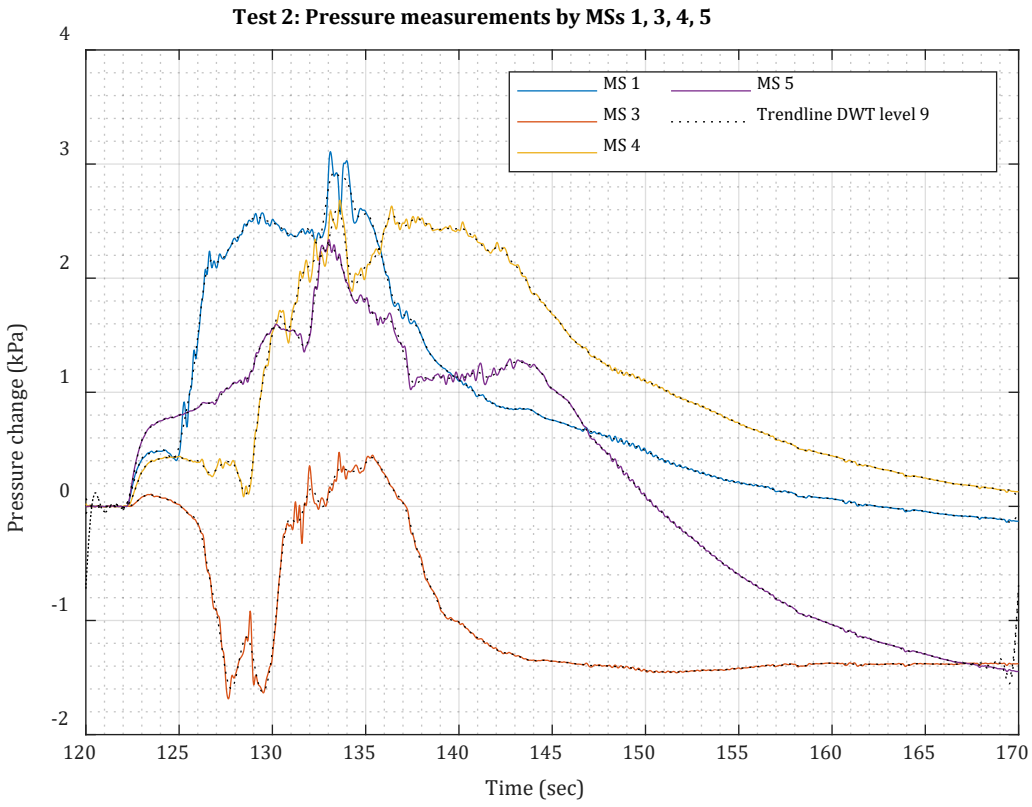
Test 2: Pressure measurements by MSs 1, 3, 4, 5
MS 1
MS 3
MS 4
MS 5
Trendline DWT level 9
Pressure change (kPa)
Time (sec)

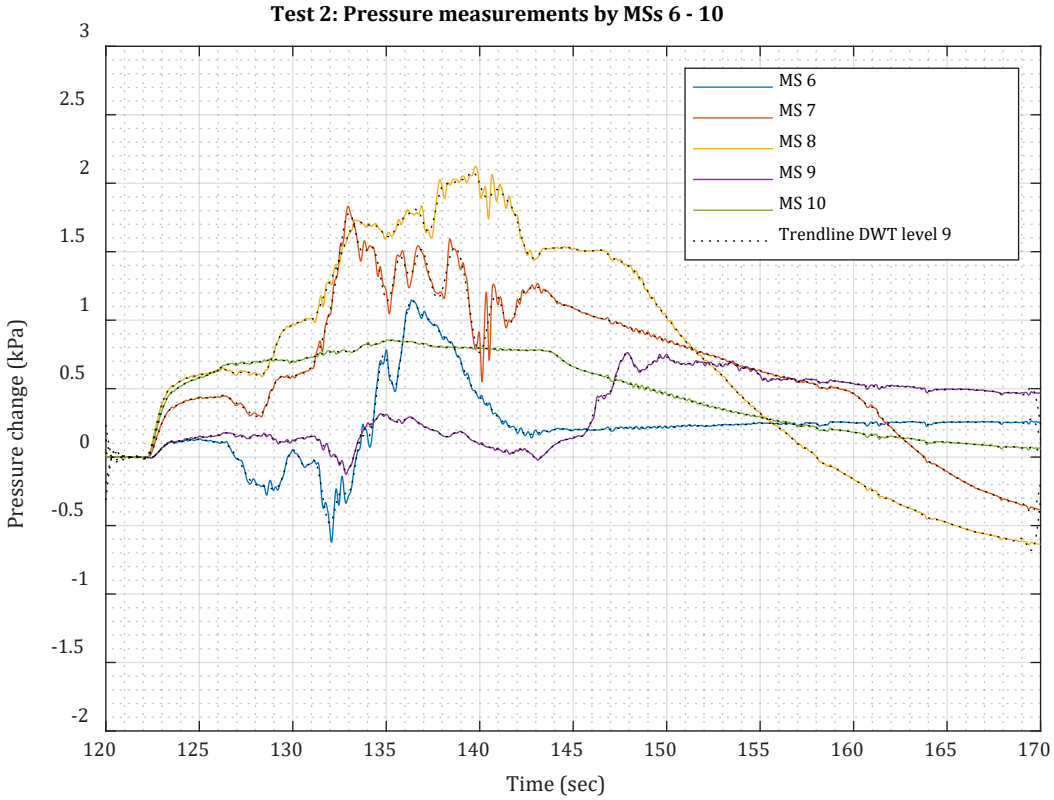
Test 2: Pressure measurements by MSs 6 - 10
MS 6
MS 7
MS 8
MS 9
MS 10
Trendline DWT level 9
Pressure change (kPa)
Time (sec)

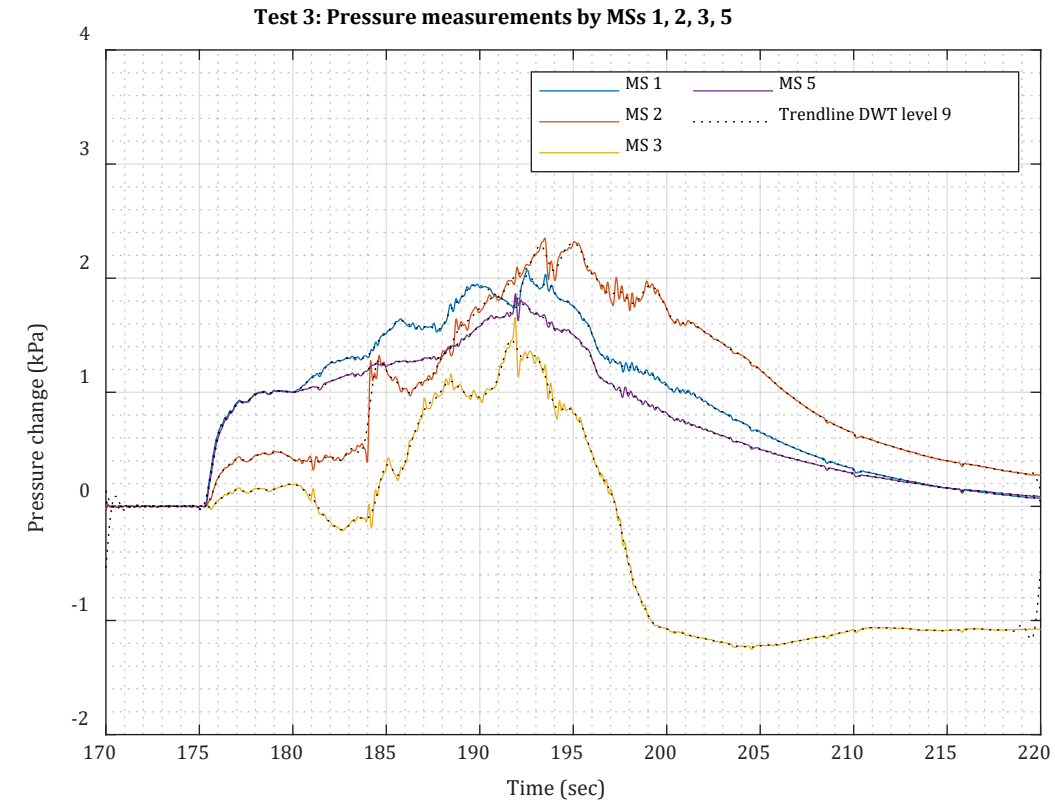
Test 3: Pressure measurements by MSs 1, 2, 3, 5
MS 1
MS 2
MS 3
MS 5
Trendline DWT level 9
Pressure change (kPa)
Time (sec)

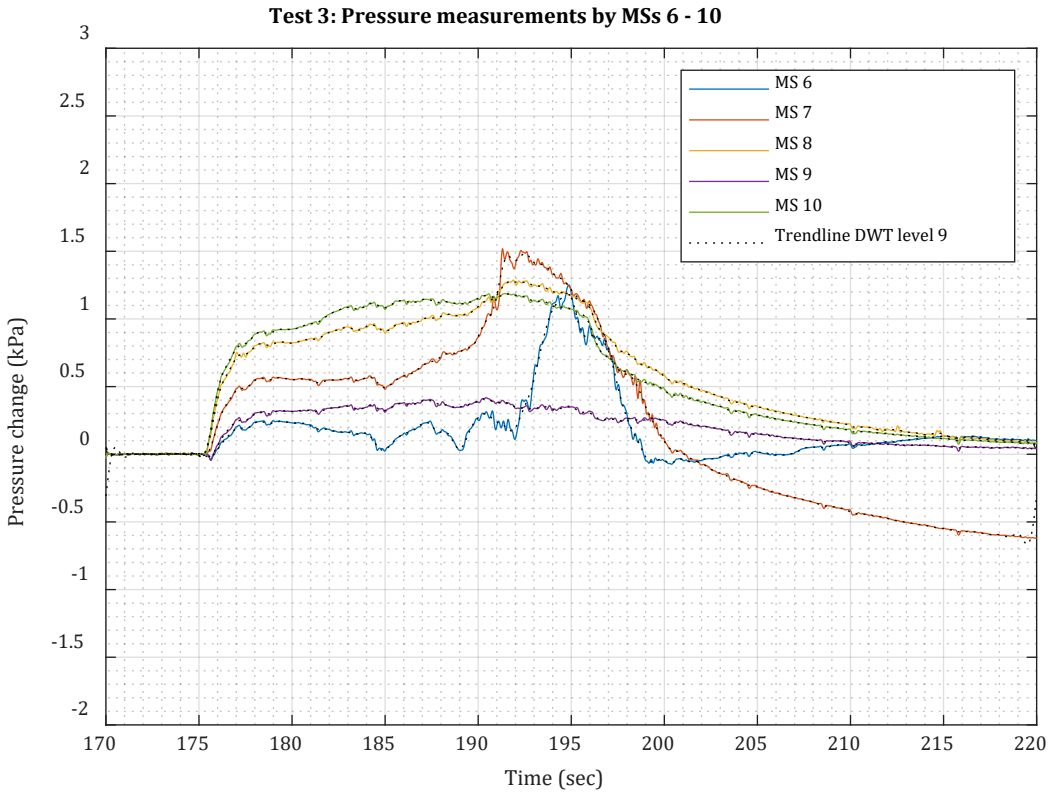
Test 3: Pressure measurements by MSs 6 - 10
MS 6
MS 7
MS 8
MS 9
MS 10
Trendline DWT level 9
Pressure change (kPa)
Time (sec)

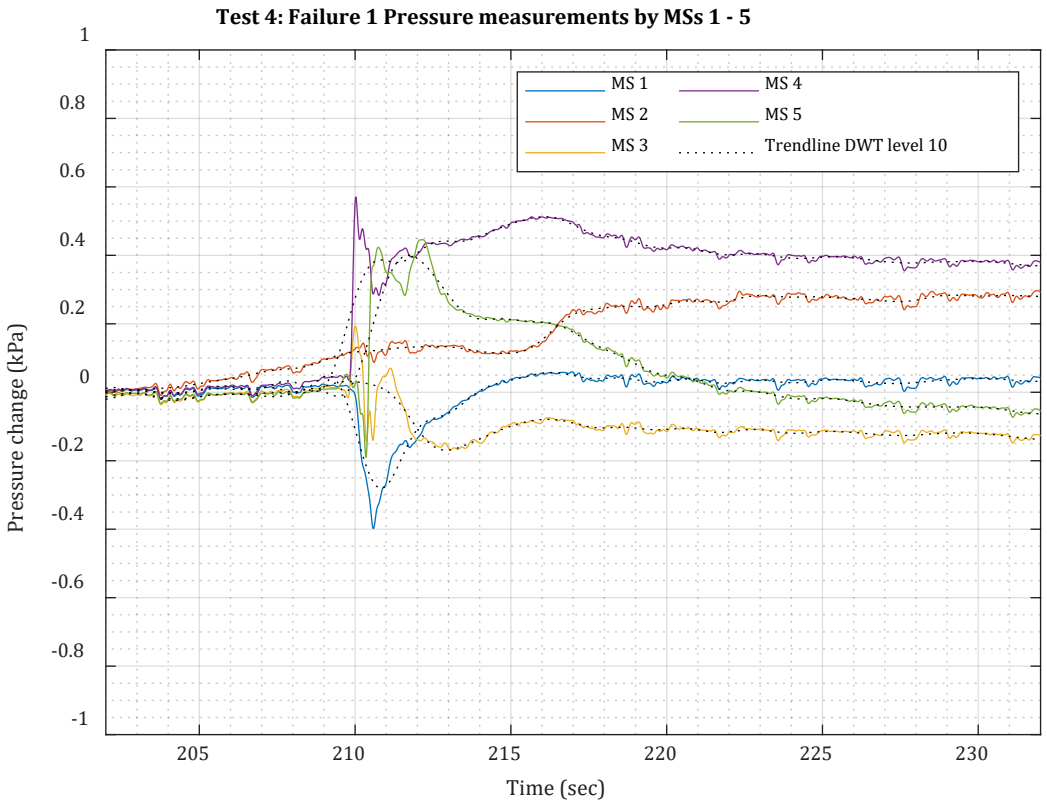
Test 4: Failure 1 Pressure measurements by MSs 1 - 5
MS 1
MS 2
MS 3
MS 4
MS 5
Trendline DWT level 10
Pressure change (kPa)
Time (sec)
1
0.8
0.6
0.4
0.2
0
-0.2
-0.4
-0.6
-0.8
-1
205
210
215
220
225
230

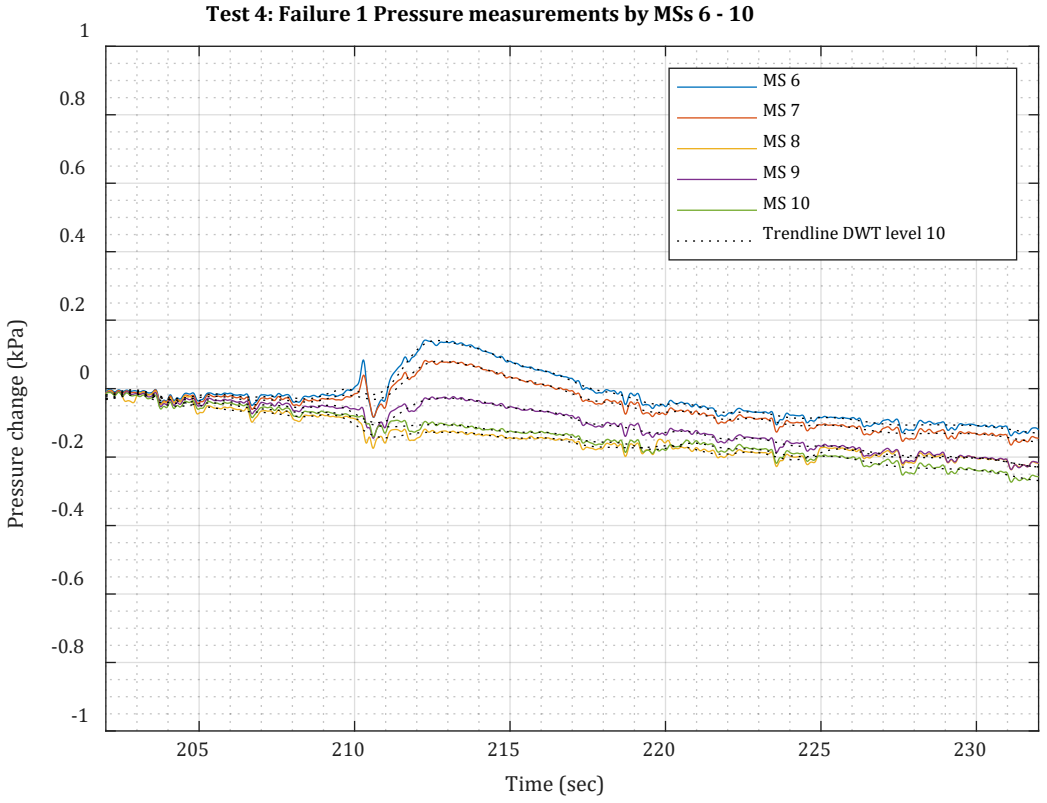
Test 4: Failure 1 Pressure measurements by MSs 6 - 10
MS 6
MS 7
MS 8
MS 9
MS 10
Trendline DWT level 10
Pressure change (kPa)
Time (sec)
1
0.8
0.6
0.4
0.2
0
-0.2
-0.4
-0.6
-0.8
-1
205
210
215
220
225
230

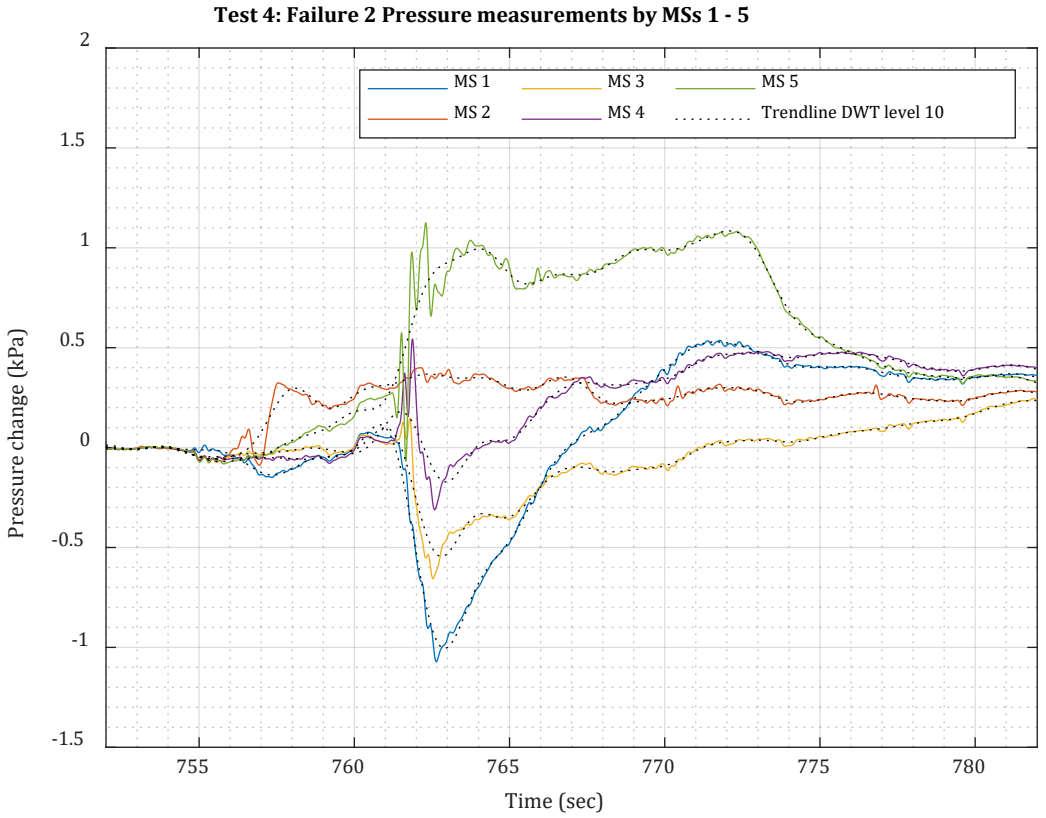
Test 4: Failure 2 Pressure measurements by MSs 1 - 5
MS 1
MS 2
MS 3
MS 4
MS 5
Trendline DWT level 10
Pressure change (kPa)
Time (sec)
2
1.5
1
0.5
0
-0.5
-1
-1.5
755
760
765
770
775
780

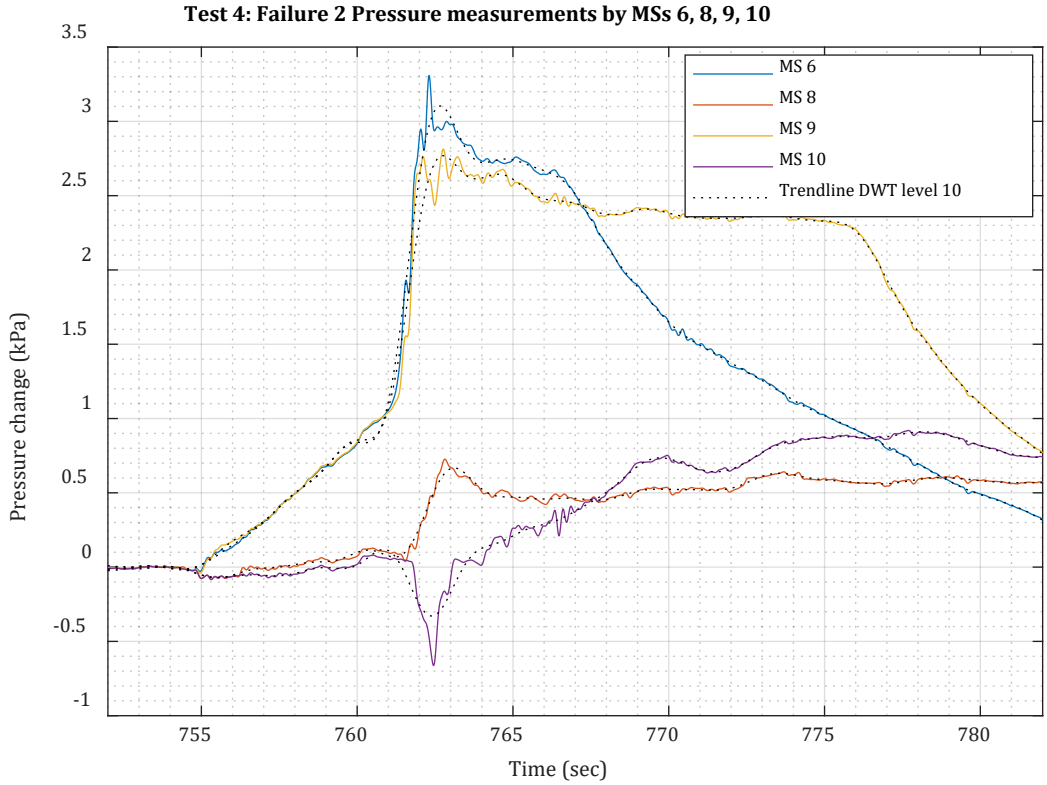
Test 4: Failure 2 Pressure measurements by MSs 6, 8, 9, 10
MS 6
MS 8
MS 9
MS 10
Trendline DWT level 10
Pressure change (kPa)
Time (sec)
3.5
3
2.5
2
1.5
1
0.5
0
-0.5
-1
755
760
765
770
775
780

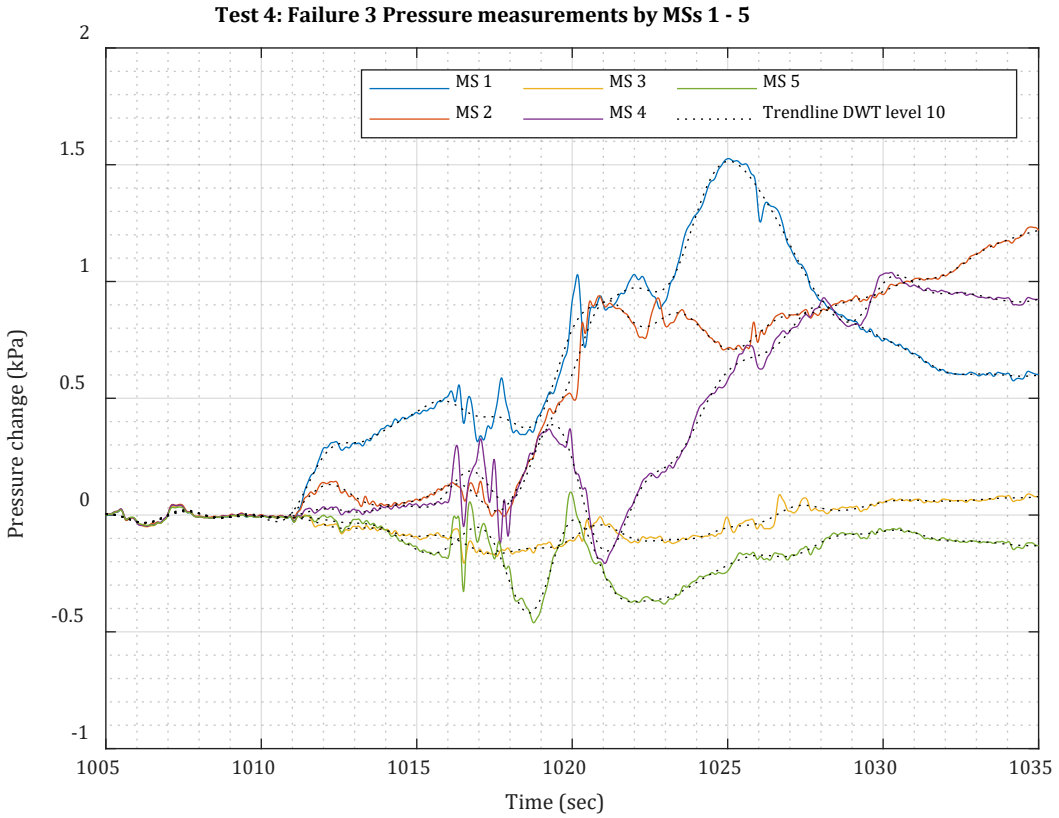
Test 4: Failure 3 Pressure measurements by MSs 1 - 5
MS 1
MS 2
MS 3
MS 4
MS 5
Trendline DWT level 10
Pressure change (kPa)
Time (sec)
2
1.5
1
0.5
0
-0.5
-1
1005
1010
1015
1020
1025
1030
1035

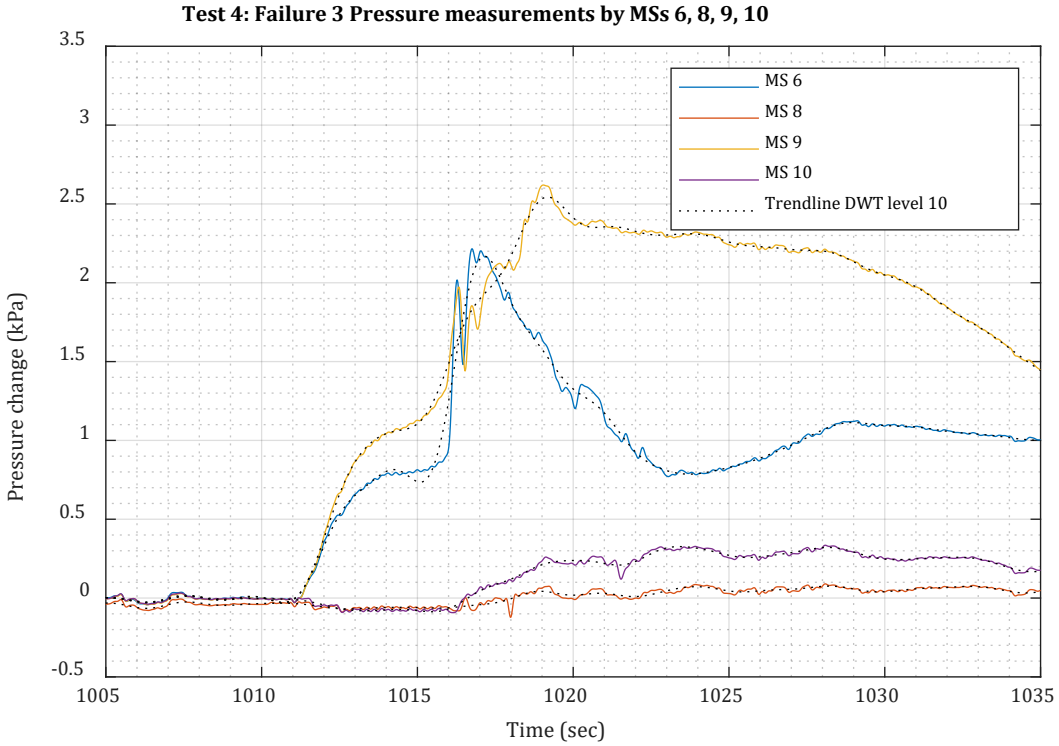
Test 4: Failure 3 Pressure measurements by MSs 6, 8, 9, 10
MS 6
MS 8
MS 9
MS 10
Trendline DWT level 10
Pressure change (kPa)
Time (sec)
3.5
3
2.5
2
1.5
1
0.5
0
-0.5
1005
1010
1015
1020
1025
1030
1035

Pressure measurements wall sensors

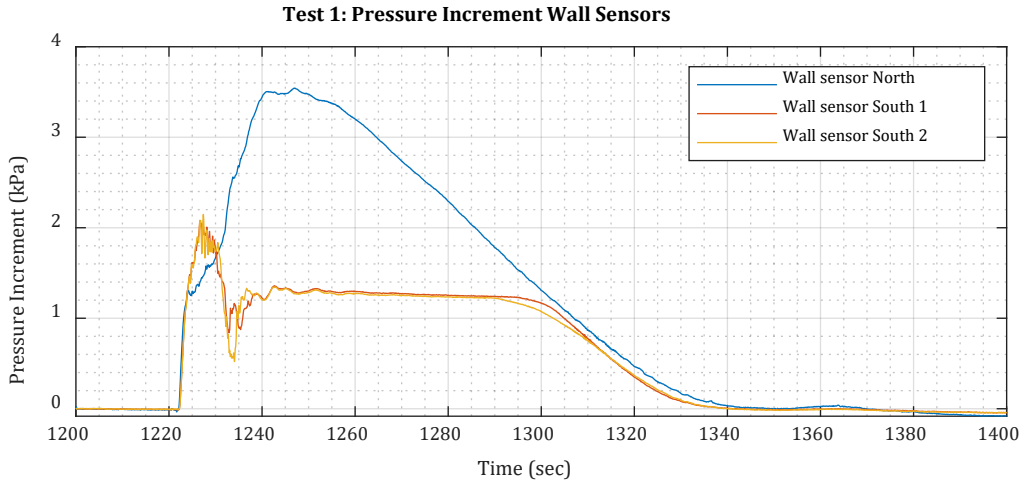

(No pressure oscillations after failure, all waves are damped by wave absorbers)

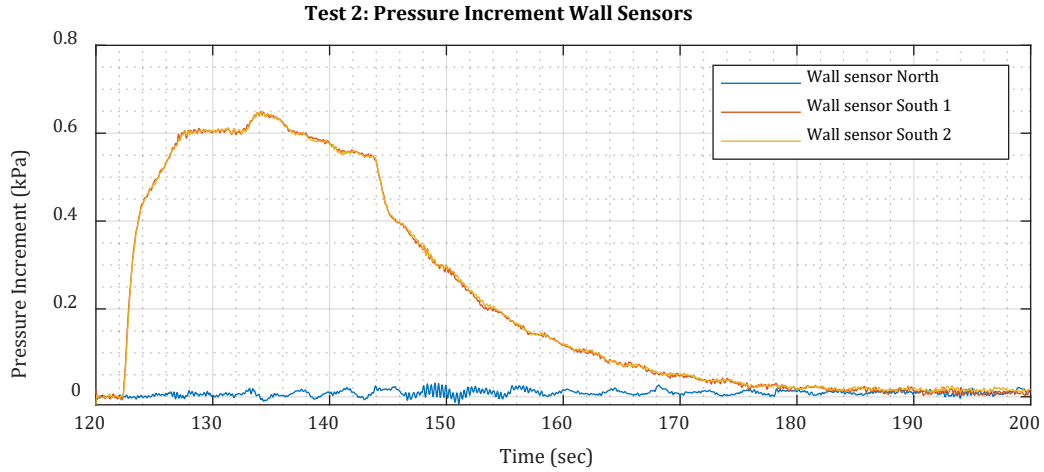

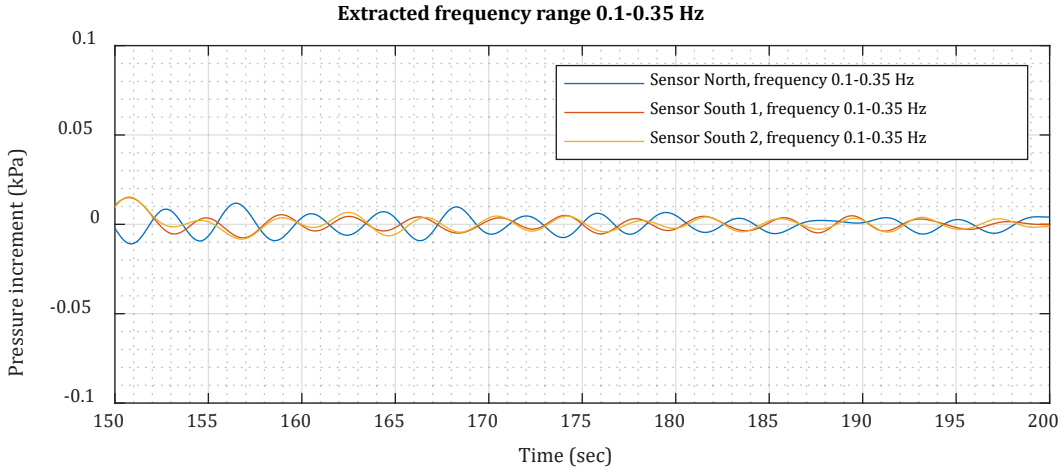

Only negligibly small pressure oscillations $\Delta p \leq \pm 0.01$ kPa

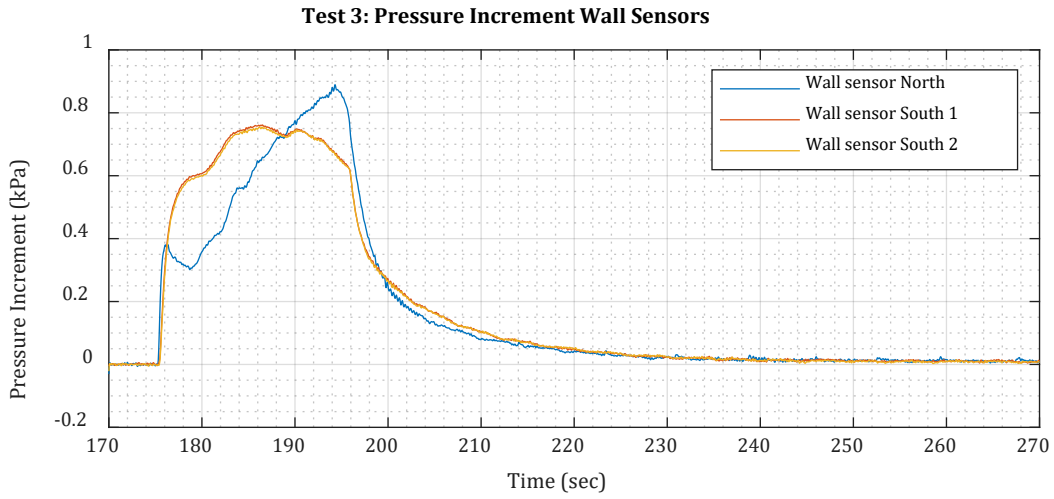

(No pressure oscillations after failure)

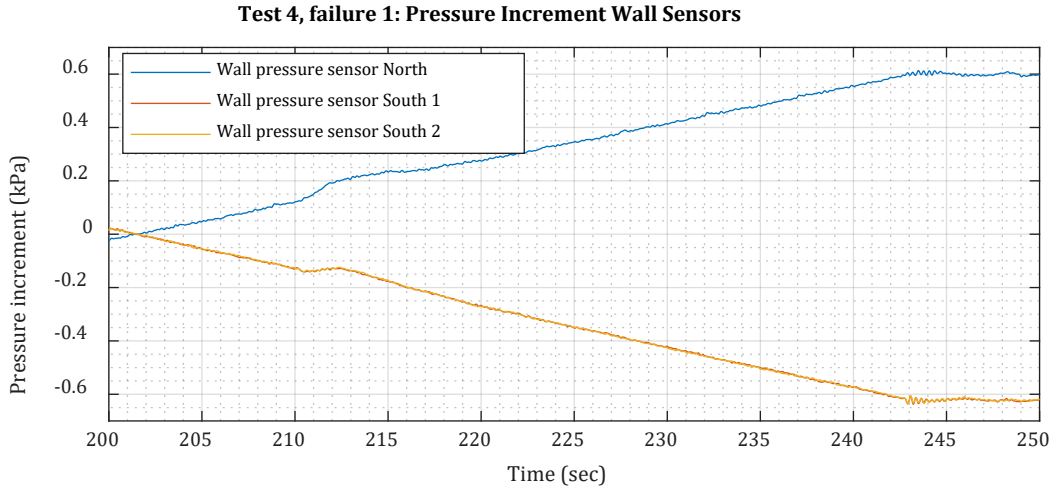

(No pressure oscillations after failure)

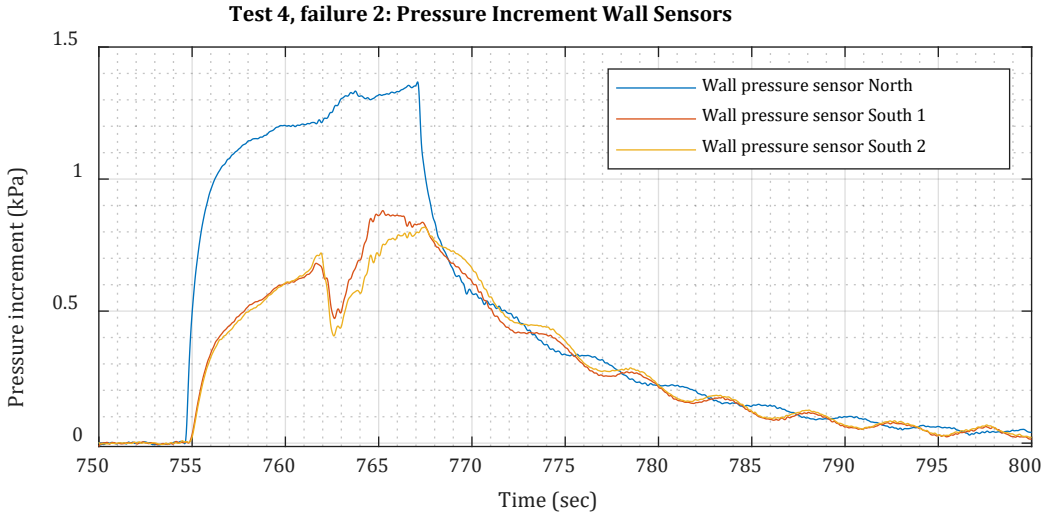

Extracted frequency range 0.15-0.35 Hz

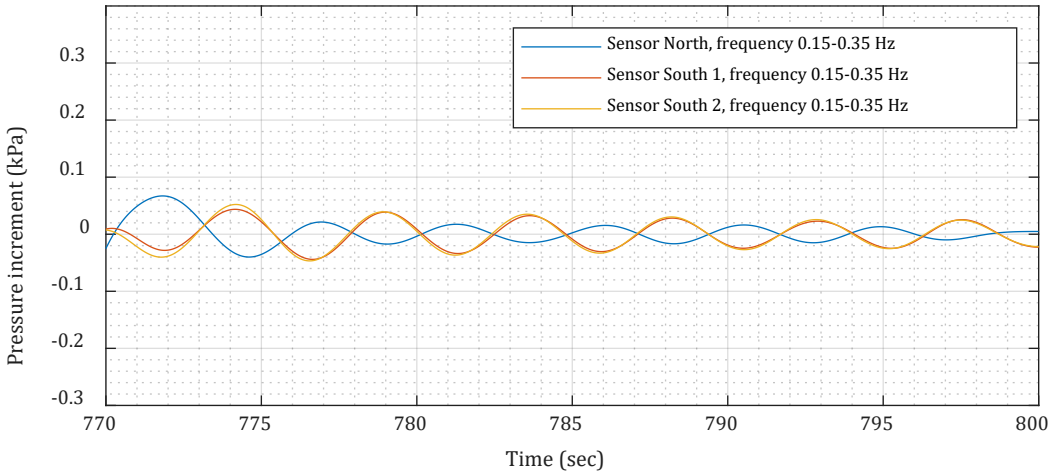

Test 4, failure 3: Pressure Increment Wall Sensors

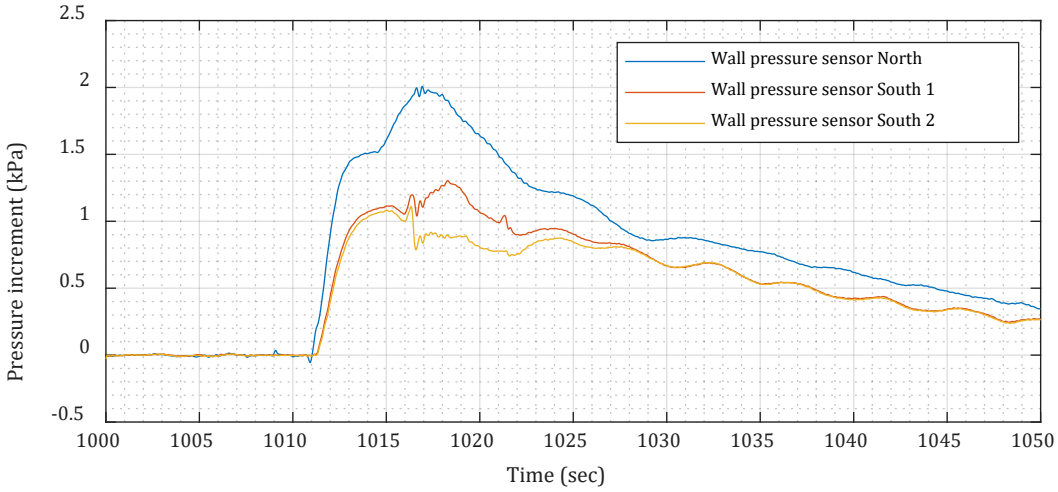

Extracted frequency range 0.15-0.35 Hz

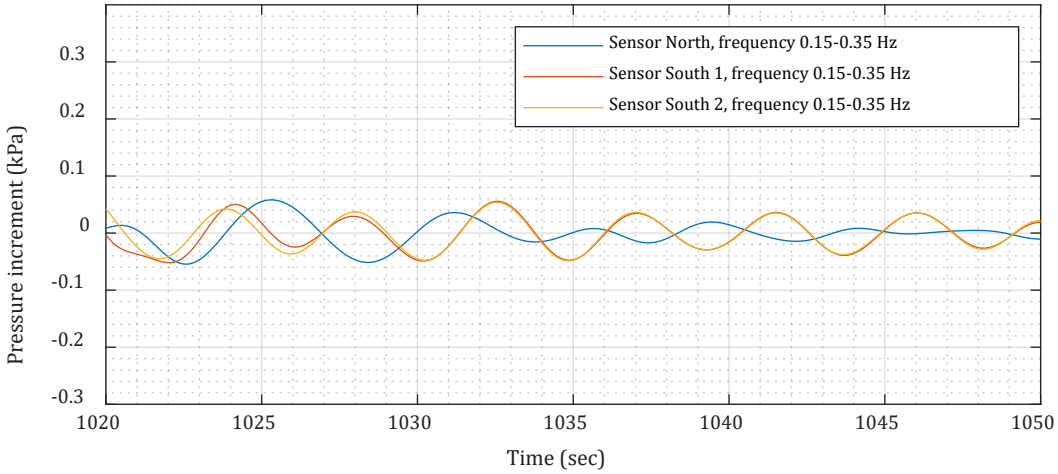

Appendix C – Validation of predictive formulae, calculation sheets

Test 1, Slope failure geometry

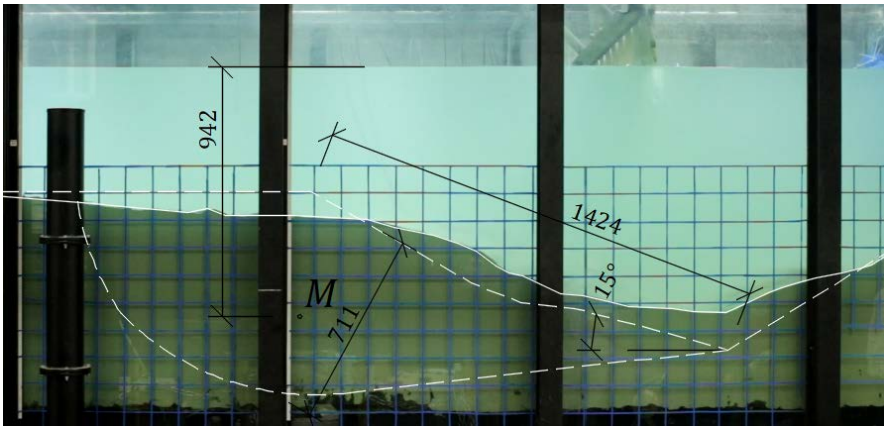

Input parameters								
Slide length L	=	1,42	[m]					
Slide width w	=	2	[m]					
Slide thickness T	=	0,711	[m]					
Initial submergence d	=	0,942	[m]					
SMF bulk density rhol	=	1,897	[kg/m^3]					
Density water	=	1	[kg/m^3]					
Slope angle theta	=	15	[°]					
Friction angle	=	0	[°]					
Coefficients				**Relative parameters**				
basal Coulomb friction Cn	=	0,25045		relative SMF density rhol/rhow	=	1,90	[-]	
hydrodynamic mass Cm	=	1		relative SMF submergence depth d/B	=	0,66	[-]	
hydrodynamic drag Cd	=	1		relative SMF thickness	=	0,50	[-]	
Estimates for the slump geometry								
Radius of curvature R	=	0,35	[m]					
Char. Distance S0	=	0,09	[m]					
Angular displac. delta Phi	=	0,48	[rad]					
Initial acceleration a0	=	0,73	[m/s^2]					
Max velocity u max (SMF)	=	0,25	[m/s]					
Char. Time t0	=	0,34	[s]					
Wave parameter								
Wave length initial	=	**1,039**	**[m]**					
Wave height initial, 2D	=	**12,085**	**[mm]**					
Wave height initial, **3D**	=	7,954	[mm]					

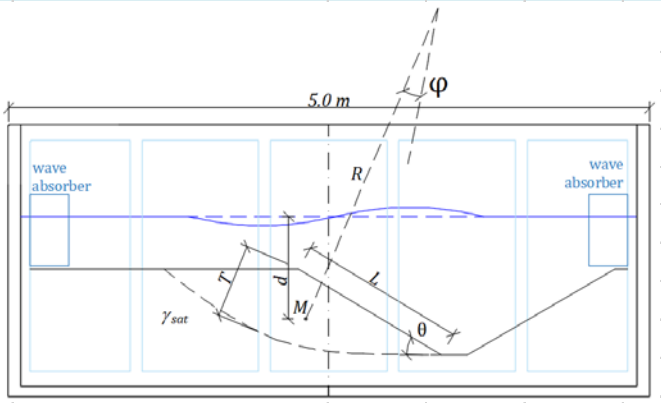

Test 4, failure 2

Slope failure geometry, initial large displacement

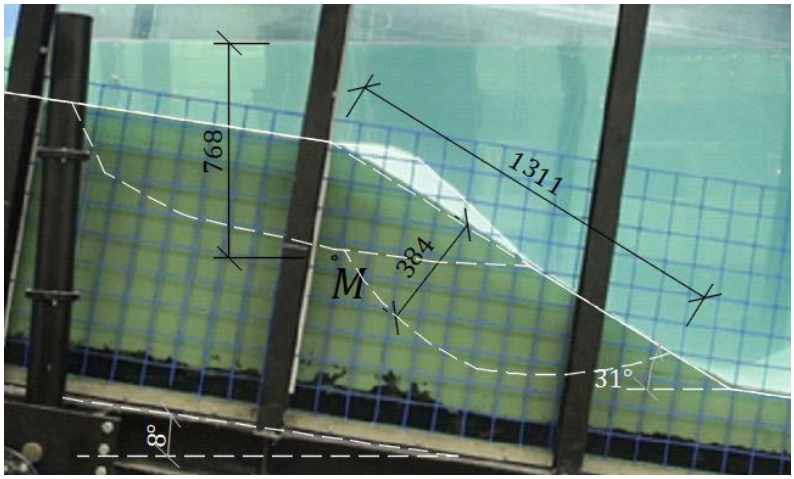

Input parameters			
Slide length L	=	1,311	[m]
Slide width w	=	1,8	[m]
Slide thickness T	=	0,38	[m]
Initial submergence d	=	0,768	[m]
SMF bulk density rhol	=	1,917	[kg/m^3]
Density water	=	1	[kg/m^3]
Slope angle theta	=	31	[°]
Friction angle	=	0	[°]

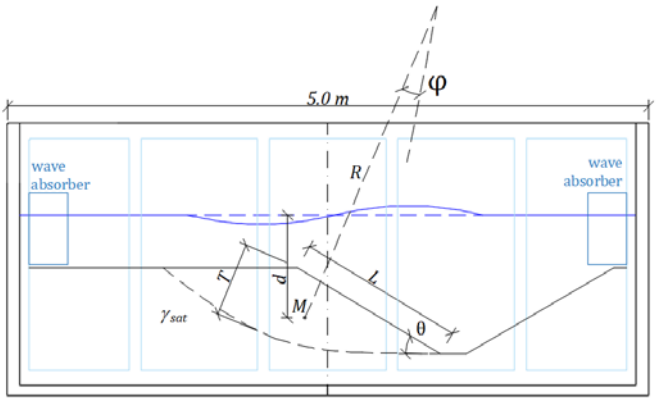

Coefficients				**Relative parameters**			
basal Coulomb friction Cn	=	0,28223		relative SMF density rhol/rhow	=	1,92	[-]
hydrodynamic mass Cm	=	1		relative SMF submergence depth d/B	=	0,59	[-]
hydrodynamic drag Cd	=	1		relative SMF thickness	=	0,29	[-]

Estimates for the slump geometry			
Radius of curvature R	=	0,57	[m]
Char. Distance S0	=	0,14	[m]
Angular displac. delta Phi	=	0,48	[rad]
Initial acceleration a0	=	0,75	[m/s^2]
Max velocity u max (SMF)	=	0,32	[m/s]
Char. Time t0	=	0,43	[s]

Wave parameter			
Wave length initial	=	**1,175**	**[m]**
Wave height initial, 2D	=	**10,970**	**[mm]**
Wave height initial, **3D**	=	6,637	[mm]

Failure 2, superficial mass flow after failure

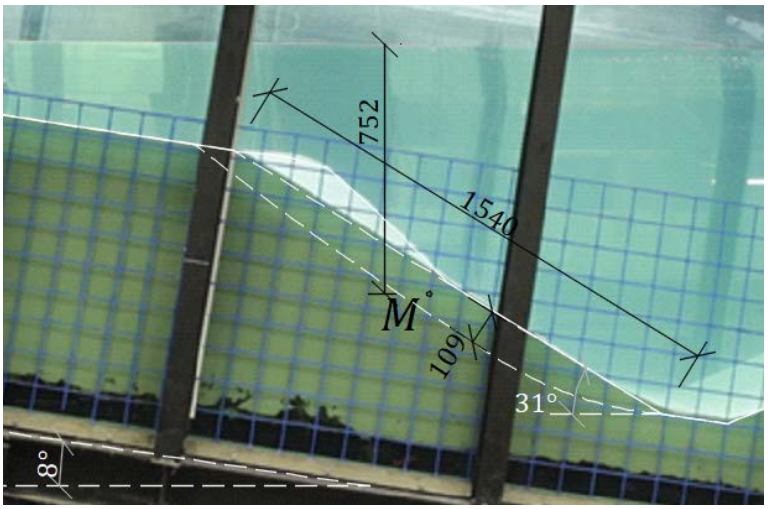

Input parameters								
Slide length L	=	1,504	[m]					
Slide width w	=	1,8	[m]					
Slide thickness T	=	0,109	[m]					
Initial submergence d	=	0,752	[m]					
SMF bulk density rhol	=	1,8	[kg/m^3]					
Density water	=	1	[kg/m^3]					
Slope angle theta	=	31	[°]					
Friction angle	=	0	[°]					
Coefficients				**Relative parameters**				
basal Coulomb friction Cn	=	0,28223		relative SMF density rhol/rhow	=	1,80	[-]	
hydrodynamic mass Cm	=	1		relative SMF submergence depth d/B	=	0,50	[-]	
hydrodynamic drag Cd	=	1		relative SMF thickness	=	0,07	[-]	
Estimates for the slump geometry								
Radius of curvature R	=	2,59	[m]					
Char. Distance S0	=	0,63	[m]					
Angular displac. delta Phi	=	0,48	[rad]					
Initial acceleration a0	=	0,68	[m/s^2]					
Max velocity u max (SMF)	=	0,65	[m/s]					
Char. Time t0	=	0,96	[s]					
Wave parameter								
Wave length initial	=	**2,613**	**[m]**					
Wave height initial, 2D	=	**6,406**	**[mm]**					
Wave height initial, **3D**	=	2,613	[mm]					

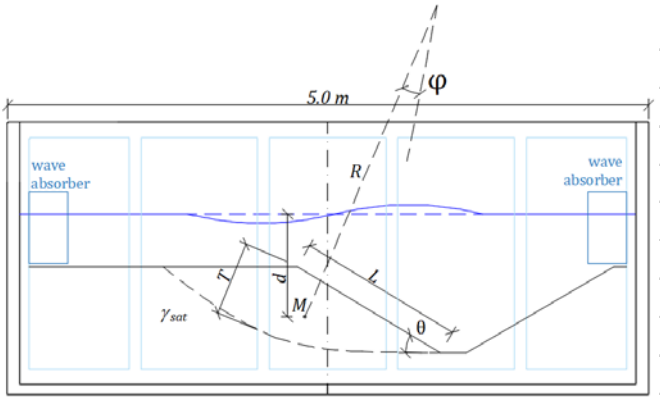

Test 4, failure 3

Slope deformation at onset of failure

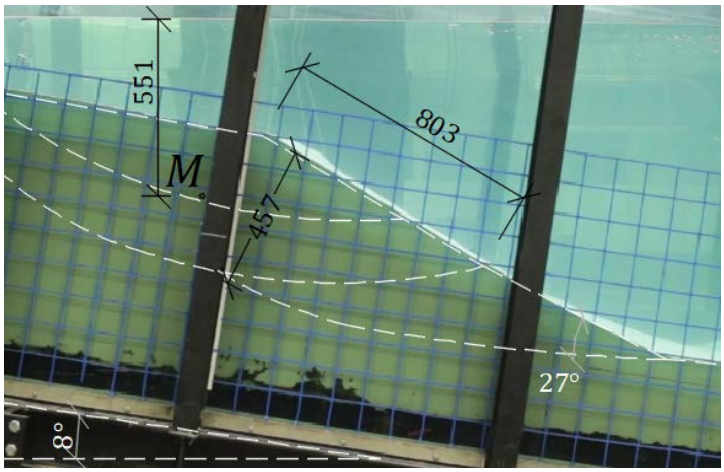

Input parameters								
Slide length L	=	0,803	[m]	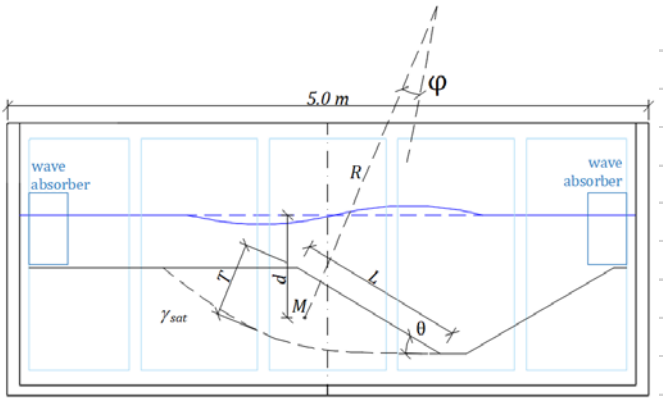				
Slide width w	=	2	[m]					
Slide thickness T	=	0,457	[m]					
Initial submergence d	=	0,551	[m]					
SMF bulk density rhol	=	1,917	[kg/m^3]					
Density water	=	1	[kg/m^3]					
Slope angle theta	=	27	[°]					
Friction angle	=	0	[°]					
Coefficients				**Relative parameters**				
basal Coulomb friction Cn	=	0,27151		relative SMF density rhol/rhow	=	1,92	[-]	
hydrodynamic mass Cm	=	1		relative SMF submergence depth d/B	=	0,69	[-]	
hydrodynamic drag Cd	=	1		relative SMF thickness	=	0,57	[-]	
Estimates for the slump geometry								
Radius of curvature R	=	0,18	[m]					
Char. Distance S0	=	0,04	[m]					
Angular displac. delta Phi	=	0,48	[rad]					
Initial acceleration a0	=	0,75	[m/s^2]					
Max velocity u max (SMF)	=	0,18	[m/s]					
Char. Time t0	=	0,24	[s]					
Wave parameter								
Wave length initial	=	**0,556**	**[m]**					
Wave height initial, 2D	=	**8,173**	**[mm]**					
Wave height initial, **3D**	=	6,395	[mm]					

Failure 3, superficial mass flow due to failure progression

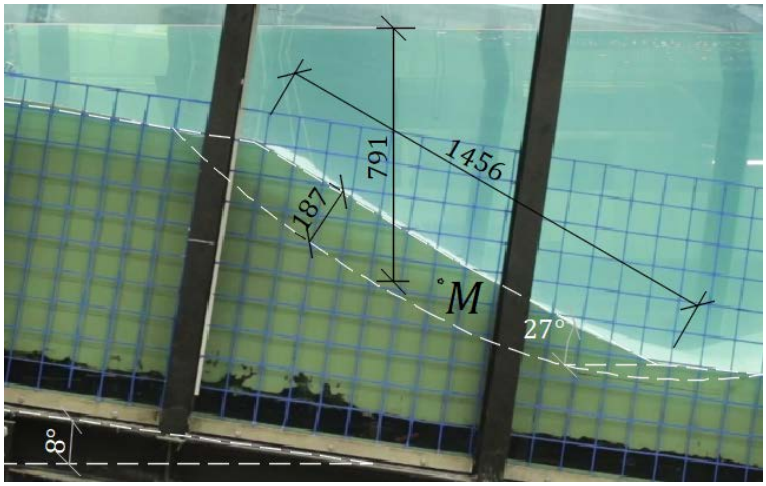

Input parameters

Slide length L	=	1,456	[m]
Slide width w	=	2	[m]
Slide thickness T	=	0,187	[m]
Initial submergence d	=	0,79	[m]
SMF bulk density rhol	=	1,8	[kg/m^3]
Density water	=	1	[kg/m^3]
Slope angle theta	=	27	[°]
Friction angle	=	0	[°]

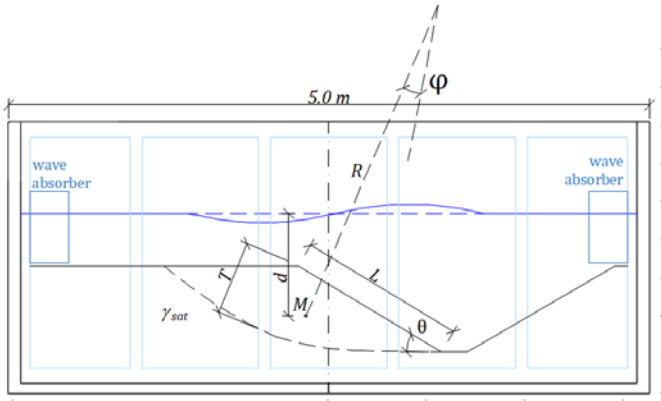

Coefficients				Relative parameters			
basal Coulomb friction Cn	=	0,27151		relative SMF density rhol/rhow	=	1,80	[-]
hydrodynamic mass Cm	=	1		relative SMF submergence depth d/B	=	0,54	[-]
hydrodynamic drag Cd	=	1		relative SMF thickness	=	0,13	[-]

Estimates for the slump geometry

Radius of curvature R	=	1,42	[m]
Char. Distance S0	=	0,34	[m]
Angular displac. delta Phi	=	0,48	[rad]
Initial acceleration a0	=	0,68	[m/s^2]
Max velocity u max (SMF)	=	0,48	[m/s]
Char. Time t0	=	0,71	[s]

Wave parameter

Wave length initial	**=**	**1,979**	**[m]**
Wave height initial, 2D	**=**	**7,780**	**[mm]**
Wave height initial, **3D**	=	3,910	[mm]

Appendix D – MatLab code for sensitivity study of predictive formulae

Predictive formulae acc. to Watts & Grilli 2005

For wave characteristics based on geometry of submarine landslide

Length and thickness

INPUT

```
test = ['Test 4, failure 2'];

L = 0.8:0.15:1.55; L(length(L)+1)=1.311;   %(m) slide length
w = 1.8;      %(m) slide width
T = 0.2:0.01:0.6; T(length(T)+1)=0.38;   %(m) slide thickness

for i = 1:length(L)
    for ii = 1:length(T)
```

```
    D = 0.768;        %(m) initial submergence of mass centre
    rhol = 1.917;     %(kg/m3) SMF bulk density
    rhow = 1.0;       %(kg/m3) water density
    theta = 31 /180*pi; % slope angle
    phi = 0    /180*pi; % friction angle
```

Coefficients

```
    Cn = 0.76/(pi*cos(theta));      % basal Coulomb friction
    Cm = 1;                         % hydrodynamic mass
    Cd = 1;                         % hydrodynamic drag

% Relative parameters
    rho = rhol/rhow;
    d(i,ii) = D/L(i);
    t(i,ii) = T(ii)/L(i);

% estimated slump geometry
    R(i,ii) = L(i)/8/t(i,ii);                       % (m) radius of curvature R
    S0(i,ii) = R(i,ii)*Cn*cos(theta);               % (m) characteristic distance
    delta_Phi(i,ii) = 2*S0(i,ii)/R(i,ii);           % (rad) angular displacement

% slope failure kinematics
    a0(i,ii) = 0.5*delta_Phi(i,ii)*9.81*(rhol-1)/(rhol+Cm);   % (m/s2) initial acceleration
    t0(i,ii) = ((R(i,ii)/9.81).*(rhol+Cm)/(rhol-1.0))^0.5;    % (sec) characteristic time
    umax(i,ii) = a0(i,ii)*t0(i,ii);                           % max velocirt slide
```

Output wave

```
wL(i,ii) = t0(i,ii)*(9.81*D)^0.5;                     % wave length (m)
```

```
wH(i,ii) = 0.0327*T(ii).*(sin(theta)^0.25)*(d(i,ii)^-1.25).*...
    ((R(i,ii)/L(i))^0.37).*delta_Phi(i,ii)^1.39*1000;  % wave amplitude (mm)
```

```
    end
error_neg(i) =  wH(i,length(T)) - min(wH(i,:));
error_pos(i) =  max(wH(i,:)) - wH(i,length(T));

end
```

Graphs

```
figure
hold on
trend = plot(L(1:length(L)-1), wH((1:length(L)-1),length(T)))
dT = errorbar(L(1:length(L)-1), wH((1:length(L)-1),length(T)),...
    error_neg(1:length(L)-1), error_pos(1:length(L)-1));
best_fit = errorbar(L(length(L)), wH((length(L)),length(T)),...
    error_neg(length(L)), error_pos(length(L)));
low_trend = plot(L(1:length(L)-1), wH((1:length(L)-1),1))
up_trend = plot(L(1:length(L)-1), wH((1:length(L)-1),length(T)-1))

% Adjust line properties (functional)
set(trend,'LineStyle', '--', 'Color', [0 0 .5])
set(low_trend,'LineStyle', '--', 'Color', [.75 .75 1])
set(up_trend,'LineStyle', '--', 'Color', [.75 .75 1])
set(dT, 'LineStyle', 'none', 'Marker', '.', 'Color', [.3 .3 .3])
set(best_fit, 'LineStyle', 'none', 'Marker', '.', 'Color', 'r')

% Adjust line properties (aesthetics)
set(trend, 'LineWidth', 2)
set(low_trend, 'LineWidth', 1)
set(up_trend, 'LineWidth', 1)
set(dT, 'LineWidth', 1, 'Marker', 'o', 'MarkerSize', 6, ...
    'MarkerEdgeColor', [.2 .2 .2], 'MarkerFaceColor' , [.7 .7 .7])
set(best_fit, 'LineWidth', 1, 'Marker', 'o', 'MarkerSize', 6, ...
    'MarkerEdgeColor', [.2 .2 .2], 'MarkerFaceColor' , 'r')

% Add labels
title(['Result of sensitivity study: landslide length and thickness'])
xlabel('Landslide length (m)');
ylabel('Wave amplitude (mm)');

% Add legend
hLegend = legend(['Trendline landslide length L'],...
    ['Wave amplitude with varied thickness T = ',num2str(min(T)),' - ',...
    num2str(max(T)),' m'], ...
    ['Best fit to measured data'], ['Lower and upper bounds'],...
    'Location', 'NorthWest');
% Adjust font
set(gca,'FontName', 'Cambria')
```

```
% Adjust axes properties
xlim([0.75 1.6])
set(gca, 'TickLength', [.01 .01], ...
    'XMinorTick', 'on', 'YMinorTick', 'on', 'YGrid', 'on', ...
    'XColor', [.3 .3 .3], 'YColor', [.3 .3 .3])
```

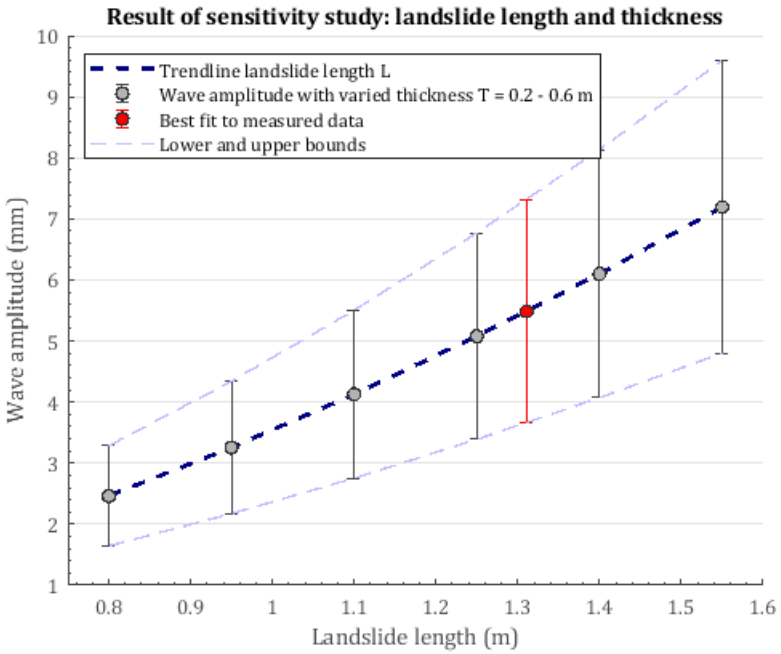

Thickness and submergence

INPUT

```
test = ['Test 4, failure 2'];

L = 1.311;   %(m) slide length
w = 1.8;      %(m) slide width
T = 0.2:0.01:0.6; T(length(T)+1)=0.384;   %(m) slide thickness
D = 0.6:0.04:0.8; D(length(D)+1)=0.768;   %(m) initial submergence of mass centre
for i = 1:length(D)
    for ii = 1:length(T)

    rhol = 1.917; %(kg/m3) SMF bulk density
    rhow = 1.0; %(kg/m3) water density
    theta = 31 /180*pi; % slope angle
    phi = 0    /180*pi; % friction angle
```

Coefficients

```
    Cn = 0.76/(pi*cos(theta));      % basal Coulomb friction
    Cm = 1;                         % hydrodynamic mass
    Cd = 1;                         % hydrodynamic drag

% Relative parameters
    rho = rhol/rhow;
    d(i,ii) = D(i)/L;
    t(i,ii) = T(ii)/L;

% estimated slump geometry
    R(i,ii) = L/8/t(i,ii);                      % (m) radius of curvature R
    S0(i,ii) = R(i,ii)*Cn*cos(theta);              % (m) characteristic distance
    delta_Phi(i,ii) = 2*S0(i,ii)/R(i,ii);          % (rad) angular displacement
```

```
% slope failure kinematics
    a0(i,ii) = 0.5*delta_Phi(i,ii)*9.81*(rhol-1)/(rhol+Cm);   % (m/s2) initial acceleration
    t0(i,ii) = ((R(i,ii)/9.81).*(rhol+Cm)/(rhol-1.0))^0.5;  % (sec) characteristic time
    umax(i,ii) = a0(i,ii)*t0(i,ii);                              % max velocirt slide
```

Output wave

```
wL(i,ii) = t0(i,ii)*(9.81*D(i))^0.5;                      % wave length (m)

wH(i,ii) = 0.0327*T(ii).*(sin(theta)^0.25)*(d(i,ii)^-1.25).*...
    ((R(i,ii)/L)^0.37).*delta_Phi(i,ii)^1.39*1000;  % wave amplitude (mm)
```

```
    end
error_neg(i) =  wH(i,length(T)) - min(wH(i,:));
error_pos(i) =  max(wH(i,:)) - wH(i,length(T));

end
```

Graphs

```
figure
hold on
trend = plot(D(1:length(D)-1), wH((1:length(D)-1),length(T)))
dT = errorbar(D(1:length(D)-1), wH((1:length(D)-1),length(T)),...
    error_neg(1:length(D)-1), error_pos(1:length(D)-1));
best_fit = errorbar(D(length(D)), wH((length(D)),length(T)),...
    error_neg(length(D)), error_pos(length(D)));
low_trend = plot(D(1:length(D)-1), wH((1:length(D)-1),1))
up_trend = plot(D(1:length(D)-1), wH((1:length(D)-1),length(T)-1))

% Adjust line properties (functional)
set(trend,'LineStyle', '--', 'Color', [0 0 .5])
set(low_trend,'LineStyle', '--', 'Color', [.75 .75 1])
set(up_trend,'LineStyle', '--', 'Color', [.75 .75 1])
set(dT, 'LineStyle', 'none', 'Marker', '.', 'Color', [.3 .3 .3])
set(best_fit, 'LineStyle', 'none', 'Marker', '.', 'Color', 'r')

% Adjust line properties (aesthetics)
set(trend, 'LineWidth', 2)
set(low_trend, 'LineWidth', 1)
set(up_trend, 'LineWidth', 1)
set(dT, 'LineWidth', 1, 'Marker', 'o', 'MarkerSize', 6, ...
    'MarkerEdgeColor', [.2 .2 .2], 'MarkerFaceColor' , [.7 .7 .7])
set(best_fit, 'LineWidth', 1, 'Marker', 'o', 'MarkerSize', 6, ...
    'MarkerEdgeColor', [.2 .2 .2], 'MarkerFaceColor' , 'r')

% Add labels
title(['Result of sensitivity study: landslide submergence and thickness'])
xlabel('Landslide initial submergence (m)');
ylabel('Wave amplitude (mm)');

% Add legend
hLegend = legend(['Trendline landslide submergence D'],...
```

```
    ['Wave amplitude with varied thickness T = ',num2str(min(T)),' - ',...
    num2str(max(T)),' m'], ...
    ['Best fit to measured data'], ['Lower and upper bounds'],...
    'Location', 'Northeast');
% Adjust font
set(gca,'FontName', 'Cambria')
% Adjust axes properties
xlim([0.59 0.81]); ylim([3 11])
set(gca, 'TickLength', [.01 .01], ...
    'XMinorTick', 'on', 'YMinorTick', 'on', 'YGrid', 'on', ...
    'XColor', [.3 .3 .3], 'YColor', [.3 .3 .3])
grid on; grid minor
```

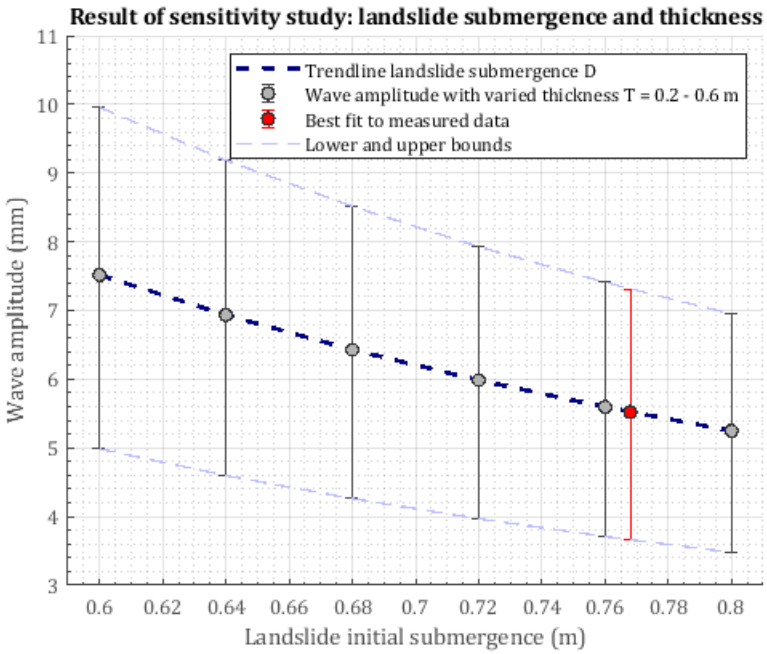

Published with MATLAB® R2018b

Appendix E – Schedule

Month/year	Phase	Month schedule, tasks and
Sept. 2018	Start	05/09/2018: approval of application for start of the master thesis. 13/09 – 22/09: Trip to Japan, project in Otsuchi-Cho with multidisciplinary team.
Oct. 2018	Literature review phase	Build-up of theoretical background knowledge, creating test ideas and formulating research questions.
Nov. 2018	Test preparation	Development and trial of required installations, such as simple wave generator, wave absorber, landslide triggering mechanism; preparation kick-off meeting and kick-off report. 23/11/2018: Kick-Off meeting
Dec. 2018 – Jan. 2019	1st testing and data analysis phase	Set up and performance of the first round of tests, data collection and filtering Interpretation of test results, assembly and organisation of data, comparison with analytical solutions given by available formulae. End January 2019: meeting with assessment committee
Feb. 2019	2nd testing and data analysis phase	Set up and performance of the next round of tests including changes and adjustments required, test data collection and analysis. End February 2019: meeting with assessment committee
Mar. 2019	Evaluation phase	Discussion and evaluation of study outcome, drawing of conclusions based on investigation results End March 2019: meeting with assessment committee
Apr. 2019	Writing phase	Preparation of the final report based on acquired knowledge and drawn conclusions. 3rd of May 2019: Green light meeting
May 2019	Final phase	Report revision, formulation of recommendations for further research, preparation for the final defence. 24th of May 2019: Final defence presentation

Bibliography

Daubechies, I. (1992). Ten Lectures on Wavelets. Society for Industrial and Applied Mathermatics, Phildelphia, Pennsylvania. Retrieved from http://books.google.com.

De Jager, R. R., Maghsoudloo, A., Askarinejad, A., & Molenkamp, F. (2017). Preliminary Results of Instrumented Laboratory Flow Slides. Procedia Engineering.

Devleker, K. (2016). Understanding Wavelets, Parts 1 - 4. MATLAB Tech Talks. Retrieved from https://www.youtube.com/watch?v=QX1-xGVFqmw.

Enet, F., Grilli, S. T. (2007). Experimental Study of Tsunami Generation. Journal of Waterway Port Coastal and Ocean Engineering-Asce, 133(6), 442-454.

Fritz, H. M. (2002). Initial phase of landslide generated impulse waves. PhD thesis, ETH Zürich.

Goda, Y., Suzuki, Y. (1976). Estimation of incident and reflected waves in random wave experiments. Proc. 15th Coastal Engineering Conference, ASCE, pp. 828–845

Grilli, S. T., Watts, P. (2005). Tsunami generation by submarine mass failure. I: Modeling experimental validation, and sensitivity analyses. Journal of Waterway Port Coastal and Ocean Engineering.

Haage, S. S. (2018). Wave Flume Experiments on Permeable Structures, The effect of arrays of cylinders on wave reflection, dissipation and transmission. MSc thesis, Delft University of Technology.

Harbitz, C. B., Løvholt, F., Pedersen, G., & Masson, D. G. (2006). Mechanisms of tsunami generation by submarine landslides: a short review. Norwegian Journal of Geology, 86(3), 255-264.

Hughes, S. A. (1993). Physical Models and Laboratory Techniques in Coastal Engineering. Singapore: World scientific, Advanced series on ocean engineering 7.

Ippen, A. T., Goda, Y. (1963). Wave induced oscillations in harbours: the solution for a rectangular harbour connected to the open-sea. Cambridge, Mass.: Hydrodynamics Laboratory, Dept. of Civil Engineering, Massachusetts Institute of Technology.

Jiang, L., Leblond, P. H. (1992). The Coupling of a Submarine Slide and the Surface-Waves Which It Generates. Journal of Geophysical Research-Oceans, 97(C8), 12731-12744.

Jiang, L., Leblond, P. H. (1994). Three-dimensional Modeling of Tsunami Generation Due to a submarine mudslide. Department of Oceanography, University of British Columbia, Vancouver. Journal of Physical Oceanography, 24, 559-572.

Klaasman, B. (2005). Manual for Matlab scripts. Laboratory of Fluid Mechanics of Delft University of Technology.

Levin, B. V., Nosov. M. A. (2005). Original: Левин, Б. В., Носов, М. А., Физика цунами и родственных явлений в океане. Геофизика. Янус-К. 5-8037-0312-5.

Lim, H. C. (2014). Optimum design of a sloping-wall-type wave absorber placed in a sinusoidal propagating wave. Ocean Engineering, 88, 588-597.

Liu, P. C. (1998). A Fifteen Minutes Introduction of Wavelet Transform and Applications. 10.13140/RG.2.1.5088.1447. Retrieved from https://www.researchgate.net/publication.

Liu, P. L. F., Wu, T. R., Raichlen, F., Synolakis, C. E., & Borrero, J. C. (2005). Runup and rundown generated by three-dimensional sliding masses. Journal of Fluid Mechanics, 536, 107-144.

Maghsoudloo, A., Askarinejad, A., De Jager, R. R., Molenkamp, F., & Hicks, M. A. (2018). Experimental investigation of pore pressure and acceleration development in static liquefaction induced failures in submerged slopes. Physical Modelling in Geotechnics, 2.

MATALA. (2019). MATALA filter media website. Retrieved from http://www.matala.com.tw/biomedia/matala-filter-media.html#tab5

McFall, B. C., Fritz, H. M. (2016). Physical modelling of tsunamis generated by three-dimensional deformable granular landslides on planar and conical island slopes. Proc. Mathematical, Physical and Engineering Sciences, 472(2188), 20160052.

Mohammed, F., & Fritz, H. M. (2012). Physical modeling of tsunamis generated by three-dimensional deformable granular landslides. Journal of Geophysical Research-Oceans, 117(C11).

Neelamani, S., Al-Salem, K., & Taqi, A. (2017). Experimental Investigation on Wave Reflection Characteristics of Slotted Vertical Barriers with an Impermeable Back Wall in Random Wave Fields. Journal of Waterway, Port, Coastal, and Ocean Engineering, 143(4).

Pelinovsky, E., & Poplavsky, A. (1996). Simplified model of tsunami generation by Submarine Landslides. Physics and Chemistry of the Earth, 21, 1–2, 13-17.

Richards, A. F., Palmer, H. D., & Perlow, M. (1975). Review of continental shelf marine geotechnics: Distribution of soils, measurement of properties, and environmental hazards. Marine Geotechnology, 1(1), 33-67.

Sassa, S., & Takagawa, T. (2018). Liquefied gravity flow-induced tsunami: first evidence and comparison from the 2018 Indonesia Sulawesi earthquake and tsunami disasters. Landslides, 16(1), 195-200.

Smolentsev, N. K. (2014). Original: Смоленцев, Н. К., Основы теории вейвлетов. Вейвлеты в MATLAB 2014. ДМК Пресс, 628 с.

Tappin, D. R., Grilli, S. T., Harris, J. C., Geller, R. J., Masterlark, T., Kirby, J. T., Mai, P. M. (2014). Did a submarine landslide contribute to the 2011 Tohoku tsunami? Marine Geology, 357, 344-361.

Tappin, D. R., Watts, P., McMurtry, G. M. (1998). Prediction of slump generated tsunamis: The July 17th 1998 Papua New Guinea event. Natural Hazards and Earth System Science, Copernicus Publications on behalf of the European Geosciences Union, 8 (2), pp.243-266.

Tiedeman, S. A., Allsop, W., Russo, V., & Brown, A. (2012). A Demountable Wave Absorber for Wave Flumes and Basins. Coastal Engineering Proceedings, 1(33).

Torrence, C., Compo, G. P. (1998). A practical guide to wavelet analysis. Bulletin of the American Meteorological Society, 79(1), 61-78.

Watts, P. (1997). Water waves generated by underwater landslides. California Institute of Technology. PhD thesis, California Institute of Technology, Pasadena, CA, USA.

Watts, P., & Grilli, S. (2005). Tsunami Generation by Submarine Mass Failure, I, wavemaker models. Journal of Waterway, Port, Coastal, and Ocean Engineering. C-ASCE 131, 283–297.

Watts, P., Grilli, S. T., Tappin, D. R., & Fryer, G. J. (2005). Tsunami generation by submarine mass failure. II: Predictive equations and case studies. Journal of Waterway Port Coastal and Ocean Engineering-Asce, 131(6), 298-310.

Wiegel, R. L. (1955). Laboratory studies of gravity waves generated by the movement of a submerged body. Transactions, American Geophysical Union, 36(5), 759-774.